

# A Systematic Study of the X-ray Cyclotron-Line Sources Observed by BeppoSAX

## **Dissertation**

der Mathematisch-Naturwissenschaftlichen Fakultät  
der Eberhard Karls Universität Tübingen  
zur Erlangung des Grades eines  
Doktors der Naturwissenschaften  
(Dr. rer. nat.)

vorgelegt von

Rozaliya Doroshenko

aus Kazan, Russland

Tübingen  
2017

Gedruckt mit Genehmigung der Mathematisch-Naturwissenschaftlichen Fakultät  
der Eberhard Karls Universität Tübingen.

Tag der mündlichen Qualifikation:	27.11.2017
Dekan:	Prof. Dr. Wolfgang Rosenstiel
1. Berichterstatter:	Prof. Dr. Andrea Santangelo
2. Berichterstatter:	Prof. Dr. Klaus Werner

---

## Abstract

---

X-ray binaries are binary systems in which a compact object accretes plasma from their non-degenerate primary stellar companions. According to the mass of the primary star, X-ray binaries are divided in two classes: low mass X-ray binaries (LMXB), in which the mass of the companion is less than or of the order of a solar mass; and high mass X-ray binaries (HMXB), in which the mass of the primary is usually more than ten solar masses.

The different phenomena observed are also related to the nature of the compact object, which can be a white dwarf, a neutron star or a black hole. The fundamental mechanism to produce the high luminosity observed in X-ray binaries ( $L \sim 10^{35} - 10^{38}$  erg/s) is accretion, by which the gravitational energy of accreted matter is released and thermalised on the surface of the compact object.

Accreting X-ray pulsars are X-ray binaries and more specifically highly magnetised neutron stars ( $B \sim 10^{12} - 10^{14}$  G) in close binary systems accreting plasma from their normal low or high mass companions. In these systems, at the so called Alfvén radius, the pressure of the infalling matter is balanced by the pressure of the magnetic field of the neutron star. The accreted plasma is channeled along the magnetic field lines (which in the simplest approximation have the form of a dipole) onto the neutron star surface. X-ray pulsations arise due to the misalignment between the spin rotation axis of the neutron star and its strong magnetic field.

The observed phenomena of accreting pulsars are rather complex. They include light curves, spin and orbital periods and their variability, energy dependence of pulse profiles, as well as pulse and time dependence of energy spectra. It is through the understanding of these phenomena, and their comparison with theoretical models, that mechanisms for the formation and transport of the radiation can be clarified.

This work presents a systematic study of a sample of X-ray pulsars observed with *BeppoSAX* mission. The sample includes all observed sources that show a cyclotron line feature in their energy spectra. In the first part of the thesis the basic properties of X-ray pulsars, the instrumentation onboard *BeppoSAX* and the

methods used for the data analysis are presented and discussed. The second part presents the results of observations of nine X-ray pulsars. Most of these *BeppoSAX* data were analysed for the first time. Among the most interesting results obtained in the work are the discovery of the cyclotron line feature in the unique source GRO J1744–28, the transient bursting pulsar with intermediate type bursts; the unprecedented temporal and spectral analysis of the *BeppoSAX* data of XTE J1946+274 during its outburst in 1998; the study of the spectrum of Her X–1 that can be described for all 35 day phases with approximately constant photon index if a partial covering component is included in the model at some phases; the comprehensive broad band timing and spectral analysis of the pulsars 4U 1626–67, 4U 1907+09, 4U 1538–52 and 4U 0115+63; the spectral and timing behaviour of Cen X–3 during its low and high states.

The third part of the thesis is devoted to the study of the sample properties of the X-ray pulsars with cyclotron lines. Through this study several correlations between the cyclotron line parameters and the continuum were analysed and discussed in the framework of the existing literature. I also show that the cyclotron line parameters can significantly depend on the choice of continuum model. The observed rich phenomena was eventually interpreted in the light of theoretical models recently developed to explain the emission of these sources.

---

## Zusammenfassung

---

Röntgendoppelsterne sind Doppelsternsysteme, in welchen ein kompaktes Objekt Plasma von seinem nicht entarteten Begleiter, dem Primärstern, akkretiert. Abhängig von der Masse des Primärsterns werden Röntgendoppelsterne in zwei Klassen unterteilt: sogenannte *low mass X-ray binaries* (LMXB), bei welchen die Masse des Begleiters in der Größenordnung von einer Sonnenmasse oder darunter liegt; und *high mass X-ray binaries* (HMXB), bei welchen die Masse des Primärsterns üblicherweise mehr als zehn Sonnenmassen beträgt.

Die zu beobachtenden, unterschiedlichen Phänomene hängen auch mit der Art des kompakten Objektes zusammen, das ein weißer Zwerg, ein Neutronenstern, oder ein schwarzes Loch sein kann. Der grundlegende Mechanismus zur Erzeugung der hohen Leuchtkraft ( $L \sim 10^{35} - 10^{38}$  erg/s), die in Röntgendoppelsternen beobachtet werden kann, ist die Akkretion, durch welche die Gravitationsenergie der akkretierten Masse freigesetzt und die Masse an der Oberfläche des kompakten Objektes aufgeheizt wird.

Akkretierende Röntgenpulsare sind Röntgendoppelsterne, beziehungsweise, genauer gesagt, stark magnetisierte Neutronensterne ( $B \sim 10^{12} - 10^{14}$  G) in engen Doppelsternsystemen, die Plasma von ihrem normalen massearmen oder -reichen Begleiter akkretieren. In diesen Systemen befindet sich am sogenannten Alfvén-Radius der Druck der einfallenden Masse mit dem Druck durch das Magnetfeld des Neutronensterns im Gleichgewicht. Das akkretierte Plasma wird entlang der Magnetfeldlinien (welche in einfachster Näherung die Form eines Dipols haben) auf die Oberfläche des Neutronensterns gelenkt.

Die beobachteten Phänomene akkretierender Pulsare sind recht komplex. Sie umfassen Lichtkurven, Spin- und Orbitalperioden, deren Veränderlichkeit, die Energieabhängigkeit von Pulsprofilen sowie die Puls- und Zeitabhängigkeit von Energiespektren. Durch das Verständnis dieser Phänomene, und den Vergleich mit theoretischen Modellen, können die Mechanismen zur Entstehung und zum Transport der Strahlung erschlossen werden.

Diese Arbeit präsentiert eine systematische Studie einer Auswahl von Röntgenpulsaren, welche mit der *BeppoSAX* Mission beobachtet wurden. Die Auswahl bein-

haltet alle beobachteten Quellen, die eine Zyklotronlinie in ihrem Energiespektrum zeigen. Im ersten Teil der Dissertation werden die grundlegenden Eigenschaften von Röntgenpulsaren, die Instrumente, mit welchen *BeppoSAX* ausgestattet ist, sowie die Methoden, die bei der Datenanalyse angewendet werden, vorgestellt und diskutiert. Der zweite Teil zeigt die Ergebnisse für Beobachtungen von neun Röntgenpulsaren. Die meisten dieser *BeppoSAX* Daten wurden zum ersten Mal analysiert. Zu den interessantesten Ergebnissen der Arbeit zählen die Entdeckung der Zyklotronlinie in der einzigartigen Quelle GRO J1744–28, dem kurzzeitig ausbrechenden Pulsar mit Zwischentypen von Ausbrüchen; die erste Zeit- und Spektralanalyse der *BeppoSAX* Daten von XTE J1946+274, welche während des Ausbruchs 1998 aufgenommen wurden; die Untersuchung des Spektrums von Her X–1, das für alle 35 Tagesphasen mit einem annähernd konstanten Photonenindex beschrieben werden kann, wenn im Modell bei manchen Phasen eine teilweise verdeckende Komponente mit einbezogen wird; die umfassende Zeit- und Spektralanalyse im breiten Energiebereich der Pulsare 4U 1626–67, 4U 1538–52 und 4U 0115+63; das spektrale und zeitliche Verhalten von Cen X–3 sowohl im Zustand niedriger als auch im Zustand hoher Leuchtkraft.

Der dritte Teil der Dissertation beschäftigt sich mit der Untersuchung der Eigenschaften der gesamten Auswahl an Röntgenpulsaren mit Zyklotronlinien. Durch diese Untersuchung wurden mehrere Zusammenhänge zwischen den Parametern der Zyklotronlinie und dem Kontinuum analysiert und im Rahmen der bestehenden Literatur diskutiert. Ich konnte ebenfalls zeigen, dass die Parameter der Zyklotronlinie maßgeblich von der Wahl des Kontinuummodells abhängen können. Die beobachteten, umfassenden Phänomene werden schließlich vor dem Hintergrund kürzlich entwickelter, theoretischer Modelle interpretiert, um die Emission dieser Quellen zu erklären.

# Contents

---

<b>I</b>	<b>Introduction</b>	<b>11</b>
<b>1</b>	<b>X-ray Binaries</b>	<b>14</b>
1.1	Neutron Stars . . . . .	14
1.2	Binary Systems . . . . .	15
1.2.1	Accretion . . . . .	17
1.2.2	Low Mass X-Ray Binaries . . . . .	18
1.2.3	High Mass X-Ray Binaries . . . . .	19
1.3	Evolution in Close Binary Systems . . . . .	20
1.3.1	Evolution of HMXB . . . . .	22
1.3.2	Evolution of LMXB . . . . .	25
1.4	Recent Results . . . . .	25
<b>2</b>	<b>Accreting Pulsars</b>	<b>26</b>
2.1	A General View on Accreting Pulsars . . . . .	26
2.2	Cyclotron Resonance Scattering Feature . . . . .	31
<b>3</b>	<b>BeppoSAX</b>	<b>35</b>
<b>4</b>	<b>Data Analysis and Spectral Models.</b>	<b>39</b>
4.1	Observations . . . . .	39
4.2	Data Analysis . . . . .	39
4.3	Spectral Models . . . . .	40
<b>II</b>	<b>Accreting Pulsars Observed with <i>BeppoSAX</i></b>	<b>45</b>

---

<b>5</b>	<b>Hercules X-1</b>	<b>47</b>
5.1	Source Description . . . . .	47
5.2	Observations . . . . .	48
5.2.1	Timing Analysis . . . . .	49
5.2.2	Spectral Analysis . . . . .	52
5.3	Conclusion . . . . .	57
<b>6</b>	<b>4U 1626-67</b>	<b>65</b>
6.1	Source Description . . . . .	65
6.2	Observations and Data Analysis . . . . .	67
6.2.1	Timing Analysis . . . . .	67
6.2.2	Spectral Analysis . . . . .	68
6.3	Conclusion . . . . .	68
<b>7</b>	<b>4U 1907+09</b>	<b>73</b>
7.1	Source Description . . . . .	73
7.2	Observations . . . . .	74
7.2.1	Timing Analysis . . . . .	74
7.2.2	Spectral Analysis . . . . .	77
7.3	Conclusion . . . . .	80
<b>8</b>	<b>4U 1538-52</b>	<b>82</b>
8.1	Source Description . . . . .	82
8.2	Observations . . . . .	83
8.2.1	Timing Analysis . . . . .	85
8.2.2	Spectral Analysis . . . . .	86
8.3	Conclusion . . . . .	91
<b>9</b>	<b>Vela X-1</b>	<b>93</b>
9.1	Source Description . . . . .	93
9.2	Observations . . . . .	94
9.2.1	Timing Analysis . . . . .	94
9.2.2	Spectral Analysis . . . . .	97
9.3	Conclusion . . . . .	99



---

<b>10 Centaurus X-3</b>	<b>108</b>
10.1 Source Description . . . . .	108
10.2 Observations . . . . .	109
10.2.1 High Energy States . . . . .	109
10.2.1.1 Timing Analysis . . . . .	109
10.2.1.2 Spectral Analysis . . . . .	114
10.2.2 Low Energy States . . . . .	120
10.3 Conclusion . . . . .	123
<b>11 4U 0115+63</b>	<b>124</b>
11.1 Source Description . . . . .	124
11.2 Observations . . . . .	125
11.2.1 Timing Analysis . . . . .	125
11.2.2 Spectral Analysis . . . . .	128
11.3 Conclusion . . . . .	130
<b>12 XTE J1946+274</b>	<b>137</b>
12.1 Source Description . . . . .	137
12.2 Observations . . . . .	138
12.2.1 Timing Analysis . . . . .	138
12.2.2 Spectral Analysis . . . . .	141
12.3 Discussion and Conclusion . . . . .	147
<b>13 GRO J1744-28</b>	<b>152</b>
13.1 Source Description . . . . .	152
13.2 Observations . . . . .	154
13.2.1 Timing Analysis . . . . .	154
13.2.2 Spectral Analysis . . . . .	159
13.2.2.1 Analysis of the Burst Spectra . . . . .	162
13.3 Conclusion . . . . .	168
<b>III Discussion and Conclusions</b>	<b>171</b>
<b>14 Summary and Interpretation of Spectral Analysis Results</b>	<b>173</b>
14.1 The Accretion Regime and the Geometry of the Emission Region	188
<b>15 Conclusion</b>	<b>193</b>
<b>Bibliography</b>	<b>196</b>



# **Part I**

# **Introduction**



Astrophysics is a branch of physics and astronomy which aims to understand the physical processes in celestial objects based on the limited observational information available. This mainly comes in form of electromagnetic waves in all energy ranges from radio to gamma. The multi-wavelength observations, which changed our view of the universe completely, became possible relatively recently: the radio in the '30s and the far infrared, far ultraviolet, X-ray and gamma-range in '60s – '80s of the last century. This work is dedicated to the analysis and interpretation of the X-ray observations of the accreting neutron stars carried out by the *BeppoSAX* mission in 1996 – 2002.

# CHAPTER 1

---

## X-ray Binaries

### 1.1 Neutron Stars

Immediately after the discovery of the neutron Landau (1932) suggested for the first time that a superdense state of matter might be realised also in macroscopic objects, i.e., *neutron stars* (NSs, see a historical review by Yakovlev et al. 2013). Soon after Baade & Zwicky (1934) suggested that such objects may form following the core collapse of massive stars. A theoretical investigation of physical conditions inside the then hypothetic NSs was published soon after by Landau (1938). In 1939 Oppenheimer & Volkoff (1939), using the work of Tolman (1939), calculated an upper bound to the mass of NSs, which is approximately 1.5 to 3.0 solar masses (*Tolman–Oppenheimer–Volkoff limit*). However, only in 1967 A. Hewish and J. Bell discovered the first NSs, observing *radio pulsars* (Hewish et al. 1968)<sup>1</sup>. A year later Pacini (1968) wrote a predictive paper about the rotating NSs, pulsars and supernova remnants. Accreting NSs in a close binary systems were later also discovered as compact X-ray sources with the first X-ray satellite *Uhuru* in 1972 (Giacconi et al. 1972).

In most cases NSs form during the core collapse of massive stars with mass on the main sequence exceeding  $8 - 10M_{\odot}$ . The core collapse is accompanied by type II or type Ib/c supernova explosions, so the total number of NSs in our Galaxy may be estimated based on the observed supernova rate, and turns out to be quite large:  $\sim 10^8 - 10^9$ . NSs are not particularly rare objects.

They do have, however, many extreme properties. The radius of a solar mass NS is just about 10 km, so matter density in the core is higher than that in atomic nuclei  $\rho_0 \approx 2.8 \cdot 10^{14} \text{ g/cm}^3$ . However, unlike in atomic nuclei, in NS the gravity is still able to balance the “strong” force making them unique natural laboratories that

---

<sup>1</sup>The Nobel Prize in Physics 1974 was awarded jointly to Sir Martin Ryle and Antony Hewish “for their pioneering research in radio astrophysics: Ryle for his observations and inventions, in particular of the aperture synthesis technique, and Hewish for his decisive role in the discovery of pulsars”.

allow to study the fundamental physics under extreme conditions. Compactness of the NSs makes them also an ideal probe to verify the predictions of general relativity with high precision.

For the discovery and long-term observations of the double pulsar PSR 1509-58, astrophysicists J. Taylor and R. Hulse received the Nobel Prize in physics in 1993<sup>2</sup>. Observations of this and similar objects provide the most precise mass estimates for the NS masses, and the most rigorous verification of the general relativity including the existence of gravitational waves<sup>3</sup>. The summary of the combined measured masses of the NSs in binary pulsars is presented on Figure 1.1.

Although theoretical lower limit of the mass of a NS is about  $0.1M_{\odot}$ , in all cases the observed masses exceed the solar mass. The maximal mass of the NS (Tolman–Oppenheimer–Volkoff limit) is also known only approximately (about  $3M_{\odot}$ ). The corresponding estimates of NS size lie in the range of 10 – 15 km. In fact, radii of NSs can be less well constrained. So far the measurements of the radius have been performed only for X-ray bursters (see for example Lattimer & Prakash 2016; Watts et al. 2016; Suleimanov et al. 2016). From the observations is also known that NSs can have ultra-strong magnetic fields, up to  $10^{12} - 10^{14}$  G (see for a review Revnivtsev & Mereghetti 2015).

## 1.2 Binary Systems

In most cases the progenitors of NSs are members of the binary systems (Fig. 1.2), and the mass transfer between the binary components is thought to play essential role in the evolution of the system and formation of NSs. However, the supernova explosion accompanying the birth of the NS is likely to disrupt the binary, so the majority of NSs are, in fact, observed as isolated radio-emitting pulsars. On the other hand, the NS might also remain in binary, and then the mass transfer from the non-degenerate might power *accretion* onto the NS. In this case the kinetic energy of in-falling matter thermalises upon impact with the surface and is then emitted in X-rays.

---

<sup>2</sup>The Nobel Prize in Physics 1993 was awarded jointly to Russell A. Hulse and Joseph H. Taylor Jr. “for the discovery of a new type of pulsar, a discovery that has opened up new possibilities for the study of gravitation”.

<sup>3</sup>The Nobel Prize in Physics 2017 was divided, one half awarded to Rainer Weiss, the other half jointly to Barry C. Barish and Kip S. Thorne “for decisive contributions to the LIGO detector and the observation of gravitational waves”.

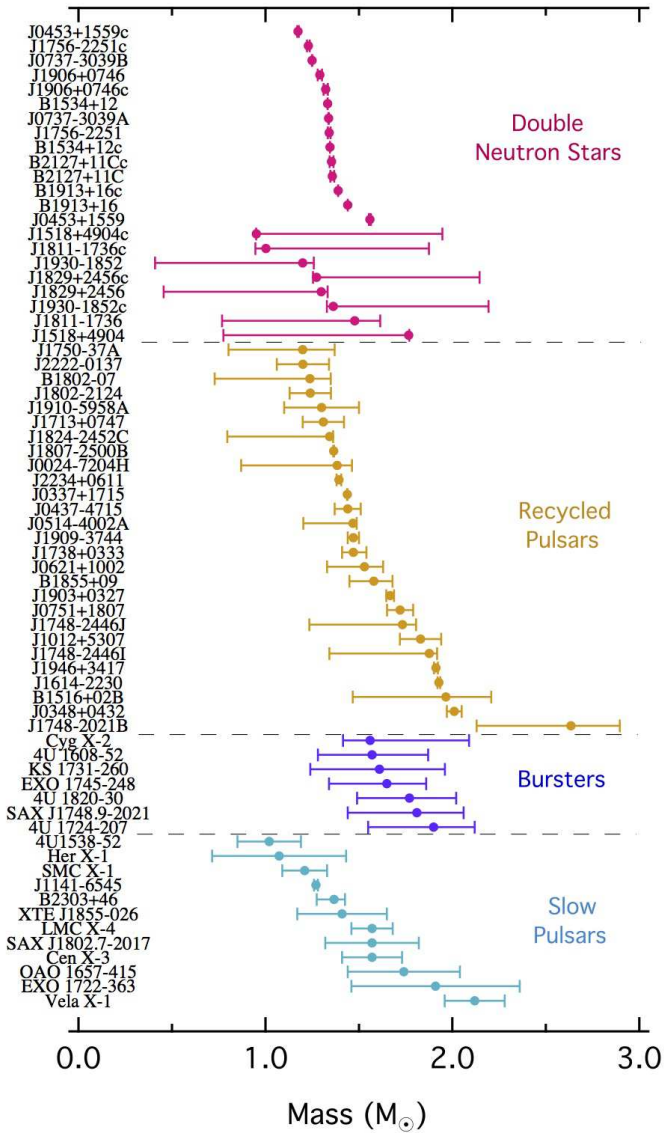


Figure 1.1: An up-to-date compilation of NS mass measurements in various source categories. From Özel & Freire (2016).



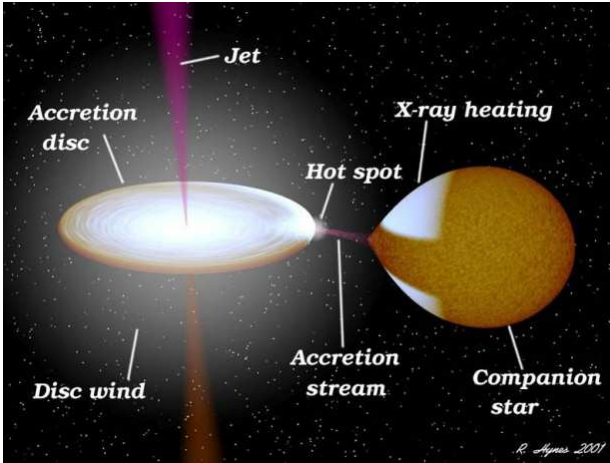


Figure 1.2: Artist's representation of a binary system with a Roche lobe accretion.

### 1.2.1 Accretion

*Accretion* is a very effective way to produce energy. So, accreting sources are amongst the most luminous objects in the Universe. Their luminosity is given by:

$$L = \frac{dE_{\text{acc}}}{dt} = G \frac{m}{r} \frac{dM}{dt} = G \frac{m}{r} \dot{M}, \quad (1.1)$$

where  $L$  is the luminosity,  $m$  and  $r$  are the mass and radius of the compact object,  $\dot{M}$  is the mass accretion rate of the mass inflow (see for a review Lipunov et al. 1992). It is seen that the higher accretion rate gives the higher luminosity. In the *X-ray binary systems* (XRBS) containing a NS or a *black hole* (BH), the luminosity  $L_X$  can reach up to  $\sim 10^{39}$  ergs  $\text{s}^{-1}$ . But there is a limit on the luminosity to the accreting source, called *Eddington luminosity*. If we look at the plasma at a distance  $R$  with the luminosity  $L$ , then the flux is given by:

$$F = \frac{L}{4\pi R^2}. \quad (1.2)$$

Photons and electrons in the plasma interact via *Thomson scattering*, and the interacting force is

$$F_i = \frac{F\sigma_T}{c}, \quad (1.3)$$

where

$$\sigma_T = \frac{8\pi}{3} \left( \frac{e^2}{m_e c^2} \right)^2 \sim 6.7 \cdot 10^{-25} \text{ cm}^2 \quad (1.4)$$

is the *Thomson scattering cross section*. The gravitational force by the central object with mass  $M$  is given by:

$$F_g = \frac{GMm_p}{R^2}. \quad (1.5)$$

And equilibrium

$$F_i = F_g \quad (1.6)$$

is possible at the critical *Eddington luminosity*:

$$L_{\text{Edd}} = \frac{4\pi GMm_p c}{\sigma_T} \approx 10^{38} \frac{M}{M_\odot} \frac{\text{erg}}{\text{s}}. \quad (1.7)$$

This is the maximum luminosity an accreting object can achieve because of accretion, assuming spherically symmetric accretion and steady flow.

Mass transfer in binary systems is always accompanied by angular momentum transfer, so, taking into account their moment of inertia, compact NSs must all be spinning. If the NS is strongly magnetised, the captured matter will be funnelled onto the magnetic poles, and the energy release will be anisotropic. Should the magnetic and rotation axes be misaligned, the X-ray flux observed by external observers will vary periodically and the NS will appear as an *X-ray pulsar* (see for a review Bildsten et al. 1997). If the magnetic field is weaker than  $\sim 10^8$  G, the matter is accumulated on the surface of the NS, which might lead to the ignition of thermonuclear burning once the temperature and density exceed certain critical values. In this case the so-called *thermo-nuclear bursts* are observed (Lewin et al. 1993).

If the angular momentum of a particle is too high, matter can not fall directly onto the compact object. Plasma follows the circular orbit with the lowest energy given its angular momentum. But dissipative processes, like viscosity, are in place, and the orbiting plasma loses angular momentum forming an *accretion disk* (Shakura & Sunyaev 1973). To form the accretion disk the orbital radius has to be larger than the effective size of the accreting object. This condition is always satisfied in case of *Roche lobe overflow* (see Section 1.3) and sometimes for wind accretion.

### 1.2.2 Low Mass X-Ray Binaries

A *low mass X-ray binary* (LMXB) is a binary system with a NS or a BH compact component orbiting the low mass optical star (less than  $2M_\odot$ , A to M spectral class) filling its Roche lobe (see for a review Tauris & van den Heuvel 2006). The accretion onto the compact object proceeds via Roche lobe overflow, and typically

an accretion disc around the compact object is formed. These systems are relatively old, and the optical luminosity of the late-type non-degenerate companion is typically much less than that of the accretion disk and of the X-ray luminosity emerging from the compact object. Being old objects, LMXBs concentrate in the thick galactic disk, the bulge, and in the globular clusters. The orbital periods of these systems range from tens of minutes to several days. Typical luminosities are of the order of  $10^{37-38} \text{ erg s}^{-1}$ . About 20% of all known LMXBs are BH candidates, while the rest mostly consists of weakly magnetised NS ( $B < 10^{10} \text{ G}$ ). LMXBs are rarely observed as X-ray pulsars.

On the other hand, they often exhibit flux and spectral variability on all timescales, including X-ray bursts, spectral state changes, and so-called *quasi-periodic oscillations* (QPOs). Most of this variability is thought to be related to the extent and stability of the accretion disk.

Systems which exhibit thermonuclear X-ray bursts are called *bursters*. This type of bursts (referred as Type I) is usually observed from systems with moderate local accretion rates which are insufficient for stable burning of matter on the NS surface. Matter thus accumulates until the temperature and the density on the surface reach certain critical value sufficient to ignite thermonuclear burning, and then a burst is observed. Systems with higher accretion rate and magnetic field sometimes also exhibit X-ray bursts (so-called Type II), which are thought to have a different origin (Lewin et al. 1993). Type II bursts appear in binaries with a higher local accretion rate and magnetic field ( $B \sim 10^{10} \text{ G}$ ). In these systems the matter follows the magnetic lines and falls down to relatively compact polar areas. This results in a higher plasma density, so the thermonuclear burning is likely to be stable. The bursts occur in this case due to the unstable accretion rather than due to unstable thermonuclear burning.

### 1.2.3 High Mass X-Ray Binaries

*High mass X-ray binaries* (HMXBs) are systems with massive giant OB (more than  $15M_{\odot}$ ) or *Be* stars (more than  $5M_{\odot}$ ). The compact object is usually a NS, and only a few systems likely host a BH. The *Be* systems have typically very eccentric orbits with eccentricity  $e \geq 0.5$ , and the accretion mainly proceeds from the equatorial wind of the *Be* star only when the NS is close to the periastron. Most of *Be* systems are, therefore, transients (see Fig. 1.3). The systems with OB companions, on the other hand, typically have almost circular orbits with short periods and the compact object accretes from the strong stellar wind of the companion (mass-loss rates are up  $10^{-5} M_{\odot}/\text{yr}$ , which implies X-ray luminosities of up to few  $10^{38} \text{ erg s}^{-1}$ ). Orbital periods of OB systems are usually from several hours to several tens of days, whereas the *Be* systems have longer periods  $\geq 100$  days. High mass stars evolve

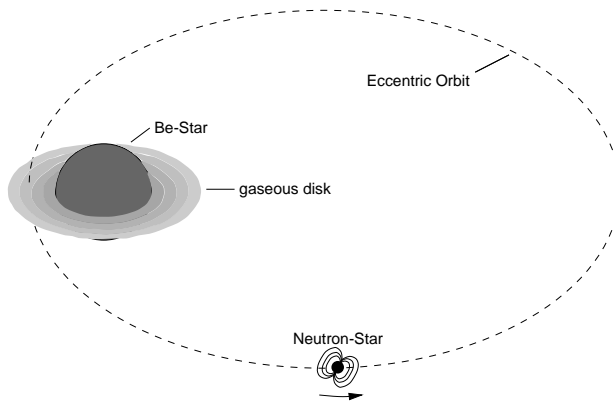


Figure 1.3: A compact object in an eccentric orbit around *Be* star (i.e. accretion is coming directly from stellar wind, see Bondi & Hoyle 1944). When the compact object is in the periastron passage - the outbursts are observed. When it is outside the periastron, the *Be*XRB is in quiescence. Image from Kreykenbohm (2004)

on timescale of  $\sim 10^6$  yr (Rose 1998), so it is clear that HMXBs are young objects. NS in this systems are typically strongly magnetised with  $B \geq 10^{12}$  G and appear as X-ray pulsars. The magnetic field is measured either indirectly using the spin evolution of the pulsar, or directly using the so-called *Cyclotron Resonance Scattering Features* (CRSF) observed in X-ray spectra of about half of all objects (see Chapter 2, Section 2.2).

### 1.3 Evolution in Close Binary Systems

The possibility of mass transfer between the components of a binary system implies different evolution paths for all system components. While all stars do lose some mass through the stellar wind, it is usually rather weak, and significant mass exchange between the components normally occurs in close binary systems where gravity of the more massive component might be sufficiently strong to allow direct mass transfer. In the evolution theory of close binary systems, the *Roche potential* is used to characterise the balance between gravitational forces from the components and the centrifugal force. For point objects with masses  $M_1 \geq M_2$  on circular orbits with semi-major axis  $a_1 + a_2 = a$  in the coordinate system with *X*-axis pointing from the first star to the second and *Z*-axis directed along the orbital angular

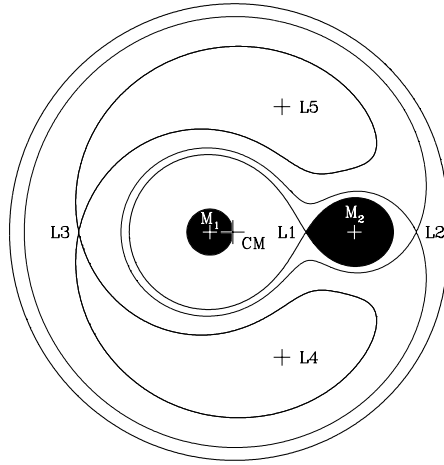


Figure 1.4: Schematic view of the cross-section for equipotential surface in the Roche theory. Some equipotential lines and the Lagrange points are indicated. The star  $M_2$  fills its Roche lobe.

momentum, the Roche potential can be expressed as:

$$\Phi = -\frac{1}{2}\omega^2 a^2 \Omega_R, \quad (1.8)$$

where the dimensionless potential  $\Omega_R(q)$  is a function of the mass ratio  $q = M_2/M_1$ . The equipotential surfaces are found from the equation  $\Phi(x, y, z) = \text{const}$ . For certain potential value the two *Roche lobes* around the components come in contact in the so-called inner *Lagrangian point*  $L_1$ . Points  $L_1$ ,  $L_2$ ,  $L_3$  on the X-axis are extremal points (maximum) for the Roche potential. In  $L_4$  and  $L_5$  the potential has there a minimum (Fig. 1.4).

The Roche lobes define volumes where the matter is gravitationally bound to a given binary member, so both components are contained within their Roche lobes. The radius of evolving star, however, changes with time and might at some point exceed the Roche lobe size. In this case the upper layers of its atmosphere become gravitationally unbound to the star. Most of the matter flows freely through the inner Lagrangian point  $L_1$  onto the other component (since there's no change in Roche potential there  $\nabla\Phi(L_1) = 0$ ), which has a profound impact on the evolution of both components. The mass transfer between the components typically happens several times during the evolution of a binary system. Initially more massive stars evolve faster, and the first mass transfer episode typically happens when the star

leaves the main sequence and becomes a giant, and its radius starts to increase. If the binary is compact enough, the giant might overflow its Roche lobe and then the excess mass is transferred to the second component on the thermal time scale of the supergiant (*Kelvin–Helmholtz timescale*):

$$\tau_M \approx \tau_{KH} \approx \frac{GM^2}{RL} \sim 3 \cdot 10^7 \left( \frac{M}{M_\odot} \right)^2 \left( \frac{R}{R_\odot} \frac{L}{L_\odot} \right)^{-1} \text{ yr.} \quad (1.9)$$

Here  $M$ ,  $L$  and  $R$  are the mass, luminosity and radius of the star respectively and  $G = 6.6739 \times 10^{-8} \text{ cm}^{-3} \text{ g}^{-1} \text{ s}^{-2}$  is the gravitational constant.

For a qualitative understanding of the evolution of close binary system it is often sufficient to assume conservative mass exchange (the full binary mass and the full momentum are conserved).

### 1.3.1 Evolution of HMXB

Considering that this thesis primarily focuses on HMXBs, allow me to summarise the evolution of two massive OB-stars in a circular orbit (Tutukov & Yungelson 1973). Such system will go through the following evolutionary stages (Fig. 1.5).

1. Both stars are confined within the respective Roche lobes. The duration of this stage depends on the life time of the more massive companion on the main sequence, and is about a few million years. At the end of this time, in the center of the more massive star, a helium core with mass about  $0.1 (M_1/M_\odot)^{1.4} M_\odot$  is formed.
2. The more massive star moves to the red supergiant region and starts to lose mass through the inner Lagrange point. The matter is transferred to the secondary star on thermal timescale (Eq. 1.9), so the duration of this stage is very short (about few thousand years). As a result of this process the initially more massive star is stripped off its hydrogen-rich atmosphere, and becomes a non-degenerate helium star with a C – O core. If the initial mass exceeded  $7 - 8 M_\odot$ , the remaining core will be quite luminous and so a strong stellar wind might be launched. In this case a *Wolf-Rayet star* (WR-star) will form.
3. Helium in the core of the WR-star is burning to carbon. The time scale of this stage is about  $10^5$  years. The number of such sources in the Galaxy is estimated to be several hundreds.
4. The C – O core of a WR-star collapses to a NS in a supernova explosion of type Ib (or Ic type if helium is left in the core). This happens in our galaxy about 1 time in 100 years. The resulting binary system is likely to become a

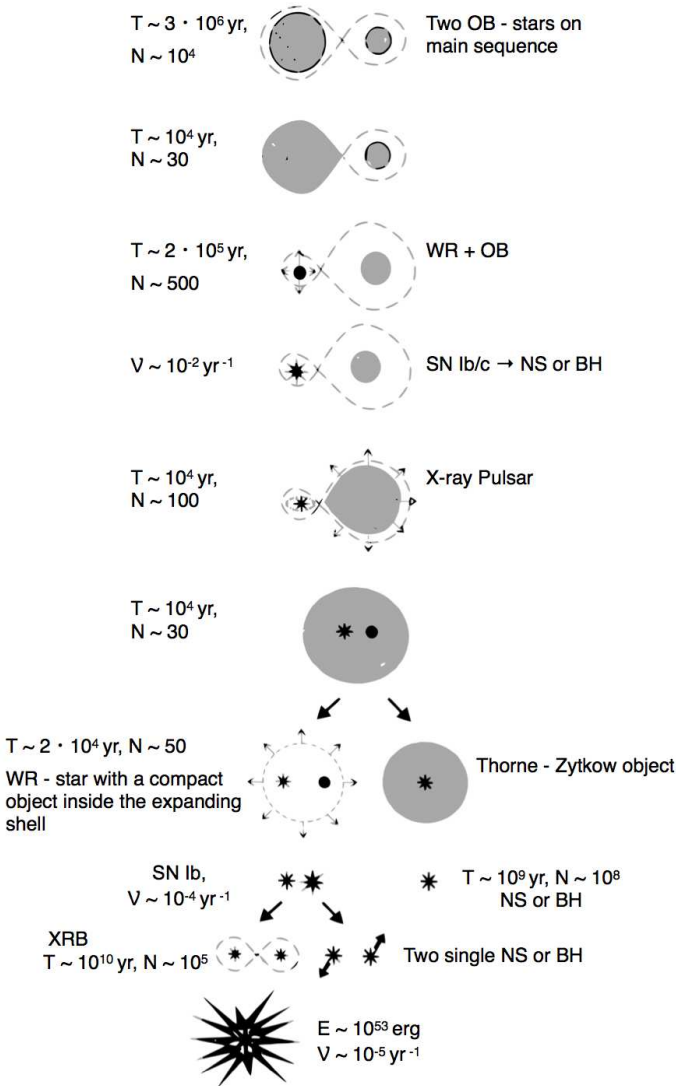


Figure 1.5: Evolution of a massive close binary system with a NSs or a BHs formation (Tutukov & Yungelson 1973).  $T$  - is the characteristic duration of the stage,  $N$  - estimate of the number of binaries in the Galaxy,  $\nu$  - frequency of events. Image from Zasov & Postnov (2011).

so-called *Be* XRB with a *Be* star and a NS in a very elongated orbit. After the supernova explosion the system can also be disrupted if the mass expulsion is more than half system mass or if the explosion is strongly asymmetric and thus the NS receives a strong “kick”.

5. At this stage the binary system consists of a fast rotating *Be* star and a NS (likely strongly magnetised) in an elliptical orbit. *Be* stars have strong equatorial stellar winds. At certain orbital phases (close to periastron) the NS passes through this wind and can capture the matter from the companion. The accretion rate can be significant, and the matter falls onto magnetic poles producing a transient X-ray pulsar. Most of the observed X-ray pulsars in the Galaxy are members of the *Be* systems. The duration of this stage is about tens of thousands of years (the time of the *Be* star evolution).
6. The secondary component gradually evolves and expands, so the NS might at some point end up going through the outer layers of the red supergiant’s atmosphere. In this case it will spiral down to the core of the supergiant on timescale of several thousands years. The orbital angular momentum is transferred to the common envelope formed around both components, which can be, therefore, expelled. The end-result of this stage is a hot helium core (WR-star) with a NS in a very close circular orbit. If the NS managed to penetrate deep into the companion’s core before the common envelope was expelled, then the hypothetical *Thorne – Zytkov object* might be formed (i.e. a NS with a dense extended envelope). Apparently the final product of the evolution of this objects is a massive single NS or a BH.
7. A WR-star at the end of its evolution explodes as a supernova type Ib/c. In most cases this leads to a disruption of the binary system, and, as a result, two single NSs are produced. They move fast in the opposite directions (the radio pulsars in the Galaxy are known to have large velocities). If after the explosion the system remains bound, a double radio pulsar system might be observed. This is expected to happen mainly in close binaries, so the two radio pulsars, orbiting each other, are expected to lose orbital momentum emitting gravitational waves: the system size decreases over time. Eventually this leads to a merger of the two NSs accompanied by a huge energy release ( $\sim 10^{53}$  erg). This energy is almost entirely converted to the gravitational wave emission. The frequency of mergers of binary NSs in the Galaxy is estimated at  $\sim 10^{-5} - 10^{-6}$  per year.

XRBs with a NS are usually classified either as LMXB and HMXB depending on the mass of the non-degenerate companion: less than  $\sim 2M_{\odot}$  or more than  $\sim 8M_{\odot}$



respectively. Systems with intermediate mass companions are very rare as they are hard to observe due to a combination of selection effects. The main reason is that the normal star is not massive and bright enough to drive strong stellar wind, like in the HMXBs, and direct mass transfer via Roche lobe overflow is usually very short (about one thousand years). Nevertheless there are known several Galactic sources with intermediate mass companion (Her X-1 and Cyg X-2 to name the most prominent ones).

### 1.3.2 Evolution of LMXB

The evolution of LMXBs is not so clear as in high mass systems. Here I refer to the scenario described by van den Heuvel (1983). The progenitor of the compact object (a NS or a BH) is a massive star, and this binary system has an extreme mass ratio.

The massive star evolves first and devours the less massive one. This is the common envelope stage, during which the orbit of the less massive star passes in the common extended envelope of a massive star. The orbital motion is slowed down and this stage ends after the ejection of the common envelope, or the merger of the two stars. During the common envelope stage the massive star (the core of the massive star) continues its evolution, and a supernova explosion happens. The core should not be very massive for the binary system to survive.

If, after the supernova explosion, the orbital period in the binary system is short enough to bring a companion with  $\sim 1M_{\odot}$  into a contact with its Roche lobe during a Hubble time, the binary becomes a LMXB with a donor of the main sequence. The orbital period of these systems is usually about 10 – 12 hours or shorter. If the orbit in the system is wider, than the mass transfer will start only then the donor expands into a giant.

## 1.4 Recent Results

To conclude this chapter I would like to show some predicted total numbers of low and high mass X-ray pulsars in the Galaxy and how many of them has been already detected. Based on the paper by Doroshenko et al. (2014) the total numbers of LMXBs and HMXBs in the Milky Way Galaxy are estimated to be  $200^{+175}_{-75}$  and  $110^{+180}_{-10}$  respectively. The soon to be launched new X-ray satellite *eRosita* will be able to discover a number of LMXBs  $N_{\text{LMXB}} = 130 - 270(75 - 95\%)$  and HMXBs  $N_{\text{HMXB}} = 105 - 220(78 - 96\%)$  in the next few years.

Catalogs of known X-ray pulsars can be found in Liu et al. (2007) and Liu et al. (2006) for the LMXBs and HMXBs respectively.

# Accreting Pulsars

### 2.1 A General View on Accreting Pulsars

In the XRBs emission is powered by accretion of matter transferred from the non-degenerate donor star to the compact object: a NS, a *white dwarf* (WD) or a BH. Accretion can proceed either from stellar wind or due to the Roche lobe overflow of the non-degenerate star (Fig. 2.1). The potential energy of the captured matter is converted into kinetic energy as the plasma falls towards the compact object, and is then thermalised either upon the impact with the surface, or due to the viscous tension in the accretion disk (see Fig. 2.1). The accretion disk is formed to remove the excess of angular momentum. The captured matter therefore can not fall directly onto the NS (Shakura & Sunyaev 1973). High kinetic energy of the accretion flow implies high temperatures of  $10^9 - 10^{10}$  K when it is released and thermalised in the emission region of the NSs, so radiation is emitted predominantly in the X-rays.

If the NS is strongly magnetised, e.g.  $B = 10^{12} - 10^{14}$  G, the magnetic field might overcome the enormous gravitational drag, and the accreting plasma then follows the magnetic field lines and falls onto the relatively small polar areas with size of  $< 1$  km. This implies that the energy release will be anisotropic, so for an external observer the emerging X-ray flux will vary periodically if the magnetic and spin axes are misaligned. These sources are called *X-ray pulsars*. As already mentioned, all accreting NSs in binary systems must be spinning due to accretion of the orbital angular momentum. The spin periods  $P$  of pulsars are in the range from milliseconds to the tens minutes.

In the optical range the normal star is usually observed. This star is also variable due to the irradiation by the compact object. The optical star can be an old star from the halo of the Galaxy or also a young massive OB or *Be* star.

The luminosities of accreting pulsars might reach  $\sim 10^{39}$  erg s $^{-1}$ , and it was realised early on (Basko & Sunyaev 1976) that in bright pulsars the radiation pressure dominates both magnetic field and gravity, and that the so-called *accretion columns*

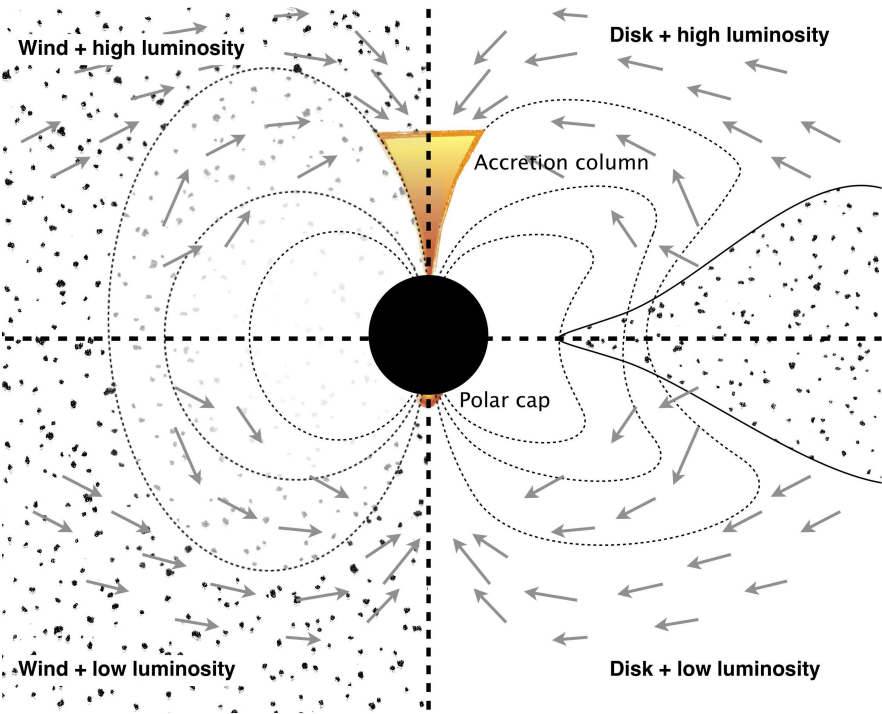


Figure 2.1: Summary of the various accretion regimes: from wind and from the accretion disk. Image from Doroshenko (2011).

must form. Within the accretion column the radiation balances the ram-pressure of the in-falling plasma stopping it at certain height while the released kinetic energy of the plasma slowly leaks through the side walls of the column. They assume that the hot plasma is significantly slowed down by the radiation pressure at some height forming the accretion column. The excess of energy is emitted through the optically thick walls of the column. Basko & Sunyaev (1976) described two kind of columns: “solid” and “hollow” (Fig. 2.2).

While this scenario is probably the only way to explain the observed X-ray luminosities of bright pulsars, the details of the accretion column formation and structure, and the implicit observational phenomena are still unclear despite forty years of studies. The column geometry and structure are defined by a complex interplay of the magnetic field structure, local beam pattern of escaping radiation, angular and spatial dependence of the opacity within column, that proved to be un-traceable

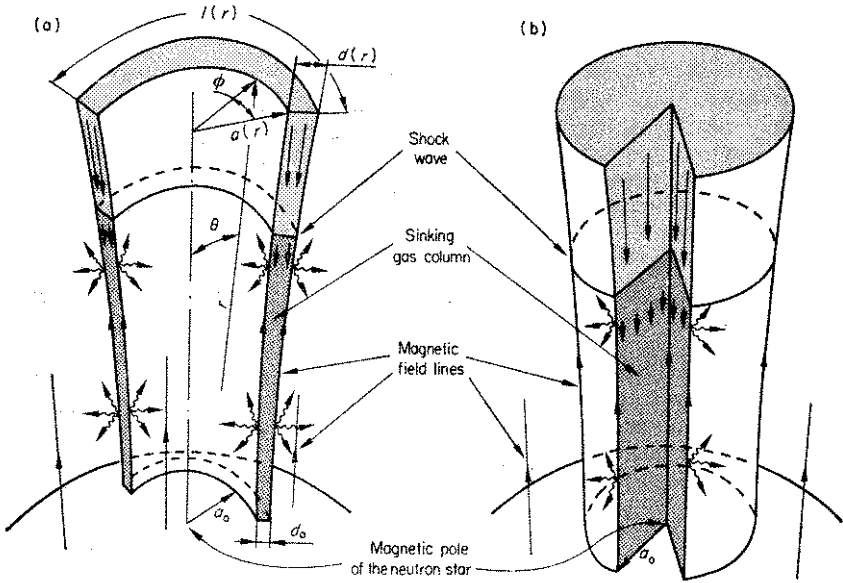


Figure 2.2: Schematic representation of the two possible geometries of the accretion column: “hollow” and “solid”, as presented by Basko & Sunyaev (1976).

analytically. Several attempts to model it numerically have recently been started, but they are far from being complete (see for example Kraus et al. 1995; Ferrigno et al. 2011; Becker et al. 2012). One way to better understand the properties of the emission region from an observational point of view is to study the pulse-phase dependence of the pulsars X-ray spectrum, which constitutes a large fraction of the present work.

The strong magnetic field starts to influence the accretion flow way before the accretion column forms. The radius where the energy density of the magnetic field exceeds the kinetic energy of the in-falling plasma is an important scale for the physics of accreting NSs and is usually referred to as the *magnetosphere radius*. The Alfvén radius or magnetosphere radius is defined as the distance at which the magnetic pressure and the ram pressure are equal:

$$P_{\text{mag}} = \frac{B^2}{8\pi} = \frac{\mu^2}{8\pi r^6}, \quad (2.1)$$

$$P_{\text{ram}} = \rho v^2 = \frac{\dot{M}}{4\pi r^2 v} v^2 = \frac{\dot{M} \sqrt{2GM}}{4\pi r^{5/2}}. \quad (2.2)$$

From the equilibrium of this two pressures the magnetosphere radius is:

$$r_{\text{m}} = 2.9 \times 10^8 M^{1/7} R_6^{-2/7} L_{37}^{-2/7} \mu^{4/7} \text{ cm}, \quad (2.3)$$

where  $M$  is given in units of  $M_{\odot}$ ,  $R_6$  is given in units of  $10^6$  cm and  $L_{37}$  is the luminosity in units of  $10^{37}$  erg  $\text{s}^{-1}$ . Within the magnetosphere, plasma basically follows the field lines, so any accretion disk is disrupted at the magnetospheric boundary. The radius of the magnetosphere affects many of the observational properties of a NS, including its variability, spin evolution and spectral properties.

The X-ray spectra of all accreting X-ray pulsars have similar shape which can be described by a power law with a high-energy cut-off and a low energy roll-over. The interpretation of the observed spectra is still not clear, although it is thought that spectra are shaped by the comptonisation of cyclotron, thermal and bremsstrahlung emission from the polar caps. The main components constituting the X-ray continuum spectrum of an accreting pulsar Her X-1, according to the model by Becker & Wolff (2007) are shown in Figure 2.3. The intrinsic spectrum is usually modified by interstellar absorption. What is often observed are fluorescent emission from several elements, most notably iron, formed in the plasma surrounding the NS. Another important feature observed in the spectra of about half of all pulsars is the so-called *Cyclotron Resonance Scattering Feature* (CRSF, Chapter 2, Section 2.2).

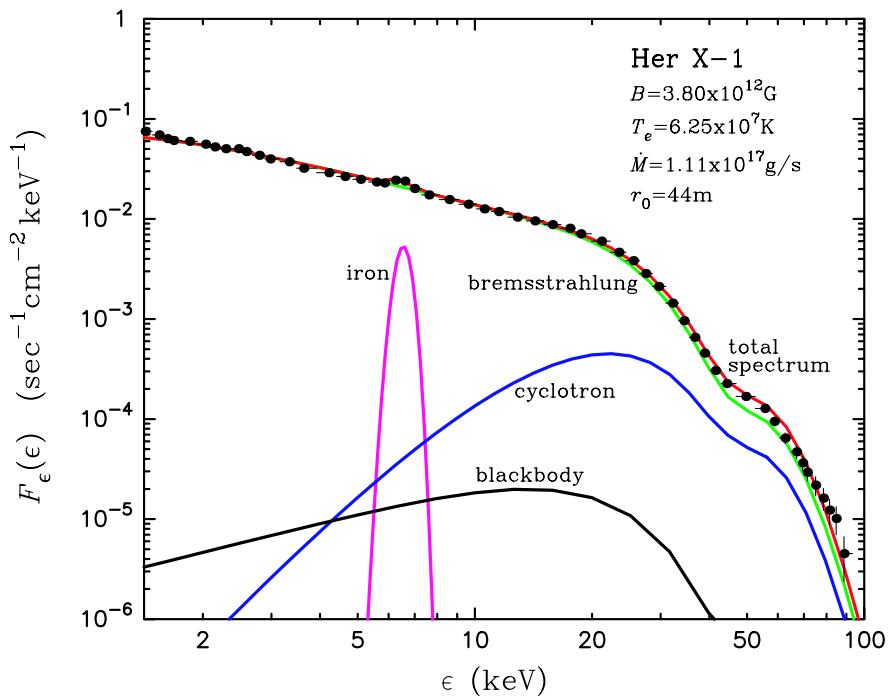


Figure 2.3: Theoretical model of the spectrum for Her X-1 by Becker & Wolff (2007). The plot shows the total spectrum as well as contributions from the comptonised thermal, bremsstrahlung and cyclotron emission.

## 2.2 Cyclotron Resonance Scattering Feature

Electrons moving in the strong magnetic field  $B$  follow a helicoidal trajectory along the lines of the magnetic force with *Larmor frequency* (the *gyration frequency*)

$$\omega_L = \frac{v_\perp}{r} = \frac{eB}{m_e}, \quad (2.4)$$

where  $e$  and  $m_e$  are the electron charge and mass respectively. The gyration radius can be derived as

$$r_L = \frac{m_e v_\perp}{eB}. \quad (2.5)$$

This equation shows that with the increasing  $B$  gets  $r_L$  smaller. The high magnetic field strength, typical for the NSs, implies a gyration radius close to the *de Broglie* wavelength

$$\lambda_{\text{deBroglie}} = \frac{\hbar}{mv}, \quad (2.6)$$

thus quantum effects become important. The electron motion perpendicular to the magnetic field is quantised (Lai 2001) in equidistant levels (*Landau levels*)

$$E_n = m_e c^2 \sqrt{1 + \left(\frac{p_\parallel}{m_e c}\right)^2} + 2n \frac{B}{B_c}, \quad (2.7)$$

where  $n$  is level number,  $p_\parallel = m_e v_\parallel$  is the momentum of the electron parallel to the magnetic field,  $B_c \approx 4.4 \cdot 10^{13}$  G is the critical magnetic field strength. In the non-relativistic case ( $B \ll B_c$ ) the difference between two Landau levels (see as a review Lipunov et al. 1992) is

$$E_{\text{cyc}} = \hbar\omega = \frac{\hbar e B}{m_e} \sim 11.57 \frac{B}{10^{12} \text{G}} \text{keV}. \quad (2.8)$$

Within the emission region of accreting pulsars electrons constantly interact with X-ray photons which scatter off the electrons and exchange energy and momentum. The fact that the momentum of electrons can only change in discrete steps implies, therefore, enormously enhanced scattering cross-section for photons with energy close to spacing between the Landau levels. This implies that these photons can not easily escape from the emission region which manifests as line-like *Cyclotron Resonance Scattering Features* (Gnedin & Sunyaev 1974) in the spectra of the X-ray pulsars. Indeed, the decay rate from the excited to lower levels is described by Latal (1986):

$$\nu_r = \left(\frac{\alpha m_e c^2}{\hbar}\right) \left(\frac{B}{B_c}\right)^{1/2} \sim 10^{15} \frac{B}{10^{12} \text{G}} \text{s}^{-1}. \quad (2.9)$$

The photons are therefore reemitted with basically constant energy  $E_n = h\nu$ , because of the short electron's life time at the high energy levels. This process is called *resonant scattering*, and leads to formation of an absorption feature in X-ray spectrum which is thus called *Cyclotron Resonance Scattering Feature* (CRSF). When  $n = 0$  we have a *fundamental* cyclotron line. For  $n > 0$  we have cyclotron line *harmonics*. The energy of the observed feature is directly related to the magnetic field, and thus cyclotron lines are believed to be the only *direct* probe of the magnetic field of a NS.

Note, however, that the line energy only gives an estimate of the magnetic field strength in the line forming region, which is uncertain in some cases. Moreover, the energy of the observed features must be red-shifted if the CRSF forms close to the surface of NS. In this case the magnetic field may be estimated as

$$E_{\text{cyc}} = \frac{11.6 \times B_{12}}{1+z} \text{keV}, \quad (2.10)$$

where  $B_{12}$  is the magnetic field strength in units of  $10^{12}$  G,  $z$  is the gravitational redshift, given by:

$$\frac{1}{1+z} = \sqrt{1 - \frac{2GM_{\text{NS}}}{Rc^2}}, \quad (2.11)$$

where  $R$  is the distance between the center of the NS and the region of the cyclotron line formation.

The first cyclotron line in an X-ray binary was discovered by Truemper et al. (1978) in the spectrum of the Her X-1 using data from balloon-borne detectors. But this feature was first primarily interpreted as an emission line at  $\sim 58$  keV (Fig. 2.4). After the start of the space age, the launch of the first X-ray satellites, and the accumulation of observational data and theoretical evidence, it became clear that the line in Her X-1 is an absorption cyclotron line at  $\sim 42$  keV (Voges et al. 1982; Mihara et al. 1990).

Only the fundamental line is significantly detected in Her X-1, however in other sources a harmonic (as for instance in 4U 1907+09), or even multiple harmonics (as in 4U 0115+63) are observed. The pulsar 4U 0115+63 was the first source in which the CRSF harmonic had been detected (White et al. 1983), and also the only with five CRSF harmonics (Santangelo et al. 1999; Ferrigno et al. 2009) detected. The list of known sources with cyclotron lines is presented in Table 2.1.



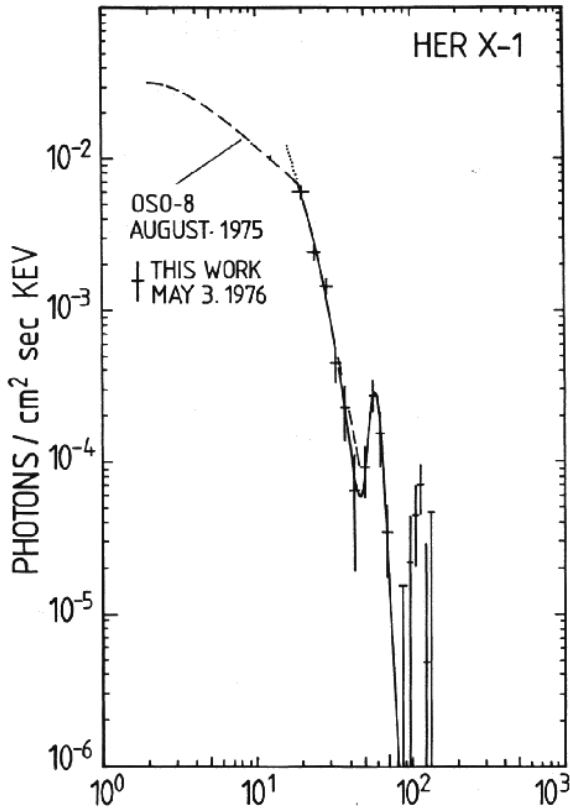


Figure 2.4: Emission line at ~ 58 keV in spectrum of Her X-1 as reported by Truemper et al. (1978). Subsequent observations showed that it was in fact an absorption feature at ~ 42 keV.

Source	$E_{\text{cyc}}$ (keV)	Mission	Reference
Her X-1	41	Balloon	Truemper et al. (1978)
4U 0115+63	14,24,36, 41,53	<i>HEAO-1</i>	Wheaton et al. (1979) Ferrigno et al. (2009)
V 0332+53	26,49,74	<i>Ginga</i>	Makishima et al. (1990)
4U 1538-52	20	<i>Ginga</i>	Clark et al. (1990)
	47	<i>RXTE, INTEGRAL</i>	Rodes-Roca et al. (2009)
CEP X-4	28	<i>Ginga</i>	Mihara et al. (1991)
	45	<i>Suzaku</i>	Jaisawal & Naik (2015a)
A 0535+26	46,100	<i>HEXE</i>	Kendziorra et al. (1992)
Vela X-1	24,52	<i>HEXE</i>	Kendziorra et al. (1992)
Cen X-3	28.5	<i>RXTE</i>	Heindl & Chakrabarty (1999)
		<i>BeppoSAX</i>	Santangelo et al. (1998)
4U 1626-67	37	<i>BeppoSAX</i>	Orlandini et al. (1998)
		<i>RXTE</i>	Heindl & Chakrabarty (1999)
4U 1907+09	18,38	<i>Ginga</i>	Makishima et al. (1999)
GX 301-2	37	<i>Ginga</i>	Makishima et al. (1999)
XTE J1946+274	36	<i>RXTE</i>	Heindl et al. (2001a)
MXB 0656-072	36	<i>RXTE</i>	Heindl et al. (2003)
XMMU J054134.7-682550	10,20?	<i>RXTE</i>	Markwardt et al. (2007)
EXO 2030+375	11	<i>RXTE</i>	Wilson et al. (2008)
	63?	<i>INTEGRAL</i>	Klochkov et al. (2008)
Swift J1626.6-5156	10	<i>RXTE</i>	Decesar et al. (2009)
1A 1118-61	55	<i>RXTE</i>	Doroshenko et al. (2010b)
GX 304-1	51	<i>Suzaku</i>	Mihara et al. (2010)
RX J0440.9+4431	32	<i>INTEGRAL, Swift, RXTE</i>	Tsygankov et al. (2012)
MAXI J1409-619	44,73,128	<i>BeppoSAX, ASCA</i>	Orlandini et al. (2012)
4U 1822-37	33	<i>Suzaku</i>	SSasano et al. (2014)
RX J0520.5-6932	31	<i>NuSTAR</i>	Tendulkar et al. (2014)
GRO J1008-57	76	<i>MAXI</i>	Yamamoto et al. (2014)
IGR J17544-2619	17	<i>NuSTAR</i>	Bhalerao et al. (2015)
GRO J1744-28	4.7	<i>NuSTAR</i>	D'Ai et al. (2015)
		<i>BeppoSAX</i>	Doroshenko et al. (2015)
2S 1553-542	23.5	<i>NuSTAR, Chandra</i>	Tsygankov et al. (2016)
IGR J16393-4643	29.3	<i>NuSTAR</i>	Bodaghee et al. (2016)
SMC X-2	27	<i>NuSTAR, Swift/XRT</i>	Jaisawal & Naik (2016)
GS 1843+00	20?	<i>Ginga</i>	Mihara (1995)
OA0 1657-415	36?	<i>BeppoSAX</i>	Orlandini et al. (1999)
LMC X-4	100?	<i>BeppoSAX</i>	Barbera et al. (2001)
GX 1+4	34?	<i>INTEGRAL</i>	Ferrigno et al. (2007)
XTE J1829-098	18?	<i>RXTE</i>	Roy et al. (2011)
IGR J18179-1621	22?	<i>INTEGRAL</i>	Li et al. (2012)
4U 1909+07	44?	<i>Suzaku</i>	Jaisawal et al. (2013)
KS 1947+300	12.2?	<i>NuSTAR</i>	Fürst et al. (2014)
4U 1700-37	37?	<i>Suzaku</i>	Jaisawal & Naik (2015b)
IGR J18027-2016	23?	<i>NuSTAR</i>	Lutovinov et al. (2016)

Table 2.1: List of sources with cyclotron line detected in the spectrum. Tentative line detections requiring an independent confirmation are marked with (?).

## CHAPTER 3

---

# BeppoSAX

In this thesis I will study the observations of accreting pulsars taken with the BeppoSAX satellite in detail. Here I would like to focus on the main features of the *BeppoSAX*.

The X-ray satellite *BeppoSAX* was a major program of the Italian Space Agency (ASI) with participation of the Netherlands Agency for Aerospace Programs (NIVR) (Boella et al. 1997a). *BeppoSAX*, *Satellite italiano per Astronomia X*, was named in honor of the Italian scientist Giuseppe (Beppo) Occhialini after the launch of the satellite from Cape Canaveral on 30 April 1996 into a low inclination ( $<4$  degree) low-Earth orbit. The nominal life time of the satellite, originally planned for 2 years, was extended several times until, on the 29th of April 2003, the satellite was decommissioned and successfully deorbited into the Pacific Ocean.

The instruments on board of *BeppoSAX* cover a broad energy range with well balanced performance from 0.1 to 300 keV. All instruments have relatively large effective areas and low background, good energy and time resolution, and imaging capabilities in the soft energy range from 0.1 to 10 keV (angular resolution of about  $1.5'$ ). Its high sensitivity allowed to use the full energy band even for weaker sources (1/20 of 3C 273) and study the broadband spectral and variability properties of several classes of objects for the first time. The *Wide Field Cameras* (WFC) and *Narrow Field Instruments* (NFI) allowed to discover and follow the X-ray afterglows of the *Gamma Ray Bursts* (GRBs)<sup>1</sup> for the first time, and to monitor the long term variability of sources with fluxes as low as about 1 mCrab.

The configuration of the scientific payload is shown in Figure 3.1. The main instruments have narrow field of view and are co-aligned with the Z axis of the satellite:

- The MECS (Medium Energy Concentrator Spectrometers): a medium energy (1.3 – 10 keV) set of three identical grazing incidence telescopes with double

---

<sup>1</sup>GRB is a narrow beam of intense radiation that is observed in distant galaxies during a supernova explosion. The initial burst is usually followed by a longer-lived “afterglow” emitted at longer wavelengths (X-ray, ultraviolet, optical, infrared, microwave and radio).

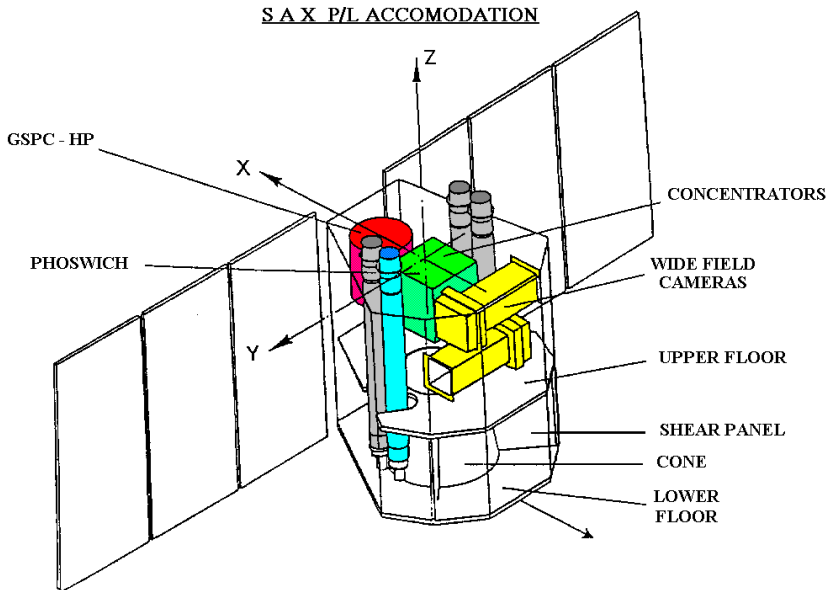


Figure 3.1: *BeppoSAX* scientific payload accommodation (Boella et al. 1997a).

cone geometry (Citterio et al. 1986; Conti 1994), with position sensitive gas scintillation proportional counters in their focal planes (Boella et al. 1997b).

- The LECS (Low Energy Concentrator Spectrometer): a low energy (0.1 – 10 keV) telescope, identical to the other three, but with a thin window position sensitive gas scintillation proportional counter in its focal plane (Parmar et al. 1997).
- The HPGSPC, a collimated High Pressure Gas Scintillation Proportional Counter (4 – 120 keV, FWHM energy resolution of 8% at 10 keV and 5.5% at 20 keV, Manzo et al. 1997). The detection chamber is filled with a mixture of the two gases, 90% Xenon and 10% Helium, at 5 atmospheres, which allows it to be sensitive up to 120 keV.
- The PDS, a collimated Phoswich Detector System (15 – 300 keV, FWHM energy resolution of 24% at 20 keV, and 14% at 60 keV, Frontera et al. 1997).

The detector consists of a square array of four independent NaI(Tl)/CsI(Na) phoswich (PHosphor and sandWICH) scintillation detectors. There are two independent collimators, one for each pair of detectors, which can independently rocked back and forth providing a direct measurement of the background, which is important at high energies.

Perpendicular to the NFI and pointed in two opposite directions there are two coded masks proportional counters (Wild Field Cameras, WFC, Jager et al. 1997). The unprecedentedly large field of view of  $20^\circ \times 20^\circ$  with an angular resolution of  $5'$  allowed to study a large number of transient sources in the energy range of 3 – 30 keV.

The four lateral active shields surrounding the PDS were also used as detectors to monitor gamma-ray activity of brighter sources with fluence exceeding  $\geq 10^{-6}$  erg/cm<sup>2</sup> in the 60 – 600 keV range with  $\sim 1$  ms time resolution.

The effective area of the *BeppoSAX* instruments as function of energy is shown in Figure 3.2. The effective area of the NFI increases with energy following a power law with the positive inclination, i.e. oppositely to the X-ray spectra of the majority of objects. The HPGSPC and PDS were generally background dominated, while the LECS and MECS were source dominated instruments. One important property of the *BeppoSAX* scientific payload is the broad overlapping energy response of the instruments, which allowed good cross-calibration of the instruments.

The main scientific result which brought the observatory *BeppoSAX* its international fame was the discovery of X-ray afterglow of gamma-ray bursts with both the WFC instrument and NFI and to determine their position of about 1 arcmin. This, in turn, allowed to detect damped optical and radio sources pointing to the origin of gamma-ray bursts with large cosmological distances (Piran & Shaviv 2004). The *BeppoSAX* also measured broadband (0.1 – 300 keV) X-ray spectra of a large number of sources, including active galactic nuclei (AGNs). With its lower background, the hard X-ray spectrometer PDS was able to obtain AGN spectra in the hard X-rays for the first time. These still remain among the highest quality X-ray broad band spectra (Perola et al. 2002; Malizia et al. 2003) ever obtained. Large exposure accumulated with WFC, permitted to accomplish a unique research of variables and transient sources in the galactic center (in't Zand et al. 2004; Cocchi et al. 1999).

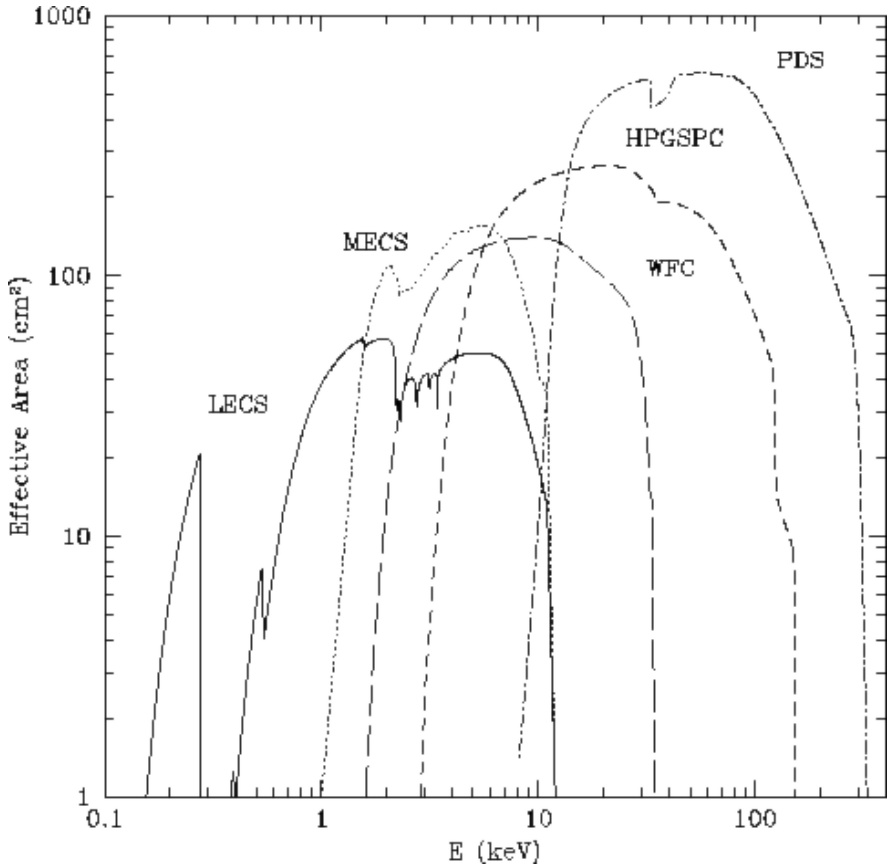


Figure 3.2: Effective area of BeppoSAX instruments as function of energy (Boella et al. 1997a). Picture courtesy of “Space Research Organisation”, Netherlands (SRON).

## CHAPTER 4

---

### Data Analysis and Spectral Models.

#### 4.1 Observations

For the 6 years of *BeppoSAX* operations a number of different sources, including X-ray binaries and pulsars, were observed. In this work I analysed high and low mass X-ray binaries which contain a cyclotron line in their spectra.

Most of these observations have been already analysed and published. We have reanalysed a good part of this data using a unified approach, and performed a more detailed analysis, including phase resolved analysis for all sources. Eventually we analysed the average properties of pulsars taking into account the full sample, comparing our results with the work by Coburn et al. (2002) and compare cyclotron line. Six different models, not only phenomenological, but also more physical, were used to fit the data. One of the aims of this work was to look how different spectral parameters, especially cyclotron line, depend on the spectral models. For all the sources we have also performed the time analysis obtaining spin periods, pulse profiles and pulse fractions. Table 4.1 shows the list of analysed sources.

#### 4.2 Data Analysis

The standard *BeppoSAX* pipeline was used for the data reduction<sup>1</sup>. In most cases the HPGSPC and PDS were operated in rocking mode to monitor the background along the orbit, and the background spectra were measured directly from the off-source position. The background for the LECS and MECS were subtracted using either the standard calibration files or spectra extracted from an annulus around the source. Details on data reduction and spectral analysis can be found in the *BeppoSAX* handbook. For the timing analysis, we transformed the arrival time of

---

<sup>1</sup><http://www.asdc.asi.it/bepposax/>

Source	Type	$P_{\text{orb}}$ days	$P_{\text{spin}}$ s	$E_{\text{cyc}}$ keV
Her X-1	LMXB	1.7	1.2377	40
4U 1626-67	LMXB	0.02917	7.6679	38
4U 1907+09	HMXB	8.38	440	19, 39
4U 1538-52	HMXB	3.73	528.218	21, 52
Vela X-1	HMXB	8.96	283	25, 55
Cen X-3	HMXB	2.09	4.8	29
4U 0115+63	HMXB, Transient	24.3	3.61	11, 22, 34, 44, 55
XTE J1946+274	HMXB, Transient	169.2	15.82	38
GRO J1744-28	LMXB, Transient, Burster	11.8	0.467	4.5

Table 4.1: List of sources with cyclotron line observed by *BeppoSAX*.

photons to the solar barycentre reference system correcting for the orbital motion of the earth and of the compact object using the orbital ephemeris for a given source (if available).

To produce background subtracted spectra and light curves we used the standard pipeline for the collimating instruments (the HPGSPC and PDS). For the imaging instruments the MECS and LECS we either followed the standard analysis procedure extracting the source spectrum from a circle with a radius of  $\sim 4$  or  $8$  arcmin around the target, and the background from a  $\sim 18$  arcmin annulus centered around the source, or used the blank-sky background calibration files. For the pulse-phase resolved spectral analysis we used the TIMEFOLD program (by A. Segreto) to produce the phase-energy matrix based on the filtered input event list, source spin period and ephemeris.

We restricted the analysis to the  $0.1 - 4$  keV energy range for the LECS,  $1.65 - 10$  keV for the MECS,  $4.5 - 34$  keV for the HPGSPC, and  $15 - 120$  keV for the PDS. For cross normalisation between the four instruments we introduce a normalisation factor for each instrument, fixed to 1 for the MECS and free (but close to unity) for the other instruments.

### 4.3 Spectral Models

To fit the extracted X-ray spectra, we used the XSPEC package (version 11.3.2 and 12<sup>2</sup>, Arnaud 1996). To systematically study the broadband X-ray continuum emission of the accreting pulsars in our sample we considered for each source several continuum models modified with additional components, i.e. interstellar absorp-

<sup>2</sup><http://heasarc.gsfc.nasa.gov/docs/xanadu/xspec/>



tion, absorption or emission lines:

- A powerlaw with high energy exponential cutoff (Cutoffpl in XSPEC):

$$\text{Cutoffpl}(E) = KE^{-\Gamma} \exp\left(-\frac{E}{E_{\text{cut}}}\right), \quad (4.1)$$

where  $K$  is a normalisation constant in photons/keV/cm<sup>2</sup>/s at 1 keV,  $\Gamma$  gives the powerlaw photon index,  $E_{\text{cut}}$  models the cutoff energy of the exponential cutoff (in keV).

- The power law plus high-energy cutoff model (Powerlaw and Highcut in XSPEC):

$$\text{Highcut}(E) \sim E^{-\Gamma} \begin{cases} 1 & (E \leq E_{\text{cut}}) \\ e^{-(E-E_{\text{cut}})/E_{\text{fold}}} & (E > E_{\text{cut}}) \end{cases}, \quad (4.2)$$

where  $\Gamma$ ,  $E_{\text{cut}}$  and  $E_{\text{fold}}$  are the photon index, cutoff and folding energies respectively. This model has a discontinuous derivative at the cutoff energy  $E_{\text{cut}}$  which can give a line-like residual errors. To successfully apply the Highcut model we add the smoothing Gaussian as suggested by Coburn et al. (2002): a narrow ( $\sigma = 0.1 \cdot E$ ), shallow Gaussian shaped absorption feature (see Eq. 4.6).

- A power law with Fermi-Dirac cutoff (Powerlaw and Fdcut in XSPEC):

$$\text{Fdcut}(E) \sim \frac{E^{-\Gamma}}{1 + e^{(E-E_{\text{cut}})/E_{\text{fold}}}}, \quad (4.3)$$

where  $\Gamma$ ,  $E_{\text{cut}}$  and  $E_{\text{fold}}$  are the photon index, cutoff and folding energies of this model (not the same with the Highcut model).

- The Negative and Positive power law EXponential model (NPEX, Mihara 1995; Makishima et al. 1999):

$$\text{NPEX}(E) = (A_1 E^{-\alpha_1} + A_2 E^{+\alpha_2}) \exp(-E/kT), \quad (4.4)$$

where  $\alpha_1$  and  $\alpha_2$  are the positive power law indices, and  $E_{\text{fold}}$  is a folding energy.

- CompTT - the analytic model by Titarchuk (1994) describing comptonisation of soft photons in a hot plasma (Sunyaev & Titarchuk 1985; Hua & Titarchuk 1995; Titarchuk & Lyubarskij 1995). We assume spherically symmetric geometry and consider input soft photon temperature, the plasma temperature, and the optical depth free parameters for this model.

- BW - theoretical model for the emission from the magnetised accretion columns which takes into account both thermal and bulk comptonisation in the accretion flow (Becker & Wolff 2007). The model parameters are:
  - the NS radius  $R_{\text{NS}}$  in km (to be fixed),
  - the NS mass  $M_{\text{NS}}$  in  $M_{\odot}$  (to be fixed),
  - the photon diffusion parameter  $\xi$  (order of some unities),
  - the comptonisation parameter  $\delta$ ,
  - the magnetic field  $B$  in units of  $10^{12}$  G,
  - the mass accretion rate  $\dot{M}$  in units of  $10^{17}$  g/s,
  - the electron temperature  $T_e$  in units of keV,
  - the column radius  $r_0$  in units of m,
  - the source distance  $D$  in units of kpc (to be fixed),
  - the normalisation of the Black body seed photon component  $BBnorm$  (fix it to zero at first),
  - the normalisation of the Cyclotron emission seed photon component  $CYCnorm$  (fix it to one),
  - the normalisation of the Bremsstrahlung emission seed photon component  $FFnorm$  (fix it to one).

The continuum emission is then modified by photoelectric absorption either around the compact object (wabs in Xspec) and in the interstellar medium, and one or several emission or absorption lines. We assume gaussian profile in either case:

- A simple gaussian line profile:

$$A(E) = \frac{K}{\sqrt{2\pi \cdot \sigma_{\text{line}}^2}} \exp\left(-0.5 \left(\frac{E - E_{\text{line}}}{\sigma_{\text{line}}}\right)^2\right), \quad (4.5)$$

where  $K$  is a total photons/cm<sup>2</sup>/s in the line.  $E_{\text{line}}$ , and  $\sigma_{\text{line}}$  are the centroid energy, and width of the line, respectively.

- A gaussian *absorption* line:

$$\text{Gauabs}(E) = \exp\left(-\frac{\delta_{\text{line}}}{\sqrt{2\pi \cdot \sigma_{\text{line}}}} \cdot e^{-0.5 \left(\frac{E - E_{\text{line}}}{\sigma_{\text{line}}}\right)^2}\right), \quad (4.6)$$

where  $\delta_{\text{line}}$ ,  $E_{\text{line}}$ , and  $\sigma_{\text{line}}$  are the optical depth, centroid energy, and width of the line, respectively.

In some sources we have found that simple a single column photoelectric absorption (wabs in Xspec) was inadequate to model the broadband spectra. In these cases we introduced a second absorber, presumably located close to the compact object:

$$PC(E) = par2 \cdot \exp(-par1 \cdot \sigma(E)) + (1 - par2). \quad (4.7)$$

Here  $\sigma(E)$  is the photo-electric cross-section (not including Thomson scattering),  $par1$  - equivalent hydrogen column (in units of  $10^{22}$  atoms/cm<sup>2</sup>),  $par2$  - covering fraction ( $0 < par2 \leq 1$ ).

The soft excess observed in some sources was modeled by the black body component (bbody or bbodyrad in Xspec):

- Bbody is a blackbody spectrum:

$$A(E) = 8.0525K \frac{E^2 dE}{(kT)^4 \left( \exp\left(\frac{E}{kT}\right) - 1 \right)}, \quad (4.8)$$

where  $K = L_{39}/D_{10}^2$ ,  $L_{39}$  is the source luminosity in units of  $10^{39}$  ergs/sec and  $D_{10}$  is the distance to the source in units of 10 kpc.

- Bbodyrad is a blackbody spectrum with normalisation proportional to the surface area:

$$A(E) = K \cdot 1.0344 \cdot 10^{-3} \frac{E^2 dE}{\exp\left(\frac{E}{kT}\right) - 1}, \quad (4.9)$$

where  $K = \left(\frac{R_{\text{km}}}{D_{10}}\right)^2$ ,  $R_{\text{km}}$  is the source radius in km and  $D_{10}$  is the distance to the source in units of 10 kpc.



**Part II**

**Accreting Pulsars Observed  
with *BeppoSAX***



## CHAPTER 5

---

### Hercules X–1

#### 5.1 Source Description

Her X–1 and Cen X–3 were the first X-ray pulsars discovered by the first space X-ray mission *Uhuru* in 1972 (Tananbaum et al. 1972; Giacconi et al. 1973). Her X–1 is one of the brightest and well studied X-ray pulsars featuring an X-ray luminosity of  $L_X \sim 2 \times 10^{37}$  erg/s, for a distance of  $\sim 7$  kpc (Reynolds et al. 1997). The binary system consists of an accreting magnetised neutron star, with 1.24 s spin period, and an optical star HZ Her (Liller 1972) - a main sequence star of spectral type A/F (Crampton & Hutchings 1974) and mass  $M \sim 2.2M_\odot$  (Deeter et al. 1981). This is a rather rare system being the mass of the companion between typical values for high and low mass X-ray binaries. The orbital period of the system is  $P_{\text{orb}} \sim 1.7^{\text{d}}$  (see ephemeris in Staubert et al. 2009b).

Besides orbital modulation, Her X–1 exhibits also a log-term periodic variability, a *superorbital*  $\sim 35$ -day cycle. During this period two so-called “on states” (when the source is bright in X-rays) are observed: the *main-on* ( $\sim 7$  orbital periods long) and the *short-on* ( $\sim 5$  orbital periods long) are separated by 4–5 orbital cycles, when the source has low X-ray flux, so-called “off-state” (Gerend & Boynton 1976; Howarth & Wilson 1983; Shakura et al. 1999). The observed drop in X-ray flux is thought to be due to the obscuration of the compact source by the outer edge of precessing accretion disk. This is justified by the fact that fluorescent lines excited by the X-ray emission from the NS are observed even during the off-states, where the flux from the pulsar ceases. The interaction of the precessing disk with the magnetosphere of the NS is also thought to be responsible for modulating the shape of X-ray pulses with the phase of the 35 day cycle.

Roughly every  $\sim 5$  years Her X–1 switches off completely, which is usually referred to as an *anomalous low states*. During these periods almost no X-ray flux is detected and the 35-day variability disappears (Parmar et al. 1985; Vrtillek et al. 1994; Parmar et al. 1999; Staubert et al. 2009a). The anomalous low states are

Start time	MJD <sub>start</sub>	N <sup>(a)</sup>	35 <sup>d</sup> <sub>phase</sub>	P, s	Orb. state	Exp <sup>(b)</sup>
24.07.1996 <sup>(c)</sup>	50288	257	~ 0.1	1.2377397(1)	main on	93
27.06.1998 <sup>(d)</sup>	50991	277	~ 0.28	1.2377260(1)	main on	25
09.07.1998 <sup>(e)</sup>	51003	277	~ 0.64	1.2377260(1)	short on	32
12.07.1998 <sup>(e)</sup>	51006	277	~ 0.7	1.2377260(1)	short on	10
14.07.1998 <sup>(e)</sup>	51008	277	~ 0.77	1.2377260(1)	short on	10
08.07.1999 <sup>(f)</sup>	51368			1.2377470(5)	anom. low	
09.10.2000 <sup>(j)</sup>	51826	301	~ 0.1	1.2377697(1)	main on	42
08.02.2001 <sup>(d)</sup>	51948	304	~ 0.6	1.2377740(1)	short on	34

<sup>(a)</sup>Number of the 35-day cycle following Staubert et al. (1983).

<sup>(b)</sup>MECS exposure, ks.

<sup>(c)</sup>dal Fiume et al. (1998)

<sup>(d)</sup>These data were not published before.

<sup>(e)</sup>Oosterbroek et al. (2000) have analysed just LECS and MECS data.

<sup>(f)</sup>Parmar et al. (1999)

<sup>(j)</sup>Oosterbroek et al. (2001)

Table 5.1: *BeppoSAX* observations of Her X-1.

thought to be due to decreased accretion rate, most likely associated with the state of the donor star.

Her X-1 was the first source, where a cyclotron absorption feature was detected at  $E_{\text{cyc}} \sim 40$  keV (Voges et al. 1982; Mihara et al. 1990; Gruber et al. 2001). However, Staubert et al. (2014) showed that the energy of the cyclotron line has decreased since then by more than 4 keV. This behaviour is unique among the accreting pulsars was associated with the accretion driven change in magnetic field configuration (Klochkov et al. 2015; Staubert et al. 2017). A broad emission iron line in the spectrum near 6.4 keV is observed (Pravdo et al. 1977; Choi et al. 1994; Ramsay et al. 2002; Zane et al. 2004).

## 5.2 Observations

Her X-1 was observed by *BeppoSAX* 8 times at different phases of the 35-day cycle (Tab. 5.1) with total MECS exposure time about 250 ks. These observations sample a substantial part of the 35-day phase cycle.



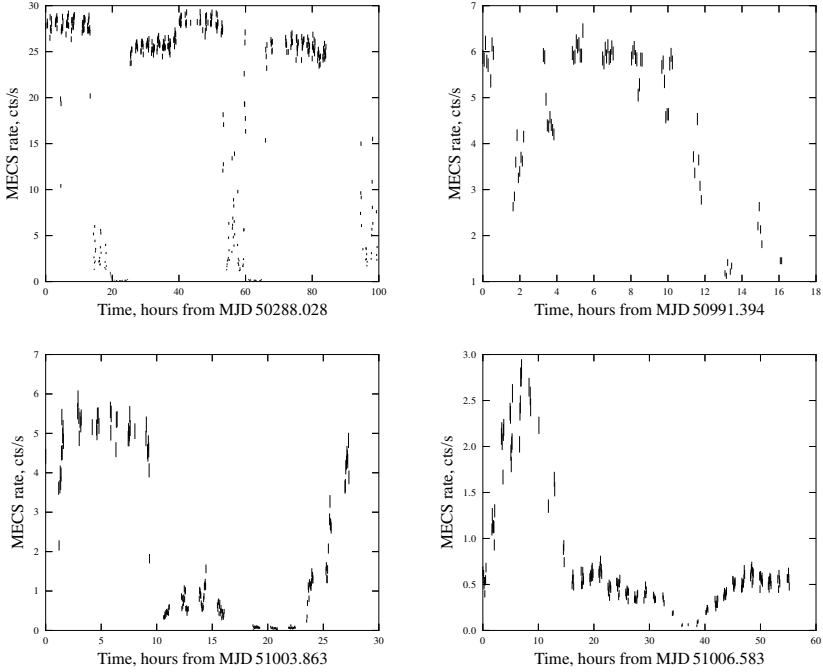


Figure 5.1: Her X-1 MECS light curves for observations summarised in Table 5.1. Top left picture is the main-on state on 24.07.1996 (257th 35<sup>d</sup> cycle), at the top right is the end of main-on state on 27.06.1998 (277). Bottom left: the short-on state on 09.07.1998 (277). Bottom right: the short-on state on 12.07.1998 (277).

### 5.2.1 Timing Analysis

The light curves with time bin of 256 s for all *BeppoSAX* observations, including the main-on, short-on and the low states as observed with the *BeppoSAX* narrow field instrument MECS in 2 – 10 keV energy range are presented in Figures 5.1, 5.2. They represent the three main-on and two short-on observations (one of them has not been analysed before), an observation when the source was eclipsed by the companion, and an observation during the anomalous low state.

Using the high resolution ( $\Delta t = 0.1$  s) *BeppoSAX* light curves and orbital ephemerides from Staubert et al. (2009b), we determined the pulse periods for all observations with high accuracy using the phase-connection technique. The results are summarised in Table 5.1.

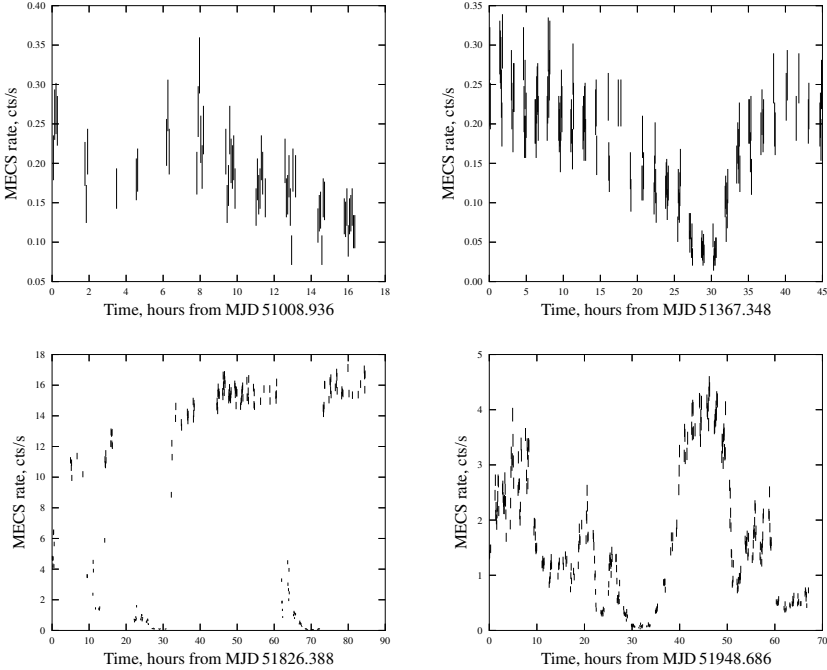


Figure 5.2: Her X-1 MECS light curve for observations summarised in Table 5.1. Top left: the short-on state (eclipse) on 14.07.1998 (277). Top right: the anomalous low state on 08.07.1999. Bottom left: the main-on state on 09.10.2000 (301). Bottom right: the short-on state on 08.02.2001 (304).

Using the determined period values we obtained the pulse profiles in several energy ranges. In Figure 5.3 the pulse profiles for the main-on state in July 1996 (257th superorbital cycle) are presented in 9 energy bands: 0.1–0.5, 0.5–1, 1–4 keV for LECS, 4–10 keV for MECS, 10–15 keV for HPGSPC and 15–20, 20–40, 40–60, 60–120 keV for PDS. As one can see, the shape of the Her X-1 pulse profile is strongly energy dependent. At low energies the single broad peak is observed, whereas two peaks may be identified at higher energies (Oosterbroek et al. 1997; Vasco et al. 2013).

It is interesting to investigate how the relative power of pulsed and non-pulsed emission changes with energy. We define the *pulse fraction* - as the ratio of the pulsed flux to the total flux as a function of energy:

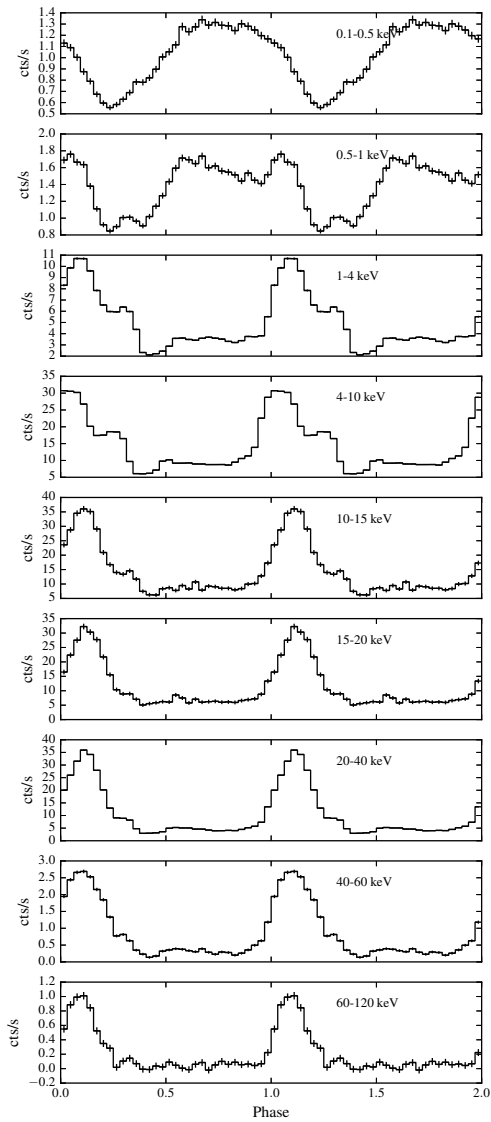


Figure 5.3: Her X-1, 24.07.1996. LECS (0.1–0.5, 0.5–1, 1–4 keV), MECS (4–10 keV), HP (10–15 keV) and PDS (15–20, 20–40, 40–60, 60–120 keV) pulse profiles.

$$F(E) = \frac{F_{\max} - F_{\min}}{F_{\max} + F_{\min}}, \quad (5.1)$$

where  $F_{\max}$  and  $F_{\min}$  are the maximal and minimal flux from the source within the X-ray pulse.

The pulse fraction of Her X-1 as function of energy calculated using the pulse profiles for the first observation in the main-on state (27.07.1996, 257) is presented in Figure 5.4. The fraction of pulsed emission steadily increases with energy from 35% to 95% and has two features associated with the fluorescent iron line at  $E_{\text{FeK}} \sim 6.4$  keV and with cyclotron line at  $E_{\text{cyc}} \sim 40$  keV.

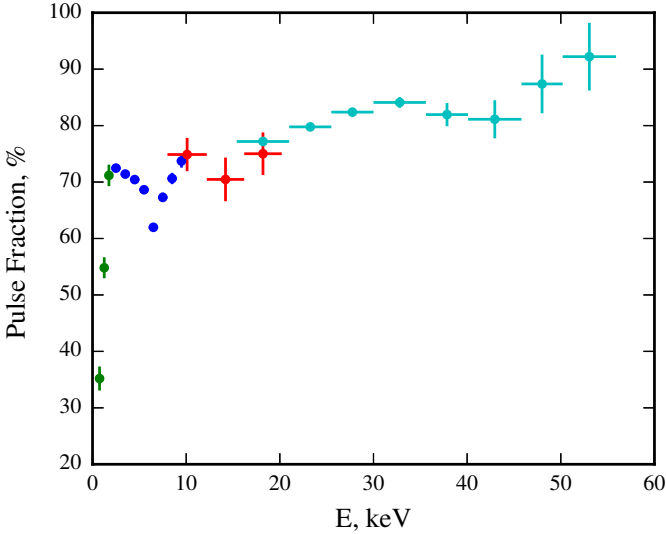


Figure 5.4: Her X-1 pulse fraction in the main-on state, 24.07.1996, 257th 35-day cycle.

### 5.2.2 Spectral Analysis

For spectral analysis of the Her X-1 we followed the standard procedures described in the introduction (see Chapter 4). Her X-1 is one of the well studied sources so we applied the models typically used in the literature for the spectral analysis. The broadband spectrum can be described with an absorbed continuum ( $N_{\text{H}} \sim 10^{20}$  atoms  $\text{cm}^{-2}$ ) consisting of a cut-off power law and soft black body component with temperature of  $\sim 0.1$  keV, which is required to account for soft excess. Two

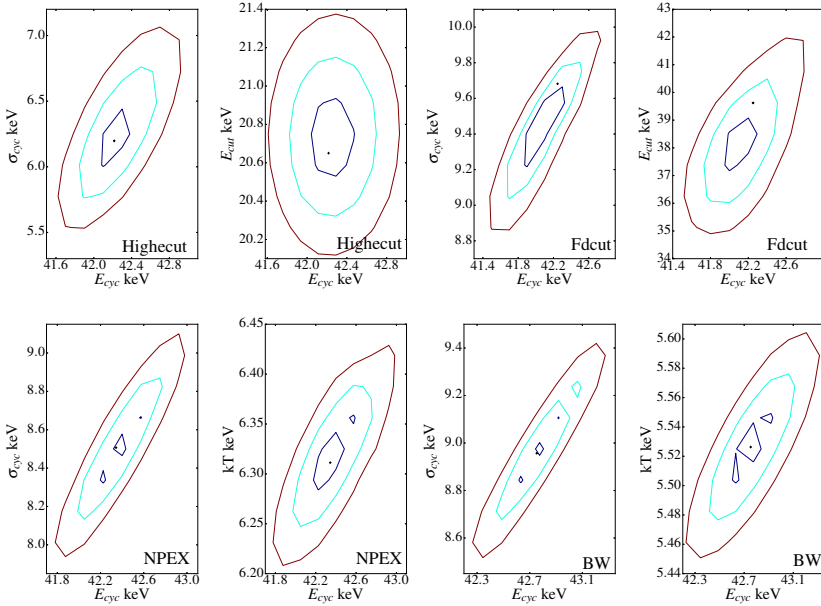


Figure 5.5: Her X-1 contours (1, 2 and  $3\sigma$ ) for different continuum models in the main-on state, 24.07.1996, 257th 35-day cycle.

fluorescent lines at  $\sim 0.9$  keV and  $\sim 6.5$  keV, and a CRSF with energy  $\sim 42$  keV (dal Fiume et al. 1998) are also required to describe the spectrum.

Her X-1 was observed by *BeppoSAX* 8 times (Tab. 5.1). The first observation on 24th of July 1996 (257 cycle) has the longest exposure with the best counting statistics. This observation was in the bright, main-on, state and was chosen as a representative observation to test all continuum models, which I used in the thesis. In the case of the Her X-1, however, only four continuum models can provide acceptable approximation of the phase averaged spectrum (Tab. 5.2): Highcut, Fdcut, NPEX and BW (see Chapter 4).

The statistically best fit has been obtained with the Highcut model. The parameters of this model are well constrained and do not exhibit strong inter-parameter correlations as can be seen from the contours presented in Figure 5.5.

Figure 5.6 shows the broadband spectrum of Her X-1, observed by *BeppoSAX* on 1996-07-24 during the main-on state (257 cycle). The top panel shows the phase average X-ray spectrum with the best fit model (absorbed cut-off power law, Highcut, with a blackbody). The second panel shows the residuals due to the

Parameter	Highecut	Fdcut	NPEX	BW
$N_H^{(a)}$	$1.09^{+0.03}_{-0.02}$	$1.12^{+0.04}_{-0.04}$	$1.08^{+0.03}_{-0.04}$	$1.07^{+0.09}_{-0.09}$
$E_{\text{FeL}}^{(b)}$	$0.89^{+0.01}_{-0.01}$	$0.88^{+0.01}_{-0.01}$	$0.86^{+0.01}_{-0.01}$	$0.90^{+0.02}_{-0.02}$
$\sigma_{\text{FeL}}^{(b)}$	$0.191^{+0.005}_{-0.003}$	$0.20^{+0.01}_{-0.01}$	$0.22^{+0.01}_{-0.01}$	$0.20^{+0.01}_{-0.01}$
$A_{\text{FeL}}^{(c)}$	$5.2^{+0.2}_{-0.1}$	$5.6^{+0.3}_{-0.3}$	$6.6^{+0.2}_{-0.1}$	$4.4^{+0.4}_{-0.3}$
$E_{\text{FeK}}^{(b)}$	$6.54^{+0.02}_{-0.02}$	$6.54^{+0.02}_{-0.02}$	$6.52^{+0.02}_{-0.02}$	$6.55^{+0.01}_{-0.01}$
$\sigma_{\text{FeK}}^{(b)}$	$0.38^{+0.03}_{-0.02}$	$0.36^{+0.04}_{-0.03}$	$0.48^{+0.03}_{-0.03}$	$0.41^{+0.03}_{-0.02}$
$A_{\text{FeK}}^{(c)}$	$0.45^{+0.01}_{-0.02}$	$0.43^{+0.01}_{-0.02}$	$0.54^{+0.02}_{-0.02}$	$0.48^{+0.02}_{-0.02}$
$E_{\text{cyc}}^{(b)}$	$42.18^{+0.15}_{-0.11}$	$42.0^{+0.29}_{-0.31}$	$42.44^{+0.22}_{-0.14}$	$42.75^{+0.30}_{-0.30}$
$\sigma_{\text{cyc}}^{(b)}$	$6.51^{+0.49}_{-0.16}$	$9.43^{+0.25}_{-0.4}$	$8.48^{+0.13}_{-0.14}$	$8.96^{+0.27}_{-0.27}$
$\delta_{\text{cyc}}$	$0.74^{+0.01}_{-0.02}$	$1.52^{+0.16}_{-0.12}$	$1.12^{+0.02}_{-0.02}$	
$\tau_{\text{cyc}}$				$29.3^{+2.0}_{-1.8}$
$kT_{\text{bb}}^{(b)}$	$0.0871^{+0.0004}_{-0.0006}$	$0.086^{+0.001}_{-0.001}$	$0.0869^{+0.0004}_{-0.0004}$	$0.089^{+0.002}_{-0.002}$
$R_{\text{bb}}^{(d)}$	$462^{+220}_{-96}$	$475^{+212}_{-160}$	$480^{+53}_{-54}$	$493^{+176}_{-167}$
$\Gamma$	$0.895^{+0.008}_{-0.002}$	$0.878^{+0.009}_{-0.008}$		
$E_{\text{cut}}^{(b)}$	$20.94^{+0.44}_{-0.06}$	$35.61^{+2.08}_{-1.79}$		
$E_{\text{fold}}^{(b)}$	$11.11^{+0.09}_{-0.13}$	$7.38^{+0.36}_{-0.45}$	$6.36^{+0.01}_{-0.04}$	
$\alpha_1$			$0.55^{+0.02}_{-0.01}$	
$kT^{(b)}$				$5.53^{+0.04}_{-0.04}$
$\xi$				$1.9(-1.0)$
$\delta$				$1.082^{+0.008}_{-0.007}$
$B^{(e)}$				$3.62$
$\dot{M}^{(f)}$				$3.68$
$r_0^{(g)}$				$265.4^{+0.4}_{-0.4}$
$D^{(h)}$				$6.6$
$\chi^2_{\text{red}} / \text{dof}$	$1.16 / 624$	$1.27 / 625$	$1.31 / 625$	$2.18 / 655$

<sup>(a)</sup> $[10^{20} \text{ atoms cm}^{-2}]$

<sup>(b)</sup> $[\text{keV}]$

<sup>(c)</sup> $[10^{-2} \text{ ph cm}^{-2} \text{ s}^{-1}]$

<sup>(d)</sup> $R_{\text{bb}}$  is the radius of the black body in km for the distance to the source

$D = 6.6 \text{ kpc.}$

<sup>(e)</sup> $[10^{12} \text{ G}]$

<sup>(f)</sup> $[10^{17} \text{ g/s}]$

<sup>(g)</sup> $[\text{km}]$

<sup>(h)</sup> $[\text{kpc}]$

Table 5.2: Her X-1. Main-on state on 1996-07-24, 257 35-day cycle. Parameters of the 4 different continuum models of the phase averaged Her X-1 spectrum. The values of an absorbed and unabsorbed fluxes are  $F_{\text{ab}} = 6.68 \times 10^{-9} \text{ erg / cm}^2/\text{s}$ ,  $F_{\text{unab}} = 6.97 \times 10^{-9} \text{ erg / cm}^2/\text{s}$  respectively.

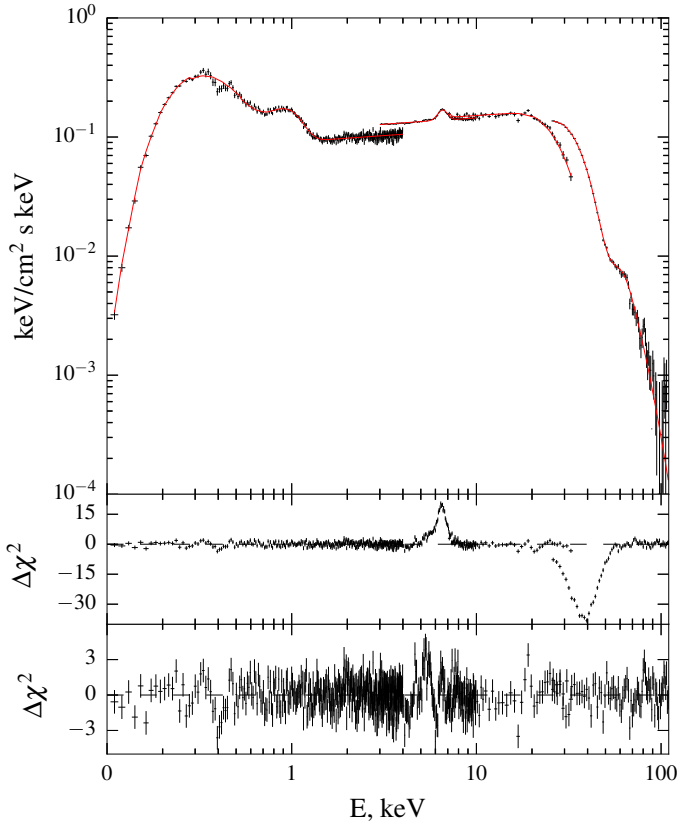


Figure 5.6: Her X–1 broadband spectrum. The top panel shows the 0.1–110 keV unfolded spectrum modeled using a cutoff power law and black body continuum model modified by Fe L and Fe K emission lines and an absorption gaussian line at  $\sim 42$  keV to account for cyclotron line during the observation on 1996-07-24. The residuals are shown in the bottom panels (1. Cyclotron and Fe K lines residuals. 2. The best fit residuals,  $\chi_{\text{red}}^2 \approx 1.16$ .)

Fe K line at  $\sim 6.5$  keV and cyclotron line at  $\sim 42$  keV. On the bottom panel the best fit residuals are shown. Her X–1 exhibits a rather broad iron line at  $\sim 6.5$  keV with a  $\sigma$  of about 0.4 keV. We approximated this line with a single Gaussian, however, some residuals remained (the bottom panel). Her X–1 also exhibits a soft-excess at low energies which is approximated with an additional black-body component

with temperature of about 0.1 keV (McCray et al. 1982). The respective radius of the blackbody emission region is  $R_{\text{bb}} \sim 500$  km.

McCray & Lamb (1976) suggested that this emission region is comparable with the *Alfven radius* of the pulsar:

$$R_A = 4.3 \times 10^8 \left( \frac{\mu_{30}^2 \epsilon m^{1/2}}{R_6 L_{37}} \right)^{2/7} \text{ cm}, \quad (5.2)$$

here  $\mu_{30}$  is the magnetic moment of the NS in units of  $10^{30}$  G $\cdot$ cm<sup>3</sup>,  $R_6$  is the NS radius in units of  $10^6$  cm,  $\epsilon = L/(GM\dot{M}/R_{\text{NS}})$  is the ratio between the observed luminosity and the total gravitational potential energy released per second by the accreting matter,  $m$  is the NS mass in units of  $M_{\odot}$  (Burderi et al. 1998). The ring at the magnetospheric boundary might intercept a substantial fraction ( $\gtrsim 10\%$ ) of the hard X-ray luminosity and reradiate it in soft X-rays.

Spectra for all the *BeppoSAX* observations of Her X-1 can be fitted using the same model (Tab. 5.3 – 5.5) consisting of:

- cyclotron line with energy  $\sim 42$  keV,
- low energy absorption  $\sim 10^{20}$  atoms cm<sup>-2</sup>,
- black body component with energy  $\sim 0.1$  keV,
- power law continuum,
- high energy cut-off,
- Fe<sub>K</sub> and Fe<sub>L</sub> iron lines at the energies  $\sim 6.5$  and  $0.9$  keV respectively,
- partial covering for some dates of observations (see text below).

For the observations close to the end of the main-on state (1998-06-27, 277 cycle) and at the short-on states (1998-07-09, 1998-07-12 and 1998-07-14, 277 cycle; 2001-02-08, 304 cycle), in which the NS is already partially eclipsed by the accretion disk, we have added a *partial covering absorption* component (PC) in XSPEC to account for this absorption. We note that in this case the continuum parameters remain stable throughout the 35-day cycle, whereas without adding the partial covering, the photon index varies strongly, which is not expected to be the case as the accretion rate does not change substantially with 35 day phase (Fig. 5.7, Tab. 5.5), see for example Vasco et al. (2013).

Phase resolved spectral analysis was also carried out (Fig. 5.8) for the main-on observations 24th of July 1996, 257 cycle. The absorbed power law model with cut-off at high energies was used to model the spectra as function of pulse phase.



The absorption column  $N_{\text{H}}$  was fixed at the average value for all phase bins. Fit results are presented in Tables 5.6, 5.7. A strong variation of the folding energy, cyclotron line energy, black body normalisation and black body temperature with pulse phase are observed (Fig. 5.8). Other parameters show no variation with the phase.

### 5.3 Conclusion

For Her X-1 the timing and spectral analysis was carried out for all *BeppoSAX* observations. Two of them (the main on from 1998, 277 35th day cycle, and the short on from 2001, 304 cycle) have been not analysed before. Also Oosterbroek et al. (2000) only reported on the analysis of LECS and MECS data for 2000-10-09 observation during the first main-on state after the longest recorded anomalous low-state. In this work the full analysis with all instruments are presented.

I determined the spin periods of the source, which are in agreement with values reported in the literature (listed in Tab. 5.1). The light curves are presented in Figures 5.1, 5.2. For the first *BeppoSAX* observation (the main on in 1996, 257 cycle) the pulse profiles in different energy ranges and pulse fraction as function of energy are also presented in Figure 5.3 and Figure 5.4.

Four of six continuum models can have a reasonably good fit of the spectrum (Tab. 5.2). The *Highcut* model provides statistically better and more stable fit for all observations. The best-fit results of this model are presented in Tables 5.3, 5.4, 5.5. I found that the spectrum can be described for all 35 day phases with approximately constant photon index if a partial covering component is included in the model at some phases (Fig. 5.7). For the first observation the pulse phase resolved analysis was also carried out. The results are presented in Tables 5.6, 5.7 and Figure 5.8.

35-day cycle	257	257	257	257	277	277
Phase of the cycle	(0.06-0.09)	(0.09-0.11)	(0.11-0.14)	(0.14-0.17)	(0.28)	(0.28)
Model	High	High	High	High	High	High+PC
$E_{\text{cyc}}^{(a)}$	42.5 <sup>+0.18</sup> <sub>-0.27</sub>	41.98 <sup>+0.27</sup> <sub>-0.26</sub>	42.63 <sup>+0.27</sup> <sub>-0.33</sub>	39.8 <sup>+0.35</sup> <sub>-0.22</sub>	41.13 <sup>+0.69</sup> <sub>-0.52</sub>	41.31 <sup>+1.15</sup> <sub>-0.93</sub>
$\sigma_{\text{cyc}}$	6.74 <sup>+0.17</sup> <sub>-0.13</sub>	6.06 <sup>+0.38</sup> <sub>-0.17</sub>	7.76 <sup>+0.23</sup> <sub>-0.16</sub>	6.77 <sup>+0.22</sup> <sub>-0.22</sub>	6.6 <sup>(b)</sup>	6.6 <sup>(b)</sup>
$\delta_{\text{cyc}}$	0.76 <sup>+0.02</sup> <sub>-0.02</sub>	0.72 <sup>+0.03</sup> <sub>-0.02</sub>	0.81 <sup>+0.03</sup> <sub>-0.03</sub>	0.92 <sup>+0.05</sup> <sub>-0.05</sub>	1.6 <sup>+0.2</sup> <sub>-0.2</sub>	0.8 <sup>+0.2</sup> <sub>-0.2</sub>
$N_{\text{H}}^{(c)}$	1.17 <sup>+0.1</sup> <sub>-0.05</sub>	1.24 <sup>+0.04</sup> <sub>-0.04</sub>	1.2 <sup>+0.06</sup> <sub>-0.04</sub>	1.26 <sup>+0.12</sup> <sub>-0.07</sub>	0.8 <sup>+0.07</sup> <sub>-0.06</sub>	1.15 <sup>+0.1</sup> <sub>-0.08</sub>
$kT_{\text{bb}}^{(a)}$	0.079 <sup>+0.001</sup> <sub>-0.001</sub>	0.083 <sup>+0.004</sup> <sub>-0.004</sub>	0.084 <sup>+0.001</sup> <sub>-0.001</sub>	0.086 <sup>+0.001</sup> <sub>-0.002</sub>	0.089 <sup>+0.001</sup> <sub>-0.001</sub>	0.079 <sup>+0.001</sup> <sub>-0.001</sub>
$R_{\text{bb}}^{(d)}$	462 <sup>+85</sup> <sub>-106</sub>	493 <sup>+62</sup> <sub>-80</sub>	397 <sup>+113</sup> <sub>-69</sub>	482 <sup>+118</sup> <sub>-113</sub>	205 <sup>+40</sup> <sub>-44</sub>	343 <sup>+63</sup> <sub>-75</sub>
$\Gamma$	0.876 <sup>+0.003</sup> <sub>-0.002</sub>	0.89 <sup>+0.003</sup> <sub>-0.005</sub>	0.844 <sup>+0.005</sup> <sub>-0.004</sub>	0.911 <sup>+0.006</sup> <sub>-0.005</sub>	0.529 <sup>+0.005</sup> <sub>-0.017</sub>	0.82 <sup>+0.02</sup> <sub>-0.01</sub>
$E_{\text{cut}}^{(a)}$	20.68 <sup>+0.06</sup> <sub>-0.1</sub>	20.61 <sup>+0.08</sup> <sub>-0.24</sub>	21.46 <sup>+0.11</sup> <sub>-0.12</sub>	24.98 <sup>+0.24</sup> <sub>-0.26</sub>	13.04 <sup>+0.18</sup> <sub>-0.3</sub>	17.33 <sup>+0.19</sup> <sub>-0.31</sub>
$E_{\text{fold}}^{(a)}$	11.21 <sup>+0.07</sup> <sub>-0.1</sub>	10.9 <sup>+0.08</sup> <sub>-0.08</sub>	11.2 <sup>+0.11</sup> <sub>-0.13</sub>	9.89 <sup>+0.26</sup> <sub>-0.25</sub>	12.07 <sup>+0.24</sup> <sub>-0.31</sub>	9.895 <sup>+0.215</sup> <sub>-0.444</sub>
$E_{\text{FeL}}^{(d)}$	0.84 <sup>+0.02</sup> <sub>-0.02</sub>	0.88 <sup>+0.01</sup> <sub>-0.01</sub>	0.86 <sup>+0.01</sup> <sub>-0.01</sub>	0.88 <sup>+0.03</sup> <sub>-0.02</sub>	0.94 <sup>+0.02</sup> <sub>-0.02</sub>	0.89 <sup>+0.04</sup> <sub>-0.09</sub>
$\sigma_{\text{FeL}}^{(a)}$	0.24 <sup>+0.01</sup> <sub>-0.02</sub>	0.19 <sup>+0.01</sup> <sub>-0.01</sub>	0.22 <sup>+0.01</sup> <sub>-0.01</sub>	0.2 <sup>+0.02</sup> <sub>-0.02</sub>	0.17 <sup>+0.02</sup> <sub>-0.01</sub>	0.17 <sup>+0.01</sup> <sub>-0.02</sub>
$A_{\text{FeL}}^{(e)}$	4.7 <sup>+0.4</sup> <sub>-0.2</sub>	4.6 <sup>+0.2</sup> <sub>-0.1</sub>	3.6 <sup>+0.1</sup> <sub>-0.1</sub>	5.3 <sup>+0.5</sup> <sub>-0.5</sub>	0.65 <sup>+0.08</sup> <sub>-0.06</sub>	0.98 <sup>+0.09</sup> <sub>-0.11</sub>
$E_{\text{FeK}}^{(a)}$	6.55 <sup>+0.03</sup> <sub>-0.02</sub>	6.53 <sup>+0.02</sup> <sub>-0.03</sub>	6.57 <sup>+0.02</sup> <sub>-0.03</sub>	6.54 <sup>+0.08</sup> <sub>-0.08</sub>	6.43 <sup>+0.04</sup> <sub>-0.04</sub>	6.52 <sup>+0.04</sup> <sub>-0.04</sub>
$\sigma_{\text{FeK}}^{(a)}$	0.48 <sup>+0.04</sup> <sub>-0.03</sub>	0.40 <sup>+0.06</sup> <sub>-0.03</sub>	0.41 <sup>+0.06</sup> <sub>-0.05</sub>	0.34 <sup>+0.1</sup> <sub>-0.08</sub>	0.44 <sup>+0.11</sup> <sub>-0.03</sub>	0.36 <sup>+0.05</sup> <sub>-0.05</sub>
$A_{\text{FeK}}^{(e)}$	0.38 <sup>+0.01</sup> <sub>-0.02</sub>	0.46 <sup>+0.03</sup> <sub>-0.03</sub>	0.37 <sup>+0.02</sup> <sub>-0.02</sub>	0.36 <sup>+0.05</sup> <sub>-0.05</sub>	0.26 <sup>+0.01</sup> <sub>-0.02</sub>	0.36 <sup>+0.05</sup> <sub>-0.05</sub>
$N_{\text{H}_p}^{(f)}$						11.35 <sup>+1.02</sup> <sub>-0.99</sub>
$C_{\text{F}_p}^{(g)}$						0.38 <sup>+0.01</sup> <sub>-0.02</sub>
$F_{\text{ab}}^{(h)}$	5.24	6.76	5.03	6.52	1.91	1.91
$F_{\text{unab}}^{(h)}$	5.28	6.87	5.12	6.9	1.93	2.03
$\chi^2_{\text{red}} / \text{dof}$	1.239 / 483	0.996 / 667	1.195 / 664	1.055 / 665	1.208 / 608	1.075 / 606

<sup>(a)</sup>[keV]

<sup>(b)</sup>This parameter was fixed.

<sup>(c)</sup>[ $10^{20}$  atoms  $\text{cm}^{-2}$ ]

<sup>(d)</sup> $R_{\text{bb}}$  is the radius of the black body in km for the distance to the source  $D = 6.6$  kpc.

<sup>(e)</sup>[ $10^{-2}$  ph  $\text{cm}^{-2}$   $\text{s}^{-1}$ ]

<sup>(f)</sup>Equivalent hydrogen column for partial covering absorption in units  $10^{22}$  atoms  $\text{cm}^{-2}$ .

<sup>(g)</sup>Covering fraction.

<sup>(h)</sup>The values of absorbed and unabsorbed fluxes in 0.1 – 120 keV energy range in units  $10^{-9}$  erg /  $\text{cm}^2$  / s.

Table 5.3: Her X-1. Changing parameters with orbital cycles of the Her X-1 in power law with high energy cut off continuum model (Highcut). Part 1, main-on states.

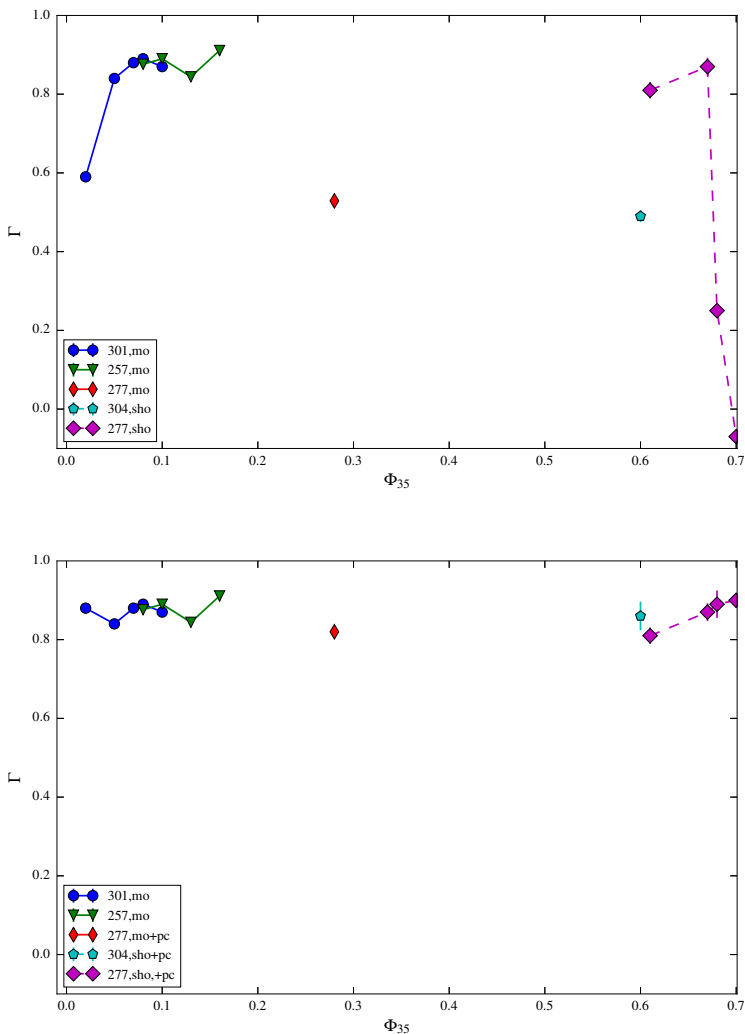


Figure 5.7: Her X–1. Photon Index as function of 35<sup>d</sup> phase with (bottom panel) and without (top panel) inclusion of the partial covering absorber.

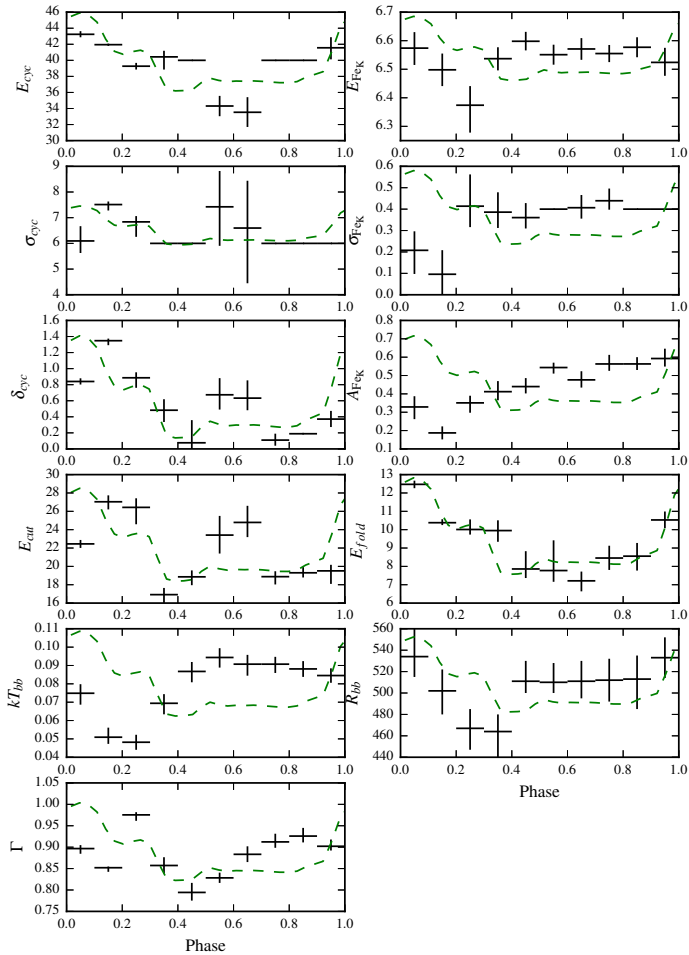


Figure 5.8: Her X-1. Variation of spectral parameters with pulse phase (dotted green line shows the MECS pulse profile for reference) during the observation on 1996-07-24 (main-on state, 257 cycle).

35-day cycle Phase of the cycle Model	301 (0-0.03) High	301 (0-0.03) High+PC	301 (0.03-0.06) High	301 (0.06-0.07) High	301 (0.07-0.09) High	301 (0.09-0.11) High
$E_{\text{cyc}}^{(a)}$	41 <sup>(h)</sup>	40.69 <sup>+1.82</sup> <sub>-1.51</sub>	40.86 <sup>+0.72</sup> <sub>-1.02</sub>	40.91 <sup>+1.31</sup> <sub>-1.13</sub>	40.13 <sup>+1.24</sup> <sub>-1.12</sub>	40.32 <sup>+1.17</sup> <sub>-0.83</sub>
$\sigma_{\text{cyc}}^{(a)}$	7 <sup>(h)</sup>	6.26 <sup>+1.29</sup> <sub>-1.64</sub>	6.45 <sup>+1.45</sup> <sub>-1.08</sub>	6.96 <sup>+2.21</sup> <sub>-1.39</sub>	7.93 <sup>+1.25</sup> <sub>-1.51</sub>	4.3 <sup>+1.14</sup> <sub>-0.64</sub>
$\delta_{\text{cyc}}$	0.61 <sup>+0.12</sup> <sub>-0.13</sub>	0.58 <sup>+0.12</sup> <sub>-0.13</sub>	0.54 <sup>+0.07</sup> <sub>-0.07</sub>	0.61 <sup>+0.15</sup> <sub>-0.09</sub>	0.65 <sup>+0.12</sup> <sub>-0.15</sub>	0.74 <sup>+0.13</sup> <sub>-0.13</sub>
$N_{\text{H}}^{(b)}$				1.6 <sup>+0.1</sup> <sub>-0.1</sub>	0.021 <sup>+0.001</sup> <sub>-0.002</sub>	
$kT_{\text{bb}}^{(a)}$				0.076 <sup>+0.001</sup> <sub>-0.002</sub>	0.071 <sup>+0.001</sup> <sub>-0.001</sub>	
$R_{\text{bb}}^{(c)}$				591 <sup>+462</sup> <sub>-349</sub>	777 <sup>+721</sup> <sub>-489</sub>	
$\Gamma$	0.59 <sup>+0.01</sup> <sub>-0.01</sub>	0.88 <sup>+0.04</sup> <sub>-0.03</sub>	0.84 <sup>+0.01</sup> <sub>-0.01</sub>	0.88 <sup>+0.01</sup> <sub>-0.01</sub>	0.89 <sup>+0.01</sup> <sub>-0.01</sub>	0.87 <sup>+0.01</sup> <sub>-0.03</sub>
$E_{\text{cut}}^{(a)}$	17.44 <sup>+1.73</sup> <sub>-1.23</sub>	16.96 <sup>+0.67</sup> <sub>-0.8</sub>	20.0 <sup>+1.26</sup> <sub>-0.84</sub>	20.91 <sup>+2.6</sup> <sub>-0.96</sub>	22.39 <sup>+1.69</sup> <sub>-2.36</sub>	20.27 <sup>+0.43</sup> <sub>-3.9</sub>
$E_{\text{fold}}^{(a)}$	10.44 <sup>+0.54</sup> <sub>-0.54</sub>	11.32 <sup>+0.78</sup> <sub>-0.7</sub>	10.5 <sup>+0.31</sup> <sub>-0.31</sub>	10.65 <sup>+0.47</sup> <sub>-0.52</sub>	10.33 <sup>+0.6</sup> <sub>-0.51</sub>	10.33 <sup>+0.52</sup> <sub>-0.687</sub>
$E_{\text{FeL}}^{(a)}$				0.89 <sup>+0.05</sup> <sub>-0.04</sub>	0.9 <sup>+0.05</sup> <sub>-0.04</sub>	
$\sigma_{\text{FeL}}^{(d)}$				0.16 <sup>+0.03</sup> <sub>-0.02</sub>	0.17 <sup>+0.03</sup> <sub>-0.03</sub>	
$A_{\text{FeL}}^{(d)}$				2.8 <sup>+0.6</sup> <sub>-0.4</sub>	3.34 <sup>+0.6</sup> <sub>-0.5</sub>	
$E_{\text{FeK}}^{(a)}$	6.42 <sup>+0.04</sup> <sub>-0.05</sub>	6.52 <sup>+0.06</sup> <sub>-0.05</sub>	6.46 <sup>+0.05</sup> <sub>-0.05</sub>	6.53 <sup>+0.07</sup> <sub>-0.07</sub>	6.55 <sup>+0.05</sup> <sub>-0.05</sub>	6.6 <sup>+0.08</sup> <sub>-0.07</sub>
$\sigma_{\text{FeK}}^{(a)}$	0.4 <sup>(h)</sup>	0.4 <sup>+0.11</sup> <sub>-0.07</sub>	0.4 <sup>(h)</sup>	0.4 <sup>(h)</sup>	0.4 <sup>(h)</sup>	0.26 <sup>+0.16</sup> <sub>-0.22</sub>
$A_{\text{FeK}}^{(d)}$	0.32 <sup>+0.03</sup> <sub>-0.02</sub>	0.24 <sup>+0.05</sup> <sub>-0.03</sub>	0.36 <sup>+0.03</sup> <sub>-0.03</sub>	0.34 <sup>+0.04</sup> <sub>-0.04</sub>	0.38 <sup>+0.03</sup> <sub>-0.03</sub>	0.4 <sup>+0.1</sup> <sub>-0.1</sub>
$N_{\text{Hp}}^{(e)}$		13.52 <sup>+1.19</sup> <sub>-1.39</sub>				
$C_{\text{Fp}}^{(f)}$		0.38 <sup>+0.04</sup> <sub>-0.04</sub>				
$F_{\text{ab}}^{(g)}$	—	3.38	—	5.59	5.67	—
$F_{\text{unab}}^{(g)}$	3.38	3.66	5.15	5.72	5.83	5.60
$\chi_{\text{red}}^2 / \text{dof}$	1.392 / 212	0.967 / 207	1.170 / 260	1.102 / 620	0.931 / 620	1.033 / 259

<sup>(a)</sup>[keV]<sup>(b)</sup>[10<sup>20</sup>atoms cm<sup>-2</sup>]<sup>(c)</sup> $R_{\text{bb}}$  is the radius of the black body in km for the distance to the source  $D = 6.6$  kpc.<sup>(d)</sup>[10<sup>-2</sup> ph cm<sup>-2</sup> s<sup>-1</sup>]<sup>(e)</sup>Equivalent hydrogen column for partial covering absorption in units 10<sup>22</sup>atoms cm<sup>-2</sup>.<sup>(f)</sup>Covering fraction.<sup>(g)</sup>The values of absorbed and unabsorbed fluxes in 0.1 – 120 keV energy range in units 10<sup>-9</sup>erg / cm<sup>2</sup>/s.<sup>(h)</sup>This parameter was fixed.

Table 5.4: Her X–1. Variation of the parameters with orbital cycles of the Her X–1 in power law with high energy cut off continuum model (Highcut). There are no low energy data (LECS) in some observations to determine values of  $N_{\text{H}}$  and  $kT_{\text{bb}}$ . Part 2, main-on states.

35-day cycle	277	277	277	277	277	277	304	304
Phase of the cycle	(~ 0.61)	(~ 0.67)	(~ 0.68)	(~ 0.68)	(~ 0.7)	(~ 0.7)	(~ 0.6)	(~ 0.6)
Model	High	High	High	High + PC	High	High +PC	High	High + PC
$E_{\text{cyc}}^{(a)}$	$41.33^{+2.23}_{-1.54}$	$44.02^{+2.11}_{-6.01}$	$41.96^{+1.22}_{-1.99}$	$41.74^{+7.67}_{-6.92}$	$41.74^{(b)}$	$41.74^{(b)}$	$42.0^{(b)}$	$42.21^{(b)}$
$\sigma_{\text{cyc}}^{(a)}$	$5.95^{+1.23}_{-0.56}$	$8.96^{+1.78}_{-2.45}$	$8.51^{+0.92}_{-1.07}$	$8.4^{(b)}$	$8.34^{(b)}$	$8.34^{(b)}$	$6.33^{+1.39}_{-1.46}$	$7.67^{+1.86}_{-0.89}$
$\delta_{\text{cyc}}$	$1.0^{+0.9}_{-0.5}$	$1.6^{+0.7}_{-0.6}$	$2.7^{+0.5}_{-0.3}$	$2.6^{+1.5}_{-0.3}$	$2.6^{+0.6}_{-0.2}$	$2.6^{(b)}$	$0.6^{+0.2}_{-0.3}$	$0.6^{+0.2}_{-0.2}$
$N_{\text{H}}^{(c)}$	$0.9^{+0.3}_{-0.2}$	$0.8^{+0.3}_{-0.3}$	$0.3^{+0.5}_{-0.2}$	$7^{+0.3}_{-0.4}$	$7.856(1)e-06$	$0.1^{+0.1}_{-0.1}$	$0.8^{+1.0}_{-0.6}$	$0.8^{+0.6}_{-0.7}$
$kT_{\text{bb}}^{(a)}$	$0.083^{+0.008}_{-0.005}$	$0.085^{+0.005}_{-0.004}$	$0.1^{+0.005}_{-0.004}$	$0.086^{+0.006}_{-0.006}$	$0.107^{+0.003}_{-0.003}$	$0.082^{+0.005}_{-0.005}$	$0.09^{+0.01}_{-0.01}$	$0.08^{+0.01}_{-0.01}$
$R_{\text{bb}}^{(a)}$	$282^{+243}_{-172}$	$271^{+172}_{-147}$	$97^{+83}_{-57}$	$184^{+117}_{-108}$	$52^{+18}_{-17}$	$121^{+57}_{-57}$	$115^{+146}_{-78}$	$171^{+232}_{-130}$
$\Gamma$	$0.81^{+0.02}_{-0.01}$	$0.87^{+0.01}_{-0.02}$	$0.25^{+0.02}_{-0.04}$	$0.89^{+0.02}_{-0.14}$	$-0.07^{+0.01}_{-0.02}$	$0.9^{+0.01}_{-0.01}$	$0.49^{+0.01}_{-0.01}$	$0.86^{+0.04}_{-0.02}$
$E_{\text{cut}}^{(a)}$	$17.22^{+1.07}_{-0.79}$	$15.91^{+2.19}_{-1.35}$	$4.6^{+0.44}_{-0.24}$	$16.36^{+0.47}_{-0.49}$	$4.65^{+0.21}_{-0.25}$	$22.59^{+0.94}_{-0.77}$	$16.49^{+0.89}_{-0.47}$	$18.94^{+0.82}_{-0.53}$
$E_{\text{fold}}^{(a)}$	$10.41^{+0.99}_{-1.4}$	$13.19^{+2.1}_{-2.62}$	$15.57^{+0.99}_{-1.72}$	$21.66^{+0.96}_{-1.61}$	$12.11^{+0.33}_{-0.25}$	$25.62^{+8.07}_{-5.05}$	$8.39^{+0.59}_{-0.86}$	$9.16^{+0.87}_{-0.97}$
$E_{\text{FeL}}^{(a)}$	$0.91^{+0.04}_{-0.06}$	$1.0^{(b)}$	$1.02^{+0.05}_{-0.08}$	$1.0^{(b)}$	$1.0^{(b)}$	—	$1.0^{(b)}$	—
$\sigma_{\text{FeL}}^{(a)}$	$0.15^{+0.07}_{-0.04}$	$0.14^{+0.04}_{-0.02}$	$0.15^{+0.09}_{-0.03}$	$0.1^{(b)}$	$0.1^{(b)}$	—	$0.05^{(b)}$	—
$A_{\text{FeL}}^{(e)}$	$0.7^{+0.3}_{-0.2}$	$0.6^{+0.1}_{-0.1}$	$0.1^{+0.1}_{-0.1}$	$0.1^{(b)}$	$0.07^{+0.03}_{-0.03}$	—	$0.05^{+0.05}_{-0.03}$	—
$E_{\text{FeK}}^{(a)}$	$6.48^{+0.05}_{-0.06}$	$6.5^{+0.06}_{-0.06}$	$6.5^{+0.05}_{-0.05}$	$6.55^{+0.05}_{-0.05}$	$6.49^{+0.06}_{-0.13}$	$6.61^{+0.08}_{-0.13}$	$6.45^{+0.03}_{-0.03}$	$6.54^{+0.04}_{-0.04}$
$\sigma_{\text{FeK}}^{(a)}$	$0.49^{+0.1}_{-0.08}$	$0.45^{+0.11}_{-0.09}$	$0.48^{+0.06}_{-0.12}$	$0.54^{+0.07}_{-0.11}$	$0.4^{(b)}$	$0.4^{(b)}$	$0.4^{(b)}$	$0.4^{(b)}$
$A_{\text{FeK}}^{(e)}$	$0.31^{+0.02}_{-0.04}$	$0.25^{+0.02}_{-0.04}$	$0.22^{+0.02}_{-0.07}$	$0.26^{+0.01}_{-0.04}$	$0.14^{+0.01}_{-0.03}$	$0.14^{+0.01}_{-0.03}$	$0.22^{+0.01}_{-0.01}$	$0.21^{+0.87}_{-0.01}$
$N_{\text{H}_p}^{(f)}$	—	—	—	$6.1^{+0.5}_{-0.5}$	—	$8.2^{+0.4}_{-0.7}$	—	$7.6^{+0.4}_{-0.9}$
$C_{\text{Fe}}^{(g)}$	—	—	—	$0.55^{+0.01}_{-0.01}$	—	$0.73^{+0.01}_{-0.01}$	—	$0.48^{+0.03}_{-0.03}$
$F_{\text{bb}}^{(b)}$	1.45	1.43	1.29	1.29	0.905	0.905	1.16	1.16
$F_{\text{unab}}^{(b)}$	1.47	1.45	1.292	1.31	0.905	1.217	1.17	1.25
$\chi^2_{\text{red}} / \text{dof}$	1.039 / 515	1.208 / 598	1.077 / 536	1.056 / 540	1.258 / 353	1.064 / 351	2.308 / 355	1.447 / 355

(a)[keV]

(b) This parameter was fixed.

(c)[ $10^{20}$ atoms  $\text{cm}^{-2}$ ](d) $R_{\text{bb}}$  is the radius of the black body in km for the distance to the source  $D = 6.6$  kpc.(e)[ $10^{-2}$  ph  $\text{cm}^{-2}$   $\text{s}^{-1}$ ](f) Equivalent hydrogen column for partial covering absorption in units  $10^{22}$ atoms  $\text{cm}^{-2}$ .

(g) Covering fraction.

(h) The values of absorbed and unabsorbed fluxes in 0.1 – 120 keV energy range in units  $10^{-9}$ erg /  $\text{cm}^2/\text{s}$ .

Table 5.5: Her X-1. Changing parameters with orbital cycles of the Her X-1 in power law with high energy cut off (Highcut) and power law, high energy cut off with partial covering continuum model. Part 3, short-on states.

Phase	0 - 0.1	0.1 - 0.2	0.2 - 0.3	0.3 - 0.4	0.4 - 0.5
$E_{\text{cyc}}^{(a)}$	43.24 <sup>+0.39</sup> <sub>-0.37</sub>	41.95 <sup>+0.14</sup> <sub>-0.17</sub>	39.27 <sup>+0.4</sup> <sub>-0.42</sub>	40.43 <sup>+0.76</sup> <sub>-1.58</sub>	40.0 <sup>(b)</sup>
$\sigma_{\text{cyc}}^{(a)}$	6.09 <sup>+0.58</sup> <sub>-0.47</sub>	7.53 <sup>+0.14</sup> <sub>-0.32</sub>	6.84 <sup>+0.44</sup> <sub>-0.58</sub>	6.05 <sup>+1.23</sup> <sub>0.22</sub>	6.0 <sup>(b)</sup>
$\delta_{\text{cyc}}$	0.84 <sup>+0.04</sup> <sub>-0.04</sub>	1.36 <sup>+0.02</sup> <sub>-0.07</sub>	0.89 <sup>+0.07</sup> <sub>-0.12</sub>	0.48 <sup>+0.14</sup> <sub>-0.15</sub>	0.1 <sup>+0.01</sup> <sub>-0.01</sub>
$kT_{\text{bb}}^{(a)}$	0.075 <sup>+0.005</sup> <sub>-0.003</sub>	0.051 <sup>+0.006</sup> <sub>-0.004</sub>	0.048 <sup>+0.004</sup> <sub>-0.004</sub>	0.069 <sup>+0.005</sup> <sub>-0.006</sub>	0.087 <sup>+0.005</sup> <sub>-0.006</sub>
$R_{\text{bb}}^{(c)}$	534 <sup>+26</sup> <sub>-19</sub>	502 <sup>+20</sup> <sub>-22</sub>	467 <sup>+18</sup> <sub>-20</sub>	464 <sup>+16</sup> <sub>-24</sub>	511 <sup>+19</sup> <sub>-11</sub>
$\Gamma$	0.897 <sup>+0.008</sup> <sub>-0.01</sub>	0.852 <sup>+0.003</sup> <sub>-0.012</sub>	0.975 <sup>+0.006</sup> <sub>-0.014</sub>	0.86 <sup>+0.02</sup> <sub>-0.02</sub>	0.79 <sup>+0.02</sup> <sub>-0.02</sub>
$E_{\text{cut}}^{(a)}$	22.45 <sup>+0.44</sup> <sub>-0.44</sub>	27.3 <sup>+0.46</sup> <sub>-1.15</sub>	26.43 <sup>+0.98</sup> <sub>-1.82</sub>	16.92 <sup>+0.73</sup> <sub>-0.9</sub>	18.86 <sup>+0.69</sup> <sub>-0.9</sub>
$E_{\text{fold}}^{(a)}$	12.47 <sup>+0.21</sup> <sub>-0.21</sub>	10.32 <sup>+0.28</sup> <sub>-0.11</sub>	10.02 <sup>+0.53</sup> <sub>-0.28</sub>	9.95 <sup>+0.56</sup> <sub>-0.61</sub>	7.86 <sup>+0.97</sup> <sub>-0.49</sub>
$E_{\text{FeL}}^{(a)}$	0.89 <sup>+0.05</sup> <sub>-0.11</sub>	—	—	0.88 <sup>+0.04</sup> <sub>-0.06</sub>	0.83 <sup>+0.05</sup> <sub>-0.08</sub>
$\sigma_{\text{FeL}}^{(a)}$	0.17 <sup>+0.07</sup> <sub>-0.04</sub>	—	—	0.16 <sup>+0.05</sup> <sub>-0.03</sub>	0.26 <sup>+0.04</sup> <sub>-0.03</sub>
$A_{\text{FeL}}^{(d)}$	0.03 <sup>+0.02</sup> <sub>-0.01</sub>	—	—	1.3 <sup>+0.4</sup> <sub>-0.3</sub>	0.11 <sup>+0.04</sup> <sub>-0.02</sub>
$E_{\text{FeK}}^{(a)}$	6.57 <sup>+0.06</sup> <sub>-0.06</sub>	6.5 <sup>+0.06</sup> <sub>-0.06</sub>	6.37 <sup>+0.07</sup> <sub>-0.09</sub>	6.54 <sup>+0.04</sup> <sub>-0.04</sub>	6.6 <sup>+0.03</sup> <sub>-0.03</sub>
$\sigma_{\text{FeK}}^{(a)}$	0.21 <sup>+0.09</sup> <sub>-0.11</sub>	0.1 <sup>+0.05</sup> <sub>-0.05</sub>	0.41 <sup>+0.15</sup> <sub>-0.1</sub>	0.39 <sup>+0.09</sup> <sub>-0.07</sub>	0.36 <sup>+0.07</sup> <sub>-0.05</sub>
$A_{\text{FeK}}^{(d)}$	0.33 <sup>+0.05</sup> <sub>-0.07</sub>	0.19 <sup>+0.04</sup> <sub>-0.03</sub>	0.35 <sup>+0.07</sup> <sub>-0.05</sub>	0.41 <sup>+0.06</sup> <sub>-0.05</sub>	0.44 <sup>+0.05</sup> <sub>-0.04</sub>
$F_{\text{ab}}^{(e)}$	10.61	11.38	6.22	3.25	2.24
$F_{\text{unab}}^{(e)}$	10.74	11.49	6.3	3.33	2.33
$\chi_{\text{red}}^2 / \text{dof}$	1.065 / 687	1.285 / 690	1.499 / 678	1.156 / 661	1.154 / 661

(a)[keV]

(b) This parameter was fixed.

(c)  $R_{\text{bb}}$  is the radius of the black body in km for the distance to the source  $D = 6.6$  kpc.(d) [ $10^{-2}$  ph cm $^{-2}$  s $^{-1}$ ](e) The values of absorbed and unabsorbed fluxes in 0.1 – 120 keV energy range in units  $10^{-9}$  erg / cm $^2$ /s.

Table 5.6: Her X-1. Spectral parameters as a function of pulse phase during the observation on 1996-07-27 (main-on state, 257 cycle). The interstellar absorption was fixed to the average value of  $N_{\text{H}} = 1.09 \times 10^{20}$  atoms cm $^{-2}$ . Part 1.

Phase	0.5 - 0.6	0.6 - 0.7	0.7 - 0.8	0.8 - 0.9	0.9 - 1
$E_{\text{cyc}}^{(a)}$	$34.32^{+1.41}_{-1.55}$	$33.53^{+2.06}_{-1.98}$	$40.0^{(b)}$	$40.0^{(b)}$	$41.56^{+1.32}_{-1.44}$
$\sigma_{\text{cyc}}^{(a)}$	$7.5^{+1.49}_{-1.77}$	$6.59^{+1.97}_{-2.29}$	$6.0^{(b)}$	$6.0^{(b)}$	$6.0^{(b)}$
$\delta_{\text{cyc}}$	$0.68^{+0.24}_{-0.22}$	$0.63^{+0.24}_{-0.17}$	$0.11^{+0.08}_{-0.07}$	$0.19^{+0.01}_{-0.01}$	$0.4^{+0.1}_{-0.1}$
$kT_{\text{bb}}^{(a)}$	$0.092^{+0.008}_{-0.004}$	$0.092^{+0.004}_{-0.008}$	$0.092^{+0.003}_{-0.007}$	$0.088^{+0.004}_{-0.004}$	$0.085^{+0.004}_{-0.004}$
$R_{\text{bb}}^{(c)}$	$510^{+18}_{-10}$	$511^{+19}_{-16}$	$512^{+20}_{-20}$	$513^{+22}_{-28}$	$533^{+19}_{-19}$
$\Gamma$	$0.83^{+0.01}_{-0.01}$	$0.88^{+0.02}_{-0.02}$	$0.91^{+0.02}_{-0.01}$	$0.93^{+0.02}_{-0.01}$	$0.9^{+0.02}_{-0.01}$
$E_{\text{cut}}^{(a)}$	$23.42^{+2.43}_{-1.32}$	$24.79^{+2.0}_{-1.5}$	$18.88^{+0.64}_{-0.95}$	$19.3^{+0.62}_{-0.51}$	$19.51^{+0.66}_{-1.42}$
$E_{\text{fold}}^{(a)}$	$7.77^{+1.71}_{-0.74}$	$7.21^{+2.49}_{-0.63}$	$8.46^{+0.72}_{-0.71}$	$8.56^{+0.72}_{-0.78}$	$10.53^{+0.46}_{-0.45}$
$E_{\text{FeL}}^{(a)}$	$0.84^{+0.07}_{-0.04}$	$0.84^{+0.04}_{-0.11}$	$0.85^{+0.03}_{-0.1}$	$0.85^{+0.04}_{-0.05}$	$0.88^{+0.03}_{-0.04}$
$\sigma_{\text{FeL}}^{(a)}$	$0.24^{+0.02}_{-0.04}$	$0.23^{+0.05}_{-0.02}$	$0.24^{+0.05}_{-0.02}$	$0.22^{+0.03}_{-0.02}$	$0.2^{+0.02}_{-0.02}$
$A_{\text{FeL}}^{(d)}$	$13.0^{+2.3}_{-3.6}$	$12.4^{+6.0}_{-0.8}$	$9.3^{+4.1}_{-1.2}$	$12.0^{+2.5}_{-2.0}$	$14.5^{+2.5}_{-2.2}$
$E_{\text{FeK}}^{(a)}$	$6.55^{+0.03}_{-0.03}$	$6.57^{+0.04}_{-0.04}$	$6.55^{+0.03}_{-0.03}$	$6.58^{+0.03}_{-0.03}$	$6.52^{+0.05}_{-0.05}$
$\sigma_{\text{FeK}}^{(a)}$	$0.4^{(b)}$	$0.41^{+0.06}_{-0.05}$	$0.44^{+0.06}_{-0.05}$	$0.4^{(b)}$	$0.4^{(b)}$
$A_{\text{FeK}}^{(d)}$	$0.54^{+0.03}_{-0.03}$	$0.48^{+0.05}_{-0.05}$	$0.56^{+0.05}_{-0.04}$	$0.56^{+0.04}_{-0.03}$	$0.59^{+0.05}_{-0.04}$
$F_{\text{ab}}^{(e)}$	3.29	3.16	3.02	3.21	5.32
$F_{\text{unab}}^{(e)}$	3.4	3.29	3.15	3.34	5.45
$\chi_{\text{red}}^2 / \text{dof}$	1.198 / 688	1.077 / 655	1.153 / 679	1.142 / 672	1.216 / 683

<sup>(a)</sup>[keV]

<sup>(b)</sup>This parameter was fixed.

<sup>(c)</sup> $R_{\text{bb}}$  is the radius of the black body in km for the distance to the source  $D = 6.6$  kpc.

<sup>(d)</sup> $[10^{-2} \text{ ph cm}^{-2} \text{ s}^{-1}]$

<sup>(e)</sup>The values of absorbed and unabsorbed fluxes in 0.1 – 120 keV energy range in units  $10^{-9} \text{ erg / cm}^2 / \text{s}$ .

Table 5.7: Her X-1. Spectral parameters as a function of pulse phase during the observation on 1996-07-27 (main-on state of 257 cycle). The interstellar absorption was fixed to the average value of  $N_{\text{H}} = 1.09 \times 10^{20} \text{ atoms cm}^{-2}$ . Part 2.



## CHAPTER 6

---

### 4U 1626–67

#### 6.1 Source Description

The low mass X-ray binary 4U 1626–67 was discovered by *Uhuru* in 1972 (Giacconi et al. 1972). It consists of an X-ray pulsar with spin period  $P \approx 7.67$  s, and an extremely low mass companion ( $0.04M_{\odot}$  for  $i = 18^{\circ}$ ,  $f \leq 1.3 \cdot 10^{-6} M_{\odot}$ , Levine et al. 1988), white dwarf KZ TrA,  $V \sim 17.5$  mag (McClintock et al. 1977, 1980). The system has a very short orbital period  $P_{\text{orb}} \approx 42$  min (Chakrabarty 1998) and therefore belongs to the class of *Ultracompact X-ray Binaries (UCXBs)*. The low mass of the companion implies that the donor must be a hydrogen-deficient, partially or fully degenerate star (see for example Rappaport et al. 1982).

Heinke et al. (2013) showed that 4U 1626–67 is indeed a persistent X-ray source powered by a He-star donor. The accretion proceeds via accretion disk (Reynolds et al. 1997) powered through the Roche-lobe overflow of the companion. The distance to the source  $5 \leq D \leq 13$  kpc was estimated from measurements of optical and X-ray fluxes (Chakrabarty 1998).

The pulse-phase averaged spectrum of 4U 1626–67 can be fitted with an absorbed black body, a power law and a high energy cutoff. It also contained the Ne line complex at  $\sim 1$  keV (Angelini et al. 1995). The Fe  $K\alpha$  line has been detected in the 2010 *Chandra* and *RXTE* observations by Koliopanos & Gilfanov (2016). A cyclotron resonance scattering feature (CRSF) at  $\sim 37$  keV was discovered by Orlandini et al. (1998) in the *BeppoSAX* broadband spectrum, from which a magnetic field of about  $3.2(1+z) \times 10^{12}$  G, where  $z$  is the gravitational redshift, was suggested. The detailed study of the cyclotron line was recently carried out by Iwakiri et al. (2012) using the *Suzaku* data.

The system exhibits a peculiar spin period evolution. Two torque reversal episodes in 4U 1626–67 were discovered. The first one occurred in 1990 from spin-up to spin-down (Wilson et al. 1993; Bildsten et al. 1994; Chakrabarty et al. 1997) and, after 18 years, in February 2008, a new spin-down to spin-up torque reversal was

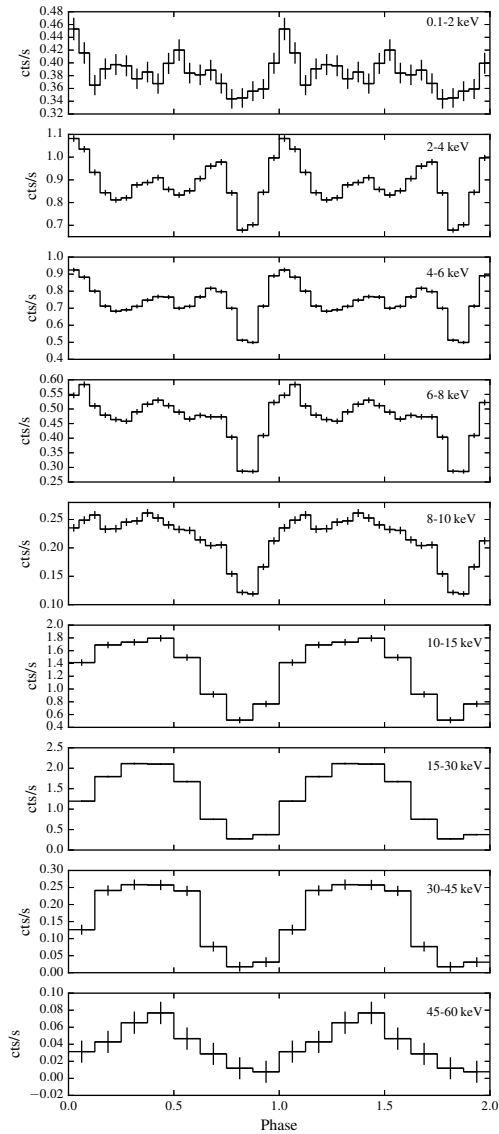


Figure 6.1: 4U 1626–67 pulse profiles as a function of energy. LECS (0.1 – 2 keV), MECS (2 – 4, 4 – 6, 6 – 8, 8 – 10 keV), HP (10 – 15 keV) and PDS (15 – 30, 30 – 45, 45 – 60 keV).

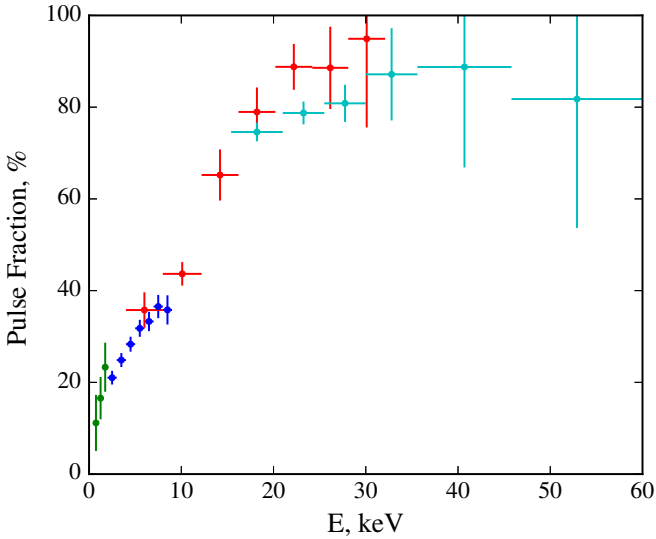


Figure 6.2: 4U 1626–67 pulse fraction computed from the pulse profiles.  $P = 7.6679(1)$  s.

observed (Camero-Arranz et al. 2010, 2012; Zhang & Li 2010). Another feature is the 48 mHz *quasi-periodic oscillation* (QPO) of the X-ray emission (Shinoda et al. 1990; Kommers et al. 1998).

## 6.2 Observations and Data Analysis

4U 1626–67 was observed by *BeppoSAX* from the 9th to the 11th of August 1996 during its science verification phase. The net exposure times were 31 ks for LECS, 97 ks for MECS, 43 ks for HPGSPC and 52 ks for PDS. Differences are because of the different criteria during passages in the South Atlantic Geomagnetic Anomaly, rocking modes of the HPGSPC and PDS and due to the LECS being operated only in satellite nighttime.

### 6.2.1 Timing Analysis

Using the epoch folding and phase connection techniques the spin period was determined to be  $P = 7.6679 \pm 0.0001$  s. Pulse profiles for the 4 NFIs folded with this period are shown at Figure 6.1. The pulse profile at low energies shows three peaks,

while the high energies pulse profile becomes sinusoidal. Therefore, we confirm the strong energy dependence of the 4U 1626–67 pulse profiles. As discussed by Kii et al. (1986) such behaviour is an indication to the anisotropy in the radiative transfer in a strong magnetic field.

We also computed the pulsed fraction as function of energy the 4U 1626–67. The results are presented in Figure 6.2. The pulsed fraction steadily increases with energy as typical for accreting pulsars.

### 6.2.2 Spectral Analysis.

The pulse phase averaged spectrum of the source is best described by a black body component with a temperature  $kT \sim 0.3$  keV and an absorbed power law with high energy cutoff ( $E_{\text{cut}} \sim 20$  keV). The Ne line complex at  $\sim 1$  keV and a cyclotron resonance feature at  $\sim 38$  keV (Fig. 6.3) are also required to describe the spectrum adequately.

From the six continuum models considered in the thesis only four of them can describe the spectrum of 4U 1626–67 adequately. It was not possible to obtain statistically acceptable fit for `Cutoffpl` and `BW` models. Best fit results for other models are shown in Table 6.1. In general the spectrum is well described, however taking into account that the aim of this work is to compare the behaviour of the continuum in different sources and for most of them the `Highecut` model describes the spectrum better than others, we choose this model as a reference for further analysis.

Phase resolved analysis using the `Highecut` model was also carried out. The variation of the parameters with pulse phase is presented in Table 6.2 and Figure 6.4. To obtain statistically significant results, we use four phase bins: the minimum, maximum, and the rising and declining parts of the PDS pulse profile. The spectrum of 4U 1626–67 strongly changes with the pulse phase: it becomes harder at the pulse maximum and softer in the minimum. As it can be seen from Table 6.2, the cyclotron and iron lines parameters and the radius of the back body do not exhibit strong phase dependence. The cutoff energy and the temperature of the black body are correlated with hard flux whereas the folding energy and the photon index are anti-correlated (Fig. 6.4).

## 6.3 Conclusion

Analysis of *BeppoSAX* observations of the LMXB pulsar 4U 1626–67 carried out in 1996 has been published by Orlandini et al. (1998); Orlandini et al. (1999), however, I re-analysed this data set coherently with other pulsars in the sample. I carried out spectral and timing analysis obtaining results consistent with those previously published. On the other hand, here, for the first time, I obtain an energy resolved pulse

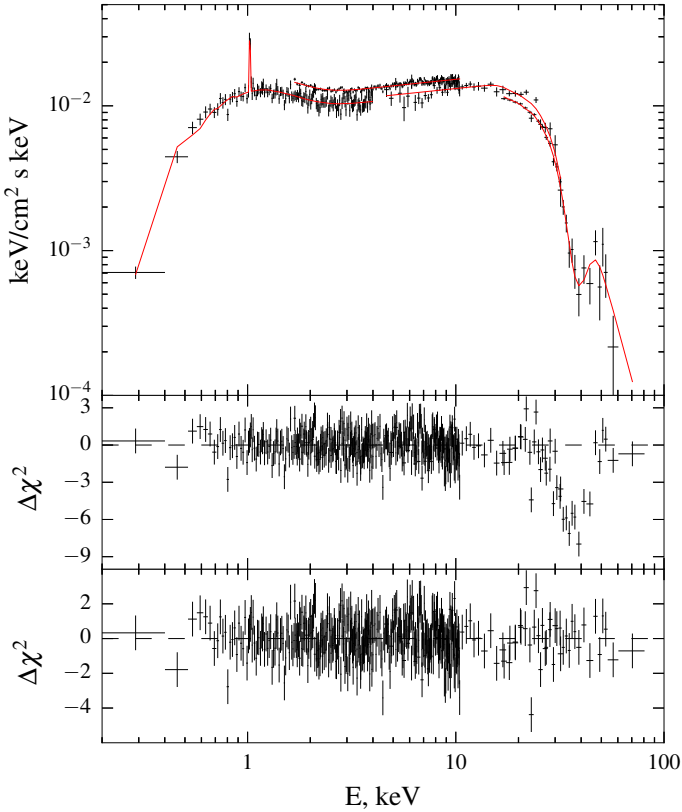


Figure 6.3: 4U 1626–67 broadband 0.2 – 100 keV unfolded spectrum described with the best fit continuum model (cutoff power law with a soft black body component, a narrow emission line at  $\sim 1$  keV and the absorption gaussian line at  $\sim 38$  keV to account for the CRSF) as observed by *BeppoSAX*. The second panel shows residuals associated with the cyclotron line. The best fit residuals are also shown in the bottom panel.

profiles (Fig. 6.1), the pulse fraction as function of energy (Fig. 6.2), and phase resolved spectral analysis (Tab. 6.2, Fig. 6.4). For spectral analysis I also explored additional continuum models: *Highcut*, *Fdcut*, *NPEX* and *ComPTT* (Tab. 6.1) all of which describe the data adequately and yield consistent results.

Parameter	Highcut	Fdcut	NPEX	CompTT
$N_{\text{H}}^{(a)}$	$9.3^{+1.9}_{-1.6}$	$9.8^{+1.9}_{-1.6}$	$6.2^{+0.7}_{-1.1}$	$4.1^{+1.1}_{-0.8}$
$E_{\text{cyc}}^{(b)}$	$38.38^{+1.28}_{-1.21}$	$38.08^{+1.27}_{-1.16}$	$38.53^{+1.16}_{-1.03}$	$38.21^{+1.11}_{-0.95}$
$\sigma_{\text{cyc}}^{(b)}$	$4.3^{+1.1}_{-1.0}$	$5.03^{+1.0}_{-0.96}$	$5.04^{+0.93}_{-0.87}$	$4.6^{+0.9}_{-0.8}$
$\delta_{\text{cyc}}^{(b)}$	$1.4^{+0.4}_{-0.3}$	$1.5^{+0.3}_{-0.3}$	$1.6^{+0.3}_{-0.3}$	$1.5^{+0.3}_{-0.3}$
$kT_{\text{bb}}^{(b)}$	$0.29^{+0.01}_{-0.01}$	$0.3^{+0.01}_{-0.01}$	$0.32^{+0.01}_{-0.01}$	$0.35^{+0.01}_{-0.01}$
$R_{\text{bb}}^{(d)}$	$14^{+8}_{-7}$	$14^{+8}_{-7}$	$13^{+6}_{-5}$	$13^{+6}_{-5}$
$E_{\text{Ne}}^{(b)}$	$1.03^{+0.04}_{-0.04}$	$1.02^{+0.04}_{-0.04}$	$1.02^{+0.04}_{-0.04}$	$1.01^{+0.04}_{-0.04}$
$\sigma_{\text{Ne}}^{(b,g)}$	0.005	0.005	0.005	0.005
$A_{\text{Ne}}^{(c)}$	$3.1^{+1.7}_{-1.6}$	$4.1^{+2.2}_{-1.9}$	$5.2^{+2.3}_{-2.3}$	$5.3^{+1.9}_{-2.2}$
$\Gamma$	$0.85^{+0.01}_{-0.01}$	$0.78^{+0.03}_{-0.03}$		
$E_{\text{cut}}^{(b)}$	$19.19^{+1.19}_{-1.03}$	$24.18^{+2.49}_{-2.59}$		
$E_{\text{fold}}^{(b)}$	$10.42^{+0.93}_{-1.0}$	$8.1^{+0.9}_{-0.8}$		
$\alpha 1$			$0.32^{+0.04}_{-0.04}$	
$\alpha 2$			-2.0	
$kT^{(b)}$			$6.1^{+0.3}_{-0.2}$	$6.0^{+0.2}_{-0.2}$
$T_{\text{p}}^{(e)}$				$0.86^{+0.05}_{-0.05}$
$\tau_{\text{p}}^{(f)}$				$15.86^{+0.42}_{-0.48}$
$\chi^2_{\text{res}} / \text{dof}$	1.036 / 363	0.981 / 365	0.978 / 365	1.043 / 365

<sup>(a)</sup>[ $10^{20}$  atoms  $\text{cm}^{-2}$ ]

<sup>(b)</sup>[keV]

<sup>(c)</sup>[ $10^{-4}$  ph  $\text{cm}^{-2}$   $\text{s}^{-1}$ ]

<sup>(d)</sup> $R_{\text{bb}}$  is the radius of the black body in km for the distance to the source  $D = 9$  kpc.

<sup>(e)</sup>Plasma temperature, keV.

<sup>(f)</sup>Plasma optical depth.

<sup>(g)</sup>This parameter has been fixed.

Table 6.1: 4U 1626–67 parameters of the 4 different continuum models of the phase averaged spectrum. The absorbed and unabsorbed fluxes in the range 0.1 – 120 keV are  $F_{\text{ab}} = 5.78 \cdot 10^{-10}$  ergs  $\text{cm}^{-2}\text{s}^{-1}$ ,  $F_{\text{unab}} = 5.92 \cdot 10^{-10}$  ergs  $\text{cm}^{-2}\text{s}^{-1}$  respectively.

Parameter	0 - 0.25	0.25 - 0.5	0.5 - 0.75	0.75 - 1
$E_{\text{cyc}}^{(a)}$	$38.39^{+1.97}_{-1.87}$	$36.91^{+0.98}_{-0.9}$	$37.76^{+3.3}_{-2.82}$	$35.95^{+5.29}_{-6.85}$
$\sigma_{\text{cyc}}^{(a)}$	$5.0^{(e)}$	$4.1^{+0.8}_{-0.8}$	$2.5^{(e)}$	$5.0^{(e)}$
$\delta_{\text{cyc}}$	$1.0^{+0.5}_{-0.5}$	$1.7^{+0.5}_{-0.3}$	$0.9^{+1.0}_{-0.7}$	$0.8^{+2.4}_{-0.4}$
$kT_{\text{bb}}^{(a)}$	$0.31^{+0.03}_{-0.03}$	$0.35^{+0.02}_{-0.02}$	$0.29^{+0.03}_{-0.02}$	$0.27^{+0.03}_{-0.03}$
$R_{\text{bb}}^{(c)}$	$12^{+9}_{-7}$	$11^{+7}_{-5}$	$14^{+9}_{-8}$	$14^{+9}_{-8}$
$E_{\text{Ne}}^{(a)}$	$0.97^{+0.14}_{-0.14}$	$0.98^{+0.04}_{-0.04}$	$1.04^{+0.05}_{-0.05}$	$1.18^{+0.05}_{-0.05}$
$\sigma_{\text{Ne}}^{(a,e)}$	$0.005$	$0.005$	$0.005$	$0.005$
$A_{\text{Ne}}^{(b)}$	$4.7^{+3.7}_{-4.4}$	$8.0^{+2.8}_{-3.7}$	$5.1^{+4.3}_{-3.3}$	$2.2^{+1.1}_{-1.1}$
$\Gamma$	$0.82^{+0.03}_{-0.03}$	$0.64^{+0.03}_{-0.02}$	$0.84^{+0.02}_{-0.01}$	$0.91^{+0.06}_{-0.08}$
$E_{\text{cut}}^{(a)}$	$16.92^{+1.43}_{-1.5}$	$25.06^{+1.32}_{-0.97}$	$21.38^{+1.54}_{-1.24}$	$7.47^{+1.59}_{-0.97}$
$E_{\text{fold}}^{(a)}$	$9.92^{+1.46}_{-1.45}$	$8.01^{+0.79}_{-0.83}$	$8.31^{+1.21}_{-1.1}$	$9.46^{+1.6}_{-1.15}$
$F_{\text{ab}}^{(d)}$	$5.04$	$5.66$	$4.63$	$2.68$
$F_{\text{unab}}^{(d)}$	$5.12$	$5.73$	$4.71$	$2.77$
$\chi^2_{\text{res}} / \text{dof}$	$1.063 / 290$	$1.135 / 347$	$0.944 / 283$	$0.971 / 204$

<sup>(a)</sup>[keV]

<sup>(b)</sup>[ $10^{-4}$  ph cm $^{-2}$  s $^{-1}$ ]

<sup>(c)</sup> $R_{\text{bb}}$  is the radius of the black body in km for the distance to the source  $D = 9$  kpc.

<sup>(d)</sup>The values of absorbed and unabsorbed fluxes in 0.1 – 120 keV energy range in units  $10^{-10}$  erg / cm $^2$ /s.

<sup>(e)</sup>This parameter has been fixed.

Table 6.2: 4U 1626–67. Best-fit parameters for the pulse phase resolved spectrum for Highcut continuum model. The interstellar absorption was fixed at the average value  $N_{\text{H}} = 9.3 \times 10^{20}$  atoms cm $^{-2}$  for all phase bins.

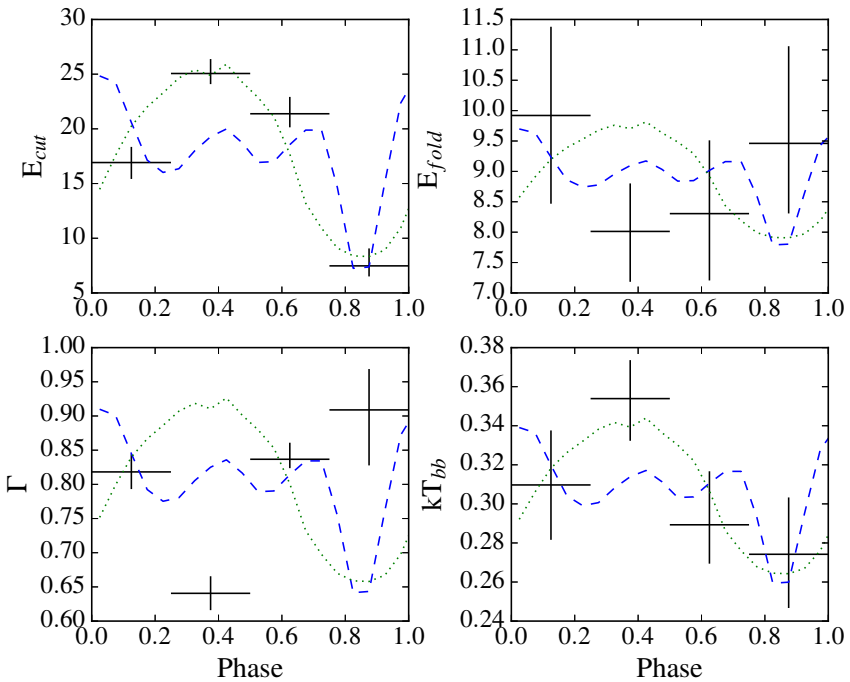


Figure 6.4: 4U 1626–67. Phase dependence of the parameters of the Hightcut continuum models (blue dashed - MECS pulse profile in 2 – 10 keV, green dotted - PDS pulse profile in 15 – 60 keV energy range).



## CHAPTER 7

---

### 4U 1907+09

#### 7.1 Source Description

4U 1907+09 was discovered by *Uhuru* in 1971 (Giacconi et al. 1971) as a hard X-ray source. The observed emission is powered by wind accretion from a companion identified in optical (Cox et al. 2005) and infrared (Nespoli et al. 2008) observations as a high-mass type O8/O9 supergiant star. The lower limit of the distance of about 5 kpc has been obtained from the analysis of interstellar atomic lines (Nespoli et al. 2008) and, together with the observed magnitude  $m = 16.37$  mag, implies a companion luminosity of  $L = 5 \times 10^5 L_{\odot}$  and a mass loss rate  $\dot{M} = 7 \times 10^{-6} \text{ yr}^{-1}$ . This is consistent with the spectral classification and the observed X-ray luminosity (Doroshenko et al. 2012).

The orbital period of the system is relatively short with  $P_{\text{orb}} = 8.3753$  d. The eccentricity is  $e = 0.28$  and the semi-major axis  $a_{\text{sin}i} = 83 \text{ lt s}$  (in 't Zand et al. 1998). Makishima et al. (1984) discovered X-ray pulsations from the source with period  $P \sim 440$  s thus establishing it as a typical wind accreting X-ray pulsar. The spin period evolution is complicated, which is also consistent with accretion from wind. The observed pulse period increased until 2004 (in 't Zand et al. 1998; Baykal et al. 2006) when it started to spin-up (Fritz et al. 2006). A second torque reversal episode was reported in 2007 – 2008 yr (Inam et al. 2009) when the observed spin period started to increase again.

A CRSF was discovered by Makishima (1992); Makishima et al. (1999) at  $\sim 19$  keV using the data from *Ginga* satellite. Later Cusumano et al. (1998) reported detection of the first harmonic at  $\sim 39$  keV. The observed line energy implies a relatively low magnetic field of about  $2.1 \times 10^{12}$  G (especially taking into account long spin period of the source). Hemphill et al. (2013) have reported some evidence for a positive correlation between the cyclotron line energy and luminosity. An emission iron line at  $\sim 6.4$  keV was also detected by Cusumano et al. (1998) in *BeppoSAX* data.

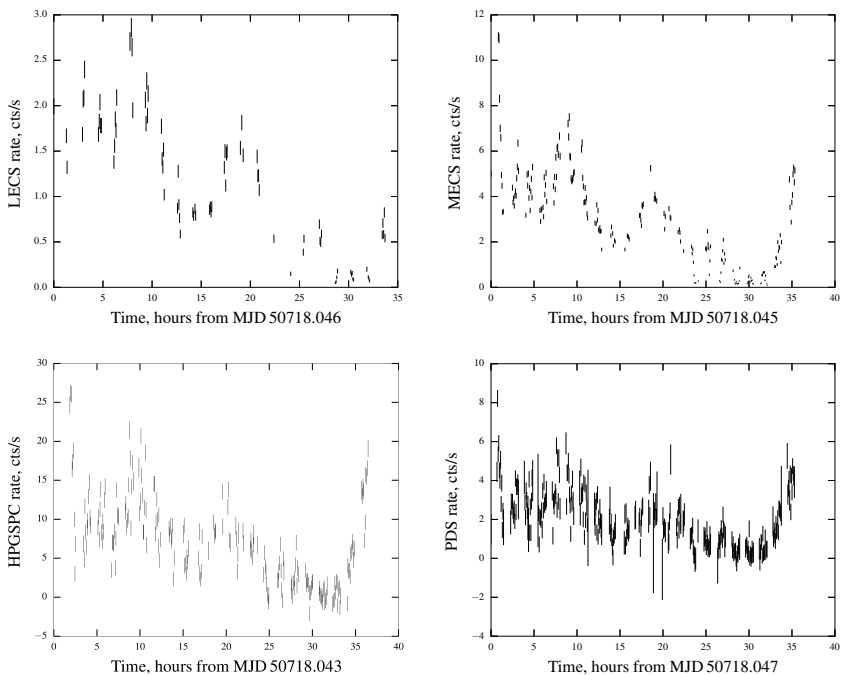


Figure 7.1: 4U 1907+09, LECS, MECS, HPGSPC and PDS light curves during the *BeppoSAX* observation.

## 7.2 Observations

The source was observed by *BeppoSAX* on 1997 September 27 – 28 with integration time of 27, 64, 29 and 31 ksec for LECS, MECS, HPGSPC and PDS respectively.

### 7.2.1 Timing Analysis

The light curves for all NFIs are presented in Figure 7.1. The gaps in the light curves are due to the satellite passages over the South Atlantic Anomaly and Earth occultations. The high intensity at the beginning of the light curve is likely associated with the periodic primary flare observed by *Tenma* (Makishima et al. 1984). Several so-called “off” states similar to that reported by Doroshenko et al. (2012) are also evident in the light curve.

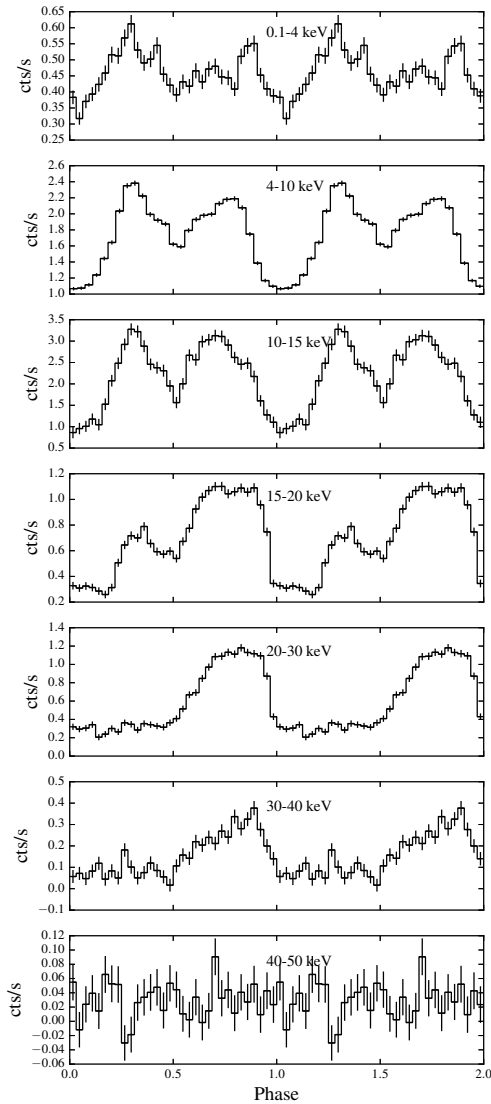


Figure 7.2: The pulse profiles of the X-ray pulsar 4U 1907+09 as a function of energy. LECS (0.1 – 4 keV), MECS (4 – 10 keV), HP (10 – 15 keV) and PDS (15 – 20, 20 – 30, 30 – 40, 40 – 50 keV).

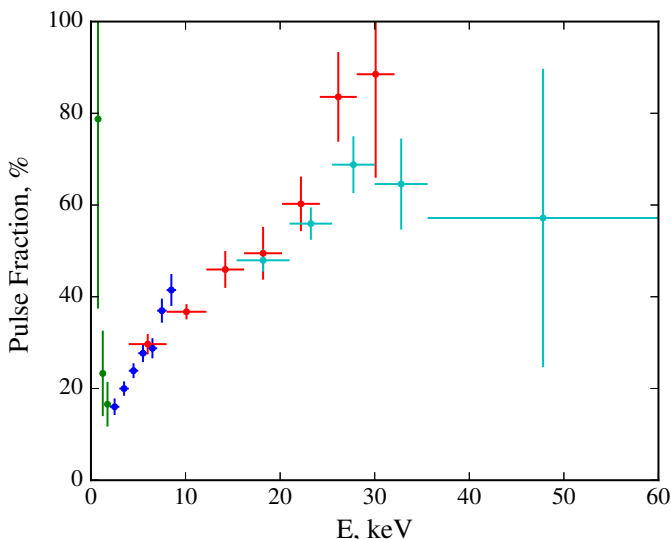


Figure 7.3: 4U 1907+09, pulse fraction.

The spin period, determined from the *BeppoSAX* data is in agreement with the historical trend reported by Fritz et al. (2006). The measured period is  $P \approx 440.99$  s. The pulse profiles for 4 NFIs (from 0.1 to 50 keV) folded with this period are shown in Figure 7.2. The pulse profiles at soft energies consist of two peaks separated by half of the pulse phase with a deep and a shallow minimum between them. At higher energies the first peak disappears and the shape of the other one changes. Note that the change of the pulse profile shape occurs around the cyclotron energy ( $\sim 19$  keV).

The pulsed fraction of 4U 1907+09 as a function of energy is presented in Figure 7.3. The fraction of the pulsed emission increases with energy in the 2 – 30 keV energy range, from 15% to 80% and has two features associated with the fluorescent iron line at  $E_{\text{FeK}} \sim 6.4$  keV and with the cyclotron line at  $E_{\text{cyc}} \sim 19$  keV, which is a strong argument in favor of the CRSF interpretation of the observed feature. Below the 2 keV and above the 30 keV the pulse fraction exhibits reverse dependence on energy.

Parameter	Highcut	Fdcut	NPEX	Cutoffpl	CompTT
$N_{\text{H}}^{(a)}$	$2.72^{+0.06}_{-0.09}$	$2.68^{+0.06}_{-0.06}$	$2.6^{+0.1}_{-0.1}$	$2.4^{+0.1}_{-0.1}$	$3.00^{+0.03}_{-0.06}$
$E_{1\text{cyc}}^{(b)}$	$19.44^{+0.59}_{-0.61}$	$20.56^{+0.5}_{-0.41}$	$20.11^{+0.59}_{-0.44}$	$19.97^{+0.66}_{-1.24}$	$20.09^{+0.58}_{-0.44}$
$\sigma_{1\text{cyc}}^{(b)}$	$1.9^{+0.8}_{-0.8}$	$3.2^{+0.5}_{-0.4}$	$3.3^{+0.6}_{-0.4}$	$0.8^{+1.6}_{-0.7}$	$3.1^{+0.5}_{-0.5}$
$\delta_{1\text{cyc}}$	$0.26^{+0.08}_{-0.06}$	$0.63^{+0.09}_{-0.08}$	$0.66^{+0.10}_{-0.09}$	$0.25^{+0.56}_{-0.16}$	$0.59^{+0.08}_{-0.08}$
$E_{2\text{cyc}}^{(b)}$	$39.57^{+1.29}_{-1.10}$	$43.2^{+1.35}_{-4.47}$	$40.32^{+2.67}_{-1.76}$	$40.07^{+1.27}_{-1.03}$	$40.95^{+3.45}_{-2.1}$
$\sigma_{2\text{cyc}}^{(b)}$	$3.06^{+1.62}_{-1.92}$	$10.28^{+1.13}_{-1.15}$	$9.62^{+2.68}_{-2.22}$	$3.79^{+1.29}_{-1.15}$	$9.65^{+2.81}_{-2.08}$
$\delta_{2\text{cyc}}$	$2.3^{+0.7}_{-0.9}$	$3.8^{+0.3}_{-1.5}$	$2.1^{+0.4}_{-0.4}$	$2.2^{+2.1}_{-0.6}$	$2.0^{+0.5}_{-0.4}$
$E_{\text{Fe}}^{(b,c)}$	$6.44^{+0.07}_{-0.03}$	$6.44^{+0.06}_{-0.06}$	$6.44^{+0.07}_{-0.05}$	$6.48^{+0.07}_{-0.06}$	$6.44^{+0.03}_{-0.09}$
$A_{\text{Fe}}^{(d)}$	$2.2^{+0.5}_{-0.4}$	$2.0^{+0.5}_{-0.4}$	$2.5^{+0.6}_{-0.5}$	$2.9^{+0.7}_{-0.7}$	$2.4^{+0.6}_{-0.5}$
$\Gamma$	$1.17^{+0.02}_{-0.02}$	$1.15^{+0.02}_{-0.02}$		$0.75^{+0.06}_{-0.06}$	
$E_{\text{cut}}^{(b)}$	$12.64^{+0.77}_{-0.55}$	$54.4^{+2.65}_{-23.36}$		$11.49^{+0.81}_{-0.71}$	
$E_{\text{fold}}^{(b)}$	$11.6^{+0.8}_{-0.77}$	$0.04^{+7.19}_{-0.04}$			
$\alpha 1$			$0.69^{+0.03}_{-0.06}$		
$\alpha 2$			$-2.0$		
$kT^{(b)}$			$6.03^{+0.09}_{-0.07}$		$6.51^{+0.68}_{-0.54}$
$T_{\text{p}}^{(e)}$					$0.17^{+0.21}_{-0.16}$
$\tau_{\text{p}}^{(f)}$					$6.2^{+0.1}_{-0.2}$
$E_{\text{bump}}^{(b)}$				$11.77^{+0.24}_{-0.25}$	
$\sigma_{\text{bump}}^{(b)}$				$2.3^{+0.3}_{-0.3}$	
$A_{\text{bump}}^{(d)}$				$32.5^{+5.2}_{-4.8}$	
$\chi^2_{\text{res}} / \text{dof}$	1.176 / 437	1.308 / 437	1.261 / 437	1.186 / 435	1.315 / 437

<sup>(a)</sup> $[10^{22} \text{atoms cm}^{-2}]$

<sup>(b)</sup> $[\text{keV}]$

<sup>(c)</sup>The width of the Fe-line has been fixed at the value  $\sigma_{\text{Fe}} = 0.005 \text{ keV}$ .

<sup>(d)</sup> $[10^{-4} \text{ ph cm}^{-2} \text{ s}^{-1}]$

<sup>(e)</sup>Plasma temperature, keV.

<sup>(f)</sup>Plasma optical depth.

Table 7.1: 4U 1907+09 parameters of the 5 different continuum models of the phase averaged spectrum. The absorbed and unabsorbed fluxes in the range 0.1 – 120 keV are  $F_{\text{ab}} = 7.72 \cdot 10^{-10} \text{ ergs cm}^{-2} \text{ s}^{-1}$ ,  $F_{\text{unab}} = 9.14 \cdot 10^{-10} \text{ ergs cm}^{-2} \text{ s}^{-1}$  respectively.

### 7.2.2 Spectral Analysis

The broad-band X-ray spectrum of 4U 1907+09 can be adequately described with an absorbed cut-off power law continuum ( $N_{\text{H}} \sim 10^{22} \text{ atoms cm}^{-2}$ ) modified by the fluorescent line at  $\sim 6.4 \text{ keV}$ , and CRSF with energy  $\sim 19 \text{ keV}$  and its first harmonic at  $\sim 39 \text{ keV}$ . In the case of the 4U 1907+09 three continuum models can provide acceptable approximation of the phase averaged spectrum, namely Highcut, NPEX and CompTT. The best-fit results are presented in Table 7.1.

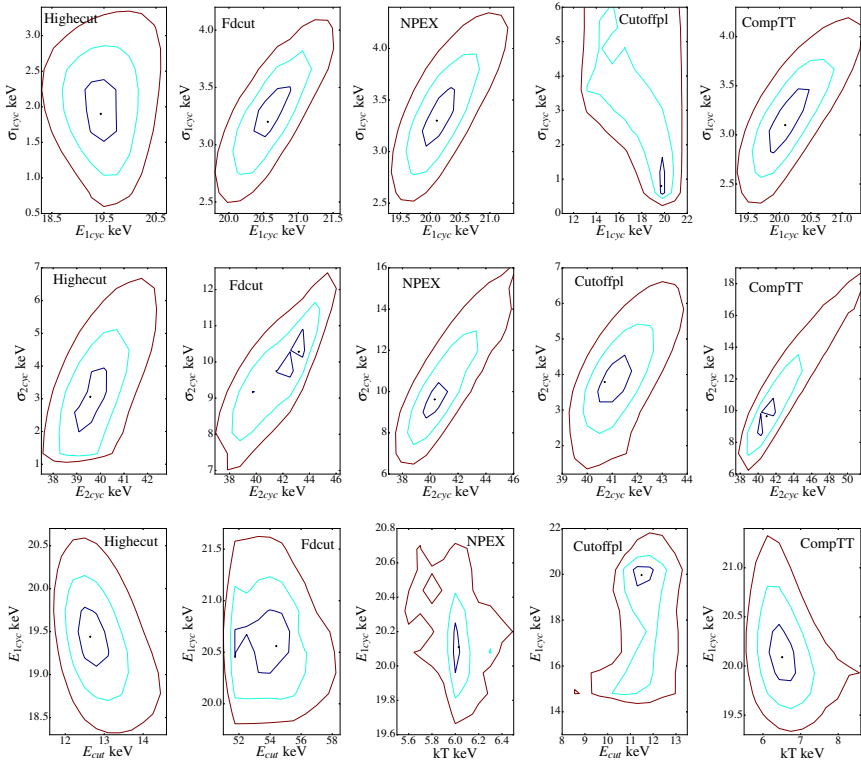


Figure 7.4: 4U 1907+09 contours (1, 2 and  $3\sigma$ ) for different continuum models.

The results for the Fdcut and Cutoffpl models are also included as it is possible to obtain statistically acceptable fit with both models. However, the best-fit cutoff and folding energy values for the Fdcut are unrealistic at  $E_{\text{cut}} \approx 54$  keV,  $E_{\text{fold}} \approx 0.04$  keV. On the other hand, the Cutoffpl model only allows to obtain a statistically acceptable fit if an additional “bump” around 12 keV is included in the fit. As such, we conclude that the description of the spectrum with this models is not feasible. The BW model is not included in the table as it can not adequately fit the spectrum.

Note that in all cases some residuals remain around 1 keV. The available statistics and energy resolution of MECS/LECS does not allow a detailed analysis of the spectrum in this region, however, we note that the observed excess most likely

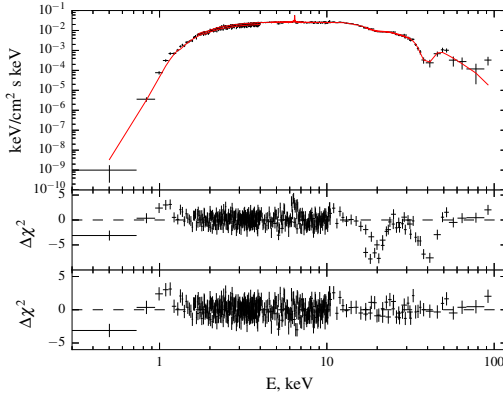


Figure 7.5: The top panel shows the 4U 1907+09 broadband 0.1 – 110 keV unfolded spectrum with high energy cutoff continuum model (Highecut) with Fe-emission line and two absorption gaussian lines at  $\sim 19$  and  $\sim 39$  keV as observed by *BeppoSAX*. The residuals are shown in the bottom panels (1. Two cyclotron and Fe-lines residuals. 2. The best fit residuals,  $\chi^2_{\text{red}} \approx 1.24$ ).

arise due to blending of several emission lines from the wind of the companion unresolved by *BeppoSAX*.

Statistically the best fit is obtained with the *Highecut* model. The parameters of this model are also well constrained and exhibit no strong inter-parameter correlations as can be seen from the contours presented in Figure 7.4.

Figure 7.5 shows the broadband spectrum of the source as observed by *BeppoSAX* on 1997 September 27 – 28. The top panel shows the phase-averaged X-ray spectrum with the best fit model (absorbed cut-off power law, with *Highecut*). The second panel shows the residuals associated with the cyclotron line and its first harmonic at  $\sim 19$  keV and  $\sim 39$  keV. In the bottom panel the best fit residuals are shown. 4U 1907+09 exhibits also a narrow iron line at  $\sim 6.4$  keV.

Phase resolved spectral analysis was also carried out (Fig. 7.6). The absorbed power law model with a cut-off at high energies was used to model the spectra as function of the pulse phase. Absorption column  $N_{\text{H}}$  and iron line parameters were fixed to the average values for all phase bins. Fit results are presented in Table 7.2. Strong variation of the cutoff and folding energies as well as of the photon index with pulse phase is apparent as shown in Figure 7.6. Other parameters show weak variation with pulse phase as expected.

Parameter	0 - 0.2	0.2 - 0.4	0.4 - 0.6	0.6 - 0.8	0.8 - 1
$E_{1\text{cyc}}^{(a)}$	$20.15^{+1.58}_{-1.21}$	$20.37^{+1.27}_{-0.81}$	$21.01^{+0.86}_{-0.71}$	$18.74^{+1.02}_{-0.99}$	$20.19^{+0.11}_{-0.11}$
$\sigma_{1\text{cyc}}^{(a)}$	$2.94^{+1.94}_{-1.69}$	$2.62^{+1.04}_{-1.14}$	$1.85^{+1.89}_{-0.76}$	$2.88^{+0.42}_{-0.35}$	$0.06^{+0.015}_{-0.03}$
$\delta_{1\text{cyc}}$	$0.57^{+0.25}_{-0.19}$	$0.48^{+0.13}_{-0.12}$	$0.5^{+0.2}_{-0.08}$	$0.58^{+0.14}_{-0.28}$	$0.97^{+0.03}_{-0.49}$
$E_{2\text{cyc}}^{(a)}$	$37.65^{+1.82}_{-2.08}$	$39.57^{+0.1}_{-4.0}$	$37.88^{+2.56}_{-1.84}$	$40.11^{+3.28}_{-2.39}$	$41.62^{+1.72}_{-1.47}$
$\sigma_{2\text{cyc}}^{(a)}$	$1.36^{+3.85}_{-0.65}$	$3.06^{+2.16}_{-2.34}$	$5.78^{+2.23}_{-1.79}$	$2.32^{+2.769}_{-1.82}$	$3.61^{+1.33}_{-1.9}$
$\delta_{2\text{cyc}}$	$6.88^{+3.12}_{-5.67}$	$2.968\text{e-}20(0.01)$	$1.84^{+1.17}_{-0.69}$	$2.18^{+7.82}_{-1.41}$	$3.37^{+9.34}_{-1.4}$
$\Gamma$	$1.42^{+0.02}_{-0.03}$	$1.08^{+0.01}_{-0.02}$	$1.2^{+0.04}_{-0.04}$	$0.98^{+0.02}_{-0.02}$	$1.39^{+0.02}_{-0.02}$
$E_{\text{cut}}^{(a)}$	$11.85^{+1.88}_{-1.5}$	$13.24^{+0.77}_{-0.52}$	$12.17^{+1.43}_{-1.0}$	$17.92^{+2.13}_{-3.35}$	$22.95^{+1.29}_{-1.46}$
$E_{\text{fold}}^{(a)}$	$13.95^{+2.63}_{-2.76}$	$6.26^{+0.6}_{-0.47}$	$13.09^{+2.36}_{-2.46}$	$7.76^{+2.7}_{-1.38}$	$15.83^{+2.84}_{-2.68}$
$F_{\text{ab}}^{(b)}$	3.76	7.0	6.1	8.2	6.23
$F_{\text{unab}}^{(b)}$	4.65	8.26	7.15	9.21	7.35
$\chi^2_{\text{res}} / \text{dof}$	1.178 / 319	1.185 / 391	1.107 / 403	0.959 / 401	1.003 / 401

<sup>(a)</sup>[keV]

<sup>(b)</sup>The values of absorbed and unabsorbed fluxes in 0.1 – 120 keV energy range in units  $10^{-10} \text{erg} / \text{cm}^2 / \text{s}$ .

Table 7.2: Phase resolved spectral parameters of 4U 1907+09 for the Hignecut continuum model. The interstellar absorption and Fe-line parameters were fixed at the average values:  $N_{\text{H}} = 2.72^{+0.06}_{-0.09} \text{atoms cm}^{-2}$ ;  $E_{\text{Fe}} = 6.44^{+0.07}_{-0.03} \text{keV}$ ,  $\sigma_{\text{Fe}} = 0.005 \text{keV}$ ,  $A_{\text{Fe}} = 2.2^{+0.5}_{-0.4} \times 10^{-4} \text{ph cm}^{-2} \text{s}^{-1}$ .

### 7.3 Conclusion

I reanalysed the data of the HMXB pulsar 4U 1907+09, observed by *BeppoSAX* in 1997 (Cusumano et al. 1998; di Salvo et al. 1999). The measured spin period is in agreement with that previously reported by di Salvo et al. (1999). Using the measured spin period I investigated the evolution of the pulse profiles (Fig. 7.2) and pulse fraction (Fig. 7.3) with energy.

The pulse phase resolved spectroscopy (Tab. 7.2, Fig. 7.6) was also carried out for the first time for this data set. For the first time I get also a good approximation of the spectrum using several continuum models (Tab. 7.1) and all NFI's, whereas Cusumano et al. (1998); di Salvo et al. (1999) only used MECS, HPGSPC and PDS.



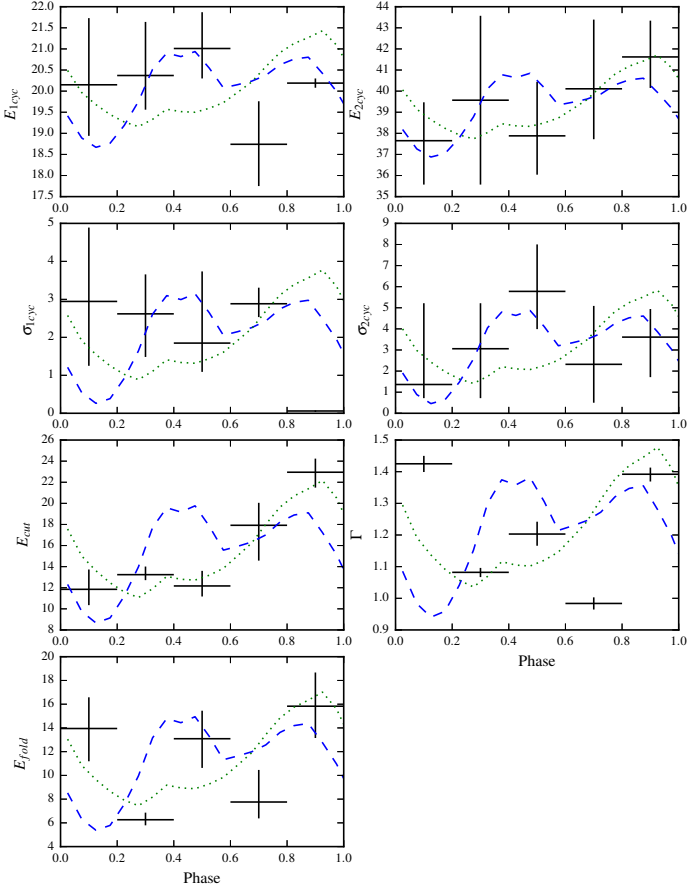


Figure 7.6: 4U 1907+09. Changing spectral parameters with phase with *HiGhec* continuum model (dashed blue line is the MECS pulse profile in 2 – 10 keV, dotted green line - PDS pulse profile in 15 – 60 keV energy ranges). Absorption column  $N_{\text{H}}$  and iron line parameters were fixed at the average values.

## CHAPTER 8

---

### 4U 1538–52

#### 8.1 Source Description

High mass X-ray binary 4U 1538–52 is an eclipsing system consisting of the B0Iab supergiant star QV Nor ( $17M_{\odot}$ , Reynolds et al. 1992) and a neutron star. This system has an orbital period of  $\sim 3.728$  d (Clark 2000; Falanga et al. 2015) and a spin period of about 529 s (Davison et al. 1977; Becker et al. 1977). It was discovered in the third *Uhuru* survey (Giacconi et al. 1974). Initially two solutions for the orbital eccentricity were reported:  $\sim 0.08$  (Corbet et al. 1993) and  $\sim 0.17$  (Clark 2000). The X-ray eclipse lasts a significant fraction of the orbit at  $\sim 0.6$  d (Becker et al. 1977). The average flux has been estimated  $\sim (5 - 20) \times 10^{-10}$  erg s $^{-1}$  cm $^{-2}$  in the 3 – 100 keV range (Rodes et al. 2008), which corresponds to the X-ray luminosity is  $\sim (2 - 7) \times 10^{36}$  erg s $^{-1}$  assuming the distance to the system of  $\sim 5.5$  kpc (Becker et al. 1977; Parkes et al. 1978). Note, however, that reported distance estimates range from  $5.5 \pm 1.5$  kpc (Crampton et al. 1978) to  $6.4 \pm 1.0$  kpc (Reynolds et al. 1992). The mass of the compact object has been also determined, and turns out to be fairly low for a NS. Rawls et al. (2011) and Falanga et al. (2015) report  $1.104 \pm 0.177M_{\odot}$  and  $1.02 \pm 0.17M_{\odot}$  respectively (assuming the eccentricity  $e = 0.18(1)$ ). In the recent work by Falanga et al. (2015) the ephemerides, the orbital period decay rate, and masses of both companions were confirmed and refined.

Nevertheless, presence of the X-ray pulsations from the compact object and the observed CRSF in its spectrum imply that the source is clearly a NS. The CRSF at  $\sim 20$  keV was discovered by Clark et al. (1990) using the *Ginga* observations. The first harmonic at  $\sim 47$  keV was later discovered using the data from the RXTE and INTEGRAL observatories (Rodes-Roca et al. 2009). The source spectrum also exhibits an emission iron line at  $\sim 6.4$  keV first reported by Makishima et al. (1987) and several other emission lines between  $\sim 1 - 3$  keV (Rodes-Roca et al. 2011). Note that the observed CRSF energy implies  $B \sim 2 \times 10^{12}$  G (Clark et al. 1990), i.e. unlike the mass, close to the canonical value.

The spin evolution of the source is quite complicated and also confirms the NS origin of the compact object. Two torque reversals have occurred, one in 1988 from spin-down to spin-up (Rubin et al. 1997) and one, back to the spin-down, in  $\sim 2009$ . Currently 4U 1538–52 is following the same spin-down trend (Finger et al. 2009; Hemphill et al. 2013).

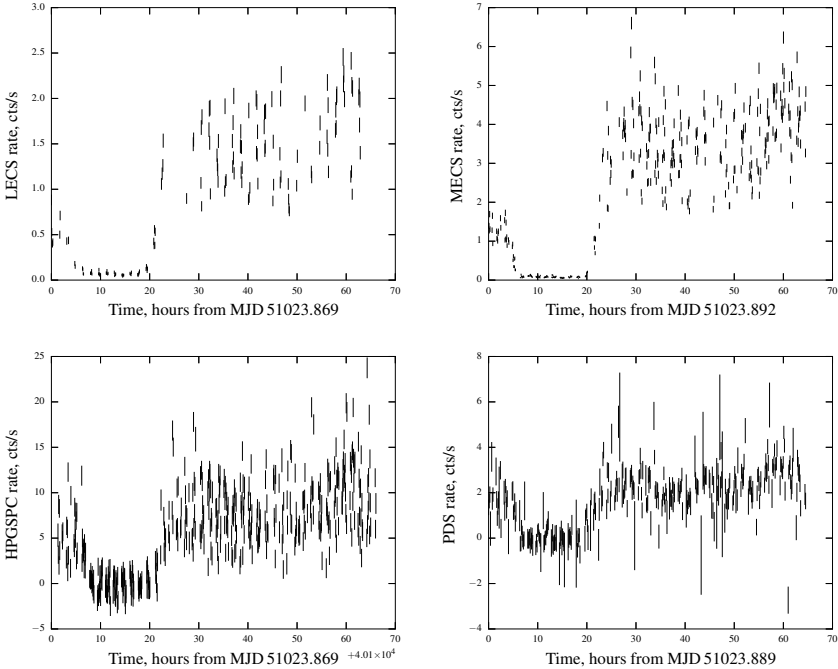


Figure 8.1: 4U 1538–52, LECS, MECS, HPGSPC (with the 256 s bin time) and PDS (455 s bin time) light curves during the *BeppoSAX* observation.

## 8.2 Observations

4U 1538–52 was observed by *BeppoSAX* from the 29th of July to the 1st of August 1998 with 32, 70, 35 and 37 ks exposure for LECS, MECS, HPGSPC and PDS respectively. The source was in eclipse during the first quarter of observation, as can be seen in the light curves of the 4U 1538–52 presented in Figure 8.1. We performed the temporal and spectral analysis on the out-of-eclipse data only.

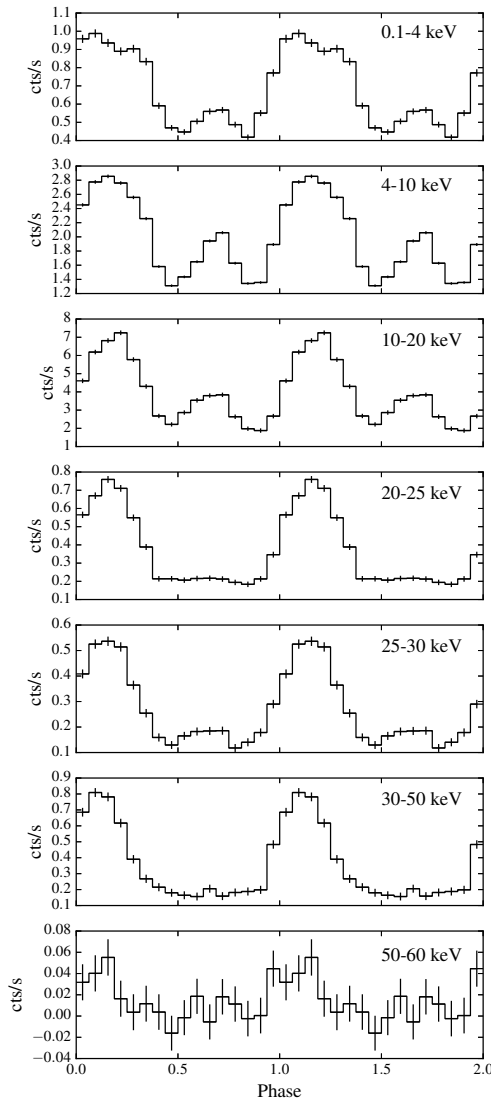


Figure 8.2: The pulse profiles of the X-ray pulsar 4U 1538–52 as a function of energy. LECS (0.1 – 4 keV), MECS (4 – 10 keV), HP (10 – 20 keV) and PDS (20 – 25, 25 – 30, 30 – 50, 50 – 60 keV).

### 8.2.1 Timing Analysis

Using the high resolution *BeppoSAX* light curves of the 4U 1538–52 and the ephemerides from Rubin et al. (1997), we determined the pulse period  $P = 528.218 \pm 0.001$  s with a high accuracy using the phase-connection technique.

Using the measured period value we obtained the pulse profiles in several energy ranges. In Figure 8.2 the pulse profiles of 4U 1538–52 in 7 energy bands are presented: 0.1 – 4 keV for LECS, 4 – 10 keV for MECS, 10 – 20 keV for HPGSPC and 20 – 25, 25 – 30, 30 – 50, 50 – 60 keV for PDS.

As one can see, the shape of the 4U 1538–52 pulse profile is strongly energy dependent. In the 0.1 – 20 keV and 25 – 35 keV energy bands the pulse profile consists of two peaks with a strong main peak and a smaller secondary. At high energies a single broad peak is observed. The secondary peak disappears at the  $\sim 20$  keV, i.e. close to the cyclotron energy (see below, 8.2.2).

Using the obtained pulse profiles we calculated the pulsed fraction as function of energy as presented in Figure 8.3. The fraction of pulsed emission increases with energy from 30% to 100% in the 5 – 20 keV and 30 – 50 keV energy ranges. Below 5 keV and above 20 keV the pulsed fraction decreases with energy. The decrease of the pulsed fraction at higher energies is likely associated with presence of the CRSF at 21 keV.

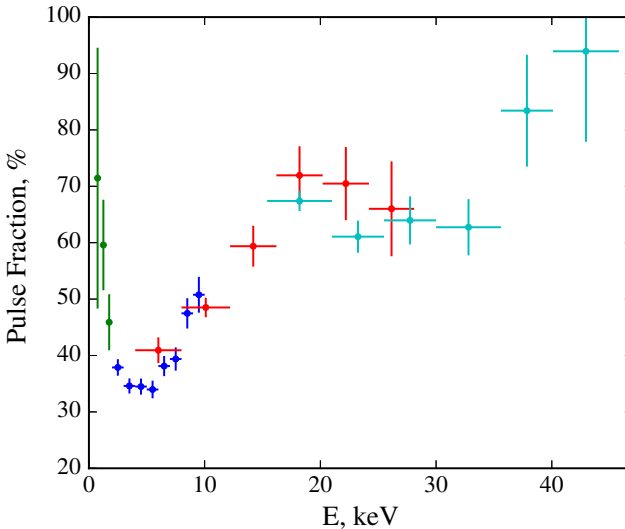


Figure 8.3: 4U 1538–52, pulse fraction.

### 8.2.2 Spectral Analysis

We performed a spectral analysis of the 4U 1538–52 for the out-of-eclipse data in the energy range 0.1 – 120 keV. The broadband spectrum can be described with an absorbed cut-off power law continuum ( $N_{\text{H}} \sim 10^{22}$  atoms  $\text{cm}^{-2}$ ) modified by a fluorescent iron line at  $\sim 6.4$  keV and two absorption features with energies  $\sim 21$  keV and  $\sim 52$  keV required to account for the CRSF and its first harmonic (Clark et al. 1990; Rodes-Roca et al. 2009; Hemphill et al. 2013).

The best-fit parameters for five considered continuum models are presented in Table 8.1: *Highcut*, *NPEX*, *Cutoffpl*, *CompTT* and *BW*. Note, however, that only the first three models provide a reasonably good approximation of the phase averaged spectrum and exhibit no systematic fluctuations in the residuals (Fig. 8.4). Furthermore, only *Highcut* and *BW* models result in a good fit for the spectrum

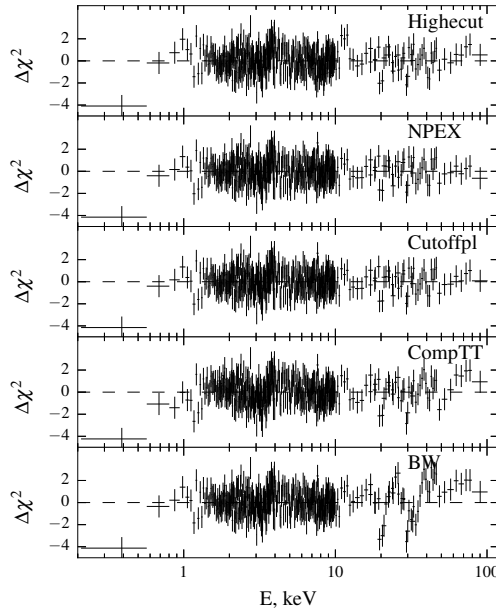


Figure 8.4: 4U 1538–52. The best-fit residuals for the considered continuum models. Note that *Fdcut* does not provide an adequate description for the spectrum. The *NPEX*, *Cutoffpl*, *CompTT* models require additional emission line-like component, i.e. “bump” at  $\sim 12$  keV which is not required for *Highcut* and *BW* models. Out of these two models the former provides a statistically better fit.

without the mysterious “bump” at 12 keV reported, but not explained in the literature for several sources. This additional component was first introduced by Coburn (2001) for several sources to account for systematic miscalibration of *RXTE* effective area due to the presence of copper line from wiring of the detector. However, subsequently a similar component was also identified in observations from other satellites, so this interpretation is questionable. On the other hand, it is quite likely that this component is associated with the oversimplified modelling of the broadband continuum, as it often appears only for a particular continuum model. For this reason, I conclude that this component has probably no physical meaning and shall be avoided if it is possible to obtain an acceptable fit without it.

To assess the inter-parameter correlations we also present several sets of contours for the most important model parameters in Figure 8.5.

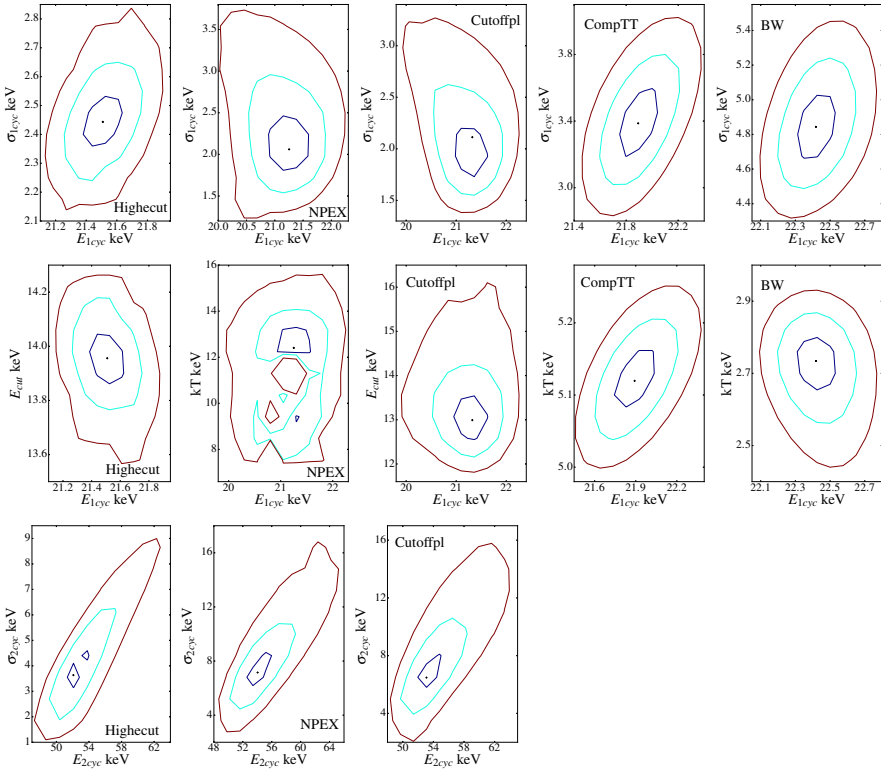


Figure 8.5: 4U 1538–52 contours (1, 2 and  $3\sigma$ ) for different continuum models.

Parameter	Highecut	NPEX	Cutoffpl	CompTT	BW
$N_H^{(a)}$	$1.66^{+0.02}_{-0.02}$	$1.49^{+0.06}_{-0.07}$	$1.49^{+0.06}_{-0.06}$	$0.88^{+0.07}_{-0.06}$	$1.29^{+0.08}_{-0.1}$
$E_{1\text{cyc}}^{(b)}$	$21.51^{+0.19}_{-0.19}$	$21.25^{+0.56}_{-0.59}$	$21.32^{+0.52}_{-0.57}$	$21.89^{+0.25}_{-0.24}$	$22.42^{+0.19}_{-0.18}$
$\sigma_{1\text{cyc}}^{(b)}$	$2.44^{+0.16}_{-0.15}$	$2.06^{+0.67}_{-0.43}$	$2.11^{+0.63}_{-0.43}$	$3.39^{+0.32}_{-0.3}$	$4.84^{+0.32}_{-0.3}$
$\delta_{1\text{cyc}}$	$0.52^{+0.03}_{-0.03}$	$0.36^{+0.08}_{-0.06}$	$0.37^{+0.07}_{-0.05}$	$0.62^{+0.04}_{-0.03}$	$17.11^{+2.01}_{-1.81}$
$\tau_{\text{cyc}}$					
$E_{2\text{cyc}}^{(b)}$	$52.09^{+2.0}_{-1.71}$	$54.02^{+4.42}_{-3.18}$	$53.05^{+4.21}_{-2.84}$		
$\sigma_{2\text{cyc}}^{(b)}$	$3.64^{+1.04}_{-1.13}$	$7.19^{+2.95}_{-2.5}$	$6.45^{+3.13}_{-2.2}$		
$\delta_{2\text{cyc}}$	$1.82^{+1.42}_{-0.81}$	$1.65^{+0.85}_{-0.62}$	$1.48^{+1.14}_{-0.53}$		
$E_{\text{Fe}}^{(b)}$	$6.34^{+0.1}_{-0.03}$	$6.39^{+0.06}_{-0.06}$	$6.39^{+0.06}_{-0.06}$	$6.36^{+0.05}_{-0.06}$	$6.38^{+0.05}_{-0.05}$
$\sigma_{\text{Fe}}^{(b)}$	0.0001(1)	0.14(5)	0.14(5)	$0.2^{+0.1}_{-0.09}$	0.17(5)
$A_{\text{Fe}}^{(c)}$	$2.7^{+0.5}_{-0.5}$	$3.4^{+0.8}_{-0.8}$	$3.4^{+0.7}_{-0.8}$	$4.0^{+0.8}_{-0.8}$	$3.6^{+0.8}_{-0.7}$
$E_{\text{bump}}^{(b)}$		$12.47^{+0.35}_{-0.25}$	$12.49^{+0.45}_{-0.28}$	$13.53^{+7.08}_{-7.19}$	
$\sigma_{\text{bump}}^{(b)}$		$3.31^{+0.31}_{-0.4}$	$3.26^{+0.64}_{-0.37}$	2.35(-5)	
$A_{\text{bump}}^{(c)}$		$56^{+42}_{-9}$	$53^{+12}_{-7}$	$15^{+29}_{-12}$	
$\Gamma$	$1.14^{+0.01}_{-0.01}$		$0.81^{+0.05}_{-0.05}$		
$E_{\text{cut}}^{(b)}$	$13.96^{+0.18}_{-0.18}$		$12.99^{+0.95}_{-0.71}$		
$E_{\text{fold}}^{(b)}$	$11.85^{+0.18}_{-0.19}$				
$\alpha_1$		$0.8^{+0.06}_{-0.16}$			
$\alpha_2$		-2.0			
$kT^{(b)}$		$12.4^{+1.36}_{-0.47}$		$5.12^{+0.07}_{-0.07}$	$2.73^{+0.11}_{-0.13}$
$T_p^{(d)}$				$0.66^{+0.02}_{-0.02}$	
$\tau_p^{(e)}$				$7.11^{+0.09}_{-0.09}$	
$\xi$					$1.38^{+0.15}_{-0.13}$
$\delta$					$3.53^{+0.69}_{-0.53}$
$B^{(f)}$					1.82
$\dot{M}^{(g)}$					1e17
$r_0^{(h)}$					$62.9^{+5.5}_{-5.9}$
$D^{(i)}$					6.4
$\chi^2_{\text{res}} / \text{dof}$	1.056 / 373	0.981 / 370	1.046 / 371	1.139 / 376	1.332 / 376

<sup>(a)</sup>[ $10^{22}$  atoms  $\text{cm}^{-2}$ ]

<sup>(b)</sup>[keV]

<sup>(c)</sup>[ $10^{-4}$  ph  $\text{cm}^{-2}$   $\text{s}^{-1}$ ]

<sup>(d)</sup>Plasma temperature, keV.

<sup>(e)</sup>Plasma optical depth.

<sup>(f)</sup>[ $10^{12}$  G]

<sup>(g)</sup>[ $10^{17}$  g/s]

<sup>(h)</sup>[km]

<sup>(i)</sup>[kpc]

Table 8.1: The best-fit parameters of the 5 different continuum models of the phase averaged spectrum of 4U 1538–52. The absorbed and unabsorbed fluxes are  $F_{\text{ab}} = 9.24 \times 10^{-10}$  erg /  $\text{cm}^2/\text{s}$ ,  $F_{\text{unab}} = 1.05 \times 10^{-9}$  erg /  $\text{cm}^2/\text{s}$  respectively.



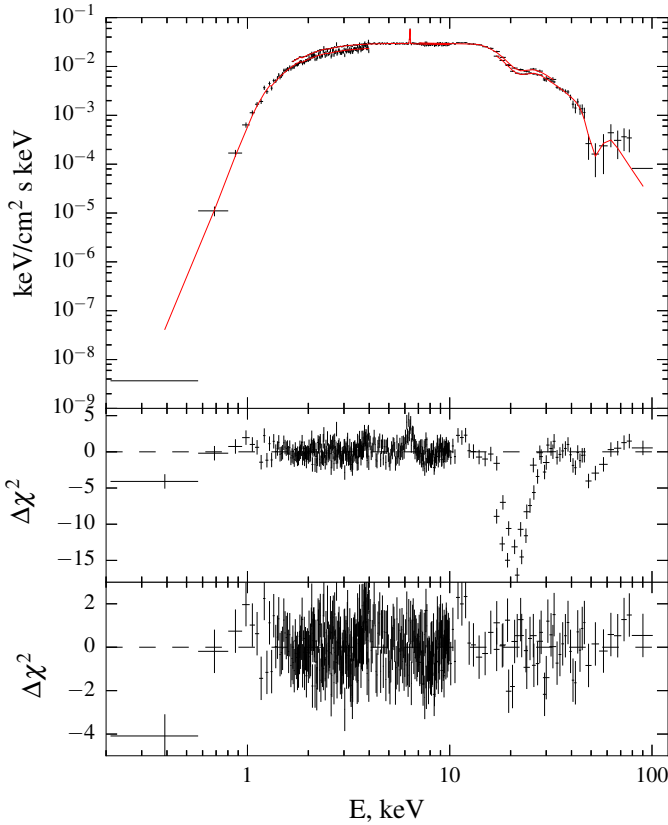


Figure 8.6: 4U 1538–52. Top panel shows the broadband 0.1 – 120 keV unfolded spectrum with the cut-off power law (Highecut) continuum model including the iron line line and two absorption features  $\sim 21$  keV and  $\sim 52$  keV as observed by *BeppoSAX*. Bottom panel shows residuals for (1. Cyclotron and Fe-lines residuals. 2. The best fit residuals with  $\chi^2_{red} \approx 1.06$ .)

Based on the results shown in Table 8.1, contours shape and residuals for the different continuum models, we conclude that the *Highecut* model provides the most robust description for the source spectrum and thus have chosen it for further analysis. The observed spectrum, modeled with the *Highecut*, and its residuals are shown in Figure 8.6. The top panel shows the pulse phase averaged X-ray spectrum with the best fit model (absorbed cut-off power law, *Highecut*). The second panel shows the residuals associated with the two cyclotron lines at  $\sim 21$  keV,  $\sim 52$  keV

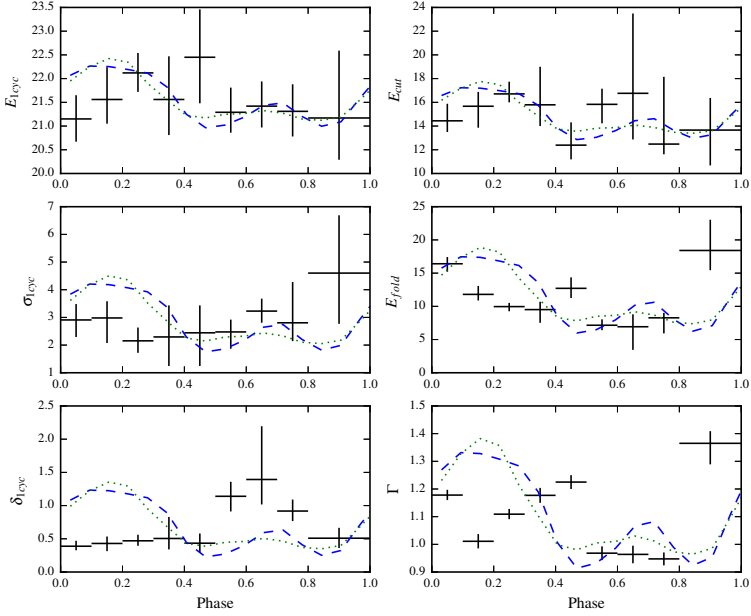


Figure 8.7: 4U 1538–52. Changing spectral parameters with phase with the *Highecut* continuum model (the dashed blue line is the MECS pulse profile in the 2 – 10 keV energy range and the dotted green line is the PDS pulse profile in the 15 – 60 keV energy range).

and the narrow iron emission line at  $\sim 6.4$  keV. In the bottom panel the best fit residuals are shown. Some residuals are still visible in the soft energy range below 1 keV, as in some other sources (e.g., 4U 1907+09, Her X–1). For 4U 1538–52 this “soft excess” can not be described with a blackbody like component, so we conclude that it is likely associated with a blend of several unresolved emission lines (Rodes-Roca et al. 2011).

Pulse-phase resolved spectral analysis was also carried out (Fig. 8.7). The absorbed cut-off power law model (*Highecut*) was used to model the spectra as a function of the pulse phase. The absorption column  $N_{\text{H}}$  and the parameters of cyclotron line harmonic ( $E_{2\text{cyc}}$ ,  $\sigma_{2\text{cyc}}$ ) were fixed at the average values for all phase bins. The Fe-line was not required for the phase resolved spectra (amplitude less than  $10^{-4}$  photons  $\text{cm}^{-2}\text{s}^{-1}$  at  $1\sigma$  confidence level).

We used 9 phase bins (0 – 0.1, 0.1 – 0.2, 0.2 – 0.3, 0.3 – 0.4, 0.4 – 0.5, 0.5 – 0.6, 0.6 – 0.7, 0.7 – 0.8, 0.8 – 1). The fit results are presented in Tables 8.2, 8.3 and Figure 8.7. A strong variation of the folding energy, photon index and depth of the fundamental cyclotron line with pulse phase is observed.  $E_{\text{fold}}$  and photon index  $\Gamma$  exhibit a similar behaviour.  $\delta_{1\text{cyc}}$  is roughly constant during the main peak and has a maximum at the secondary one. Other parameters only exhibit minor variation with phase as expected.

### 8.3 Conclusion

I presented the results of the detailed timing and spectral analysis of the HMXB pulsar 4U 1538–52 observed by *BeppoSAX* in 1998. The measured spin period is in agreement with the value published by Robba et al. (2001) who reported on the analysis of the *BeppoSAX* data including the eclipse. Here I only considered the data out of eclipse which allowed to study the energy dependence of the pulse profiles (Fig. 8.2) and pulsed fraction as function of energy (Fig. 8.3) in more detail. For the average spectrum, I investigated multiple continuum models and conclude that the best one is the *Highecut* (Tab. 8.1, Fig. 8.4, 8.5, 8.6). The pulse phase resolved spectroscopy in 9 energy bins was also carried out (Tab. 8.2, 8.3, Fig. 8.7). Most of the spectral parameters exhibit little variation with pulse phase, however, CRSF parameters do change significantly.

Parameter	0 - 0.1	0.1 - 0.2	0.2 - 0.3	0.3 - 0.4	0.4 - 0.5
$E_{1\text{cyc}}^{(a)}$	$21.15^{+0.5}_{-0.48}$	$21.56^{+0.68}_{-0.51}$	$22.12^{+0.42}_{-0.4}$	$21.56^{+0.91}_{-0.75}$	$22.45^{+1.01}_{-0.97}$
$\sigma_{1\text{cyc}}^{(a)}$	$2.91^{+0.57}_{-0.62}$	$2.98^{+0.6}_{-0.91}$	$2.15^{+0.48}_{-0.43}$	$2.29^{+1.14}_{-1.05}$	$2.44^{+0.99}_{-1.2}$
$\delta_{1\text{cyc}}$	$0.39^{+0.08}_{-0.06}$	$0.43^{+0.1}_{-0.12}$	$0.47^{+0.09}_{-0.07}$	$0.5^{+0.32}_{-0.16}$	$0.43^{+0.15}_{-0.14}$
$\Gamma$	$1.18^{+0.02}_{-0.02}$	$1.01^{+0.03}_{-0.03}$	$1.11^{+0.02}_{-0.02}$	$1.18^{+0.03}_{-0.03}$	$1.22^{+0.02}_{-0.02}$
$E_{\text{cut}}^{(a)}$	$14.44^{+1.44}_{-0.94}$	$15.67^{+1.21}_{-1.81}$	$16.71^{+1.03}_{-0.71}$	$15.79^{+3.21}_{-1.79}$	$12.39^{+1.92}_{-1.2}$
$E_{\text{fold}}^{(a)}$	$16.41^{+1.01}_{-1.2}$	$11.8^{+1.27}_{-0.92}$	$9.96^{+0.56}_{-0.704}$	$9.51^{+1.18}_{-1.99}$	$12.71^{+1.65}_{-1.46}$
$F_{\text{ab}}^{(b)}$	10.88	12.42	11.01	8.21	5.12
$F_{\text{unab}}^{(b)}$	12.44	13.58	12.39	9.3	5.92
$\chi^2_{\text{res}} / \text{dof}$	0.962 / 465	0.994 / 384	1.193 / 453	0.932 / 354	1.138 / 359

<sup>(a)</sup>[keV]

<sup>(b)</sup>The values of absorbed and unabsorbed fluxes in the 0.1 – 120 keV energy range in units  $10^{-10}\text{erg} / \text{cm}^2 / \text{s}$ .

Table 8.2: 4U 1538–52. Phase resolved spectral parameters for the Highcut continuum model. The interstellar absorption and parameters of the first cyclotron line harmonic were fixed at the average values:  $N_{\text{H}} = 2.72^{+0.06}_{-0.09}$  atoms  $\text{cm}^{-2}$ ;  $E_{2\text{cyc}} = 52.09^{+2.0}_{-1.71}$  keV,  $\sigma_{2\text{cyc}} = 3.64^{+1.04}_{-1.13}$  keV. Part 1.

Parameter	0.5 - 0.6	0.6 - 0.7	0.7 - 0.8	0.8 - 1
$E_{1\text{cyc}}^{(a)}$	$21.29^{+0.52}_{-0.43}$	$21.42^{+0.52}_{-0.45}$	$21.31^{+0.57}_{-0.53}$	$21.17^{+1.42}_{-0.88}$
$\sigma_{1\text{cyc}}^{(a)}$	$2.48^{+0.44}_{-0.61}$	$3.23^{+0.45}_{-0.42}$	$2.81^{+1.47}_{-0.66}$	$4.6^{+2.09}_{-1.83}$
$\delta_{1\text{cyc}}$	$1.14^{+0.22}_{-0.23}$	$1.39^{+0.8}_{-0.38}$	$0.92^{+0.17}_{-0.15}$	$0.51^{+0.16}_{-0.15}$
$\Gamma$	$0.97^{+0.02}_{-0.02}$	$0.96^{+0.03}_{-0.03}$	$0.95^{+0.02}_{-0.02}$	$1.36^{+0.04}_{-0.08}$
$E_{\text{cut}}^{(a)}$	$15.83^{+1.32}_{-1.6}$	$16.76^{+6.73}_{-3.89}$	$12.48^{+5.67}_{-0.86}$	$13.66^{+2.71}_{-2.98}$
$E_{\text{fold}}^{(a)}$	$7.153^{+0.89}_{-0.743}$	$6.93^{+1.87}_{-3.48}$	$8.27^{+0.75}_{-2.34}$	$18.41^{+4.63}_{-2.97}$
$F_{\text{ab}}^{(b)}$	5.79	7.16	6.5	5.36
$F_{\text{unab}}^{(b)}$	6.62	7.89	7.12	6.39
$\chi^2_{\text{res}} / \text{dof}$	1.016 / 344	1.031 / 306	1.026 / 345	1.033 / 400

<sup>(a)</sup>[keV]

<sup>(b)</sup>Absorbed and unabsorbed fluxes in the 0.1 – 120 keV energy range in units  $10^{-10}\text{erg} / \text{cm}^2 / \text{s}$ .

Table 8.3: 4U 1538–52. Dependence of spectral parameters of 4U 1538–52 on pulse phase for the Highcut continuum model. The interstellar absorption and parameters of the first cyclotron line harmonic were fixed at the average values:  $N_{\text{H}} = 2.72^{+0.06}_{-0.09}$  atoms  $\text{cm}^{-2}$ ;  $E_{2\text{cyc}} = 52.09^{+2.0}_{-1.71}$  keV,  $\sigma_{2\text{cyc}} = 3.64^{+1.04}_{-1.13}$  keV. Part 2.

## CHAPTER 9

---

### Vela X–1

#### 9.1 Source Description

The eclipsing HMXB Vela X–1 was discovered in 1967 (Chodil et al. 1967) and it is today one of the most well-studied X-ray pulsars. It exhibits pulsations with a period of  $\sim 283$  s (McClintock et al. 1976) modulated with an orbital period of 8.964 days (Forman et al. 1973; van Kerkwijk et al. 1995).

The optical companion star is a massive ( $M = 23M_{\odot}$  and  $R = 34R_{\odot}$ ) B0.5Ib supergiant HD 77581 (Brucato & Kristian 1972; Hiltner et al. 1972; Nagase 1989), which loses mass at an estimated rate of  $(1 - 7) \times 10^{-6} M_{\odot} \text{ yr}^{-1}$  (Hutchings 1976; Dupree et al. 1980; Kallman & White 1982; Sadakane et al. 1985; Sato et al. 1986; Sako et al. 1999) through a fast wind with a terminal velocity of  $\sim 1700 \text{ km s}^{-1}$  (Dupree et al. 1980). The compact object in Vela X–1 is one of the most massive NSs ( $1.9M_{\odot}$ ) (Barziv et al. 2001; Quaintrell et al. 2003). Due to the small distance between the two components of the system (orbital radius is of just about 1.7 stellar radii) the NS is deeply embedded in the stellar wind of the supergiant (Nagase 1989). Together with its relatively close distance of  $\sim 2$  kpc (Nagase 1989), this makes Vela X–1 one of the brightest persistent X-ray pulsars in the sky and a prototypical wind-accreting system.

The matter from the wind of the optical companion is accreted by the NS yielding average X-ray luminosity of  $\sim 4 \times 10^{36} \text{ erg s}^{-1}$ . Note however, that Vela X–1 is an extremely variable on short time scales. The system is known to exhibit so-called giant flares with flux increasing by a factor of 20 on a timescale of hours, and the “off-states” where the source becomes basically undetectable for several pulse periods (Staubert et al. 2004; Kreykenbohm et al. 2008; Doroshenko et al. 2011).

In the X-ray spectrum of Vela X–1 a strong variation of the absorption column on short time scales and with orbital phase is observed (Haberl & White 1990; Fürst et al. 2010). The spectrum also exhibits a variable iron emission line at  $\sim 6.4 \text{ keV}$  as well as a number of lines from other elements. Two cyclotron lines at  $\sim 25 \text{ keV}$  and

Date	Obs. time (ksec, MECS)	Orb. phase <sup>(a)</sup>	Period (sec)
1996-07-14 <sup>(b)</sup>	48	0.28-0.35	283.201(1)
1996-12-23 <sup>(c)</sup>	96	0.38-0.5	283.271(1)
1996-12-24 <sup>(c)</sup>	99	0.51-0.63	283.271(1)
1997-11-24 <sup>(d)</sup>	100	0.83-1.00 (+eclipse)	283.5549(1)
1997-12-24 <sup>(d)</sup>	76	0.22-0.32	283.452(1)
1997-12-25 <sup>(c)</sup>	76	0.32-0.42	283.452(1)

<sup>(a)</sup>Ephemerides from Falanga et al. (2015).

<sup>(b)</sup>Orlandini et al. (1998)

<sup>(c)</sup>La Barbera et al. (2003)

<sup>(d)</sup>These data were not published before.

Table 9.1: *BeppoSAX* observations of *Vela X-1* analysed in our work.

~ 55 keV have also been reported in the source (Kendziorra et al. 1992; Kreykenbohm et al. 1999, 2002; La Barbera et al. 2003; Maitra & Paul 2013b).

## 9.2 Observations

*Vela X-1* was observed by *BeppoSAX* several times within 1996 – 1997 (Tab. 9.1) with a total MECS exposure of about 535 ks.

The light curves with time bin of 256 s for all *BeppoSAX* observation as observed with the MECS in the 2 – 10 keV energy range are presented in Figure 9.1. They illustrate the variability features briefly mentioned above, i.e. the flares, low and off-states, as well as a period when the NS was eclipsed by the companion. Note that unlike the off-states the fluorescent lines are still observed during the eclipse, i.e. the source is still emitting the X-rays.

### 9.2.1 Timing Analysis

Using the high resolution *BeppoSAX* light curves and orbital ephemerides from Falanga et al. (2015), we determined the pulse periods for all observations using the phase-connection technique. The results are presented in Table 9.1.

We choose the 1996-12-24 observation as a reference for the further total timing and spectral analysis as it has longest exposure. Using the measured pulse period values we obtained the pulse profiles in several energy bands. In Figure 9.2 the pulse profiles for the observation 1996-12-24 are presented in 6 energy bands: 0.1 – 4 keV for the LECS, 4 – 7, 7 – 10 keV for the MECS, 10 – 20 keV for the HPGSPC and 20 – 60, 60 – 120 keV for the PDS. As one can see, the morphology of the

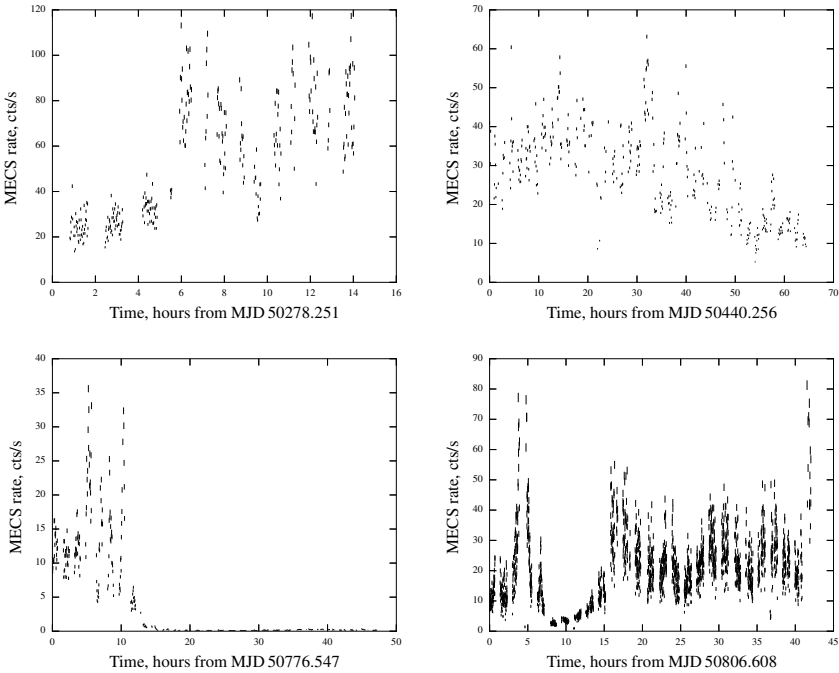


Figure 9.1: The MECS light curves of Vela X-1 in 2 – 10 keV energy range. On the top panels are observations from 1996-07-14 (low and high states; left) and 1996-12-23/24 (right). Bottom: 1997-11-24 (the low state, the high state, contains several flares, and the eclipse; left) and 1997-12-24/25 (during this observation a few flares and the off-state were observed; right) dates of observations.

Vela X-1 pulse profile is strongly energy dependent. At low energies five peaks are observed, whereas only two peaks may be identified at higher energies. The pulsations are detected up to  $\sim 120$  keV.

The pulse fraction of Vela X-1 as function of energy calculated using the pulse profiles for the observation in 1996-12-24 is presented in Figure 9.3. The fraction of the pulsed flux increases with energy in the 5 – 60 keV energy range, from 35% to 75%. Below 5 keV the pulse fraction shows a reverse dependence on energy similarly to more other pulsars in the sample.

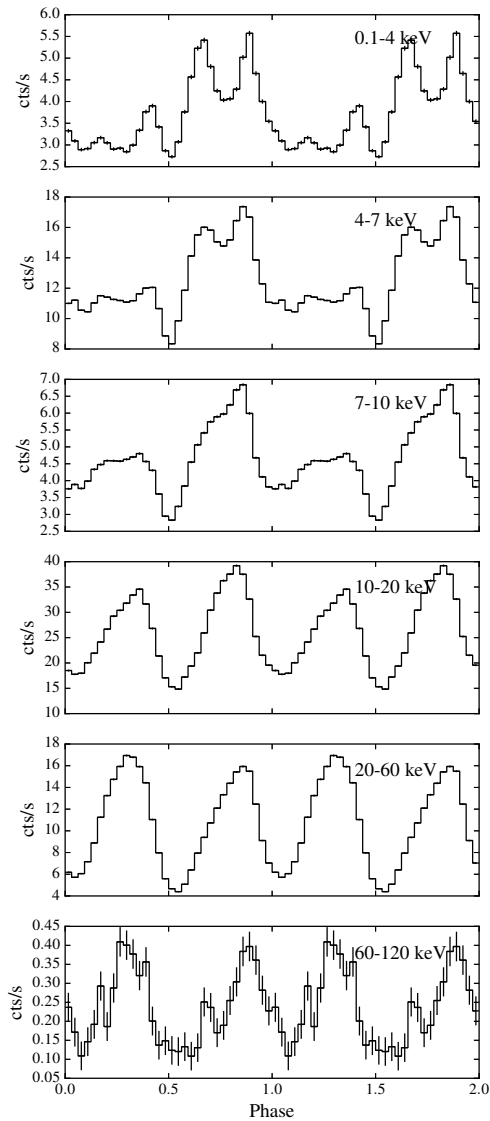


Figure 9.2: The pulse profiles of the X-ray pulsar Vela X-1, in 1996-12-24, as a function of energy. LECS (0.1 – 4 keV), MECS (4 – 7, 7 – 10 keV), HPGSPC (10 – 20 keV) and PDS (20 – 60, 60 – 120 keV).



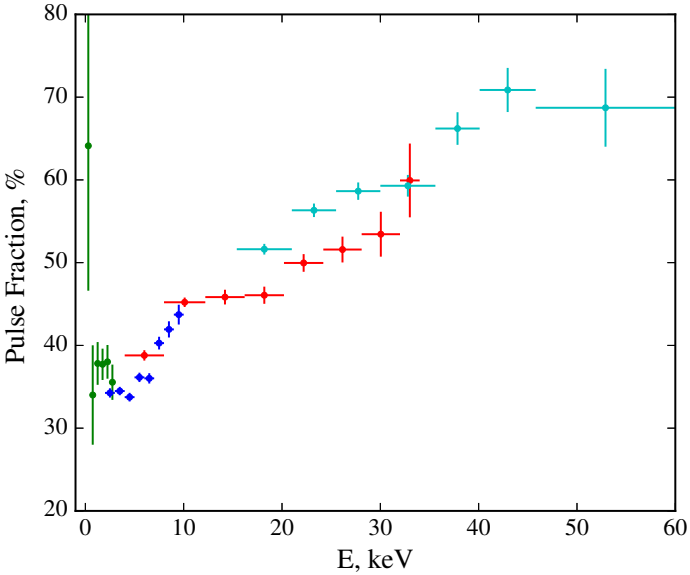


Figure 9.3: Vela X-1, 1996-12-24, pulse fraction.

### 9.2.2 Spectral Analysis

To assess possible spectral variability I extracted the broadband spectra in the 2 to 120 keV energy range separately for all observations. The broadband spectrum may be described with an absorbed continuum consisting of a cut-off power law. In some observations the complex intrinsic absorption is evident which I account for using the partial covering absorption model (see Chapter 4). The emission Gaussian line at  $\sim 6.5$  keV, and two CRSFs with energies  $\sim 25$  keV and  $\sim 55$  keV are also required to approximate the spectrum.

Vela X-1 was observed by *BeppoSAX* several times (Tab. 9.1). As already said, I chose the observation on 24th of December 1996 as a representative observation to test all continuum models which I use in the thesis. In the case of the Vela X-1, however, only four continuum models provided acceptable fit for the phase averaged spectrum (Tab. 9.2, Fig. 9.4): *Highcut*, *Fdcut*, *NPEX* and *CompTT*.

Figure 9.5 shows the broadband spectrum of Vela X-1 as observed by *BeppoSAX* on 1996-12-24. The top panel shows the phase averaged X-ray spectrum with the best fit model, i.e. the absorbed cut-off power law (*Highcut*) modified by a partial covering absorption. The second panel shows the residuals due to the *Fe-K* line at  $\sim 6.5$  keV and cyclotron lines at  $\sim 25$  keV and  $\sim 55$  keV. In the bottom panel the best fit residuals are shown.

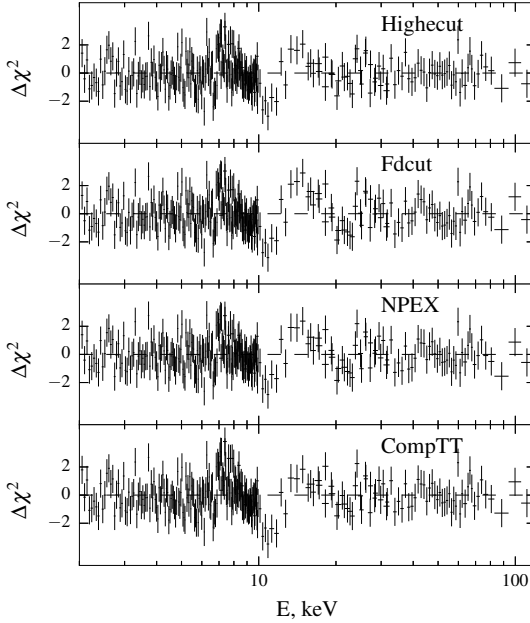


Figure 9.4: *Vela X-1* spectral residuals for four different continuum models in 1996-12-24.

Spectra for all the *BeppoSAX* observations of *Vela X-1* can be approximated using the same model (Tab. 9.3, 9.4). The best fit residuals and the residuals of the cyclotron lines for all observations with *Highcut* continuum model are shown at Figures 9.6, 9.7 respectively.

Pulse phase-resolved spectral analysis was also carried out (Fig. 9.8) for the observation performed on 1996-12-24. The absorbed power law model with cutoff at high energies (*Highcut*) was used to model the spectra also in this case. The absorption column  $N_{\text{H}}$  was fixed at the average value for all phase bins. Fit results are presented in Tables 9.5, 9.6. Most parameters exhibit a strong variation with phase as illustrated in Figure 9.8.

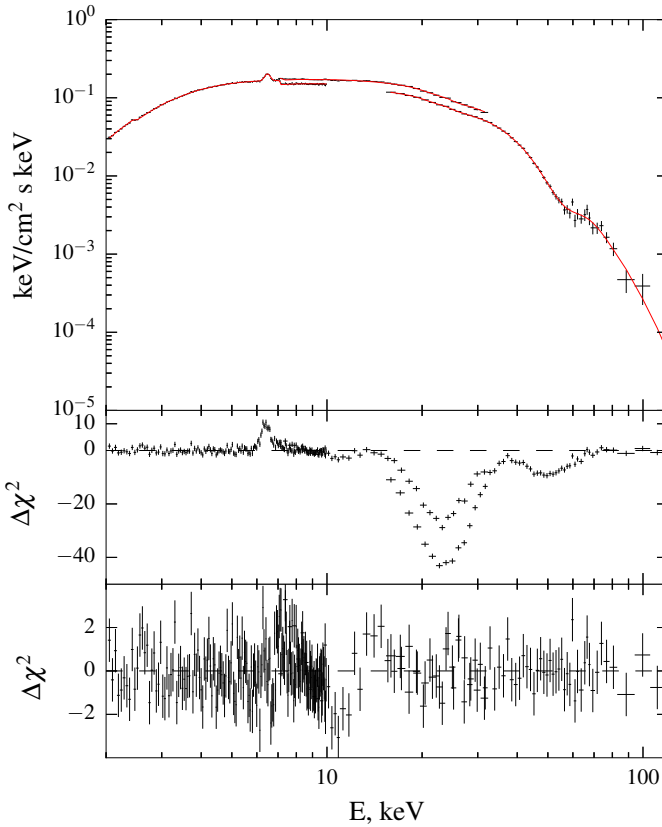


Figure 9.5: Top panel shows the broadband 2 – 120 keV unfolded spectrum of Vela X–1 observed on 1996-12-24 approximated with a cutoff power law continuum model (Highecut) modified by Fe-emission line and absorption Gaussian lines at  $\sim 25$  keV and  $\sim 55$  keV. Bottom panel shows residuals for: 1) Cyclotron and Fe-lines residuals; 2) The best fit residuals. ( $\chi_{\text{red}}^2 \approx 0.8$ .)

### 9.3 Conclusion

Vela X–1 was observed by *BeppoSAX* several times (Tab. 9.1). Part of these data were analysed and published (Orlandini et al. 1998; La Barbera et al. 2003), however, analysis of the observations on 1996-12-24 (second part), 1997-11-24 and 1997-12-24 is reported for the first time here.

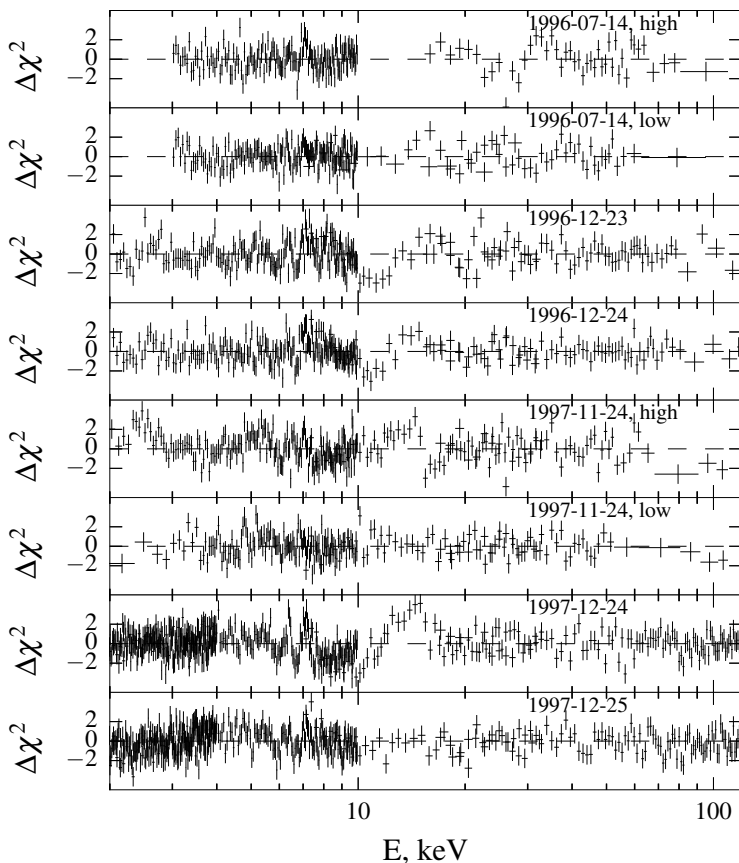


Figure 9.6: The best-fit residuals for *Vela X-1* broadband spectrum for all *BeppoSAX* observations and *Highcut* continuum model.

For all observations a basic spectral and timing analysis was carried out. More detailed analysis was done for the longest observation (1996-11-24) including:

- evolution of the pulse profiles with energy (Fig. 9.2),
- analysis of the pulsed fraction as a function of energy (Fig. 9.3),

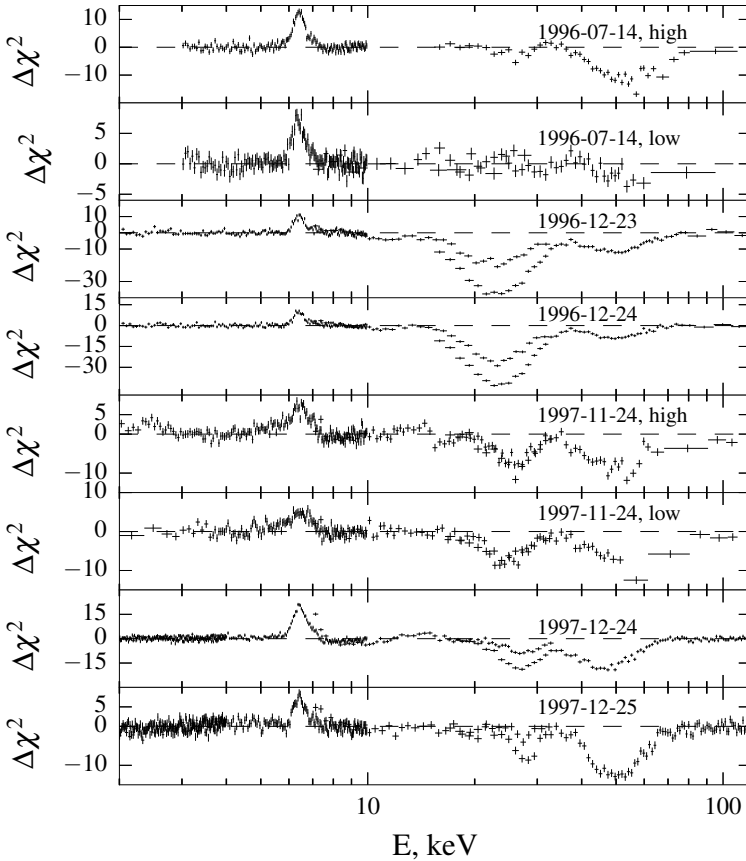


Figure 9.7: Vela X-1 spectral residuals after exclusion from the model of the emission iron and cyclotron lines for all *BeppoSAX* observations (again, for Highcut continuum model).

- detailed spectral analysis with several (Highcut, Fdcut, NPEX CompTT) continuum models (Tab. 9.2, Fig. 9.4),
- pulse phase-resolved spectral analysis (Tab. 9.5, 9.6, Fig. 9.8).

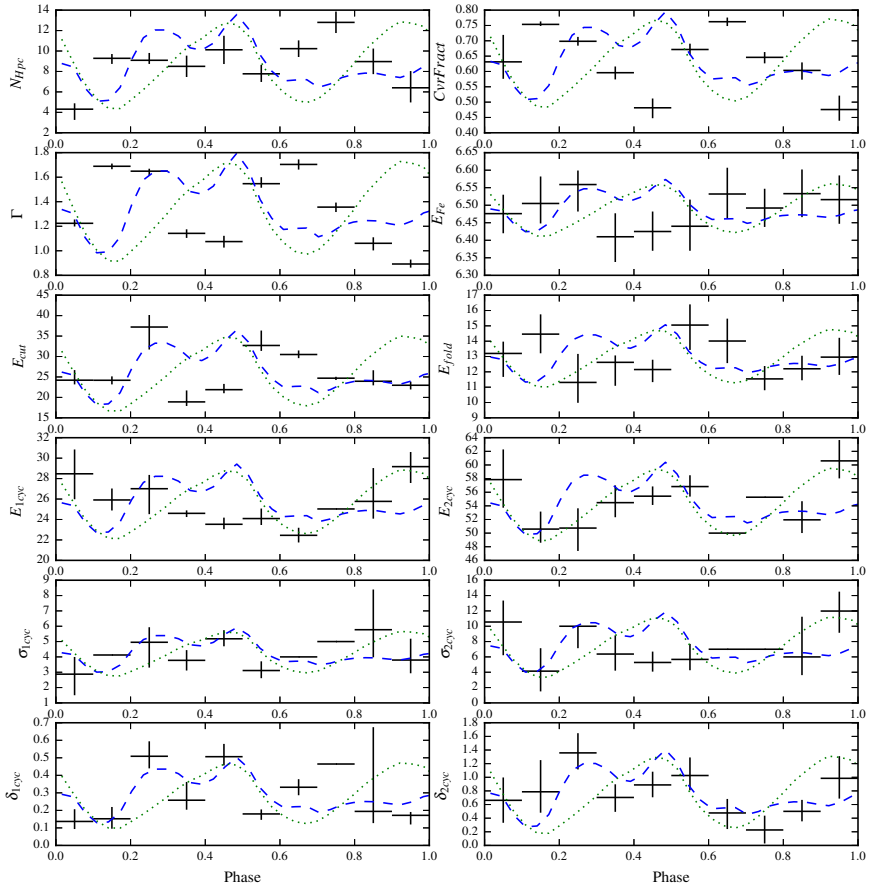


Figure 9.8: *Vela X-1*, 1996-12-24. Variation of the best-fit spectral parameters with pulse phase for **Highcut** continuum model. For reference the pulse profiles in the 2 – 10 keV (MECS data, dashed blue line), and 15 – 120 keV energy ranges (PDS data, dotted green line) are also shown.

Parameter	Highecut	Fdcut	NPEX	CompTT
$N_{\text{H}}^{(a)}$	$3.15^{+0.03}_{-0.04}$	$3.06^{+0.04}_{-0.02}$	$2.84^{+0.3}_{-0.59}$	$3.52^{+0.29}_{-0.46}$
$E_{1\text{cyc}}^{(b)}$	$25.03^{+0.18}_{-0.16}$	$26.88^{+0.22}_{-0.2}$	$26.8^{+0.49}_{-0.61}$	$26.68^{+0.71}_{-0.45}$
$\sigma_{1\text{cyc}}^{(b)}$	$4.68^{+0.21}_{-0.15}$	$5.07^{+0.24}_{-0.21}$	$6.0^{+0.6}_{-0.9}$	$5.62^{+0.82}_{-0.49}$
$\delta_{1\text{cyc}}$	$0.26^{+0.01}_{-0.01}$	$0.24^{+0.01}_{-0.01}$	$0.32^{+0.04}_{-0.06}$	$0.23^{+0.03}_{-0.02}$
$E_{2\text{cyc}}^{(b)}$	$55.27^{+0.6}_{-0.57}$	$55.47^{+0.29}_{-0.16}$	$55.35^{+1.49}_{-1.1}$	$55.5^{+1.5}_{-1.14}$
$\sigma_{2\text{cyc}}^{(b)}$	$6.9^{+0.43}_{-0.44}$	$14.35^{+0.1}_{-0.17}$	$12.59^{+1.72}_{-1.25}$	$11.06^{+1.44}_{-1.32}$
$\delta_{2\text{cyc}}$	$0.62^{+0.05}_{-0.04}$	$1.96^{+0.03}_{-0.03}$	$1.19^{+0.14}_{-0.17}$	$0.99^{+0.14}_{-0.14}$
$E_{\text{Fe}}^{(b)}$	$6.48^{+0.03}_{-0.03}$	$6.47^{+0.03}_{-0.02}$	$6.48^{+0.03}_{-0.03}$	$6.47^{+0.04}_{-0.03}$
$\sigma_{\text{Fe}}^{(b)}$	0.13(1)	0.11(1)	0.103(5)	0.082(5)
$A_{\text{Fe}}^{(c)}$	$1.8^{+0.2}_{-0.3}$	$1.8^{+0.2}_{-0.2}$	$2.1^{+0.3}_{-0.2}$	$2.1^{+0.4}_{-0.2}$
$N_{\text{H}_p}^{(d)}$	$9.21^{+0.14}_{-0.19}$	$8.96^{+0.16}_{-0.21}$	$9.01^{+0.94}_{-1.14}$	$10.18^{+0.91}_{-0.99}$
$C_{\text{Fp}}^{(e)}$	$0.627^{+0.004}_{-0.005}$	$0.631^{+0.005}_{-0.006}$	$0.59^{+0.07}_{-0.02}$	$0.62^{+0.06}_{-0.04}$
$\Gamma$	$1.332^{+0.006}_{-0.003}$	$1.307^{+0.011}_{-0.005}$		
$E_{\text{cut}}^{(b)}$	$23.9^{+0.13}_{-0.13}$	$51.85^{+0.38}_{-0.41}$		
$E_{\text{fold}}^{(b)}$	$13.59^{+0.15}_{-0.14}$	$7.82^{+0.23}_{-0.22}$		
$\alpha 1$			$0.72^{+0.03}_{-0.04}$	
$\alpha 2$			-2.0	
$kT^{(b)}$			$7.38^{+0.05}_{-0.07}$	$7.77^{+0.23}_{-0.11}$
$T_{\text{p}}^{(f)}$				$0.001^{+6.016}_{0.0}$
$\tau_{\text{p}}^{(g)}$				$10.6^{+0.2}_{-0.2}$
$\chi^2_{\text{res}} / \text{dof}$	0.813 / 283	0.856 / 284	0.789 / 284	0.900 / 284

(a) [ $10^{22}$  atoms  $\text{cm}^{-2}$ ]

(b) [keV]

(c) [ $10^{-3}$  ph  $\text{cm}^{-2}$   $\text{s}^{-1}$ ]

(d) Equivalent hydrogen column for partial covering absorption in units  $10^{22}$  atoms  $\text{cm}^{-2}$ .

(e) Covering fraction.

(f) Plasma temperature, keV.

(g) Plasma optical depth.

Table 9.2: The best-fit parameters of the broadband phase averaged spectrum of Vela X-1 for four different continuum models (for the representative observation performed on 1996-12-24). The absorbed and unabsorbed fluxes in 2 – 120 keV energy range are  $F_{\text{ab}} = 6.2 \times 10^{-9}$  erg /  $\text{cm}^2/\text{s}$ ,  $F_{\text{unab}} = 7.2 \times 10^{-9}$  erg /  $\text{cm}^2/\text{s}$  respectively.

Parameter	1996-07-14/high	1996-07-14/low	1996-12-23	1996-12-24
$N_{\text{H}}^{(a)}$	$1.74^{+0.11}_{-0.07}$	$8.47^{+0.1}_{-0.16}$	$1.39^{+0.02}_{-0.02}$	$3.14^{+0.03}_{-0.04}$
$E_{1\text{cyc}}^{(b)}$			$25.01^{+0.21}_{-0.26}$	$25.03^{+0.18}_{-0.16}$
$\sigma_{1\text{cyc}}^{(b)}$			$5.41^{+0.45}_{-0.17}$	$4.68^{+0.21}_{-0.15}$
$\delta_{1\text{cyc}}$			$0.21^{+0.01}_{-0.01}$	$0.26^{+0.01}_{-0.01}$
$E_{2\text{cyc}}^{(b)}$	$60.11^{+1.03}_{-0.97}$	$60.11^{(g)}$	$57.27^{+0.56}_{-0.52}$	$55.27^{+0.6}_{-0.57}$
$\sigma_{2\text{cyc}}^{(b)}$	$8.15^{+0.43}_{-0.6}$	$6.94^{+1.68}_{-1.63}$	$8.45^{+0.36}_{-0.36}$	$6.9^{+0.43}_{-0.44}$
$\delta_{2\text{cyc}}$	$1.4^{+0.1}_{-0.1}$	$0.6^{+0.3}_{-0.2}$	$0.77^{+0.05}_{-0.04}$	$0.62^{+0.05}_{-0.04}$
$E_{\text{Fe}}^{(b)}$	$6.48^{+0.02}_{-0.02}$	$6.46^{+0.03}_{-0.03}$	$6.49^{+0.03}_{-0.03}$	$6.48^{+0.03}_{-0.03}$
$\sigma_{\text{Fe}}^{(b)}$	$0.13^{+0.04}_{-0.04}$	$0.15^{+0.07}_{-0.06}$	$0.12(1)$	$0.13(1)$
$A_{\text{Fe}}^{(c)}$	$8.2^{+0.6}_{-0.4}$	$4.2^{+0.5}_{-0.3}$	$2.2^{+0.2}_{-0.3}$	$1.8^{+0.2}_{-0.3}$
$\Gamma$	$1.09^{+0.01}_{-0.01}$	$1.24^{+0.01}_{-0.01}$	$1.397^{+0.003}_{-0.003}$	$1.332^{+0.006}_{-0.003}$
$E_{\text{cut}}^{(b)}$	$21.0^{+1.18}_{-0.92}$	$24.89^{+0.57}_{-1.38}$	$24.08^{+0.16}_{-0.13}$	$23.9^{+0.13}_{-0.13}$
$E_{\text{fold}}^{(b)}$	$13.39^{+0.9}_{-1.1}$	$11.33^{+0.47}_{-0.43}$	$14.89^{+0.18}_{-0.17}$	$13.59^{+0.15}_{-0.14}$
$N_{\text{H}_p}^{(d)}$			$12.49^{+0.63}_{-0.78}$	$9.21^{+0.14}_{-0.19}$
$C_{\text{F}_p}^{(e)}$			$0.25^{+0.01}_{-0.01}$	$0.627^{+0.004}_{-0.005}$
$F_{\text{ab}}^{(f)}$	17.2	8.8	6.9	6.2
$F_{\text{unab}}^{(f)}$	17.7	9.8	7.5	7.2
$\chi^2_{\text{res}} / \text{dof}$	1.058 / 187	1.033 / 206	0.997 / 282	0.813 / 283

<sup>(a)</sup> [ $10^{22}$  atoms  $\text{cm}^{-2}$ ]

<sup>(b)</sup> [keV]

<sup>(c)</sup> [ $10^{-3}$  ph  $\text{cm}^{-2}$   $\text{s}^{-1}$ ]

<sup>(d)</sup> Equivalent hydrogen column for partial covering absorption in units  $10^{22}$  atoms  $\text{cm}^{-2}$ .

<sup>(e)</sup> Covering fraction.

<sup>(f)</sup> The values of absorbed and unabsorbed fluxes in the 2 – 120 keV energy range in units  $10^{-9}$  erg /  $\text{cm}^2$  / s.

<sup>(g)</sup> This parameter was fixed.

Table 9.3: Variation of the spectral parameters of Vela X-1 with time/orbital phase for the cutoff power law continuum model (Highecut). Part 1.



Parameter	1997-11-24/high	1997-11-24/low	1997-12-24	1997-12-25
$N_{\text{H}}^{(a)}$	$27.97^{+0.22}_{-0.23}$	$18.58^{+0.3}_{-0.25}$	$2.26^{+0.02}_{-0.02}$	$1.47^{+0.01}_{-0.02}$
$E_{1\text{cyc}}^{(b)}$	$26.15^{+0.42}_{-0.5}$	$25.23^{+0.86}_{-0.45}$	$27.54^{+0.41}_{-0.23}$	$27.82^{+0.32}_{-0.53}$
$\sigma_{1\text{cyc}}^{(b)}$	$2.49^{+0.41}_{-0.49}$	$2.61^{+0.85}_{-0.43}$	$2.66^{+0.18}_{-0.36}$	$0.71^{+0.17}_{-0.13}$
$\delta_{1\text{cyc}}$	$0.09^{+0.01}_{-0.01}$	$0.13^{+0.02}_{-0.01}$	$0.103^{+0.004}_{-0.014}$	$0.15^{+0.03}_{-0.03}$
$E_{2\text{cyc}}^{(b)}$	$56.52^{+0.98}_{-1.09}$	$59.59^{+1.61}_{-2.59}$	$54.45^{+0.36}_{-0.26}$	$56.34^{+0.34}_{-0.38}$
$\sigma_{2\text{cyc}}^{(b)}$	$8.0^{+0.91}_{-0.84}$	$9.44^{+1.68}_{-1.7}$	$8.3^{+0.69}_{-0.33}$	$7.35^{+0.27}_{-0.19}$
$\delta_{2\text{cyc}}$	$0.9^{+0.1}_{-0.1}$	$1.2^{+0.3}_{-0.2}$	$0.8^{+0.03}_{-0.03}$	$0.81^{+0.04}_{-0.04}$
$E_{\text{Fe}}^{(b)}$	$6.48^{+0.02}_{-0.05}$	$6.52^{+0.03}_{-0.07}$	$6.52^{+0.01}_{-0.01}$	$6.51^{+0.02}_{-0.04}$
$\sigma_{\text{Fe}}^{(b)}$	$0.35^{+0.05}_{-0.04}$	$0.35^{+0.1}_{-0.08}$	$0.2^{+0.02}_{-0.01}$	$0.15^{+0.06}_{-0.04}$
$A_{\text{Fe}}^{(c)}$	$7.1^{+1.0}_{-0.6}$	$3.9^{+0.7}_{-0.4}$	$9.8^{+0.3}_{-0.3}$	$3.2^{+0.2}_{-0.3}$
$\Gamma$	$0.91^{+0.02}_{-0.01}$	$0.98^{+0.02}_{-0.02}$	$0.66^{+0.006}_{-0.002}$	$1.215^{+0.002}_{-0.002}$
$E_{\text{cut}}^{(b)}$	$20.98^{+0.88}_{-0.15}$	$20.21^{+0.61}_{-0.36}$	$22.21^{+0.13}_{-0.04}$	$23.23^{+0.08}_{-0.11}$
$E_{\text{fold}}^{(b)}$	$11.2^{+0.14}_{-0.55}$	$14.09^{+1.0}_{-0.7}$	$9.89^{+0.18}_{-0.24}$	$13.94^{+0.07}_{-0.14}$
$N_{\text{H}_p}^{(d)}$				
$C_{\text{F}_p}^{(e)}$				
$F_{\text{ab}}^{(f)}$	16.4	7.0	9.8	7.7
$F_{\text{unab}}^{(f)}$	20.1	8.4	10.0	7.9
$\chi^2_{\text{res}} / \text{dof}$	1.576 / 286	1.130 / 225	1.345 / 555	1.366 / 573

<sup>(a)</sup> $[10^{22} \text{atoms cm}^{-2}]$

<sup>(b)</sup> $[\text{keV}]$

<sup>(c)</sup> $[10^{-3} \text{ph cm}^{-2} \text{s}^{-1}]$

<sup>(d)</sup>Equivalent hydrogen column for partial covering absorption in units  $10^{22} \text{atoms cm}^{-2}$ .

<sup>(e)</sup>Covering fraction.

<sup>(f)</sup>The values of absorbed and unabsorbed fluxes in 2 – 120 keV energy range in units  $10^{-9} \text{erg / cm}^2 / \text{s}$ .

Table 9.4: Variation of the spectral parameters of Vela X–1 with time/orbital phase for the cutoff power law continuum model (Highecut). Part 2.

Parameter	0 - 0.1	0.1 - 0.2	0.2 - 0.3	0.3 - 0.4	0.4 - 0.5
$E_{1\text{cyc}}^{(a)}$	$28.47^{+2.38}_{-2.49}$	$25.91^{+1.12}_{-1.03}$	$27.01^{+1.35}_{-2.49}$	$24.6^{+0.29}_{-0.36}$	$23.53^{+0.65}_{-0.48}$
$\sigma_{1\text{cyc}}^{(a)}$	$2.87^{+1.12}_{-1.38}$	$4.12^{(d)}$	$4.95^{+0.98}_{-1.65}$	$3.78^{+0.67}_{-0.66}$	$5.18^{+0.56}_{-0.49}$
$\delta_{1\text{cyc}}$	$0.14^{+0.07}_{-0.04}$	$0.15^{+0.07}_{-0.06}$	$0.51^{+0.08}_{-0.07}$	$0.26^{+0.1}_{-0.05}$	$0.51^{+0.07}_{-0.05}$
$E_{2\text{cyc}}^{(b)}$	$57.85^{+4.43}_{-4.12}$	$50.59^{+2.57}_{-2.0}$	$50.74^{+2.9}_{-3.36}$	$54.47^{+2.53}_{-2.14}$	$55.42^{+1.43}_{-1.29}$
$\sigma_{2\text{cyc}}^{(b)}$	$10.55^{+2.8}_{-4.33}$	$4.14^{+2.99}_{-2.64}$	$10.0^{(d)}$	$6.37^{+2.43}_{-2.17}$	$5.27^{+1.42}_{-1.2}$
$\delta_{2\text{cyc}}$	$0.66^{+0.34}_{-0.33}$	$0.79^{+0.46}_{-0.31}$	$1.36^{+0.29}_{-0.24}$	$0.7^{+0.19}_{-0.21}$	$0.89^{+0.19}_{-0.18}$
$E_{\text{Fe}}^{(b)}$	$6.48^{+0.05}_{-0.06}$	$6.5^{+0.08}_{-0.06}$	$6.56^{+0.04}_{-0.08}$	$6.41^{+0.07}_{-0.07}$	$6.42^{+0.06}_{-0.06}$
$\sigma_{\text{Fe}}^{(b)}$	$5\text{e-}11(1)$	$0.09(1)$	$0.1^{(d)}$	$2\text{e-}25(5)$	$1\text{e-}25(1)$
$A_{\text{Fe}}^{(c)}$	$1.8^{+0.4}_{-0.3}$	$1.6^{+0.5}_{-0.4}$	$1.8^{+0.4}_{-0.4}$	$1.5^{+0.4}_{-0.4}$	$2.0^{+0.5}_{-0.5}$
$\Gamma$	$1.22^{+0.03}_{-0.03}$	$1.69^{+0.02}_{-0.02}$	$1.65^{+0.02}_{-0.04}$	$1.14^{+0.03}_{-0.04}$	$1.08^{+0.05}_{-0.05}$
$E_{\text{cut}}^{(a)}$	$24.21^{+2.47}_{-1.03}$	$24.19^{+0.95}_{-1.01}$	$37.21^{+2.94}_{-5.5}$	$18.9^{+2.8}_{-1.0}$	$21.89^{+1.41}_{-0.87}$
$E_{\text{fold}}^{(a)}$	$13.2^{+0.77}_{-1.53}$	$14.46^{+1.29}_{-1.25}$	$11.31^{+1.86}_{-1.33}$	$12.62^{+0.45}_{-1.53}$	$12.15^{+0.64}_{-0.82}$
$N_{\text{H}_p}^{(d)}$	$4.31^{+0.57}_{-1.05}$	$9.28^{+0.42}_{-0.55}$	$9.09^{+0.72}_{-0.36}$	$8.5^{+1.05}_{-1.04}$	$10.12^{+1.37}_{-1.39}$
$C_{\text{F}_p}^{(e)}$	$0.63^{+0.09}_{-0.06}$	$0.754^{+0.01}_{-0.005}$	$0.67^{+0.01}_{-0.01}$	$0.6^{+0.02}_{-0.02}$	$0.48^{+0.03}_{-0.03}$
$F_{\text{ab}}^{(b)}$	4.3	2.6	4.4	5.8	6.7
$F_{\text{unab}}^{(b)}$	4.9	3.4	5.8	6.8	7.8
$\chi^2_{\text{res}} / \text{dof}$	1.1 / 354	0.888 / 354	1.04 / 355	0.913 / 353	0.828 / 353

<sup>(a)</sup>[keV]

<sup>(b)</sup>The values of absorbed and unabsorbed fluxes in 2 – 120 keV energy range in units  $10^{-9}\text{erg} / \text{cm}^2/\text{s}$ .

<sup>(c)</sup>[ $10^{-3} \text{ph cm}^{-2} \text{s}^{-1}$ ]

<sup>(d)</sup>This parameter was fixed.

Table 9.5: Part 1. The best-fit parameters for pulse phase resolved spectral analysis of Vela X-1 using the *Highecut* continuum model (observation 1996-12-24). The absorption column has been fixed to the average value  $N_{\text{H}} = 3.15^{+0.03}_{-0.04} \text{atoms cm}^{-2}$ .

Parameter	0.5 - 0.6	0.6 - 0.7	0.7 - 0.8	0.8 - 0.9	0.9 - 1
$E_{1\text{cyc}}^{(a)}$	24.09 <sup>+0.98</sup> <sub>-0.63</sub>	22.45 <sup>+0.74</sup> <sub>-0.7</sub>	25.0 <sup>(d)</sup>	25.77 <sup>+3.26</sup> <sub>-1.69</sub>	29.17 <sup>+1.43</sup> <sub>-1.6</sub>
$\sigma_{1\text{cyc}}^{(a)}$	3.1 <sup>+0.6</sup> <sub>-0.5</sub>	4.0 <sup>(d)</sup>	5.0 <sup>(d)</sup>	5.77 <sup>+2.62</sup> <sub>-1.8</sub>	3.79 <sup>+1.39</sup> <sub>-0.86</sub>
$\delta_{1\text{cyc}}$	0.18 <sup>+0.03</sup> <sub>-0.03</sub>	0.33 <sup>+0.05</sup> <sub>-0.05</sub>	0.46 <sup>+0.04</sup> <sub>-0.04</sub>	0.19 <sup>+0.48</sup> <sub>-0.07</sub>	0.17 <sup>+0.02</sup> <sub>-0.05</sub>
$E_{2\text{cyc}}^{(b)}$	56.83 <sup>+1.66</sup> <sub>-1.47</sub>	50.0 <sup>(d)</sup>	55.0 <sup>(d)</sup>	51.95 <sup>+2.73</sup> <sub>-1.94</sub>	60.6 <sup>+3.06</sup> <sub>-2.57</sub>
$\sigma_{2\text{cyc}}^{(b)}$	5.67 <sup>+2.02</sup> <sub>-1.41</sub>	7.0 <sup>(d)</sup>	7.0 <sup>(d)</sup>	6.0 <sup>+5.24</sup> <sub>-2.38</sub>	11.98 <sup>+2.53</sup> <sub>-2.83</sub>
$\delta_{2\text{cyc}}$	1.03 <sup>+0.26</sup> <sub>-0.22</sub>	0.48 <sup>+0.21</sup> <sub>-0.24</sub>	0.23 <sup>+0.21</sup> <sub>-0.2</sub>	0.5 <sup>+0.17</sup> <sub>-0.15</sub>	0.98 <sup>+0.32</sup> <sub>-0.3</sub>
$E_{\text{Fe}}^{(b)}$	6.44 <sup>+0.08</sup> <sub>-0.07</sub>	6.53 <sup>+0.08</sup> <sub>-0.07</sub>	6.49 <sup>+0.06</sup> <sub>-0.05</sub>	6.53 <sup>+0.07</sup> <sub>-0.07</sub>	6.52 <sup>+0.07</sup> <sub>-0.07</sub>
$\sigma_{\text{Fe}}^{(b)}$	1e-25(1)	0.1 <sup>(d)</sup>	0.1 <sup>(d)</sup>	0.1 <sup>(d)</sup>	0.1 <sup>(d)</sup>
$A_{\text{Fe}}^{(c)}$	1.5 <sup>+0.6</sup> <sub>-0.3</sub>	1.9 <sup>+0.4</sup> <sub>-0.4</sub>	1.8 <sup>+0.3</sup> <sub>-0.4</sub>	1.7 <sup>+0.4</sup> <sub>-0.4</sub>	1.8 <sup>+0.4</sup> <sub>-0.4</sub>
$\Gamma$	1.55 <sup>+0.05</sup> <sub>-0.03</sub>	1.7 <sup>+0.04</sup> <sub>-0.04</sub>	1.36 <sup>+0.04</sup> <sub>-0.04</sub>	1.06 <sup>+0.05</sup> <sub>-0.06</sub>	0.89 <sup>+0.04</sup> <sub>-0.03</sub>
$E_{\text{cut}}^{(a)}$	32.7 <sup>+3.65</sup> <sub>-1.33</sub>	30.49 <sup>+0.99</sup> <sub>-0.89</sub>	24.7 <sup>+0.34</sup> <sub>-0.45</sub>	23.95 <sup>+2.69</sup> <sub>-1.0</sub>	22.97 <sup>+0.88</sup> <sub>-1.03</sub>
$E_{\text{fold}}^{(a)}$	15.05 <sup>+1.35</sup> <sub>-1.62</sub>	14.01 <sup>+1.46</sup> <sub>-1.44</sub>	11.54 <sup>+0.84</sup> <sub>-0.74</sub>	12.2 <sup>+0.85</sup> <sub>-0.75</sub>	12.96 <sup>+1.26</sup> <sub>-1.16</sub>
$N_{\text{H}_p}^{(d)}$	7.8 <sup>+0.9</sup> <sub>-0.8</sub>	10.23 <sup>+0.81</sup> <sub>-0.82</sub>	12.8 <sup>+1.06</sup> <sub>-1.04</sub>	8.97 <sup>+1.27</sup> <sub>-1.23</sub>	6.4 <sup>+1.6</sup> <sub>-1.4</sub>
$C_{\text{F}_p}^{(e)}$	0.67 <sup>+0.02</sup> <sub>-0.02</sub>	0.76 <sup>+0.01</sup> <sub>-0.01</sub>	0.65 <sup>+0.02</sup> <sub>-0.02</sub>	0.6 <sup>+0.03</sup> <sub>-0.03</sub>	0.48 <sup>+0.04</sup> <sub>-0.04</sub>
$F_{\text{ab}}^{(b)}$	4.8	3.2	3.8	5.1	5.6
$F_{\text{unab}}^{(b)}$	5.9	4.4	4.8	5.9	6.1
$\chi_{\text{res}}^2 / \text{dof}$	1.101 / 353	1.087 / 357	1.257 / 358	0.899 / 354	1.035 / 354

<sup>(a)</sup>[keV]

<sup>(b)</sup>The values of absorbed and unabsorbed fluxes in 2 – 120 keV energy range in units  $10^{-9} \text{erg} / \text{cm}^2 / \text{s}$ .

<sup>(c)</sup>[ $10^{-3} \text{ph cm}^{-2} \text{s}^{-1}$ ]

<sup>(d)</sup>This parameter was fixed.

Table 9.6: Part 2. The best-fit parameters for pulse phase resolved spectral analysis of Vela X-1 using the Highcut continuum model (observation 1996-12-24). The absorption column has been fixed to the average value  $N_{\text{H}} = 3.15_{-0.04}^{+0.03} \text{atoms cm}^{-2}$ .

---

## Centaurus X–3

### 10.1 Source Description

Cen X–3 was the first discovered in 1967 (Chodil et al. 1967) and several years later recognised as a pulsar based on *Uhuru* observations (Giacconi et al. 1971; Schreier et al. 1972). In fact, it was the first X-ray binary pulsar ever discovered observationally. Cen X–3 is also among the brightest accreting X-ray sources with known orbital parameters. The spin period of the NS is 4.8 s, the orbital period is 2.1 days (see ephemeris by Raichur & Paul 2010; Falanga et al. 2015). The system is eclipsing, which, combined with X-ray timing, allowed to determine the NS mass at  $1.34^{+0.16}_{-0.14} M_{\odot}$  (van der Meer et al. 2007). The optical companion star was identified as the O 6–8 III supergiant V779 Cen (Krzeminski 1974) with a mass of  $M = 20.5 \pm 0.7 M_{\odot}$  (Hutchings et al. 1979; Ash et al. 1999). The distance to the source is uncertain. Krzeminski (1974), assuming a B0 II companion, obtained a distance estimate of  $\sim 8$  kpc. Day & Tennant (1991), using dust-scattering measurements, estimated a distance of  $5.4 \pm 0.3$  kpc. This difference of  $\sim 2.5$  kpc leads to a factor of about two on the uncertainty for estimates of the X-ray luminosity.

Accretion in the system proceeds via an accretion disc (Takeshima et al. 1991; Bildsten et al. 1997) fed through the X-ray excited stellar wind (Day & Stevens 1993). The system exhibits two so-called “high” and “low” intensity states with luminosities of about  $(5 - 10) \times 10^{37}$  erg s $^{-1}$  and  $(1 - 5) \times 10^{36}$  erg s $^{-1}$ , respectively. These states last from a few to  $\sim 110$  days without any apparent periodicity (Paul et al. 2005). The origin of this behaviour is still debated.

A cyclotron line and fluorescent iron emission line (at  $6.5 \pm 0.1$  keV) in the X-ray spectrum of the source were first reported based on *Ginga* data (Nagase et al. 1992). The cyclotron line at  $\sim 28$  keV was later also confirmed with *BeppoSAX* observations (Santangelo et al. 1998). The magnetic field of the NS is thus estimated at  $B \sim (2.4 - 3.0) \times 10^{12}$  G. Observations with *ASCA* revealed that the earlier reported iron line at 6.5 keV is actually a complex of lines at 6.4 keV, 6.7 keV and 6.97 keV (Ebisawa et al. 1996).

Start time	MJD <sub>start</sub>	P <sup>(a)</sup> , s	Orb. state	Exposure <sub>MECS</sub> , ks
12.08.1996 <sup>(b)</sup>	50307	4.823(1)	low	24
27.02.1997 <sup>(c)</sup>	50506	4.814(1)	eclipse+high	33
24.06.1999 <sup>(d)</sup>	51353	4.923(1)	high+eclipse	29
06.06.2000 <sup>(e)</sup>	51701	5.007(1)	low+eclipse	43

<sup>(a)</sup>with the ephemeris from Falanga et al. (2015)

<sup>(b)</sup>del Sordo et al. (2000); Farinelli et al. (2016)

<sup>(c)</sup>Santangelo et al. (1998); Burderi et al. (2000); del Sordo et al. (2000); Devasia et al. (2010), MECS data; Farinelli et al. (2016)

<sup>(d)</sup>These data were not published before.

<sup>(e)</sup>Devasia et al. (2010), MECS data.

Table 10.1: *BeppoSAX* observations of Cen X–3.

## 10.2 Observations

Cen X–3 was observed by *BeppoSAX* four times (Tab. 10.1). Observations covered all typical accretion states observed in the system as illustrated by the background extracted light curves with a bin time of 128 s at Figure 10.1. The first observation of Cen X–3 by *BeppoSAX* was performed on the 12th of August, 1996 in the low state. Another low state observation was made on the 6th of June, 2000 although the pulsar was eclipsed for a large part of this observation. During the other two observations the source was in the high state, also undergoing an eclipse. We excluded eclipses from the analysis of all observations.

From the *BeppoSAX* data, using the orbital ephemeris by Falanga et al. (2015), we determined the pulse periods of Cen X–3 for all observations as listed in Table 10.1.

The broadband X-ray spectrum of Cen X–3 is typical for accreting pulsars and can be approximated with an absorbed power-law with a high energy cut-off. As already mentioned, it exhibits also a fluorescent iron line complex and a cyclotron line at  $\sim 30$  keV. The iron line complex in Cen X–3 is also detected during the eclipse, i.e. the lines likely originate from stellar wind ionised by X-rays from the pulsar (Naik et al. 2011).

### 10.2.1 High Energy States

#### 10.2.1.1 Timing Analysis

Using the high resolution *BeppoSAX* light curves of Cen X–3 and the ephemerides from Falanga et al. (2015), we determined the pulse periods for all observations with a high accuracy using the phase-connection technique (Tab. 10.1).

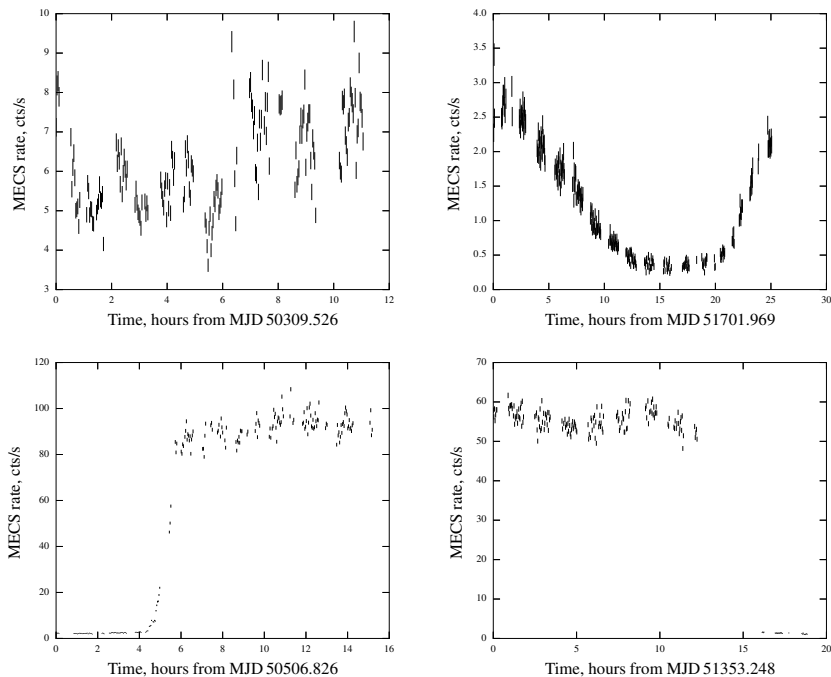


Figure 10.1: On the top panels are the Cen X-3 light curves during the low states using the MECS data. The left panel shows the light curve on 1996-08-12, the right panel illustrates an X-ray eclipse during the low state on 2000-06-06. On the bottom panels are the Cen X-3 light curves during the high states using the MECS data. The two panels correspond to observations performed on 1997-02-27 (left) and 1999-06-24 (right). Both light curves also illustrate the X-ray eclipse. The time binning is 128 s in all cases.

We made a detailed timing and spectral analysis of Cen X-3 during the high states (excluding the eclipse data). Using the measured period value we obtained the pulse profiles in several energy ranges presented in Figures 10.2, 10.3. The energy bands are 0.1 – 2, 2 – 4 keV for the LECS, 4 – 7, 7 – 10 keV for the MECS, 10 – 15 keV for the HPGSPC (for the observation in 1997-02-27) and 15 – 20, 20 – 40, 40 – 60 keV for the PDS data. The pulse profile is double-peaked at low energies (from 0.1 to ~ 10 keV). At high energies a single broad peak is observed (see also Nagase et al. 1992).

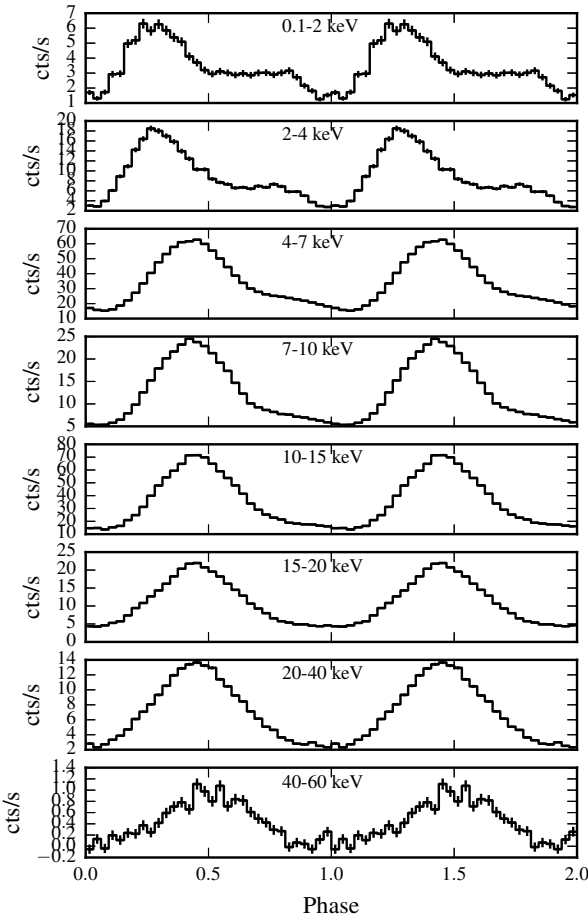


Figure 10.2: The pulse profiles of the X-ray pulsar Cen X-3 from the 1997-02-27 observation as a function of energy using the LECS (0.1 – 2, 2 – 4 keV), MECS (4 – 7, 7 – 10 keV), HP (10 – 15 keV) and PDS (15 – 20, 20 – 40, 40 – 60 keV) data.

From the pulse profiles we calculated the fraction of pulsed flux as function of energy as shown in Figure 10.4. The energy dependence of the pulse fraction is similar in both high state observations. It decreases from 0.1 to  $\sim 2$  keV and then increases with energy. Features near the iron line and the cyclotron lines at  $\sim 30$  keV can also be identified.

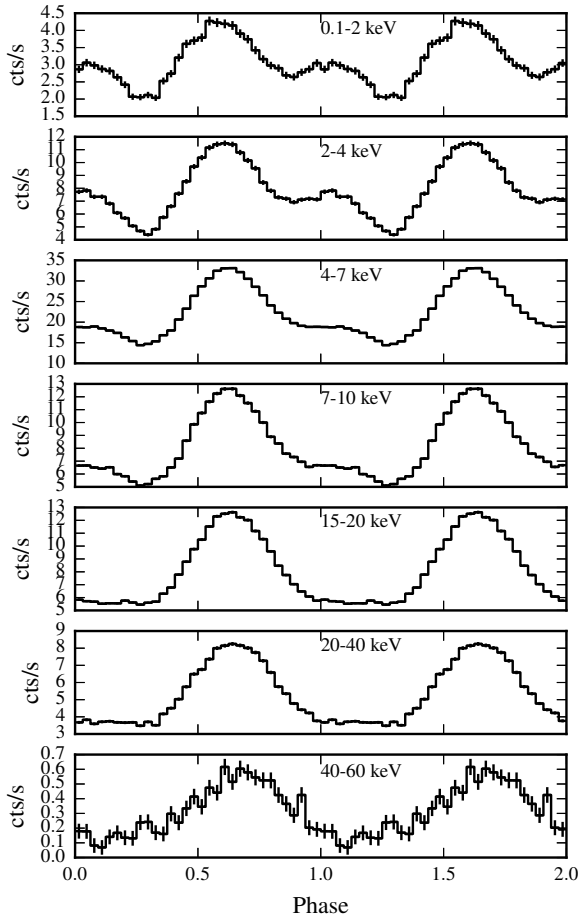


Figure 10.3: The pulse profiles of the X-ray pulsar Cen X-3 from the 1999-06-24 observations as a function of energy using the LECS (0.1 – 2, 2 – 4 keV), MECS (4 – 7, 7 – 10 keV) and PDS (15 – 20, 20 – 40, 40 – 60 keV) data.



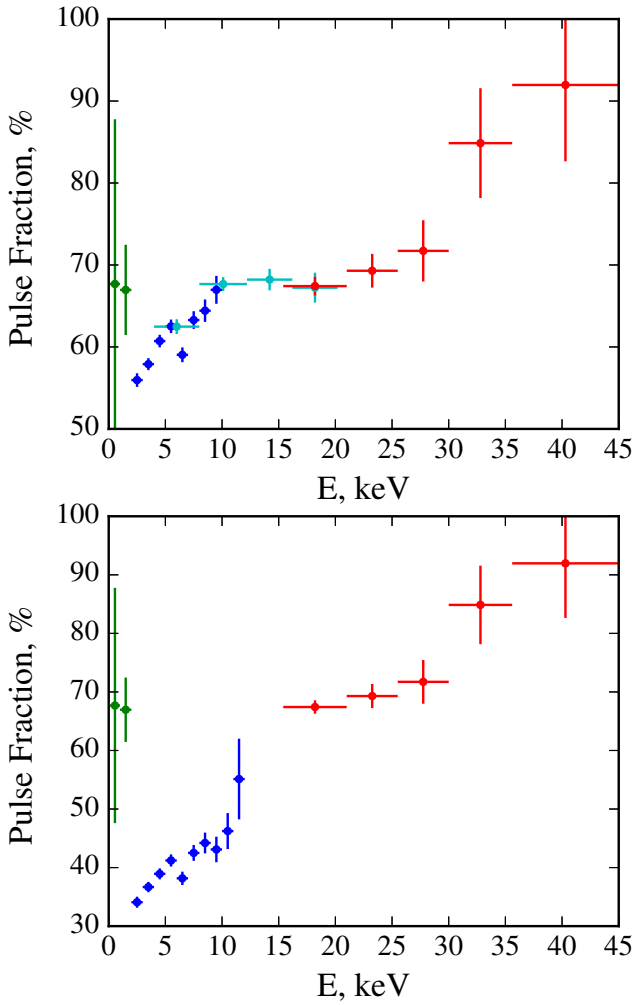


Figure 10.4: Cen X-3 pulse fractions in high states: 1997-02-27 (top) and 1999-06-24 (bottom).

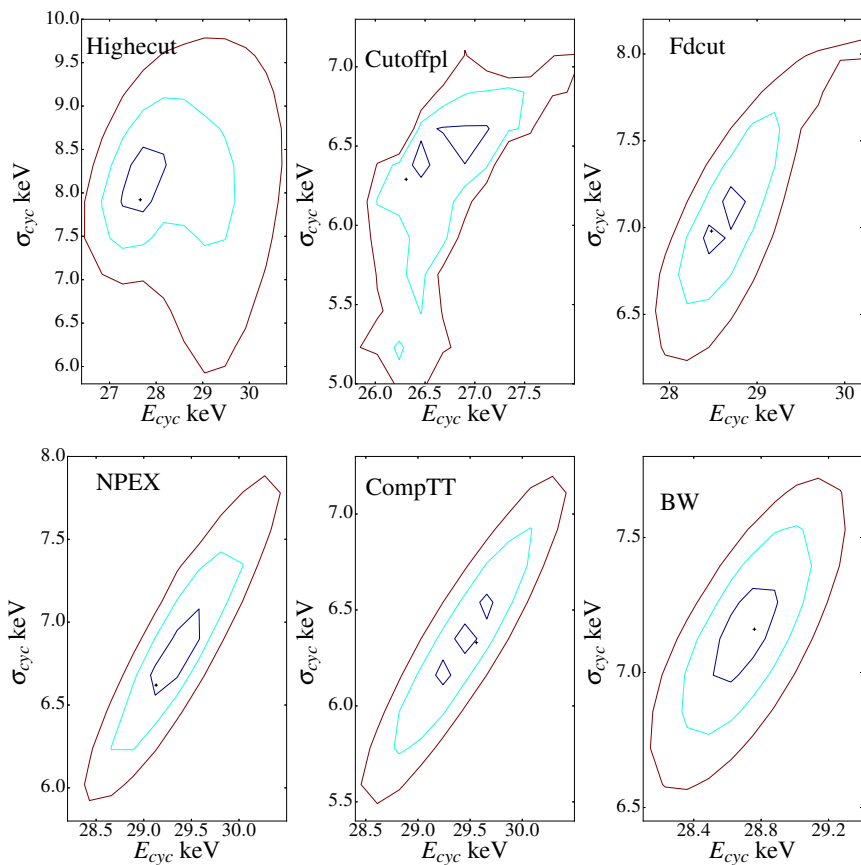


Figure 10.5:  $E_{cyc} - \sigma_{cyc}$  contours for the different continuum models used for Cen X-3. High state, 1997-02-27.

### 10.2.1.2 Spectral Analysis

Spectral analysis was performed for out of eclipse data of the high state observations 1997-02-27 and 1999-06-24 in a broad energy range of 0.1 – 110 keV.

For the first observation we tested six different spectral continuum models used in our work, and an acceptable fit could be achieved for all models. However, the Cutoffpl model needs a bump (a broad gaussian line) at  $\sim 9$  keV with a width of  $\sim 8$  keV. The best-fit parameters for all models are presented in Table 10.2.

To understand which continuum model provides better constraints for the CRSF parameters we plotted the contours of the cyclotron line energy and the width for all these models (for the first observation 1997-02-27, see Fig. 10.5). Taking into account the best-fit statistics, the shape of the contours for the CRSF parameters, and the fact that the *Highcut* model works better for the majority of the sources in our sample, we selected this model for the remaining analysis.

The best-fit results with the *Highcut* model for the observation in high state on 1999-06-24 are presented in Table 10.2.

Note that a black body, to model the soft excess, and two Gaussian to fit an iron emission lines were also included in the fit. The observed spectrum of Cen X-3 in high state in 1997-02-27 with a *Highcut* model, and residuals are shown in Figure 10.6.

The *BeppoSAX* results are thus generally consistent with earlier reports. The prominent soft excess (in the region 0.1 – 1 keV) first reported by Burderi et al. (2000) implies a radius  $R_{\text{bb}} \sim 3 \times 10^8$  cm if modelled with a blackbody. This result is consistent with findings by Burderi et al. (2000) and is comparable with the Alfvén radius (Eq. 5.2). Similar excesses were reported for several sources in the literature including Her X-1 (see the Chapter 5). It can also be fitted by a black body model with approximately the same temperature of about 0.1 keV. The energy range from 1 to 110 keV is characterised by a power law continuum with a cutoff at high energies. This is a typical spectrum for the X-ray pulsars. Cen X-3 also exhibits an absorption feature interpreted as a cyclotron line, at the energy  $E_{\text{cyc}} \sim 30$  keV. Two iron lines were also observed at  $\sim 6.4$  keV and  $\sim 6.8$  keV.

The pulse-phase resolved spectral analysis was also carried out for the high state observation on 1997-02-27 (Fig. 10.7). The absorbed power law model with a cutoff at high energies (*Highcut*) was used to model the spectra. The absorption column  $N_{\text{H}}$  and the black body parameters were fixed at the average values for all phase bins.

We used five phase bins (0 – 0.2, 0.2 – 0.4, 0.4 – 0.6, 0.6 – 0.8, 0.8 – 1). The best-fit results are presented in Table 10.3 and Figure 10.7. The cutoff and folding energies, as well as the cyclotron line parameters do not exhibit significant variability with the pulse phase (see Tab. 10.3). On the other hand, the photon index  $\Gamma$  and  $A_{\text{Fe}2}$  seem to be anti-correlated with the flux and the energies of both iron lines and  $A_{\text{Fe}1}$  seem to be correlated with the flux.

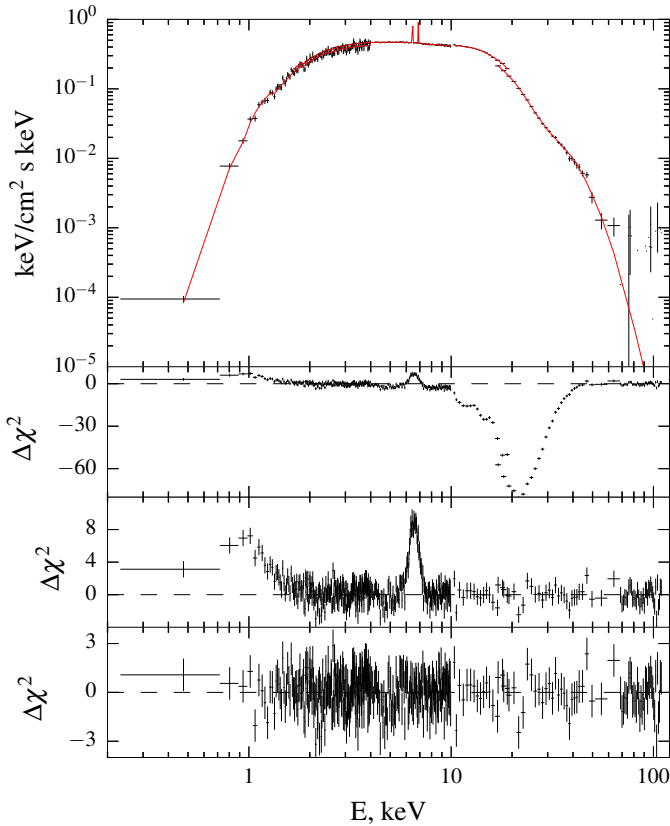


Figure 10.6: The top panel shows the broadband 0.1 – 110 keV unfolded spectrum of Cen X-3 during the observation 1997-02-27 modeled with a power law, a high energy cutoff (Highecut), a black body soft excess, and two narrow iron emission lines. The absorption gaussian line at  $\sim 28$  keV was also included to account for the CRSF. The other panels show the fit residuals for: 1) Cyclotron, Fe-lines and the black-body component residuals. 2) Fe-lines and black-body residuals. 3) The best fit residuals.

Parameter	1997-02-27						1999-06-24
	Highecut	Cutoffpl	Fdcut	NPEX	CompTT	BW	Highecut
$N_{\text{H}}^{(a)}$	1.88 <sup>+0.04</sup> <sub>-0.07</sub>	1.81 <sup>+0.02</sup> <sub>-0.02</sub>	1.80 <sup>+0.06</sup> <sub>-0.03</sub>	1.65 <sup>+0.1</sup> <sub>-0.06</sub>	2.17 <sup>+0.01</sup> <sub>-0.06</sub>	0.87 <sup>+0.14</sup> <sub>-0.12</sub>	1.74 <sup>+0.03</sup> <sub>-0.04</sub>
$E_{\text{FeI}}^{(b)}$	6.44 <sup>+0.06</sup> <sub>-0.06</sub>	6.42 <sup>+0.06</sup> <sub>-0.04</sub>	6.44 <sup>+0.05</sup> <sub>-0.06</sub>	6.42 <sup>+0.06</sup> <sub>-0.06</sub>	6.43 <sup>+0.05</sup> <sub>-0.05</sub>	6.43 <sup>+0.04</sup> <sub>-0.04</sub>	6.52 <sup>+0.08</sup> <sub>-0.1</sub>
$A_{\text{FeI}}^{(c)}$	3.6 <sup>+0.7</sup> <sub>-0.7</sub>	3.7 <sup>+0.6</sup> <sub>-0.7</sub>	3.4 <sup>+0.6</sup> <sub>-0.6</sub>	3.6 <sup>+0.7</sup> <sub>-0.6</sub>	3.4 <sup>+0.6</sup> <sub>-0.6</sub>	3.3 <sup>+0.3</sup> <sub>-0.3</sub>	3.7 <sup>+0.9</sup> <sub>-1.6</sub>
$E_{\text{Fe2}}^{(b)}$	6.87 <sup>+0.08</sup> <sub>-0.07</sub>	6.86 <sup>+0.04</sup> <sub>-0.05</sub>	6.86 <sup>+0.08</sup> <sub>-0.05</sub>	6.86 <sup>+0.07</sup> <sub>-0.06</sub>	6.85 <sup>+0.03</sup> <sub>-0.06</sub>	6.85 <sup>+0.03</sup> <sub>-0.02</sub>	6.9 <sup>+0.15</sup> <sub>-0.14</sub>
$A_{\text{Fe2}}^{(c)}$	3.2 <sup>+0.7</sup> <sub>-0.8</sub>	3.2 <sup>+0.6</sup> <sub>-0.7</sub>	3.0 <sup>+0.6</sup> <sub>-0.7</sub>	3.2 <sup>+0.7</sup> <sub>-0.7</sub>	2.9 <sup>+0.6</sup> <sub>-0.6</sub>	2.8 <sup>+0.3</sup> <sub>-0.2</sub>	2.2 <sup>+1.3</sup> <sub>-1.2</sub>
$E_{\text{cyc}}^{(d)}$	27.66 <sup>+0.73</sup> <sub>-0.65</sub>	26.31 <sup>+0.27</sup> <sub>-0.14</sub>	28.48 <sup>+0.73</sup> <sub>-0.34</sub>	29.13 <sup>+0.75</sup> <sub>-0.38</sub>	29.56 <sup>+0.38</sup> <sub>-0.71</sub>	28.76 <sup>+0.34</sup> <sub>-0.34</sub>	29.08 <sup>+0.75</sup> <sub>-0.67</sub>
$\sigma_{\text{cyc}}^{(d)}$	7.92 <sup>+0.99</sup> <sub>-0.43</sub>	6.29 <sup>+0.22</sup> <sub>-0.09</sub>	6.98 <sup>+0.73</sup> <sub>-0.34</sub>	6.62 <sup>+0.78</sup> <sub>-0.26</sub>	6.33 <sup>+0.44</sup> <sub>-0.53</sub>	7.16 <sup>+0.31</sup> <sub>-0.29</sub>	6.16 <sup>+1.08</sup> <sub>-0.68</sub>
$\delta_{\text{cyc}}^{(d)}$	0.77 <sup>+0.11</sup> <sub>-0.08</sub>	0.71 <sup>+0.23</sup> <sub>-0.02</sub>	1.13 <sup>+0.25</sup> <sub>-0.13</sub>	0.88 <sup>+0.09</sup> <sub>-0.06</sub>	0.84 <sup>+0.02</sup> <sub>-0.09</sub>		0.36 <sup>+0.05</sup> <sub>-0.04</sub>
$\tau_{\text{cyc}}^{(d)}$						20.6 <sup>+2.6</sup> <sub>-2.2</sub>	
$kT_{\text{bb}}^{(d)}$	0.103 <sup>+0.008</sup> <sub>-0.009</sub>	0.106 <sup>+0.006</sup> <sub>-0.007</sub>	0.099 <sup>+0.011</sup> <sub>-0.007</sub>	0.11 <sup>+0.01</sup> <sub>-0.01</sub>	0.104 <sup>+0.004</sup> <sub>-0.012</sub>	0.14 <sup>+0.02</sup> <sub>-0.03</sub>	0.097 <sup>+0.005</sup> <sub>-0.004</sub>
$R_{\text{bb}}^{(e)}$	2.9 <sup>+1.02</sup> <sub>0.51</sub>	2.2 <sup>+1.3</sup> <sub>0.33</sub>	3.1 <sup>+0.85</sup> <sub>0.48</sub>	1.3 <sup>+0.78</sup> <sub>0.41</sub>	3.3 <sup>+1.79</sup> <sub>0.51</sub>	0.3 <sup>+0.06</sup> <sub>0.05</sub>	3.0 <sup>+0.51</sup> <sub>0.25</sub>
$\Gamma^{(f)}$	1.19 <sup>+0.02</sup> <sub>-0.04</sub>	0.95 <sup>+0.02</sup> <sub>-0.01</sub>	1.15 <sup>+0.03</sup> <sub>-0.02</sub>				1.23 <sup>+0.01</sup> <sub>-0.02</sub>
$E_{\text{cut}}^{(d)}$	17.49 <sup>+0.69</sup> <sub>-1.09</sub>	9.27 <sup>+0.09</sup> <sub>-0.08</sub>	22.99 <sup>+2.6</sup> <sub>-1.66</sub>				13.7 <sup>+1.34</sup> <sub>-3.64</sub>
$E_{\text{fold}}^{(d)}$	7.09 <sup>+0.39</sup> <sub>-0.30</sub>		5.41 <sup>+0.42</sup> <sub>-0.46</sub>				8.21 <sup>+0.15</sup> <sub>-0.18</sub>
$\alpha_1$				0.56 <sup>+0.05</sup> <sub>-0.02</sub>			
$\alpha_2$				-2.0			
$kT^{(d)}$				4.28 <sup>+0.03</sup> <sub>-0.04</sub>	4.50 <sup>+0.03</sup> <sub>-0.09</sub>	2.81 <sup>+0.11</sup> <sub>-0.12</sub>	
$T_{\text{p}}^{(f)}$					0.20 <sup>+0.03</sup> <sub>-0.08</sub>		
$\tau_{\text{p}}^{(g)}$					14.69 <sup>+0.18</sup> <sub>-0.04</sub>		
$\xi$						1.31 <sup>+0.06</sup> <sub>-0.06</sub>	
$\delta$						4.2 <sup>+0.4</sup> <sub>-0.4</sub>	
$B^{(h)}$						3.5	
$M^{(i)}$						3.7	
$r_0^{(j)}$						71 <sup>+4</sup> <sub>-4</sub>	
$D^{(k)}$						8.0	
$E_{\text{bump}}^{(d)}$		9.17 <sup>+0.07</sup> <sub>-1.84</sub>					
$\sigma_{\text{bump}}^{(d)}$		8.34 <sup>+0.6</sup> <sub>-0.07</sub>					
$A_{\text{bump}}^{(c)}$		370.9 <sup>+4.4</sup> <sub>-5.0</sub>					
$\chi_{\text{res}}^2/\text{dof}$	0.805 / 383	0.807 / 382	0.888 / 384	0.850 / 384	0.944 / 384	1.323 / 416	1.126 / 487

<sup>(a)</sup>[10<sup>22</sup>atoms cm<sup>-2</sup>]

<sup>(b)</sup>[keV]. Width of the iron line fixed at  $\sigma = 0.01$  keV

<sup>(c)</sup>[10<sup>-3</sup> ph cm<sup>-2</sup> s<sup>-1</sup>]

<sup>(d)</sup>[keV]

<sup>(e)</sup> $R_{\text{bb}}$  is the radius of the black body in 10<sup>3</sup>km for the distance to the source of  $D = 8.0$  kpc.

<sup>(f)</sup>Plasma temperature, keV.

<sup>(g)</sup>Plasma optical depth.

<sup>(h)</sup>Magnetic field in units 10<sup>12</sup> G.

<sup>(i)</sup>Mass accretion rate in units 10<sup>17</sup> g/s.

<sup>(j)</sup>Column radius, km.

<sup>(k)</sup>Distance to the source, kpc.

Table 10.2: Cen X-3. The best-fit parameters for different continuum models for the high state observations 1997-02-27 and 1999-06-24. The absorbed and unabsorbed fluxes in the range of 0.1 – 120 keV for the first observation are  $F_{\text{ab}} = 9.55 \cdot 10^{-9}$  erg cm<sup>-2</sup>s<sup>-1</sup>,  $F_{\text{unab}} = 2.74 \cdot 10^{-8}$  erg cm<sup>-2</sup>s<sup>-1</sup> respectively. For the second observation:  $F_{\text{ab}} = 1.03 \cdot 10^{-8}$  erg cm<sup>-2</sup>s<sup>-1</sup>,  $F_{\text{unab}} = 4.65 \cdot 10^{-8}$  erg cm<sup>-2</sup>s<sup>-1</sup>.

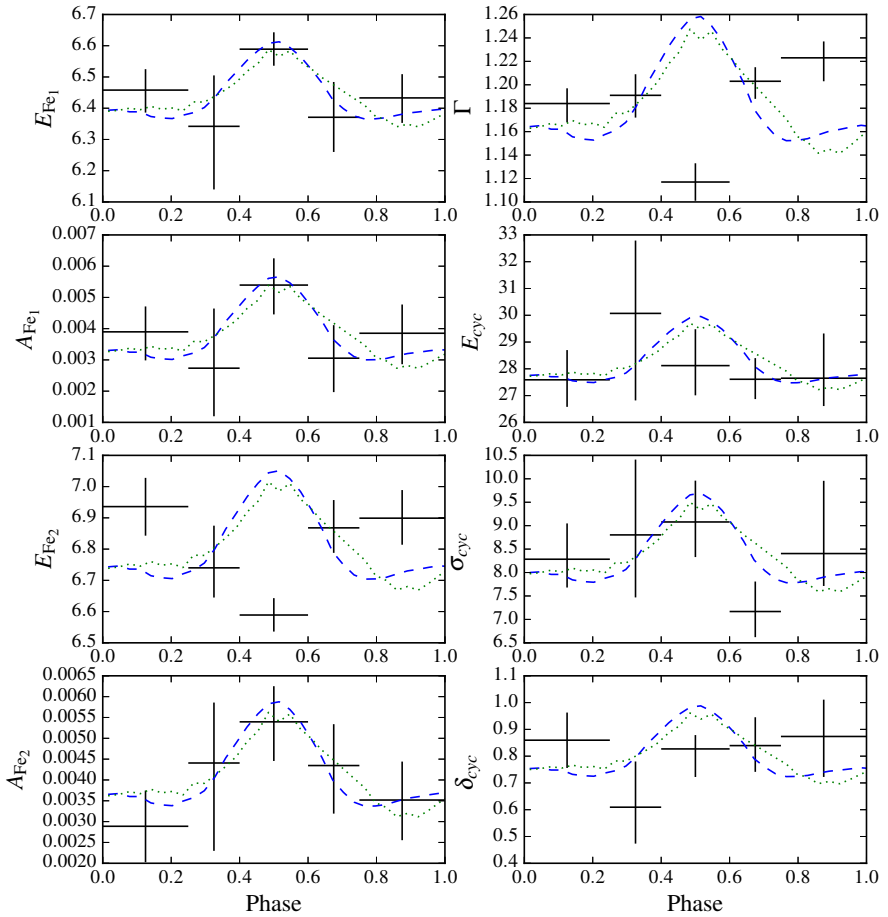


Figure 10.7: Cen X-3. Variation of spectral parameters with the pulse phase (dashed blue line shows the MECS pulse profile for reference, dotted green line shows the PDS) during the observation on 1997-02-27 (high state).

Parameter	0 - 0.2	0.2 - 0.4	0.4 - 0.6	0.6 - 0.8	0.8 - 1
$E_{\text{Fe1}}^{(a)}$	$6.46^{+0.07}_{-0.07}$	$6.34^{+0.16}_{-0.2}$	$6.59^{+0.05}_{-0.05}$	$6.37^{+0.11}_{-0.11}$	$6.43^{+0.08}_{-0.08}$
$A_{\text{Fe1}}^{(b)}$	$3.4^{+0.8}_{-0.9}$	$2.7^{+1.9}_{-1.5}$	$5.4^{+0.9}_{-0.9}$	$3.1^{+1.1}_{-1.1}$	$3.8^{+0.9}_{-1.0}$
$E_{\text{Fe2}}^{(a)}$	$6.94^{+0.09}_{-0.09}$	$6.74^{+0.13}_{-0.09}$	$6.59^{+0.05}_{-0.05}$	$6.87^{+0.09}_{-0.08}$	$6.9^{+0.09}_{-0.08}$
$A_{\text{Fe2}}^{(b)}$	$2.9^{+0.9}_{-0.9}$	$4.4^{+1.4}_{-2.1}$	$5.4^{+0.9}_{-0.9}$	$4.3^{+1.0}_{-1.1}$	$3.5^{+0.9}_{-1.0}$
$E_{\text{cyc}}^{(c)}$	$27.59^{+1.11}_{-1.01}$	$30.07^{+2.72}_{-3.25}$	$28.12^{+1.36}_{-1.11}$	$27.61^{+0.79}_{-0.74}$	$27.65^{+1.67}_{-1.04}$
$\sigma_{\text{cyc}}^{(a)}$	$8.28^{+0.76}_{-0.6}$	$8.8^{+1.61}_{-1.33}$	$9.08^{+0.88}_{-0.75}$	$7.17^{+0.64}_{-0.55}$	$8.4^{+1.55}_{-0.69}$
$\delta_{\text{cyc}}$	$0.9^{+0.1}_{-0.1}$	$0.61^{+0.17}_{-0.14}$	$0.83^{+0.05}_{-0.1}$	$0.84^{+0.11}_{-0.1}$	$0.87^{+0.14}_{-0.15}$
$\Gamma$	$1.18^{+0.01}_{-0.02}$	$1.19^{+0.02}_{-0.02}$	$1.12^{+0.02}_{-0.02}$	$1.2^{+0.01}_{-0.01}$	$1.22^{+0.01}_{-0.02}$
$E_{\text{cut}}^{(c)}$	$18.28^{+0.59}_{-0.67}$	$15.88^{+3.35}_{-0.84}$	$17.1^{+0.54}_{-0.61}$	$17.92^{+0.79}_{-0.72}$	$18.1^{+1.13}_{-1.53}$
$E_{\text{fold}}^{(c)}$	$6.78^{+0.4}_{-0.33}$	$7.81^{+0.69}_{-1.24}$	$6.99^{+0.4}_{-0.34}$	$7.27^{+0.37}_{-0.35}$	$6.98^{+0.67}_{-0.42}$
$F_{\text{ab}}^{(d)}$	0.96	1.07	1.34	1.08	0.92
$F_{\text{unab}}^{(d)}$	3.41	3.53	3.93	3.02	5.17
$\chi^2_{\text{res}} / \text{dof}$	0.915 / 460	0.957 / 413	0.888 / 459	1.042 / 464	0.845 / 546

<sup>(a)</sup>[keV]. Width of the iron line fixed at  $\sigma = 0.005$  keV

<sup>(b)</sup>[ $10^{-3}$  ph cm $^{-2}$  s $^{-1}$ ]

<sup>(c)</sup>[keV]

<sup>(d)</sup>The values of absorbed and unabsorbed fluxes in the 0.1 – 120 keV energy range in units of  $10^{-8}$  erg cm $^{-2}$ s $^{-1}$ .

Table 10.3: Phase resolved spectral parameters of Cen X–3 during the high state observation in 1997-02-27 with the Highcut continuum model. The interstellar absorption and black body parameters have been fixed at the average values.

### 10.2.2 Low Energy States

Cen X-3 was observed by *BeppoSAX* in the low states on 1996 August 12 and 2000 June 6 (Fig. 10.1). For the first observation the period of  $P = 4.823(1)$  s was measured. The pulse profile obtained using the MECS data in the range of 2 – 10 keV is single peaked as shown in Figure 10.8.

Spectral analysis for the low states was performed also using the same model as for the high state. Figure 10.9 shows the best-fit spectrum for the first observation. Note that, similar to previous reports for the low state, additionally we had to include a partial covering fraction absorption component (PC model, see also Naik et al. 2011) in order to achieve an acceptable fit. The soft excess is still present and is approximated with a black-body with a temperature of  $kT_{\text{bb}} \sim 0.1$  keV. The iron lines at  $\sim 6.4$  keV,  $\sim 6.8$  keV and the cyclotron line are also detected. The cyclotron line has a slightly lower energy than during the high state with  $E_{\text{cyc}} \sim 26$  keV assuming the fixed line width of  $\sigma_{\text{cyc}} = 3$  keV (which is not constrained by the fit). The best-fit parameters are presented in Table 10.4.

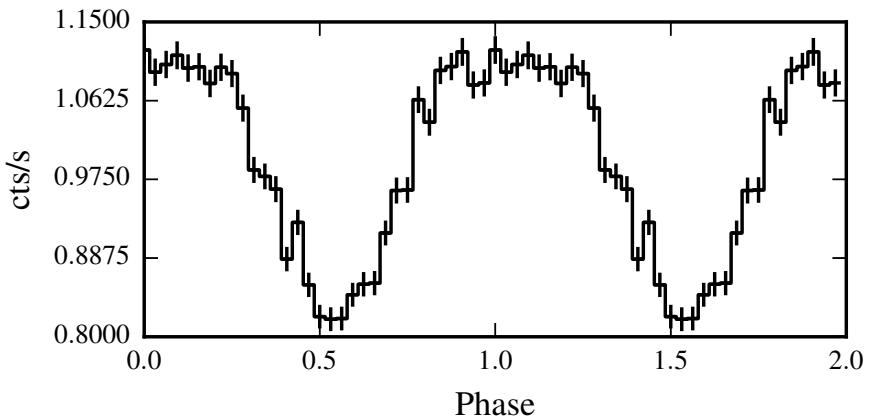


Figure 10.8: Cen X-3. MECS pulse profile in the low state in 1996-08-12 with the period of  $P = 4.823(1)$  s.



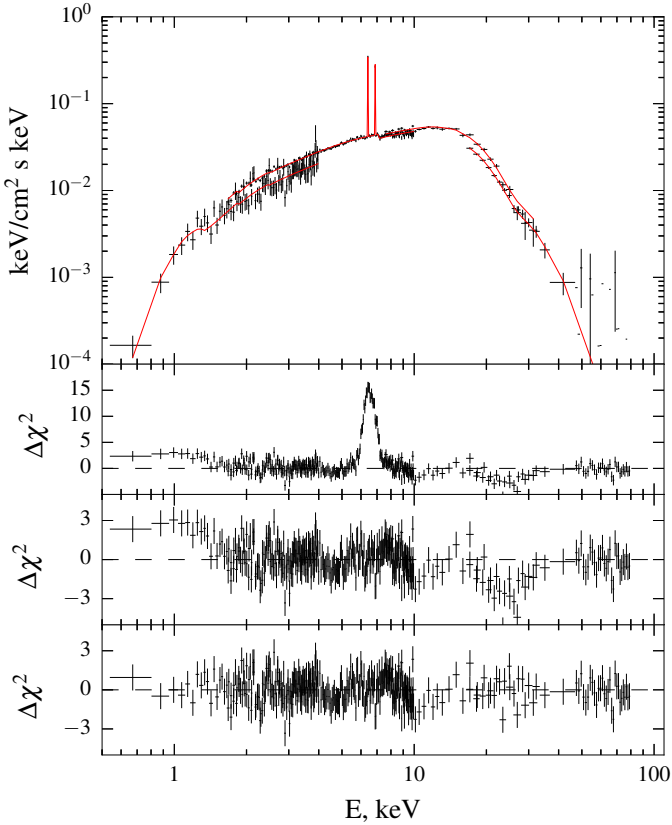


Figure 10.9: Cen X-3, observation 1996-08-12, low state. The top panel shows the broad-band 0.5–100 keV unfolded spectrum modeled with partial covered absorbed cutoff power law (Highecut). The black-body excess, two iron lines and the absorption feature at  $\sim 26$  keV are also included in the fit. The other panels shows residuals associated with 1) The cyclotron, the iron lines, and the soft-excess. 2) The cyclotron line and the soft excess. 3) The best-fit residuals.

Parameter	Highecut+PC	
	1996-08-12	2000-06-06
$N_{\text{H}}, 10^{22} \text{atoms cm}^{-2}$	$1.7^{+0.2}_{-0.2}$	$1.3^{+0.2}_{-0.3}$
$E_{\text{Fe1}}^{(a)}, \text{keV}$	$6.41^{+0.02}_{-0.02}$	$6.52^{+0.04}_{-0.02}$
$A_{\text{Fe1}}, 10^{-3} \text{ph cm}^{-2} \text{s}^{-1}$	$2.2^{+0.1}_{-0.1}$	$0.6^{+0.1}_{-0.1}$
$E_{\text{Fe2}}^{(a)}, \text{keV}$	$6.88^{+0.03}_{-0.03}$	$6.98^{+0.05}_{-0.04}$
$A_{\text{Fe2}}, 10^{-3} \text{ph cm}^{-2} \text{s}^{-1}$	$1.6^{+0.1}_{-0.2}$	$0.5^{+0.1}_{-0.1}$
$E_{\text{cyc}}^{(b)}, \text{keV}$	$26.3^{+1.31}_{-1.5}$	$26.0^{+3.8}_{-2.4}$
$\delta_{\text{cyc}}$	$0.3^{+0.2}_{-0.1}$	$0.04^{+0.01}_{-0.01}$
$kT_{\text{bb}}, \text{keV}$	$0.11^{+0.02}_{-0.02}$	$0.12^{+0.01}_{-0.01}$
$R_{\text{bb}}^{(c)}, \text{km}$	$0.9^{+0.26}_{-0.11}$	$0.4^{+0.1}_{-0.05}$
$\Gamma$	$0.81^{+0.07}_{-0.05}$	$0.84^{+0.06}_{-0.06}$
$E_{\text{cut}}, \text{keV}$	$14.61^{+0.53}_{-0.46}$	$13.7^{+0.8}_{-0.81}$
$E_{\text{fold}}, \text{keV}$	$6.4^{+0.3}_{-0.5}$	$7.02^{+0.78}_{-0.53}$
$N_{\text{Hpc}}, 10^{22} \text{atoms cm}^{-2}$	$18.04^{+3.96}_{-3.38}$	$26.89^{+6.63}_{-7.38}$
$C_{\text{pc}}^d$	$0.41^{+0.04}_{-0.04}$	$0.4^{+0.06}_{-0.1}$
$F_{\text{ab}}^{(d)}, 10^{-9} \text{ergs cm}^{-2} \text{s}^{-1}$	1.35	0.35
$F_{\text{unab}}^{(d)}, 10^{-9} \text{ergs cm}^{-2} \text{s}^{-1}$	2.46	0.52
$\chi^2_{\text{res}} / \text{dof}$	1.055 / 327	1.346 / 226

<sup>(a)</sup>Width of the iron line fixed at  $\sigma = 0.005 \text{ keV}$ .

<sup>(b)</sup>Width of the cyclotron line fixed at  $\sigma = 3 \text{ keV}$ .

<sup>(c)</sup>Radius of the black body in  $10^3 \text{ km}$  for the distance to the source  $D = 8.0 \text{ kpc}$ .

<sup>(d)</sup>Values of absorbed and unabsorbed fluxes in  $0.1 - 120 \text{ keV}$  energy range.

Table 10.4: Parameters of the phase averaged spectrum of Cen X-3 in low states with Highecut+PC continuum model.

### 10.3 Conclusion

The X-ray pulsar Cen X-3 was observed by *BeppoSAX* four times (Tab. 10.1). Two observations cover high state and the other two cover low state. I determined the pulse periods, obtained the pulse profiles and the fraction of pulsed flux as a function of energy for the high state observations. For the first observation in the low state the period and the pulse profile were obtained using the MECS data in the energy range 2 – 10 keV (Fig. 10.8). The spectral analysis was carried out for all observations (Tab. 10.2, 10.4). For the first observation in the high state several continuum models were tested and similarly to other sources, the *Highecut* seems to provide the most consistent results.

The *BeppoSAX* data of Cen X-3 in the high state on 1999-06-24 was analysed for the first time. For this data set the following results were obtained:

- the pulse period,
- the energy resolved pulse profiles were plotted (Fig. 10.3),
- the pulse fraction as function of energy (Fig. 10.4),
- the spectral analysis using the *Highecut* continuum model (Tab. 10.2).

## CHAPTER 11

---

### 4U 0115+63

#### 11.1 Source Description

The bright HMXB pulsar with  $\sim 3.6$  s spin period 4U 0115+63 was discovered with the *Uhuru* X-ray satellite (Giacconi et al. 1972; Forman et al. 1978; Rappaport et al. 1978; Cominsky et al. 1978). The binary has an eccentric orbit of  $e \approx 0.34$  with an orbital period of  $\sim 24.3$  days and  $a_x \sin i \approx 140$  lt s. The mass function is  $f(M) \approx 5M_\odot$  (Rappaport et al. 1978; Tamura et al. 1992; Lutovinov et al. 1994). The donor star is the *Be* star V635 Cas (Hutchings & Crampton 1981) with the B0.2Ve spectral type. The companion is strongly reddened with an apparent magnitude of  $V \approx 15.5$  and the distance to the system is estimated at 7 kpc (Negueruela & Okazaki 2001).

Typically for *Be* systems 4U 0115+63 is an X-ray transient source. It mainly exhibits giant outbursts every 3 – 5 years (Wheaton et al. 1979; Okazaki & Negueruela 2001) with a luminosity of more than  $10^{37}$  erg s $^{-1}$ , although normal outbursts were also detected. The quiescent luminosity is below  $10^{34}$  erg s $^{-1}$  (Campana et al. 2001).

The CRSF was first detected in the spectrum of the pulsar about 30 years ago. The source is famous for being the one with the most (four in addition to the fundamental) cyclotron line harmonics detected (Wheaton et al. 1979; Heindl et al. 1999; Santangelo et al. 1999; Mihara et al. 2004; Lutovinov et al. 2000; Tsygankov et al. 2007; Ferrigno et al. 2009, 2011). The energy of the fundamental one at  $E_{\text{cyc}} \sim 11$  keV has been reported to show some variation with luminosity from  $\sim 11$  keV at  $5 \times 10^{37} - 2 \times 10^{38}$  erg s $^{-1}$  to  $\sim 16$  keV when the luminosity falls below  $\sim 5 \times 10^{37}$  erg s $^{-1}$  (Mihara et al. 1998; Nakajima et al. 2006; Tsygankov et al. 2007). However, Müller et al. (2013) investigated this behaviour systematically and no anti-correlation between the energy of the cyclotron line and the source luminosity could be confirmed. On the other hand, Boldin et al. (2013) attribute this inconsistency to the use of a broad emission feature in some works to model the continuum, so the issue is still not resolved. A possible solution was proposed

by Iyer et al. (2015) based on *Suzaku*, *RXTE*, *Swift* and *INTEGRAL* observations during the 2011 outburst. These authors suggested a possible presence of two independent sets of CRSFs with  $\sim 11$  keV and  $\sim 15$  keV fundamental lines which can change the relative depth with luminosity thus changing the observed energy of the CRSF.

Besides the complex X-ray spectrum, the source also shows drastic variations of the pulse profile with energy and luminosity. Its pulse profile is similar to other transient pulsars, i.e. it is double-peaked at the low energies and turns into single-peaked above  $\sim 20$  keV (Lutovinov & Tsygankov 2009). Furthermore, the shape changes around the cyclotron line and harmonics. This complex behaviour has been investigated in detail by several authors (Lutovinov et al. 2000; Tsygankov et al. 2007; Ferrigno et al. 2011; Sasaki et al. 2012).

## 11.2 Observations

The source was observed by *BeppoSAX* four times during the outburst in 1999. The observation log is presented in Table 11.1. One observation was carried out during the rising part of the outburst while the other three were in the declining phase. Two additional observations were performed after the outburst in 1999 and 2000 (Fig. 11.1).

### 11.2.1 Timing Analysis

Using the high resolution light curves and orbital ephemerides from Li et al. (2012), we determined the pulse periods for four observations during the outburst with high accuracy, using the phase-connection technique. The results are presented in Table 11.1.

Using the obtained periods we extracted the pulse profiles in several energy ranges for all observations. In Figure 11.2 pulse profiles for the observation in 1999-03-22 are presented in 11 energy bands: 0.1 – 2 keV for LECS, 2 – 4, 4 – 6, 6 – 8, 8 – 10 keV for MECS, 10 – 15, 15 – 20 keV for HPGSPC and 20 – 30, 30 – 60, 60 – 90, 90 – 120 keV for PDS. As one can see, the shape of the 4U 0115+63 pulse profile is strongly energy dependent. At high energies the single broad peak is observed, whereas two peaks can be identified at lower energies. The detailed analysis of the 4U 0115+63 pulse profiles in conjunction with the geometry and beam pattern was made by Sasaki et al. (2012).

The pulse fraction as function of energy calculated using the pulse profiles for the first observation in 1999-03-06 is presented in Figure 11.3. The fraction of pulsed emission steadily increases with energy from 15% to 90%. Despite relatively broad energy bands used, the pulse fraction also exhibits some features associated with

Start time	MJD <sub>start</sub>	P, s <sup>(a)</sup>	$L_X^{(b)}$ , $10^{37}$ erg s <sup>-1</sup>	Exp., ks <sup>(c)</sup>
1999-03-06 <sup>(d)</sup>	51243	3.6137(1)	3.5	49
1999-03-19 <sup>(e)</sup>	51256	3.6141(1)	3.65	31
1999-03-22 <sup>(f)</sup>	51259	3.6139(1)	3.32	36
1999-03-26 <sup>(g)</sup>	51263	3.6136(1)	2.37	48
1999-08-03 <sup>(h)</sup>	51393	quiescence		35
2000-08-13 <sup>(i)</sup>	51769	quiescence		85

<sup>(a)</sup>with the ephemeris from Li et al. (2012).

<sup>(b)</sup>luminosity in the 2 – 10 keV energy range for the distance to the source 7 kpc.

<sup>(c)</sup>MECS exposure.

<sup>(d)</sup>Ferrigno et al. (2011)

<sup>(e)</sup>Santangelo et al. (1999); Ferrigno et al. (2011); Farinelli et al. (2016)

<sup>(f)</sup>These data were not published before.

<sup>(g)</sup>Ferrigno et al. (2009, 2011); Farinelli et al. (2016)

<sup>(h)</sup>Campana et al. (2001)

<sup>(i)</sup>Campana et al. (2002)

Table 11.1: *BeppoSAX* observations of 4U 0115+63.

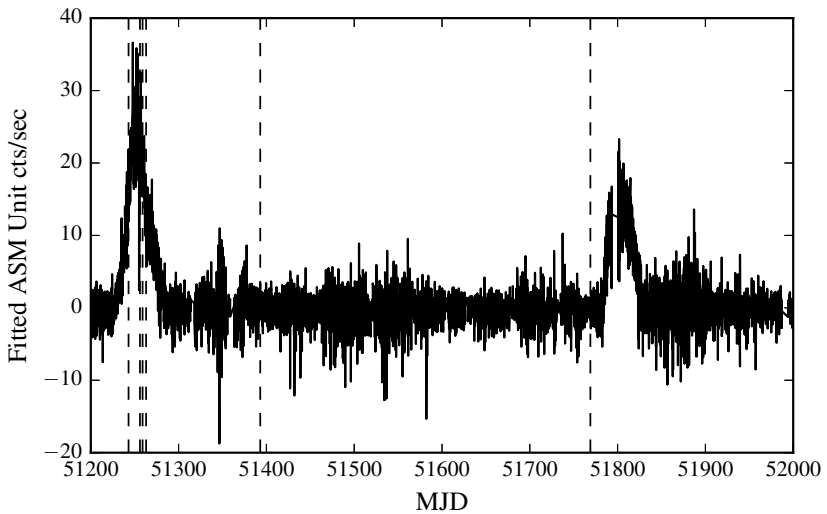


Figure 11.1: 4U 0115+63. ASM light curve. Dashed lines are the *BeppoSAX* observations: 1999-03-06, 1999-03-19, 1999-03-22, 1999-03-26, 1999-08-03, 2000-08-13.

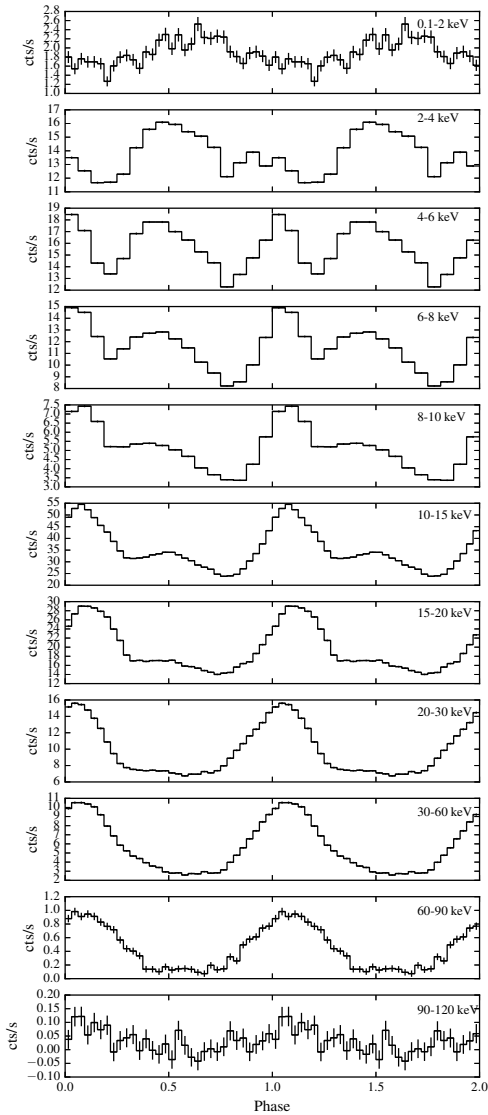


Figure 11.2: The pulse profiles of 4U 0115+63 as observed on 1999-03-22 as a function of energy. LECS (0.1 – 2 keV), MECS (2 – 4, 4 – 6, 6 – 8, 8 – 10 keV), HPGSPC (10 – 15, 15 – 20 keV) and PDS (20 – 30, 30 – 60, 60 – 90, 90 – 120 keV).

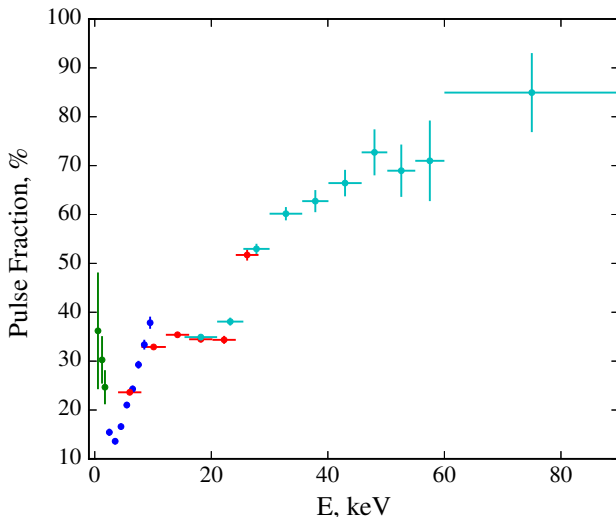


Figure 11.3: 4U 0115+63 pulse fraction in 1999-03-06.

cyclotron line harmonics. Similarly to many other sources in the sample the pulse fraction decreases with energy below  $\sim 3$  keV.

### 11.2.2 Spectral Analysis

We performed the spectral analysis in the energy range 0.1 – 120 keV for all outburst observations. The broadband spectrum can be described as a typical absorbed ( $N_{\text{H}} \sim 10^{22}$  atoms  $\text{cm}^{-2}$ ) cutoff power law continuum with a fluorescent line at  $\sim 6.6$  keV. The signature feature of the spectrum is the five absorption features with energies of  $\sim 13$  keV,  $\sim 23$  keV,  $\sim 34$  keV,  $\sim 45$  keV and  $\sim 55$  keV.

Fit parameters for the first observation in 1999-03-06 for four continuum models are shown in Table 11.2. Acceptable fit can be achieved with `Highcut`, `Fdcut`, `NPEX` and `CompTT`. However, the `Highcut` model fit is slightly better from a statistical point of view. As it is the case also for the other sources in the sample, we use the `Highcut` for further analysis. The best-fit residuals for all spectral models are presented in Figure 11.4.

The best-fit spectrum for the 1999-03-06 observation and the `Highcut` model together with the residuals are shown in Figure 11.5. The top panel shows the phase averaged X-ray spectrum, the second panel shows the residuals due to the iron emission line at  $\sim 6.6$  keV, and in the bottom panel are the best fit residuals.



Parameter	Highecut	Fdcut	NPEX	CompTT
$N_{\text{H}}^{(a)}$	$1.13^{+0.01}_{-0.03}$	$0.99^{+0.01}_{-0.01}$	$1.28^{+0.01}_{-0.01}$	$0.8^{+0.02}_{-0.01}$
$E_{\text{Fe}}^{(b)}$	$6.56^{+0.06}_{-0.05}$	$6.602^{+0.001}_{-0.001}$	$6.58^{+0.06}_{-0.06}$	$6.55^{+0.06}_{-0.06}$
$A_{\text{Fe}}^{(c)}$	$3.4^{+0.4}_{-0.4}$	$2.92^{+0.02}_{-0.01}$	$2.0^{+0.3}_{-0.4}$	$2.1^{+0.4}_{-0.3}$
$E_{\text{cyc1}}^{(d)}$	$13.39^{+0.07}_{-0.04}$	$13.62^{+0.01}_{-0.01}$	$14.56^{+0.01}_{-0.02}$	$13.97^{+0.02}_{-0.02}$
$\sigma_{\text{cyc1}}^{(d)}$	$2.75^{+0.04}_{-0.05}$	$2.58^{+0.01}_{-0.04}$	$3.91^{+0.01}_{-0.02}$	$3.44^{+0.02}_{-0.02}$
$\delta_{\text{cyc1}}^{(e)}$	$0.357^{+0.007}_{-0.007}$	$0.574^{+0.001}_{-0.002}$	$1.143^{+0.002}_{-0.018}$	$0.948^{+0.004}_{-0.015}$
$E_{\text{cyc2}}^{(e)}$	$22.55^{+0.05}_{-0.07}$	$21.8^{+0.01}_{-0.01}$	$23.4^{+0.02}_{-0.02}$	$22.55^{+0.06}_{-0.03}$
$\delta_{\text{cyc2}}^{(e)}$	$0.78^{+0.01}_{-0.01}$	$1.28^{+0.001}_{-0.001}$	$1.86^{+0.01}_{-0.01}$	$1.714^{+0.012}_{-0.005}$
$E_{\text{cyc3}}^{(e)}$	$33.94^{+0.46}_{-0.09}$	$31.15^{+0.01}_{-0.01}$	$33.32^{+0.1}_{-0.02}$	$32.15^{+0.09}_{-0.03}$
$\delta_{\text{cyc3}}^{(e)}$	$0.71^{+0.01}_{-0.01}$	$1.065^{+0.001}_{-0.001}$	$1.85^{+0.01}_{-0.01}$	$1.57^{+0.01}_{-0.01}$
$E_{\text{cyc4}}^{(e)}$	$44.08^{+0.96}_{-0.17}$	$39.9^{+0.01}_{-0.01}$	$43.18^{+0.04}_{-0.05}$	$41.34^{+0.14}_{-0.05}$
$\delta_{\text{cyc4}}^{(e)}$	$0.62^{+0.02}_{-0.02}$	$1.089^{+0.001}_{-0.001}$	$1.64^{+0.01}_{-0.01}$	$1.47^{+0.01}_{-0.02}$
$E_{\text{cyc5}}^{(e)}$	$54.32^{+0.44}_{-0.43}$	$50.81^{+0.01}_{-0.01}$	$53.95^{+0.11}_{-0.11}$	$52.0^{+0.12}_{-0.11}$
$\delta_{\text{cyc5}}^{(e)}$	$0.52^{+0.03}_{-0.03}$	$1.006^{+0.001}_{-0.001}$	$1.29^{+0.03}_{-0.02}$	$1.27^{+0.02}_{-0.03}$
$\Gamma$	$0.442^{+0.002}_{-0.003}$	$0.274^{+0.001}_{-0.001}$		
$E_{\text{cut}}^{(d)}$	$8.62^{+0.03}_{-0.06}$	$14.29^{+1.07}_{-1.07}$		
$E_{\text{fold}}^{(d)}$	$10.38^{+0.02}_{-0.03}$	$8.156^{+0.001}_{-0.001}$		
$\alpha 1$			$0.472^{+0.003}_{-0.016}$	
$\alpha 2$			-2.0	
$kT^{(d)}$			$5.506^{+0.004}_{-0.003}$	$5.56^{+0.01}_{-0.01}$
$T_{\text{p}}^{(f)}$				$0.63^{+0.004}_{-0.003}$
$\tau_{\text{p}}^{(g)}$				$27.07^{+0.05}_{-0.14}$
$\chi^2_{\text{res}}/\text{dof}$	1.2 / 581	1.692 / 582	1.654 / 582	1.575 / 582

<sup>(a)</sup>[ $10^{22}$  atoms  $\text{cm}^{-2}$ ]

<sup>(b)</sup>[keV]. Width of the iron line fixed at  $\sigma_{F_e} = 0.1$  keV

<sup>(c)</sup>[ $10^{-3}$  ph  $\text{cm}^{-2}$   $\text{s}^{-1}$ ]

<sup>(d)</sup>[keV]

<sup>(e)</sup>[keV].  $\sigma_{\text{cyc}2,3,4,5} = 4$  keV

<sup>(f)</sup>Plasma temperature, keV.

<sup>(g)</sup>Plasma optical depth.

Table 11.2: 4U 0115+63. Continuum models for the observation in the 1999-03-06. The absorbed and unabsorbed fluxes in the range 0.1 – 120 keV are  $F_{\text{ab}} = 1.42 \cdot 10^{-8}$  erg  $\text{cm}^{-2}\text{s}^{-1}$ ,  $F_{\text{unab}} = 1.49 \cdot 10^{-8}$  erg  $\text{cm}^{-2}\text{s}^{-1}$  respectively.

The residuals associated with the CRSF and its harmonics are shown in Figure 11.6. 4U 0115+63 is only known source exhibiting the fundamental cyclotron line with four harmonics.

Spectra for all *BeppoSAX* observations during the outburst in 1999 can be described using the same model (Tab. 11.3). The best fit residuals for all observations with the Highecut continuum model are shown at Figure 11.7.

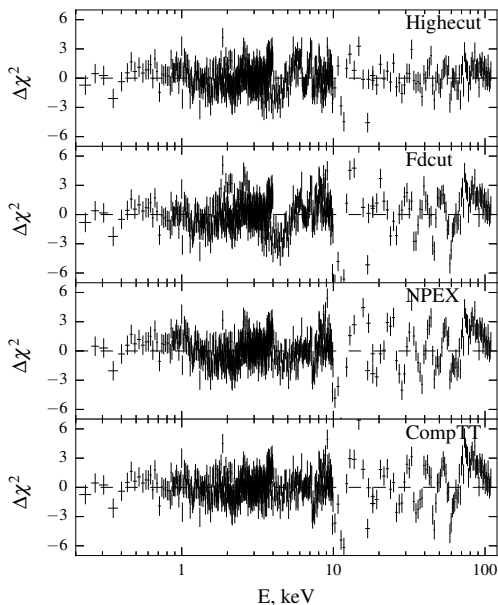


Figure 11.4: 4U 0115+63 spectral residuals for four different continuum models tested for the first *BeppoSAX* observation on 1999-03-06.

Pulse-phase resolved spectral analysis (in 10 equal phase bins) was also carried out for the 1999-03-06 observation (Fig. 11.8). The same continuum model as above was used with the absorption column  $N_{\text{H}}$ , the iron line energy  $E_{\text{Fe}}$  and width  $\sigma_{\text{Fe}}$ , all cyclotron line widths and the cyclotron line harmonics energy  $E_{\text{cyc}5}$  (in the last five phases) fixed to the phase-average values. Fit results are presented in Tables 11.4, 11.5. All parameters exhibit strong variation with phase as shown in Figure 11.8.

### 11.3 Conclusion

I analysed the data from *BeppoSAX* observations of the transient pulsar 4U 0115+63 during the 1999 outburst (Tab. 11.1). For all observations the pulse periods have been determined. Using the obtained periods, the pulse profile evolution with energy has been assessed (Fig. 11.2, 11.3). The phase-averaged analysis was car-

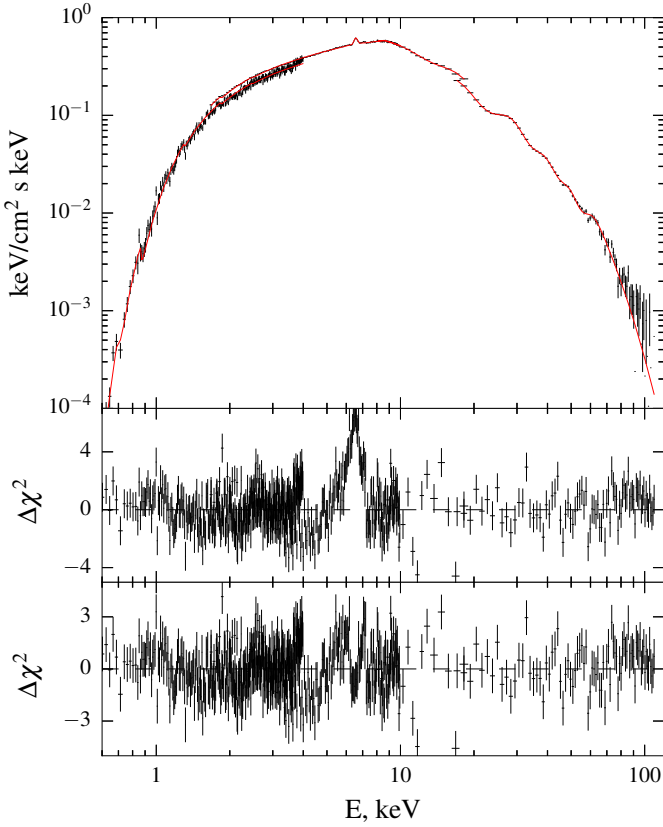


Figure 11.5: The top panel shows the broadband 0.6 – 120 keV unfolded spectrum of 4U 0115+63 modeled as a cutoff power law (Highecut) continuum modified by a Fe-emission line and a cyclotron line with its harmonics for the 1999-03-06 observation. The other panels show the residuals associated with: 1) the iron line, 2) the best-fit residuals ( $\chi_{\text{red}}^2 \approx 1.2$ ).

ried out testing several continuum models including Highecut, which was then used for all observations (Tab. 11.3). The results for the 1999-03-22 observation of 4U 0115+63 were reported for the first time. The phase resolved spectroscopy was also done for the 1999-03-06 observation using the Highecut continuum model (Tab. 11.4, 11.5, Fig. 11.8).

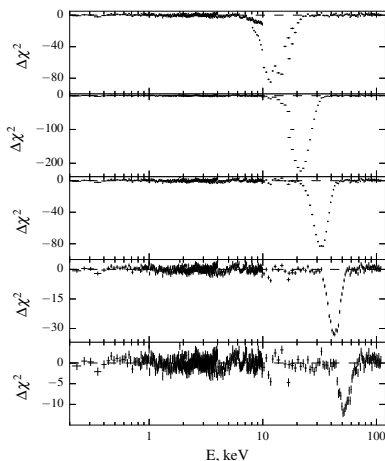


Figure 11.6: 4U 0115+63 residuals associated with the cyclotron line and its harmonics for the 1999-03-06 observation (Highcut continuum model) from top to bottom respectively:  $E_{\text{cyc}1} = 13.39^{+0.07}_{-0.04}$  keV,  $E_{\text{cyc}2} = 22.55^{+0.05}_{-0.07}$  keV,  $E_{\text{cyc}3} = 33.94^{+0.46}_{-0.09}$  keV,  $E_{\text{cyc}4} = 44.08^{+0.96}_{-0.17}$  keV,  $E_{\text{cyc}5} = 54.32^{+0.44}_{-0.43}$  keV.

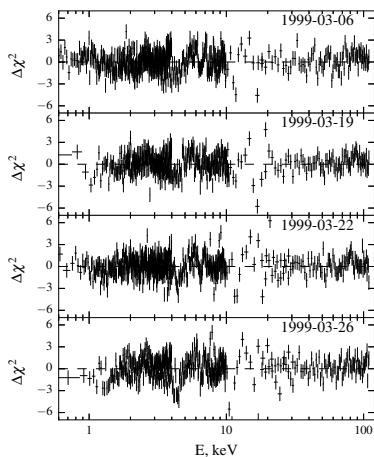


Figure 11.7: 4U 0115+63 spectral residuals for four *BeppoSAX* observations during the 1999 outburst with the Highcut continuum model.

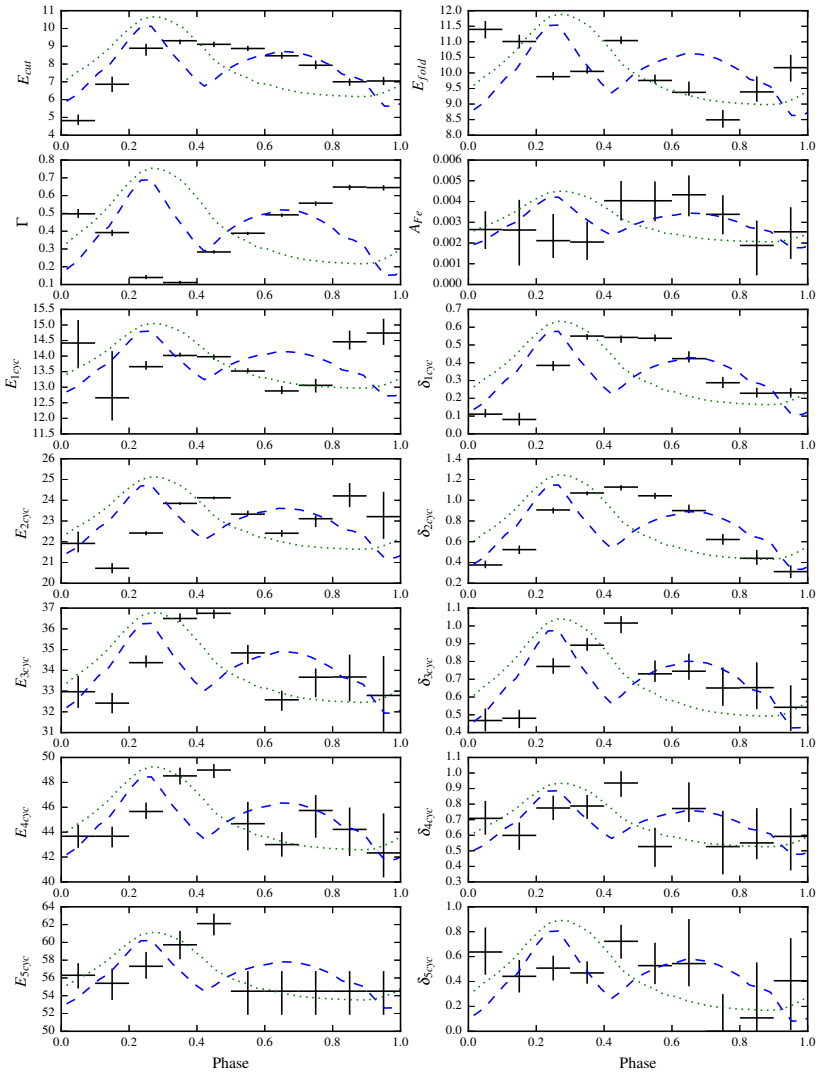


Figure 11.8: 4U 0115+63. Variation of the spectral parameters with phase during the 1999-03-06 observation for the `Highcut` continuum model (dashed blue line is the MECS pulse profile in 2 – 10 keV, dotted green line is the PDS pulse profile in 15 – 120 keV energy ranges).

Parameter	1999-03-06	1999-03-19	1999-03-22	1999-03-26
$N_{\text{H}}^{(a)}$	$1.13^{+0.01}_{-0.03}$	$1.08^{+0.02}_{-0.02}$	$1.03^{+0.02}_{-0.01}$	$0.96^{+0.02}_{-0.01}$
$E_{\text{Fe}}^{(b)}$	$6.56^{+0.06}_{-0.05}$	$6.55^{+0.06}_{-0.05}$	$6.53^{+0.07}_{-0.06}$	$6.62^{+0.07}_{-0.07}$
$A_{\text{Fe}}^{(c)}$	$3.4^{+0.4}_{-0.4}$	$3.4^{+0.5}_{-0.5}$	$3.2^{+0.4}_{-0.4}$	$2.2^{+0.3}_{-0.3}$
$E_{\text{cyc1}}^{(d)}$	$13.39^{+0.07}_{-0.04}$	$12.8^{+0.17}_{-0.07}$	$12.97^{+0.16}_{-0.05}$	$12.88^{+0.08}_{-0.07}$
$\sigma_{\text{cyc1}}^{(d)}$	$2.75^{+0.04}_{-0.05}$	$2.11^{+0.26}_{-0.05}$	$2.48^{+0.06}_{-0.06}$	$2.24^{+0.07}_{-0.04}$
$\delta_{\text{cyc1}}^{(e)}$	$0.357^{+0.007}_{-0.007}$	$0.269^{+0.022}_{-0.007}$	$0.302^{+0.009}_{-0.007}$	$0.282^{+0.008}_{-0.009}$
$E_{\text{cyc2}}^{(e)}$	$22.55^{+0.05}_{-0.07}$	$23.13^{+0.08}_{-0.1}$	$23.12^{+0.06}_{-0.08}$	$22.6^{+0.05}_{-0.07}$
$\delta_{\text{cyc2}}^{(e)}$	$0.78^{+0.01}_{-0.01}$	$0.58^{+0.05}_{-0.01}$	$0.66^{+0.01}_{-0.01}$	$0.71^{+0.01}_{-0.01}$
$E_{\text{cyc3}}^{(e)}$	$33.94^{+0.46}_{-0.09}$	$34.98^{+0.13}_{-0.13}$	$34.97^{+0.12}_{-0.1}$	$34.25^{+0.15}_{-0.09}$
$\delta_{\text{cyc3}}^{(e)}$	$0.71^{+0.01}_{-0.01}$	$0.64^{+0.08}_{-0.01}$	$0.71^{+0.01}_{-0.01}$	$0.67^{+0.01}_{-0.01}$
$E_{\text{cyc4}}^{(e)}$	$44.08^{+0.96}_{-0.17}$	$46.35^{+0.25}_{-0.26}$	$46.32^{+0.25}_{-0.26}$	$44.49^{+0.27}_{-0.32}$
$\delta_{\text{cyc4}}^{(e)}$	$0.62^{+0.02}_{-0.02}$	$0.62^{+0.04}_{-0.03}$	$0.62^{+0.02}_{-0.02}$	$0.52^{+0.02}_{-0.02}$
$E_{\text{cyc5}}^{(e)}$	$54.32^{+0.44}_{-0.43}$	$58.39^{+1.59}_{-1.57}$	$56.94^{+0.98}_{-1.01}$	$55.41^{+0.63}_{-0.68}$
$\delta_{\text{cyc5}}^{(e)}$	$0.52^{+0.03}_{-0.03}$	$0.25^{+0.11}_{-0.05}$	$0.33^{+0.05}_{-0.04}$	$0.44^{+0.05}_{-0.04}$
$\Gamma$	$0.442^{+0.002}_{-0.003}$	$0.453^{+0.005}_{-0.002}$	$0.42^{+0.004}_{-0.003}$	$0.43^{+0.005}_{-0.002}$
$E_{\text{cut}}^{(d)}$	$8.62^{+0.03}_{-0.06}$	$7.77^{+0.03}_{-0.05}$	$8.24^{+0.04}_{-0.05}$	$8.16^{+0.03}_{-0.05}$
$E_{\text{fold}}^{(d)}$	$10.38^{+0.02}_{-0.03}$	$10.35^{+0.21}_{-0.05}$	$10.38^{+0.15}_{-0.02}$	$10.57^{+0.04}_{-0.03}$
$F_{\text{ab}}^{(f)}$	1.42	1.51	1.4	0.99
$F_{\text{unab}}^{(f)}$	1.49	1.58	1.46	1.03
$\chi^2_{\text{res}} / \text{dof}$	1.2 / 581	1.091 / 468	1.151 / 564	1.41 / 419

<sup>(a)</sup>[ $10^{22}$  atoms  $\text{cm}^{-2}$ ]

<sup>(b)</sup>[keV] Width of the iron line fixed at  $\sigma_{Fe} = 0.1$  keV

<sup>(c)</sup>[ $10^{-3}$  ph  $\text{cm}^{-2}$   $\text{s}^{-1}$ ]

<sup>(d)</sup>[keV]

<sup>(e)</sup>[keV],  $\sigma_{\text{cyc}2,3,4,5} = 4$  keV

<sup>(f)</sup>The values of absorbed and unabsorbed fluxes in the 2 – 120 keV energy range in units of  $10^{-8}$  erg /  $\text{cm}^2$  / s.

Table 11.3: Variation of the spectral parameters of 4U 0115+63 with luminosity during the outburst from *BeppoSAX* observations and the *Highecut* continuum model.

Parameter	0 - 0.1	0.1 - 0.2	0.2 - 0.3	0.3 - 0.4	0.4 - 0.5
$E_{1\text{cyc}}^{(a)}$	14.42 <sup>+0.74</sup> <sub>-0.8</sub>	12.66 <sup>+1.5</sup> <sub>-0.73</sub>	13.66 <sup>+0.18</sup> <sub>-0.1</sub>	14.03 <sup>+0.09</sup> <sub>-0.05</sub>	13.98 <sup>+0.07</sup> <sub>-0.1</sub>
$\delta_{1\text{cyc}}$	0.11 <sup>+0.03</sup> <sub>-0.02</sub>	0.08 <sup>+0.04</sup> <sub>-0.03</sub>	0.38 <sup>+0.02</sup> <sub>-0.03</sub>	0.55 <sup>+0.01</sup> <sub>-0.02</sub>	0.54 <sup>+0.01</sup> <sub>-0.03</sub>
$E_{2\text{cyc}}^{(a)}$	21.92 <sup>+0.57</sup> <sub>-0.43</sub>	20.72 <sup>+0.25</sup> <sub>-0.24</sub>	22.42 <sup>+0.09</sup> <sub>-0.11</sub>	23.85 <sup>+0.06</sup> <sub>-0.07</sub>	24.12 <sup>+0.06</sup> <sub>-0.08</sub>
$\delta_{2\text{cyc}}$	0.38 <sup>+0.04</sup> <sub>-0.03</sub>	0.52 <sup>+0.04</sup> <sub>-0.04</sub>	0.91 <sup>+0.02</sup> <sub>-0.03</sub>	1.07 <sup>+0.02</sup> <sub>-0.02</sub>	1.13 <sup>+0.02</sup> <sub>-0.03</sub>
$E_{3\text{cyc}}^{(a)}$	32.97 <sup>+0.77</sup> <sub>-0.78</sub>	32.42 <sup>+0.49</sup> <sub>-0.49</sub>	34.37 <sup>+0.35</sup> <sub>-0.23</sub>	36.51 <sup>+0.27</sup> <sub>-0.21</sub>	36.75 <sup>+0.18</sup> <sub>-0.26</sub>
$\delta_{3\text{cyc}}$	0.47 <sup>+0.07</sup> <sub>-0.06</sub>	0.48 <sup>+0.05</sup> <sub>-0.05</sub>	0.77 <sup>+0.05</sup> <sub>-0.04</sub>	0.89 <sup>+0.04</sup> <sub>-0.04</sub>	1.02 <sup>+0.04</sup> <sub>-0.06</sub>
$E_{4\text{cyc}}^{(a)}$	43.67 <sup>+0.92</sup> <sub>-0.93</sub>	43.67 <sup>+0.77</sup> <sub>-0.89</sub>	45.66 <sup>+0.72</sup> <sub>-0.6</sub>	48.52 <sup>+0.76</sup> <sub>-0.8</sub>	48.99 <sup>+0.48</sup> <sub>-0.64</sub>
$\delta_{4\text{cyc}}$	0.71 <sup>+0.11</sup> <sub>-0.11</sub>	0.6 <sup>+0.08</sup> <sub>-0.09</sub>	0.77 <sup>+0.08</sup> <sub>-0.08</sub>	0.79 <sup>+0.08</sup> <sub>-0.1</sub>	0.94 <sup>+0.08</sup> <sub>-0.09</sub>
$E_{5\text{cyc}}^{(a)}$	56.3 <sup>+1.36</sup> <sub>-1.49</sub>	55.4 <sup>+1.65</sup> <sub>-1.87</sub>	57.31 <sup>+1.62</sup> <sub>-1.39</sub>	59.74 <sup>+1.8</sup> <sub>-1.89</sub>	62.11 <sup>+1.12</sup> <sub>-1.32</sub>
$\delta_{5\text{cyc}}$	0.64 <sup>+0.2</sup> <sub>-0.18</sub>	0.44 <sup>+0.13</sup> <sub>-0.13</sub>	0.51 <sup>+0.1</sup> <sub>-0.1</sub>	0.47 <sup>+0.11</sup> <sub>-0.1</sub>	0.72 <sup>+0.13</sup> <sub>-0.14</sub>
$A_{\text{Fe}}^{(b)}$	2.6 <sup>+0.9</sup> <sub>-0.9</sub>	2.6 <sup>+1.4</sup> <sub>-1.7</sub>	2.1 <sup>+1.3</sup> <sub>-0.8</sub>	2.0 <sup>+1.1</sup> <sub>-0.9</sub>	4.0 <sup>+0.9</sup> <sub>-0.9</sub>
$\Gamma$	0.5 <sup>+0.03</sup> <sub>-0.02</sub>	0.39 <sup>+0.02</sup> <sub>-0.02</sub>	0.14 <sup>+0.01</sup> <sub>-0.01</sub>	0.11 <sup>+0.01</sup> <sub>-0.01</sub>	0.28 <sup>+0.01</sup> <sub>-0.01</sub>
$E_{\text{cut}}^{(a)}$	4.82 <sup>+0.34</sup> <sub>-0.24</sub>	6.86 <sup>+0.43</sup> <sub>-0.44</sub>	8.89 <sup>+0.25</sup> <sub>-0.42</sub>	9.31 <sup>+0.07</sup> <sub>-0.19</sub>	9.11 <sup>+0.14</sup> <sub>-0.16</sub>
$E_{\text{fold}}^{(a)}$	11.4 <sup>+0.27</sup> <sub>-0.29</sub>	11.01 <sup>+0.22</sup> <sub>-0.22</sub>	9.88 <sup>+0.15</sup> <sub>-0.11</sub>	10.05 <sup>+0.16</sup> <sub>-0.08</sub>	11.04 <sup>+0.14</sup> <sub>-0.11</sub>
$F_{\text{ab}}^{(c)}$	1.0	1.25	1.58	1.45	1.22
$F_{\text{unab}}^{(c)}$	1.06	1.32	1.61	1.5	1.27
$\chi_{\text{res}}^2 / \text{dof}$	1.807 / 581	1.593 / 580	1.723 / 594	2.262 / 571	1.768 / 561

<sup>(a)</sup>[keV]

<sup>(b)</sup>[ $10^{-3}$  ph cm<sup>-2</sup> s<sup>-1</sup>]

<sup>(c)</sup>The values of absorbed and unabsorbed fluxes in the 0.1 – 120 keV energy range in units of  $10^{-8}$  erg / cm<sup>2</sup>/s.

Table 11.4: Part 1. Variation of the spectral parameters of 4U 0115+63 with pulse phase during the observation 1999-03-06 for Highcut continuum model. The absorption column, the iron line energy and the width, and all cyclotron lines widths have been fixed to the phase-average values.

Parameter	0.5 - 0.6	0.6 - 0.7	0.7 - 0.8	0.8 - 0.9	0.9 - 1
$E_{1\text{cyc}}^{(a)}$	13.52 <sup>+0.09</sup> <sub>-0.04</sub>	12.88 <sup>+0.16</sup> <sub>-0.1</sub>	13.06 <sup>+0.21</sup> <sub>-0.23</sub>	14.46 <sup>+0.36</sup> <sub>-0.25</sub>	14.74 <sup>+0.46</sup> <sub>-0.38</sub>
$\delta_{1\text{cyc}}$	0.54 <sup>+0.02</sup> <sub>-0.02</sub>	0.42 <sup>+0.04</sup> <sub>-0.02</sub>	0.29 <sup>+0.03</sup> <sub>-0.03</sub>	0.23 <sup>+0.03</sup> <sub>-0.02</sub>	0.23 <sup>+0.03</sup> <sub>-0.03</sub>
$E_{2\text{cyc}}^{(a)}$	23.33 <sup>+0.17</sup> <sub>-0.06</sub>	22.41 <sup>+0.16</sup> <sub>-0.17</sub>	23.11 <sup>+0.16</sup> <sub>-0.4</sub>	24.21 <sup>+0.62</sup> <sub>-0.54</sub>	23.21 <sup>+1.2</sup> <sub>-1.07</sub>
$\delta_{2\text{cyc}}$	1.04 <sup>+0.03</sup> <sub>-0.03</sub>	0.9 <sup>+0.06</sup> <sub>-0.03</sub>	0.62 <sup>+0.05</sup> <sub>-0.05</sub>	0.44 <sup>+0.08</sup> <sub>-0.06</sub>	0.31 <sup>+0.06</sup> <sub>-0.06</sub>
$E_{3\text{cyc}}^{(a)}$	34.84 <sup>+0.39</sup> <sub>-0.54</sub>	32.58 <sup>+0.44</sup> <sub>-0.53</sub>	33.67 <sup>+0.42</sup> <sub>-0.97</sub>	33.68 <sup>+1.08</sup> <sub>-1.17</sub>	32.79 <sup>+1.9</sup> <sub>-1.75</sub>
$\delta_{3\text{cyc}}$	0.73 <sup>+0.07</sup> <sub>-0.04</sub>	0.74 <sup>+0.1</sup> <sub>-0.05</sub>	0.65 <sup>+0.12</sup> <sub>-0.1</sub>	0.65 <sup>+0.14</sup> <sub>-0.12</sub>	0.54 <sup>+0.12</sup> <sub>-0.13</sub>
$E_{4\text{cyc}}^{(a)}$	44.68 <sup>+1.75</sup> <sub>-2.14</sub>	43.0 <sup>+1.0</sup> <sub>-0.97</sub>	45.74 <sup>+1.24</sup> <sub>-2.19</sub>	44.22 <sup>+1.76</sup> <sub>-2.14</sub>	42.33 <sup>+3.18</sup> <sub>-1.96</sub>
$\delta_{4\text{cyc}}$	0.53 <sup>+0.12</sup> <sub>-0.13</sub>	0.77 <sup>+0.17</sup> <sub>-0.09</sub>	0.53 <sup>+0.23</sup> <sub>-0.18</sub>	0.55 <sup>+0.22</sup> <sub>-0.1</sub>	0.59 <sup>+0.18</sup> <sub>-0.22</sub>
$\delta_{5\text{cyc}}$	0.53 <sup>+0.18</sup> <sub>-0.15</sub>	0.54 <sup>+0.36</sup> <sub>-0.18</sub>	0.0 <sup>+0.3</sup> <sub>-0.3</sub>	0.11 <sup>+0.5</sup> <sub>-0.5</sub>	0.4 <sup>+0.34</sup> <sub>-0.4</sub>
$A_{\text{Fe}}^{(b)}$	4.0 <sup>+0.9</sup> <sub>-1.0</sub>	4.3 <sup>+0.9</sup> <sub>-1.0</sub>	3.4 <sup>+0.9</sup> <sub>-1.0</sub>	1.9 <sup>+1.2</sup> <sub>-1.4</sub>	2.5 <sup>+1.2</sup> <sub>-1.3</sub>
$\Gamma$	0.39 <sup>+0.01</sup> <sub>-0.01</sub>	0.49 <sup>+0.01</sup> <sub>-0.01</sub>	0.56 <sup>+0.01</sup> <sub>-0.01</sub>	0.65 <sup>+0.01</sup> <sub>-0.02</sub>	0.64 <sup>+0.01</sup> <sub>-0.02</sub>
$E_{\text{cut}}^{(a)}$	8.87 <sup>+0.15</sup> <sub>-0.14</sub>	8.46 <sup>+0.2</sup> <sub>-0.17</sub>	7.93 <sup>+0.26</sup> <sub>-0.21</sub>	7.0 <sup>+0.18</sup> <sub>-0.23</sub>	7.05 <sup>+0.23</sup> <sub>-0.23</sub>
$E_{\text{fold}}^{(a)}$	9.76 <sup>+0.19</sup> <sub>-0.1</sub>	9.38 <sup>+0.35</sup> <sub>-0.11</sub>	8.49 <sup>+0.32</sup> <sub>-0.25</sub>	9.39 <sup>+0.5</sup> <sub>-0.32</sub>	10.17 <sup>+0.41</sup> <sub>-0.45</sub>
$F_{\text{ab}}^{(c)}$	1.15	1.11	1.05	0.89	0.96
$F_{\text{unab}}^{(c)}$	1.21	1.18	1.13	0.97	1.04
$\chi_{\text{res}}^2 / \text{dof}$	2.083 / 577	1.786 / 592	1.835 / 600	1.788 / 591	1.783 / 590

<sup>(a)</sup>[keV]

<sup>(b)</sup>[ $10^{-3}$  ph cm $^{-2}$  s $^{-1}$ ]

<sup>(c)</sup>The values of absorbed and unabsorbed fluxes in the 0.1 – 120 keV energy range in units of  $10^{-8}$ erg / cm $^2$ /s.

Table 11.5: Part 2. Variation of the spectral parameters of 4U 0115+63 with pulse phase during the observation 1999-03-06 for Highcut continuum model. The absorption column, the iron line energy and the width, all cyclotron lines widths and the cyclotron line harmonic energy  $E_{\text{cyc}5}$  have been fixed to the phase-average values.



## CHAPTER 12

---

### XTE J1946+274

The content of this chapter has been mostly published in Doroshenko et al. (2017).

#### 12.1 Source Description

The transient X-ray pulsar XTE J1946+274 was discovered, at a flux level  $F_{(2-12)\text{keV}} \sim 90$  mCrab, on September 15, 1998 by the *All Sky Monitor (ASM)* on board the *Rossi X-ray Timing Explorer (RXTE)* (Smith & Takeshima 1998a). From archival data, it was found that the source had been brightening from  $\sim 13$  mCrab on September 5 to  $\sim 60$  mCrab on September 15. Coherent pulsations at  $\sim 15.83$  s were discovered in follow-up pointed observations by *RXTE* (Smith & Takeshima 1998a). The source was also observed by *BATSE* on board *CGRO* (Wilson et al. 1998) which reported a (20 – 50 keV) flux of  $\sim 15$  mCrab.

The pulsar remained active for about three years as monitored by the *RXTE/ASM*. Following the *RXTE* outburst detection, the *BeppoSAX* Target of Opportunity Observation Program on Hard X-ray Transients was activated at  $F_{(1-10)\text{keV}} \sim 44$  mCrab (Campana et al. 1998), in the decline of the first, giant, outburst. The source was also observed by the *Indian X-ray Astronomy Experiment (IXAE)* (Paul et al. 2001) that revealed double peaked pulse profiles with a pulse fraction of  $\sim 30\%$  in the 2 – 6 keV and 6 – 18 keV energy band, and confirmed the secular spin-up of the pulsar. The observed outbursts are most likely associated with the orbital motion. Campana et al. (1999) based on *RXTE/ASM* data reported evidence for the  $\sim 80$  d periodicity, while Wilson et al. (2003) confirmed a 169.2 d orbital period based on the X-ray timing measurements.

Verecchia et al. (2002) identified the most likely optical counterpart as a  $R \sim 14$  mag *Be* star, that shows a strong  $H_\alpha$  emission line. This allowed them to estimate a distance of 8 – 10 kpc to the source based on the observed extinction. Wilson et al. (2003), using evidence for an accretion disc, estimated the distance to be  $d = 9.5 \pm 2.9$  kpc.

Several weaker outbursts followed the first one from 1998 to 2001 (Campana et al. 1999; Paul et al. 2001; Wilson et al. 2003). Similar behaviour has been also observed in other *Be* systems (see for example Caballero et al. 2013). The first outburst is, therefore, considered to be a giant one.

XTE J1946+274 remained in quiescence until June 2010, when the Burst Alert Telescope (*BAT*) on board *Swift* and the Gamma-ray Burst Monitor (*GBM*) on board *Fermi* observed a new outburst (Krimm et al. 2010; Finger 2010). The source has been observed with *INTEGRAL* (Caballero et al. 2010), *Swift* and *RXTE* (Müller et al. 2012), and *Suzaku* (Maitra & Paul 2013a; Marcu-Cheatham et al. 2015). Also on this occasion, the source exhibited several outbursts of decreasing intensity, following the first one (Müller et al. 2012).

Based on the *RXTE* data from the outburst in 1998, the broadband X-ray spectrum of the source was found to be similar to that of other accreting pulsars, and a cyclotron line near 35 keV, has been reported by Heindl et al. (2001b). However, based on data from the 2010 outburst, the presence of a cyclotron line at 35 keV was excluded by Müller et al. (2012), who suggested possible evidence for a cyclotron feature at  $\sim 25$  keV. On the contrary, based on *Suzaku* data, Maitra & Paul (2013a) and Marcu-Cheatham et al. (2015) found marginal evidence for a line near 35 – 38 keV, and no indication of the 25 keV absorption feature. In our work we focused on the unpublished analysis of the 1998 observations of the source made with *BeppoSAX*, focusing on the timing and spectral properties of the source.

## 12.2 Observations

XTE J1946+274 was observed by *BeppoSAX* in the framework of the AO2 programme aimed at monitoring the spectral and timing behaviour of hard pulsating transients as a function of luminosity. During the decline of the 1998 giant outburst (Fig. 12.1) of the source, six pointed observations, at different luminosities, were performed using the NFIs (Tab. 12.1). The analysis of this data has been published by Doroshenko et al. (2017) for the first time.

### 12.2.1 Timing Analysis

We performed a detailed timing and spectral analysis of all *BeppoSAX* data. For the timing analysis, the photon arrival times were corrected for motion in the solar system, and in the binary system assuming ephemeris derived by Wilson et al. (2003). To search for pulsation we used epoch folding, and the obtained period value and uncertainties were refined using the phase-connection technique. We were not able to find a common timing solution for all observations assuming a smooth variation of the period, and within individual observations the pulse arrival times are

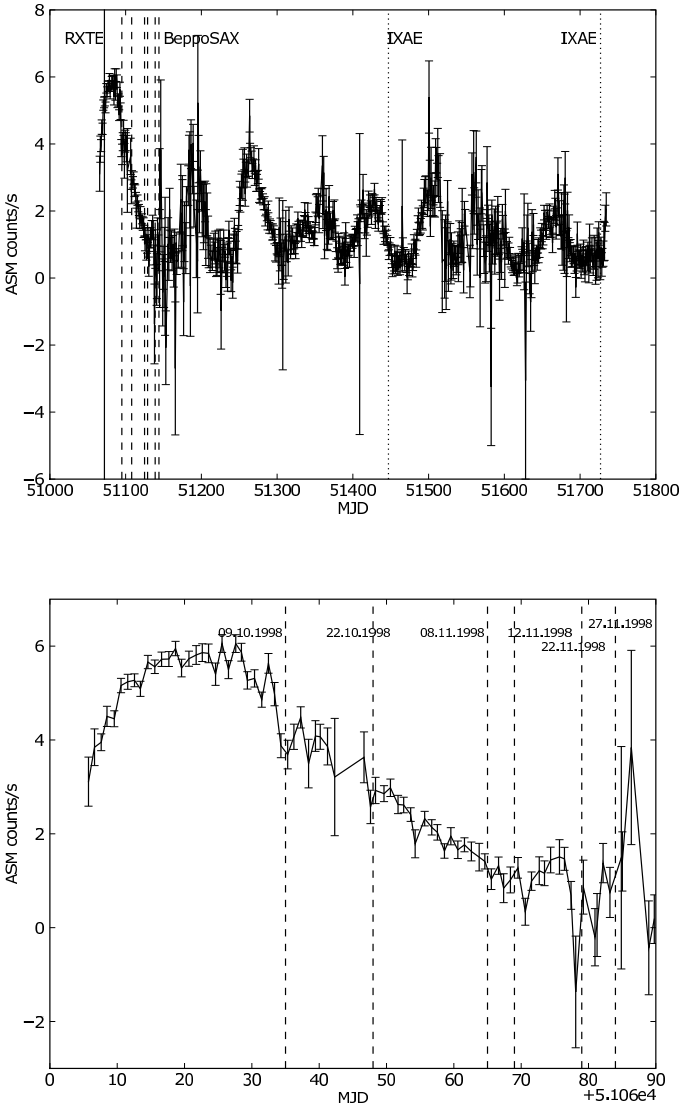


Figure 12.1: Light curves of XTE J1946+274 as observed by *RXTE*/*ASM*. Dashed lines are *BeppoSAX* observations.

Date	MECS exposure time, ks	$F_{\text{unab}}^*$ , $10^{-9}$ erg/cm <sup>2</sup> /s	$L^{**}$ , $10^{37}$ erg/s
1998.10.09	29	4.42	4.48
1998.10.22	23	3.15	3.4
1998.11.08	28	1.37	1.48
1998.11.12	28	1.16	1.25
1998.11.22	12	0.63	0.68
1998.11.27	33	0.42	0.45

\*Unabsorbed fluxes in 0.1 – 120 keV range.

\*\*X-ray luminosity for the distance  $d = 9.5$  kpc.

Table 12.1: Observations of the X-ray pulsar XTE J1946+274 by *BeppoSAX*.

consistent with constant periods as listed in Table 12.2 (all uncertainties are given at 90% confidence level unless stated otherwise). The comparison of the periods measurements during the outburst reveals a generic spin-up trend as shown in Figure 12.2, which can be approximated as  $P = 15.81951(2)$  s,  $\dot{P} = -2.99(2) \times 10^{-9}$  s/s,  $\ddot{P} = 3.82(4) \times 10^{-16}$  s/s<sup>2</sup>.

The pulse profiles folded with the best-fit period for the brightest *BeppoSAX* observation are presented in Figure 12.3. The pulse profile significantly changes

Date	MJD	Satellite	$P$ , s	$\dot{P} \times 10^{-9}$ , s/s
16.09.1998	51072	<i>RXTE</i>	15.83(2)	—
09.10.1998	51095	<i>SAX</i>	15.81955(4)	0
22.10.1998	51108	<i>SAX</i>	15.81662(4)	0
08.11.1998	51125	<i>SAX</i>	15.81440(4)	0
12.11.1998	51129	<i>SAX</i>	15.81414(4)	0
22.11.1998	51139	<i>SAX</i>	15.8137(2)	0
27.11.1998	51144	<i>SAX</i>	15.81369(3)	0
24.09.1999	51447	<i>IXAE</i>	15.78801(4)	-1.54(37)
02.07.2000	51727	<i>IXAE</i>	15.76796(18)	1.86(49)
20.06.2010	55367	<i>RXTE</i>	15.755(3)	-3.0(3)
30.06.2010	55377	<i>RXTE</i>	15.767(3)	-3.0(3)
11.10.2010	55480	<i>Suzaku</i>	15.75(11)	—

Table 12.2: Pulse-period history of XTE J1946+274. For the *BeppoSAX* data, pulsations have been obtained using the phase connection method. Values for *RXTE*, *IXAE* and *Suzaku* are known from Smith & Takeshima (1998b); Paul et al. (2001); Müller et al. (2012); Maitra & Paul (2013a).

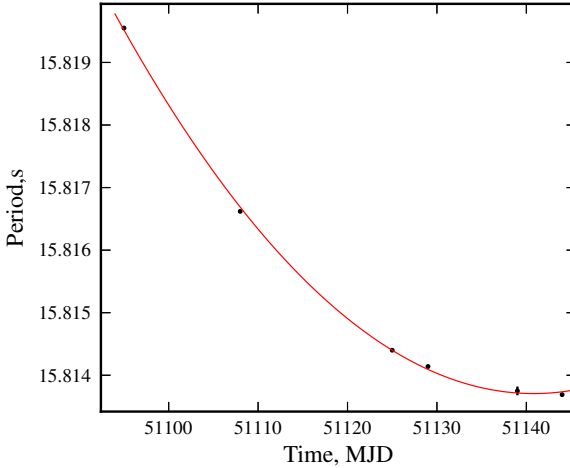


Figure 12.2: XTE J1946+274 pulse period as observed by *BeppoSAX*. Uncertainties errors are given with  $1\sigma$  confidence level (for the most points errors are inside the circles).

with the energy and it is characterised by two main phase regions: a “soft” peak at phases  $\sim (0.5 - 1)$ , and a “hard” peak at  $\sim (0 - 0.5)$ . The soft peak dominates at low energies, while the hard peak appears at  $\sim 1$  keV and steadily increases with respect to the soft peak till at energies  $\geq 30$  keV it is the only emission left. Pulsations extend up to  $\sim 70$  keV. The phase difference between the soft and hard peaks is about half a phase.

The pulse profile shape also changes with luminosity as can be seen from Figure 12.4. In particular, both peaks become more pronounced at lower luminosities, while the shift between the soft and hard peaks remains relatively constant.

The fraction of pulsed flux (Fig. 12.5) decreases until  $\sim 4$  keV, and then increases in 4 – 60 keV with a possible feature at  $\sim 38$  keV (see, Section 12.2.2).

### 12.2.2 Spectral Analysis

The broadband X-ray continuum of the pulse-phase averaged spectrum can be described with an absorbed power law cutoff at high energies. In addition, an iron line at  $\sim 6.4 - 6.6$  keV, and an absorption line at  $\sim 38$  keV for the CRSF are required (Fig. 12.6) by the data.

As a first step of the spectral analysis, we verified that the spectrum of the source during the brightest *BeppoSAX* observation (which also happens to be one with the

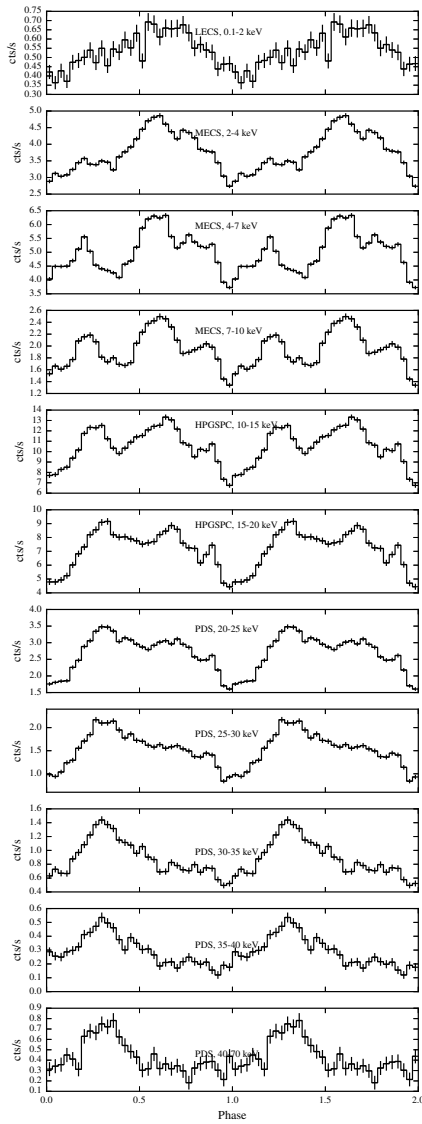


Figure 12.3: The pulse profiles of XTE J1946+274 in 11 energy bands observed with the *BeppoSAX* satellite by LECS, MECS, HPGSPC and PDS instruments in 9th of October, 1998.

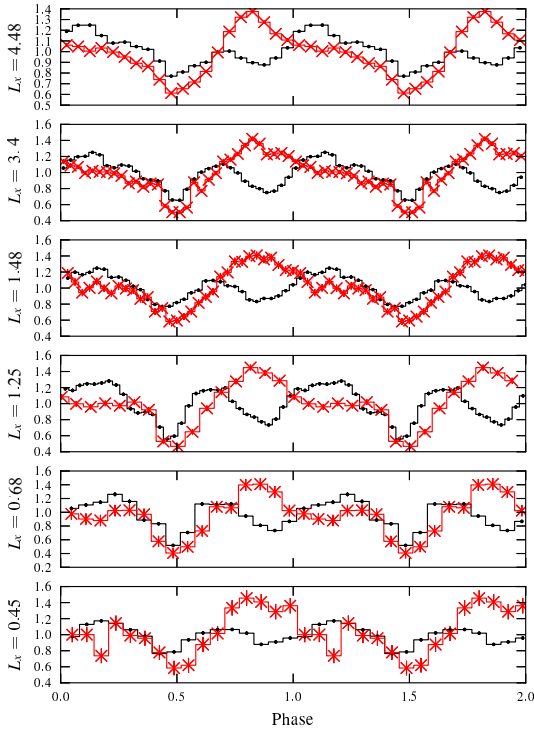


Figure 12.4: The luminosity dependence of the soft (MECS data in 2 – 10 keV range, black points), and hard (PDS data in 20 – 40 keV, red crosses) normalised pulse profiles along the outburst.

best counting statistics) can indeed be described with the several continuum models (Tab. 12.3): *Highcut*, *Fdcut*, *NPEX* and *CompTT*. For all considered continuum models the addition of an iron line at  $\sim 6.4 - 6.6$  keV, an absorption line with Gaussian optical depth profile (Hemphill et al. 2013) at  $\sim 38$  keV and a blackbody-like component (bb) with temperature of  $\sim 2$  keV were necessary.

The parameters of the CRSF were best constrained when the continuum was fitted with the *Highcut* model. We use this model below (see Fig. 12.6, Tab. 12.4) for all observations.

To account for the residuals around 10 keV, similar to those reported by Müller et al. (2012), either a partial covering absorber (PC) or another absorption line at  $\sim 10$  keV (with the width of  $\sim 2$  keV) was required. The quality of the fit was comparable for all models tested. We have also found that the PC might be

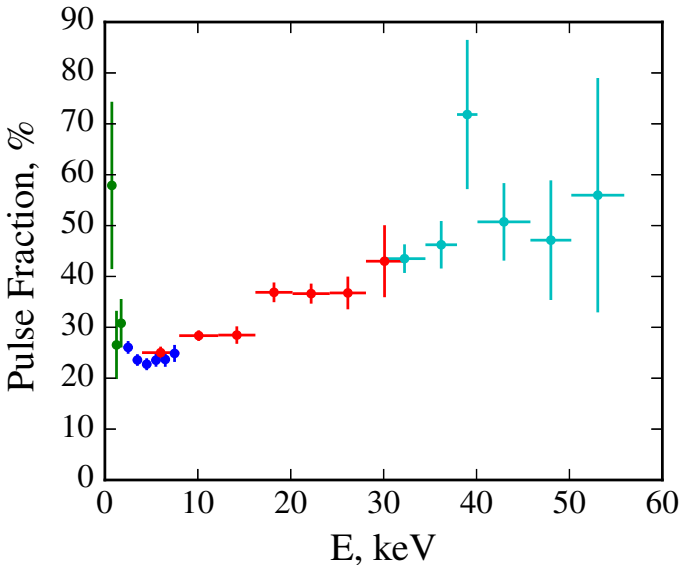


Figure 12.5: XTE J1946+274 pulse fraction for the brightest *BeppoSAX* observation in 10-09-1998. The emission feature is around cyclotron line energy,  $E_{\text{cyc}} \sim 38$  keV.

substituted with an additional blackbody-like component (bb) with temperature of  $\sim 2$  keV.

The best-fit parameters for the three different models: with the PC and *Higiecut* (i.e. the same as used by Maitra & Paul 2013a); with *Higiecut* and bb; and with *Fdcut* and additional absorption feature (Gauss at  $E_G = 10.2(5)$  keV with  $\sigma_G = 2.1(5)$  keV, i.e. the same model as reported by Müller et al. 2012), are presented in Table 12.5.

We note that the CRSF parameters are consistent within uncertainties for all models. The cyclotron line parameters are significantly constrained in the first of the *BeppoSAX* observations. The feature is required also for the second observation, however, the line width becomes unconstrained. Following Maitra & Paul (2013a), who reported that the line remains narrow at fluxes comparable with the dimmest *BeppoSAX* observations, for the second observation we fixed the line width to the same value of the first observation, which resulted in slightly higher value of the CRSF energy  $E_{\text{cyc}} = 41(2)$  keV.

We have also performed pulse-phase resolved analysis for the brightest observation. To describe the phase resolved spectra, we used a *Higiecut* model, modified



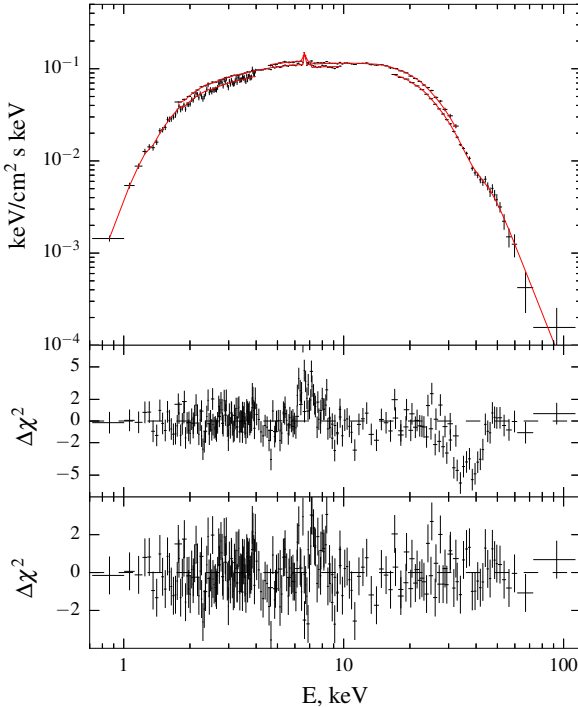


Figure 12.6: Unfolded spectrum of XTE J1946+274 on 1998-10-09 fitted with Highcut+bb continuum model (top panel). The middle and bottom panels show the best-fit residuals without and with inclusion of iron and cyclotron lines, respectively.

by partial covering or blackbody. We have found that at lower counting statistics the parameters of the CRSF are better constrained when the additional blackbody component is used.

Taking into account the observed pulse profile morphology and significant statistics, we divided the data in five phase bins. In the case with the bb we fixed the absorption, energy and width of the emission iron and cyclotron lines and the temperature of the blackbody component at the average values (Tab. 12.6). The phase dependence of the best fit parameters is shown in Figure 12.7. It is interesting to note that the depth of the cyclotron feature becomes consistent with zero at the first pulse phases, meaning that the CRSF is statistically not significant. In fact, it is

Parameter	Highecut	Fdcut	NPEX	CompTT
$N_{\text{H}}^{(a)}$	$1.32^{+0.07}_{-0.06}$	$1.26^{+0.08}_{-0.06}$	$1.47^{+0.12}_{-0.19}$	$1.37^{+0.06}_{-0.06}$
$E_{\text{cyc}}^{(b)}$	$38.34^{+1.45}_{-1.3}$	$37.4^{+3.97}_{-1.42}$	$38.49^{+1.49}_{-1.56}$	$38.6^{+1.17}_{-1.22}$
$\sigma_{\text{cyc}}^{(b)}$	$4.55^{+1.35}_{-1.21}$	$10.39^{+1.21}_{-0.85}$	$10.34^{+1.31}_{-1.8}$	$8.96^{+0.99}_{-1.28}$
$\delta_{\text{cyc}}^{(b)}$	$0.3^{+0.1}_{-0.1}$	$1.66^{+0.83}_{-0.79}$	$0.75^{+0.18}_{-0.18}$	$0.68^{+0.11}_{-0.14}$
$E_{\text{Fe}}^{(b,g)}$	$6.62^{+0.05}_{-0.05}$	$6.61^{+0.04}_{-0.05}$	$6.62^{+0.05}_{-0.05}$	$6.62^{+0.05}_{-0.05}$
$A_{\text{Fe}}^{(c)}$	$1.1^{+0.1}_{-0.2}$	$1.1^{+0.1}_{-0.2}$	$1.0^{+0.1}_{-0.2}$	$1.1^{+0.2}_{-0.1}$
$kT_{\text{bb}}^{(b)}$	$1.87^{+0.12}_{-0.11}$	$1.59^{+0.13}_{-0.04}$	$1.8^{+0.08}_{-0.04}$	$1.6^{+0.05}_{-0.04}$
$R_{\text{bb}}^{(d)}$	$1.4^{+0.8}_{-0.4}$	$1.6^{+0.9}_{-0.8}$	$2.4^{+1.0}_{-1.1}$	$2.2^{+0.8}_{-0.8}$
$\Gamma$	$0.88^{+0.03}_{-0.03}$	$0.79^{+0.04}_{-0.04}$		
$E_{\text{cut}}^{(b)}$	$18.04^{+0.53}_{-0.35}$	$35.55^{+7.95}_{-8.94}$		
$E_{\text{fold}}^{(b)}$	$9.36^{+0.36}_{-0.54}$	$5.12^{+1.76}_{-1.11}$		
$\alpha 1$			$1.16^{+0.22}_{-0.36}$	
$\alpha 2$			$-2.0$	
$kT^{(b)}$			$5.42^{+0.02}_{-0.01}$	$5.62^{+0.14}_{-0.16}$
$T_{\text{p}}^{(e)}$				$0.01^{+0.68}_{-0.01}$
$\tau_{\text{p}}^{(f)}$				$19.05^{+0.29}_{-0.57}$
$\chi_{\text{res}}^2 / \text{dof}$	1.065 / 599	1.089 / 600	1.069 / 600	1.086 / 600

<sup>(a)</sup>  $[10^{22} \text{atoms cm}^{-2}]$

<sup>(b)</sup> [keV]

<sup>(c)</sup>  $[10^{-3} \text{ph cm}^{-2} \text{s}^{-1}]$

<sup>(d)</sup>  $R_{\text{bb}}$  is the radius of the black body in km for the distance to the source  $D = 9.5 \text{ kpc}$ .

<sup>(e)</sup> Plasma temperature, keV.

<sup>(f)</sup> Plasma optical depth.

<sup>(g)</sup>  $\sigma_{\text{Fe}} = 0.01 \text{ keV}$ .

Table 12.3: XTE J1946+274 parameters of the four continuum models applied to the phase averaged spectrum during the brightest observation. The absorbed and unabsorbed fluxes reported in the range 0.1 – 120 keV are  $F_{\text{ab}} = 4.03 \cdot 10^{-9} \text{ ergs cm}^{-2} \text{ s}^{-1}$ ,  $F_{\text{unab}} = 4.27 \cdot 10^{-9} \text{ ergs cm}^{-2} \text{ s}^{-1}$  respectively.

only significant in the soft peak of the pulse profile, even if the counting statistics is lower at this phase. We also note that the for the third phase bin the spectrum is consistent with a pure power law, so the additional soft component or partial covering are not required at this phase.

Parameter	1998.10.09	1998.10.22	1998.11.08	1998.11.12	1998.11.22	1998.11.27
$N_{\text{H}}^{(a)}$	$1.32^{+0.07}_{-0.06}$	$1.12^{+0.12}_{-0.1}$	$0.92^{+0.16}_{-0.08}$	$1.21^{+0.16}_{-0.17}$	$1.27^{+0.47}_{-0.54}$	$1.05^{+0.26}_{-0.17}$
$E_{\text{cyc}}^{(b)}$	$38.34^{+1.45}_{-1.3}$	$40.79^{+2.2}_{-1.92}$	$36.0^{(f)}$	$38.33^{+2.76}_{-1.95}$	$38.0^{(f)}$	$35.17^{+2.51}_{-1.78}$
$\sigma_{\text{cyc}}^{(b)}$	$4.55^{+1.35}_{-1.21}$	$4.0^{(f)}$	$4.0^{(f)}$	$0.9^{+2.8}_{-0.8}$	$4.0^{(f)}$	$0.4^{+2.9}_{-0.3}$
$\delta_{\text{cyc}}$	$0.3^{+0.1}_{-0.1}$	$0.3^{+0.1}_{-0.2}$	$0.12^{+0.01}_{-0.01}$	$1.1^{+0.9}_{-0.9}$	$0.59^{+0.01}_{-0.01}$	$0.3^{+0.7}_{-0.1}$
$E_{\text{Fe}}^{(b,g)}$	$6.62^{+0.05}_{-0.05}$	$6.66^{+0.09}_{-0.09}$	$6.6^{+0.1}_{-0.1}$	$6.6^{+0.1}_{-0.1}$	$6.62^{+0.05}_{-0.05}$	$6.4^{+0.1}_{-0.1}$
$A_{\text{Fe}}^{(c)}$	$1.1^{+0.1}_{-0.2}$	$0.7^{+0.2}_{-0.2}$	$0.3^{+0.1}_{-0.1}$	$0.2^{+0.1}_{-0.1}$	$0.05^{+0.01}_{-0.01}$	$0.15^{+0.05}_{-0.05}$
$kT_{\text{bb}}^{(b)}$	$1.87^{+0.12}_{-0.11}$	$1.96^{+0.18}_{-0.12}$	$2.12^{+0.16}_{-0.12}$	$2.37^{+0.23}_{-0.28}$	$2.4^{+0.27}_{-0.43}$	$1.98^{+0.21}_{-0.28}$
$R_{\text{bb}}^{(d)}$	$1.4^{+0.8}_{-0.4}$	$1.2^{+0.7}_{-0.6}$	$0.9^{+0.4}_{-0.4}$	$0.7^{+0.4}_{-0.2}$	$0.7^{+0.4}_{-0.4}$	$0.7^{+0.4}_{-0.3}$
$\Gamma$	$0.88^{+0.03}_{-0.03}$	$0.82^{+0.05}_{-0.05}$	$0.8^{+0.08}_{-0.04}$	$0.92^{+0.06}_{-0.11}$	$1.17^{+0.21}_{-0.41}$	$0.98^{+0.14}_{-0.11}$
$E_{\text{cut}}^{(b)}$	$18.04^{+0.53}_{-0.35}$	$18.45^{+0.84}_{-0.5}$	$19.37^{+2.51}_{-0.95}$	$19.16^{+1.16}_{-1.97}$	$26.84^{+6.57}_{-10.16}$	$18.54^{+7.42}_{-5.98}$
$E_{\text{fold}}^{(b)}$	$9.36^{+0.36}_{-0.54}$	$8.9^{+0.38}_{-0.53}$	$8.95^{+0.43}_{-0.68}$	$9.8^{+0.8}_{-0.9}$	$9.3^{+4.6}_{-3.4}$	$10.35^{+1.06}_{-2.27}$
$F_{\text{ab}}^{(e)}$	4.03	2.9	1.28	1.11	0.63	0.4
$F_{\text{unab}}^{(e)}$	4.27	3.0	1.33	1.16	0.66	0.42
$\chi_{\text{res}} / \text{dof}$	1.065 / 599	1.104 / 151	0.971 / 283	0.91 / 173	0.888 / 63	0.894 / 212

<sup>(a)</sup>[ $10^{22}$  atoms  $\text{cm}^{-2}$ ]

<sup>(b)</sup>[keV]

<sup>(c)</sup>[ $10^{-3}$  ph  $\text{cm}^{-2}$   $\text{s}^{-1}$ ]

<sup>(d)</sup> $R_{\text{bb}}$  is the radius of the black body in km for the distance to the source  $D = 9.5$  kpc.

<sup>(e)</sup>The values of absorbed and unabsorbed fluxes in 0.1 – 120 keV energy range in units  $10^{-9}$  erg /  $\text{cm}^2$  / s.

<sup>(f)</sup>This parameter was fixed.

<sup>(g)</sup> $\sigma_{\text{Fe}} = 0.01$  keV.

Table 12.4: Variation parameters of XTE J1946+274 with flux, during decay of the 1998 yr outburst observed by *BeppoSAX* with *Highcut* continuum model.

### 12.3 Discussion and Conclusion

We have analysed observations of XTE J1946+274 performed with *BeppoSAX* during the October – November 1998 outburst of the source. We found that the broadband spectrum of the source has a complex shape, which is not described adequately by the typically used phenomenological models, particularly in the energy region around  $\sim 10$  keV. This is indeed in agreement with what reported by Müller et al. (2012) who, analysed observations of the 2010/2011 outburst of the source taken with *INTEGRAL*, *RXTE* and *Swift*. Müller et al. (2012) accounted for the residuals around  $\sim 10$  keV by including additional absorption line. However, based on the broadband spectra of accreting pulsars observed by *BeppoSAX* (see for example Robba et al. 2001; Doroshenko et al. 2015), we argue that residuals around 10 keV are due to an incorrect modelling of the entire continuum rather than to some local physical feature.

Parameter	Highecut+bb	Highecut+PC	Fdcut+Gauss
$N_{\text{H}}^{(a)}$	$1.32^{+0.07}_{-0.06}$	$1.63^{+0.05}_{-0.11}$	$1.32^{+0.06}_{-0.06}$
$E_{\text{cyc}}^{(b)}$	$38.34^{+1.45}_{-1.3}$	$38.47^{+1.54}_{-1.43}$	$37.88^{+1.36}_{-1.28}$
$\sigma_{\text{cyc}}^{(b)}$	$4.55^{+1.35}_{-1.21}$	$4.6^{+1.5}_{-1.3}$	$7.22^{+1.08}_{-1.38}$
$\delta_{\text{cyc}}$	$0.30^{+0.08}_{-0.08}$	$0.27^{+0.08}_{-0.08}$	$0.5^{+0.1}_{-0.1}$
$E_{\text{Fe}}^{(b,e)}$	$6.62^{+0.05}_{-0.05}$	$6.66^{+0.05}_{-0.06}$	$6.61^{+0.05}_{-0.05}$
$A_{\text{Fe}}^{(c)}$	$1.1^{+0.1}_{-0.2}$	$1.01^{+0.22}_{-0.16}$	$1.2^{+0.2}_{-0.2}$
$\Gamma$	$0.88^{+0.03}_{-0.03}$	$1.14^{+0.02}_{-0.04}$	$0.7^{+0.04}_{-0.05}$
$E_{\text{cut}}^{(b)}$	$18.04^{+0.53}_{-0.34}$	$18.57^{+0.4}_{-0.17}$	$16.3^{+1.32}_{-1.98}$
$E_{\text{fold}}^{(b)}$	$9.4^{+0.4}_{-0.5}$	$9.98^{+0.41}_{-0.42}$	$8.1^{+0.3}_{-0.3}$
$kT_{\text{bb}}^{(b)}$	$1.87^{+0.12}_{-0.11}$	—	—
$K_{\text{bb}}^{(d)}$	$2.2^{+0.6}_{-0.5}$	—	—
$N_{\text{Hpc}}^{(a)}$	—	$12.53^{+1.72}_{-3.57}$	—
$C_{\text{pc}}$	—	$0.27^{+0.03}_{-0.03}$	—
$E_{\text{G}}^{(b)}$	—	—	$10.2^{+0.3}_{-0.5}$
$\sigma_{\text{G}}^{(b)}$	—	—	$2.1^{+0.5}_{-0.5}$
$\delta_{\text{G}}$	—	—	$0.09^{+0.02}_{-0.01}$
$\chi_{\text{red}}^2 / \text{dof}$	1.065/599	1.122/599	1.034/599

<sup>(a)</sup> $[10^{22} \text{ atoms cm}^{-2}]$

<sup>(b)</sup> $[\text{keV}]$

<sup>(c)</sup> $[10^{-3} \text{ ph cm}^{-2} \text{ s}^{-1}]$

<sup>(d)</sup> $K_{\text{bb}} = R^2/D_{10}^2$ , where  $R^2$  is the black body radius in km,  $D_{10}^2$  is the distance to the source in units of 10 kpc.

For the XTE J1946+274  $D = 9.5$  kpc.

<sup>(e)</sup> $\sigma_{\text{Fe}} = 0.01$  keV.

Table 12.5: Parameters of the spectrum of XTE J1946+274 in 1998-10-09 with different description of the continuum: Highecut + bb, Highecut + PC and Fdcut + Gauss. The values of absorbed and unabsorbed fluxes in 0.1 – 120 keV energy range are  $F_{\text{ab}} = 4.04 \times 10^{-9} \text{ erg/cm}^2/\text{s}$ ,  $F_{\text{unab}} = 4.27 \times 10^{-9} \text{ erg/cm}^2/\text{s}$ .

In fact, following Maitra & Paul (2013a) who analysed *Suzaku* observations of the 2010 outburst of the source, we successfully modelled the broadband *BeppoSAX* spectrum of XTE J1946+274 using an additional partial covering absorber in combination with the widely used phenomenological model Highecut. This implies that part of the emission is absorbed within the binary system. To obtain a statistically acceptable fit, a more elaborate modelling of the soft X-ray absorption has

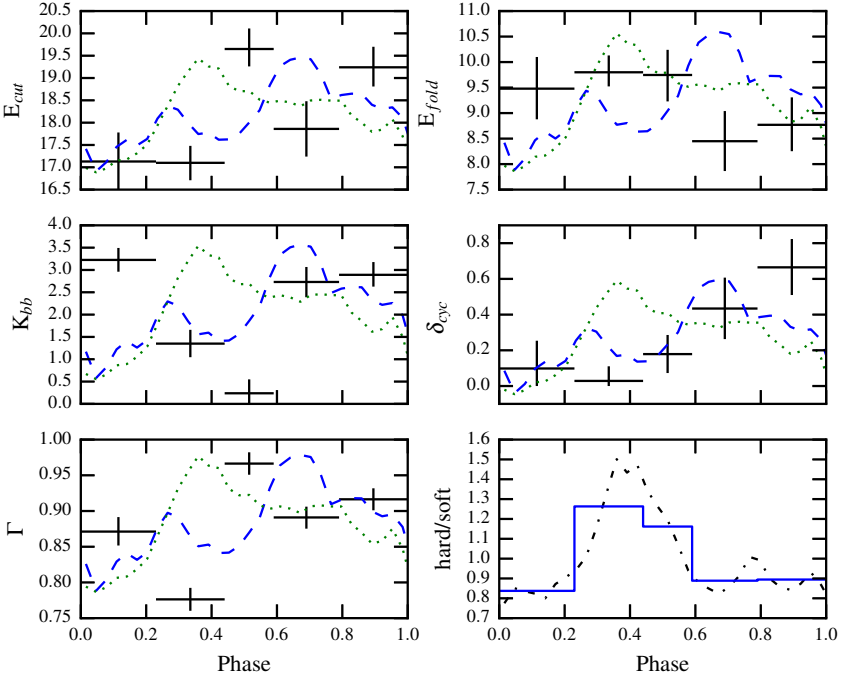


Figure 12.7: Phase dependence of the spectral parameters for the brightest observation with Highcut+bb model. Blue dashed and green dotted lines show for reference MECS (2 – 10 keV) and PDS (15 – 120 keV) pulse profiles, scaled to match the respective parameter range. The lower right panel shows the hardness ratio for the same energy bands.

been used by Marcu-Cheatham et al. (2015), who, analysing a *Suzaku* observation of the source at lower luminosity, considered absorption by different components of the ISM.

In our analysis we have found evidence of a cyclotron line at  $\sim 38$  keV. The observed line energy implies a value of the magnetic field of  $3.3(1+z) \times 10^{12}$  G assuming  $E_{\text{cyc}} \approx 11.56 B_{12} / (1+z)$ , where  $z$  is the gravitational redshift of the scattering region. As seen in Table 12.5, our result is independent of the continuum model used.

Our finding is consistent within 3-sigma with the value reported by Heindl et al. (2001b) on the basis of *RXTE* data of the same outburst, but at the higher luminosity.

Parameter	0 - 0.15	0.15 - 0.35	0.35 - 0.55	0.55 - 0.8	0.8 - 1
$\delta_{\text{cyc}}$	$0.10^{+0.01}_{-0.01}$	$0.03^{+0.01}_{-0.01}$	$0.11^{+0.04}_{-0.04}$	$0.44^{+0.17}_{-0.17}$	$0.66^{+0.16}_{-0.16}$
$A_{\text{Fe}}^{(a)}$	$1.2^{+0.2}_{-0.2}$	$1.2^{+0.3}_{-0.3}$	$1.0^{+0.3}_{-0.3}$	$1.1^{+0.3}_{-0.3}$	$0.6^{+0.3}_{-0.3}$
$R_{\text{bb}}^{(b)}$	$1.7^{+0.5}_{-0.5}$	$1.1^{+0.5}_{-0.5}$	$0.4^{+0.1}_{-0.1}$	$1.6^{+0.6}_{-0.6}$	$1.6^{+0.5}_{-0.5}$
$\Gamma$	$0.87^{+0.02}_{-0.02}$	$0.78^{+0.02}_{-0.02}$	$0.97^{+0.02}_{-0.02}$	$0.89^{+0.02}_{-0.02}$	$0.92^{+0.02}_{-0.02}$
$E_{\text{cut}}^{(c)}$	$17.13^{+0.65}_{-0.62}$	$17.1^{+0.38}_{-0.39}$	$19.65^{+0.47}_{-0.39}$	$17.86^{+0.62}_{-0.63}$	$19.24^{+0.46}_{-0.43}$
$E_{\text{fold}}^{(c)}$	$9.48^{+0.62}_{-0.6}$	$9.8^{+0.33}_{-0.28}$	$9.75^{+0.5}_{-0.52}$	$8.45^{+0.59}_{-0.59}$	$8.77^{+0.54}_{-0.52}$
$F_{\text{ab}}^{(d)}$	2.44	3.38	3.23	3.66	3.14
$F_{\text{unab}}^{(d)}$	2.59	3.56	3.43	3.91	3.36
$\chi^2_{\text{res}} / \text{dof}$	0.990 / 398	0.869 / 400	0.975 / 407	1.017 / 419	0.985 / 419

<sup>(a)</sup> [ $10^{-3}$  ph cm $^{-2}$  s $^{-1}$ ]

<sup>(b)</sup>  $R_{\text{bb}}$  is the radius of the black body in km for the distance to the source  $D = 9.5$  kpc.

<sup>(c)</sup> [keV]

<sup>(d)</sup> The values of absorbed and unabsorbed fluxes in 0.1 – 120 keV energy range in units  $10^{-9}$  erg/cm $^2$ /s.

Table 12.6: XTE J1946+274, 1998-10-09. Variation of the spectral parameters with pulse phase assuming Highcut continuum model. The absorption, the energy and width of the emission iron and cyclotron lines and the temperature of the black body component were fixed at the average values.

Our result is also in agreement with the value of the CRSF energy reported by Maitra & Paul (2013a) with the *Suzaku*. We note, that the considered *BeppoSAX* observation had been performed at significantly higher luminosity, than the *Suzaku* observations. So there appears to be no strong correlation of the CRSF centroid energy with luminosity. On the other hand, the centroid of the not very significant ( $\sim 2.8\sigma$ ) line at  $\sim 35$  keV reported by Marcu-Cheatham et al. (2015) is slightly lower. In our analysis we do not find evidence of any line at  $\sim 25$  keV as suggested by Müller et al. (2012), even if we use the same continuum used by Müller et al. (2012). Since the source had comparable luminosity in the two observations, the reason for such a dramatic change is unclear. Conversely, Müller et al. (2012) report that they find two alternative fit solutions with lines at  $\sim 30$  keV and  $\sim 40$  keV, and while the solution with a line at 25 keV is most significant of the three, its significance remains low at  $\leq 2\sigma$ .

A suggestion of the CRSF being located at 38 keV follows from the pulsed fraction energy dependance which exhibits a feature around  $\sim 40$  keV (see Fig. 12.5). Although the feature is marginally significant, we observe that a similar behaviour has also been observed in other sources and can be associated with change of the pulsar beam pattern around the resonance energy (Ferrigno et al. 2009; Schönherr et al. 2014).

We have also carried out the pulse-phase resolved analysis for the brightest *Bep-poSAX* observation. Surprisingly, the CRSF is only detected at certain pulse phases, namely in the second peak of the two peaked pulse profile. The statistical quality of the phase-resolved spectra is comparable in all phase bins, so the feature does indeed change intensity and energy with pulse phase. This could be understood considering again the pulse profiles of the source.

As already discussed, the pulse profiles observed by *Bep-poSAX* strongly evolve with the energy (see Fig. 12.3). The two peaks are separated by about half a phase, and, therefore, likely represent two emission components with roughly orthogonal beam patterns. Paul et al. (2001) suggested that the two peaks might be related to the emission from the two poles of the NS not diametrically positioned to each other. On the other hand, the pulse profile evolution, and in particular the  $\sim 180^\circ$  phase shift between the soft and hard peaks can be qualitatively explained in terms of the simultaneous presence of a “hard pencil” (aligned with cylindrical symmetry about the dipole axis) and a “soft fan” (cylindrically symmetric around the axis perpendicular to the dipole axis) beam components (Woo et al. 1996). Provided that  $\Theta + \Phi < 90^\circ$  ( $\Theta$  is the inclination of the spin axis,  $\Phi$  is the angle between the spin and dipole axis) a single-peak pulse profile is produced by either pencil and fan beams.

The absence of the CRSF at certain phases might be explained, therefore, if only one of the components exhibits a CRSF in its spectrum. A similar scenario is realised in the model proposed by Poutanen et al. (2013a) where reflection off the surface of the NS is responsible for CRSF formation. Here we would like to note that the reflected component is likely to be softer than incident emission, and the CRSF in XTE J1946+274 is only detected in soft peak. The fact that the CRSF parameters remain essentially unchanged despite an order of magnitude change in luminosity, which was already noted previously by Marcu-Cheatham et al. (2015), also suggests that the CRSF shall be formed close to the surface of the NS, rather than in a tall accretion column. This can be either due to reflection, or simply because the source consistently accretes in the subcritical regime as suggested by Marcu-Cheatham et al. (2015). A detailed modelling of the pulse profile, X-ray continuum and CRSF formation is required to move from the suggested qualitative interpretation to unambiguous and quantitative description of the observed phase and luminosity of the spectrum. This modelling must take into account several effects, from local beam pattern formation to propagation to the observer, which includes gravitational light bending (Kraus 2001; Kraus et al. 2003; Sasaki et al. 2012).

## CHAPTER 13

---

### GRO J1744–28

In this chapter I summarise my work on the accreting pulsar GRO J1744–28 which was observed by *BeppoSAX* during the outburst in 1997 and in quiescence in 1998. The content of this chapter has been mostly published in Doroshenko et al. (2015).

#### 13.1 Source Description

The peculiar transient X-ray source GRO J1744–28 also known as the bursting pulsar, was discovered on December 2, 1995, with the Burst and Transient Source Experiment (*BATSE*), onboard the Compton Gamma Ray Observatory (*CGRO*; Fishman et al. 1995; Kouveliotou et al. 1996). Three major outbursts have been observed since the discovery. The first lasted from the end of 1995 until the beginning of 1996, the second from December 1996 until April 1997, and the third from January to May 2014 (Degenaar et al. 2014; Younes et al. 2015; D’Ài et al. 2015). The peak outburst luminosity in X-rays reaches  $L_X \sim 10^{37} - 10^{38} \text{ erg s}^{-1}$  (Woods et al. 1999), while the quiescent luminosity is  $L_X \sim 10^{33-34} \text{ erg s}^{-1}$  (Wijnands & Wang 2002; Daigne et al. 2002; Degenaar et al. 2012). The source exhibits coherent pulsations with a period of  $\sim 0.467 \text{ s}$ , associated with the rotation of the NS i.e. it is an accreting X-ray pulsar in a binary system. Finger et al. (1996) determined the orbital period and semimajor axis to be  $P_{\text{orb}} = 11.8 \text{ days}$  and  $a = 1.12R_{\odot}$  ( $\sim 7.8 \times 10^{10} \text{ cm}$ ) respectively. The mass function was estimated to be  $f(M) = 1.36 \times 10^{-4} M_{\odot}$  implying, for the canonical NS mass of  $M_{\text{NS}} = 1.4M_{\odot}$ , accretion via Roche lobe overflow from a strongly evolved red giant remnant with mass about  $0.2 - 0.7M_{\odot}$  (Daumerie et al. 1996; Miller 1996; Sturmer & Dermer 1996; Bildsten & Brown 1997; Rappaport & Joss 1997). The photoelectric absorption does not change significantly during the outbursts and is comparable with interstellar absorption  $N_{\text{H}} \sim (5 - 6) \times 10^{22} \text{ cm}^{-2}$  in the direction of the Galactic center where the source is thought to be located at distance of  $\sim 8 \text{ kpc}$  (Dotani et al. 1996; Nishiuchi et al. 1999).



Probably the most unusual property of GRO J1744–28 is the relatively short  $\sim 10$  s bursts observed from the source. Since the discovery, several thousands of bursts have been detected (Woods et al. 2000). During the bursts the flux increases by an order of magnitude, and it is often followed by a drop to below the pre-burst level for several tens of seconds to minutes depending on the burst fluence (Lewin et al. 1996; Nishiuchi et al. 1999; Younes et al. 2015). Pulsations are observed during the bursts, although with a phase shift of  $\sim 5\%$  with respect to the persistent emission (Kouveliotou et al. 1996; Strickman et al. 1996).

A similar bursting activity has been observed only in another source, the transient LMXB MXB 1730–335, usually referred to as the Rapid Burster (RB) (Lewin et al. 1976; Lewin et al. 1993). For both sources, it has been suggested that the origin of the bursts could be due to accretion flow instabilities which intermittently enhance the accretion rate onto the NS (so-called Type II bursts). However details are still unclear. For instance, unlike the RB, Type I bursts, associated with thermonuclear flashes on the surface of NS, are generally thought not to occur in GRO J1744–28. On the other hand, contrary to the RB case, the duration of the GRO J1744–28 bursts is remarkably stable ( $\sim 10$  s), and a large fraction of the bursts exhibit a temporal profile characterised by a fast rise followed by an exponential decay typical of classical bursters. Type II bursts in RB have rather irregular profiles. These differences are likely related to the different magnetic field strengths of the NS companion, which is expected, given the presence of pulsations, to be stronger in GRO J1744–28. In the case of GRO J1744–28, Finger et al. (1996) reported an upper limit on the magnetic field strength of  $B \leq 6 \times 10^{11}$  G. This estimate is based on the requirement that the plasma at the inner edge of the accretion disk (disrupted by the magnetosphere) moves faster than the magnetic field lines as otherwise the accretion would be centrifugally inhibited (so-called “propeller” regime, Illarionov & Sunyaev 1975). Later Cui (1997) found a possible transition to the “propeller” regime in *RXTE* data at lower luminosity, which allowed for an estimate of the magnetic field at  $\sim 2.4 \times 10^{11}$  G. Recently D’Ài et al. (2015) reported the observation of an absorption feature at  $E \sim 4.7$  keV, during the 2014 outburst of the source. Interpreting the line as due to cyclotron resonance scattering, the authors estimated a magnetic field of  $\sim 5.3 \times 10^{11}$  G in good agreement with earlier theoretical expectations. In our paper (Doroshenko et al. 2015) we confirm the presence of the cyclotron line at  $\sim 4.5$  keV.

MJD	Exposure time, ks	Period, s	$L_X$ erg s <sup>-1</sup> 2–10 keV	Orbital phase <sup>a</sup>
50528	117.5	0.467044(1)	$2.8 \times 10^{37}$	0.9
50534	101.9	0.467044(1)	$1.8 \times 10^{37}$	0.4
50550	51.6	0.46705(1)	$0.46 \times 10^{37}$	0.8
50905	62.5	source in		0.8
50911	34.5	quiescent	$3.8 \times 10^{34}$ , <sup>b</sup>	0.3
50913	67.5	state		0.5

<sup>a</sup>Ephemeris from Kouveliotou et al. (1996)

<sup>b</sup>The average luminosity for 3 observations in quiescence.

Table 13.1: Observations of the X-ray source GRO J1744–28 by *BeppoSAX*. Luminosity is estimated using unabsorbed flux in the energy range 2 – 10 keV (MECS) for the distance  $D = 8$  kpc.

## 13.2 Observations

GRO J1744–28 was observed by *BeppoSAX* several times from March 1997 to April 1998 (Tab. 13.1). In Figure 13.1 the long term source light curve observed by the ASM *RXTE* (Bradt et al. 1993) with superimposed *BeppoSAX* observations is presented. The first three observations of *BeppoSAX* were performed in the declining edge of the 1997 outburst, with a total exposure time for MECS of approximately 270 ks. In our work we use LECS, MECS, and PDS in 0.7 – 4 keV, 2 – 10 keV and 15 – 120 keV energy ranges respectively. The HPGSPC was, unfortunately, not operating during the first three observations. In the last three observations, the source was in quiescence and below the sensitivity thresholds of *BeppoSAX*, so it was not detected. The data from the quiescence, however, proved very useful for the background subtraction of the outburst PDS data.

### 13.2.1 Timing Analysis

The 2 – 10 keV MECS light curve of the first observation (MJD 50528) is presented in Figure 13.2. Bursts are clearly visible in the first two observations, whereas none is detected in the last observation carried out close to the end of the outburst at significantly lower luminosity. We detected 25 and 17 major bursts in the first two observations respectively, with a flux increase of a count rate a factor 10 or higher at the burst peak with respect to the persistent rate. Typical burst duration and the interval between the bursts are  $\sim 10$  s and  $\sim 2000$  s respectively (see also Fig. 13.3, where all detected bursts are reported). The inter-burst to burst fluence ratio in

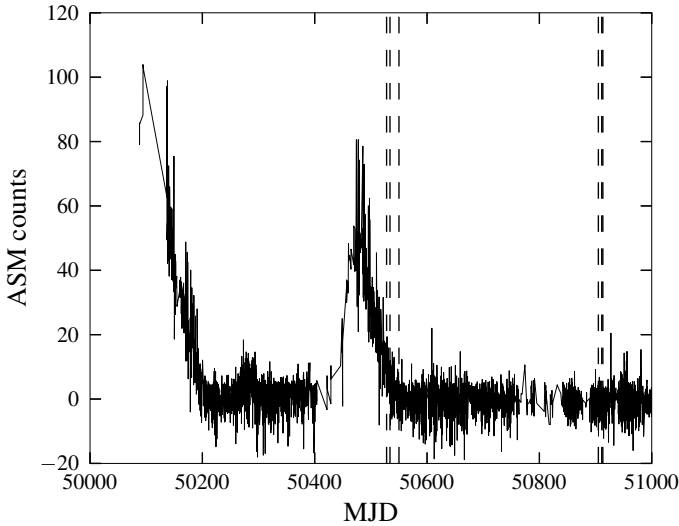


Figure 13.1: The light curve of GRO J1744–28 observed by the ASM onboard *RXTE*. Dashed lines mark the *BeppoSAX* observations (Tab. 13.1).

the energy range 2 – 20 keV is between 3 and 18, i.e. compatible with earlier reports (Lewin et al. 1996; Jahoda et al. 1997). The burst profiles exhibit variety of shapes: most are rather symmetric and in this respect are similar to Type II bursts observed in RB (Lewin et al. 1976). However, about twenty percent (for example, the next to last one in Fig. 13.3) exhibit the characteristic exponential decay typical of thermonuclear Type I bursts. The source also exhibited a few “smaller” bursts, a factor of  $\sim 6$  less luminous than the major bursts. These have already been reported by Nishiuchi et al. (1999) based on the *ASCA* data. We confirm the presence of the low luminosity bursts, although the statistical quality of the data is not sufficient for any detailed analysis.

As reported earlier by several authors (Lewin et al. 1996; Younes et al. 2015), a flux drop following the burst is a relative common feature in GRO J1744–28. Such a drop is observed in more than half of the bursts in our sample. In Figure 13.2 a fragment of the light curve in the 2 – 10 keV is presented. The decrease of the mean flux from the source after the burst, for about 100 s, is evident. Note that a similar flux depression is observed after Type II bursts of the RB and is usually associated with the depletion of the inner edge of the accretion disk after the bursting event due to enhanced accretion (Lewin et al. 1996).

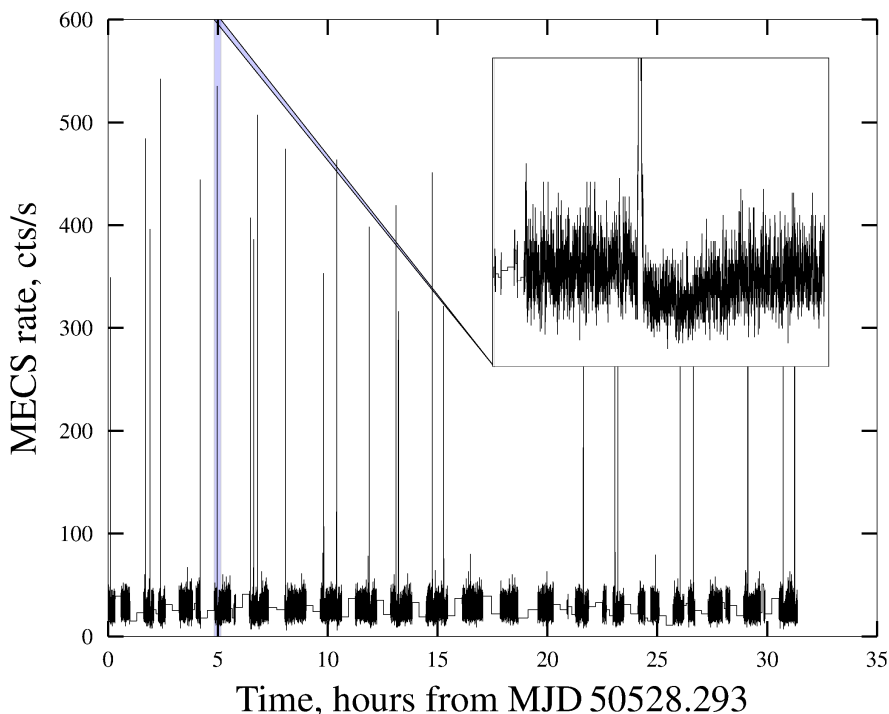


Figure 13.2: MECS light curve with bursts of the pulsar GRO J1744–28 in 1997-03-21 with 2 s bin time in 2 – 10 keV energy range. On the zoom picture the flux drop after the burst is shown.

To study coherent pulsations, we corrected the photon arrival time for Doppler delays due to the orbital motion of the spacecraft and the pulsar (using the orbital ephemeris of Kouveliotou et al. 1996). Using the phase-connection technique (see for instance Doroshenko et al. 2010a) we measure the spin period to be  $P = 0.467044(1)$  s,  $P = 0.467044(1)$  s and  $P = 0.46705(1)$  s for the March and the two April 1997 observations (all uncertainties are for 90% confidence level unless stated otherwise). Folding the light curves reveals sinusoidal, single-peaked pulse profiles (Fig. 13.4). We find that the phase of the pulsed profiles during the bursts is shifted by  $\sim 5\%$  relative to the persistent state, which is consistent with earlier reports by Kouveliotou et al. (1996); Strickman et al. (1996). The morphology of the pulse profiles appears to be consistent between the two observations and shows no apparent dependence on luminosity.



Figure 13.3: Light curves of all bursts of the pulsar GRO J1744–28 in 1997-03-21 (top) and 1997-03-27 (bottom), MECS.

The fraction of pulsed emission does change with energy. To estimate it we assumed standard backgrounds for all instruments and also took the contamination from the nearby sources to the PDS data (see Section 13.2.2). We found that the

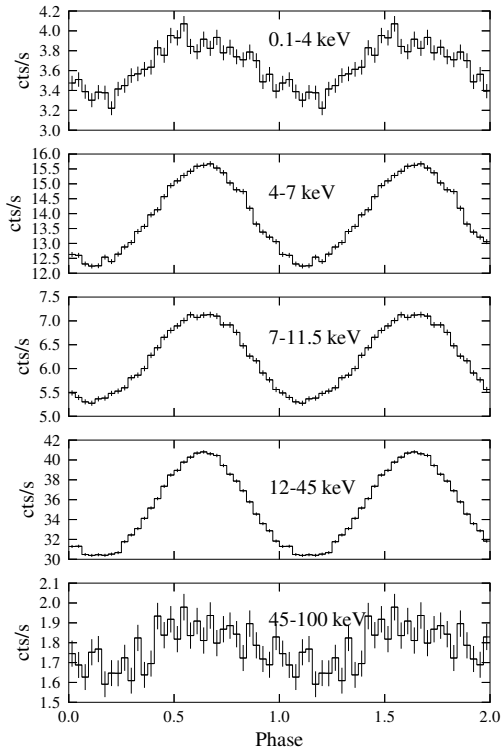


Figure 13.4: Pulse profiles of the pulsar GRO J1744–28 in 1997-03-21 for LECS (0.1 – 4 keV), MECS (4 – 7, 7 – 11.5 keV) and PDS (12 – 45, 45 – 100 keV). The spin period is  $P = 0.467044(1)$  s.

pulse fraction increases between 2 and 10 keV from about 5% to 20% (with a notable exception of a region close to the fluorescent iron line, see also D’Ài et al. 2015), and then remains fairly constant between  $\sim 10\%$  and  $\sim 30\%$  for the first two observations and between 20 – 80% for the third one. From 0.1 to 2 keV, the pulse fraction decreases from 20 – 30% to 5% although our findings are at the lowest energies and for the third observation are hampered by low statistics (Fig. 13.5).

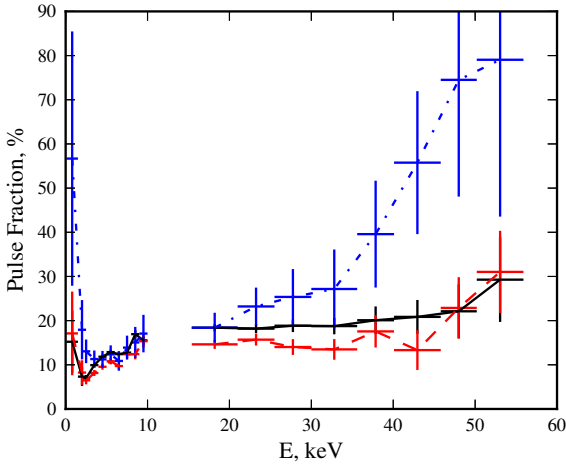


Figure 13.5: Pulse fraction of the pulsar GRO J1744–28 for 1997-03-21 - solid black line, 1997-03-27 - dashed red line, 1997-04-12 - dashed dotted blue line.

### 13.2.2 Spectral Analysis

GRO J1744–28 is located in the crowded Galactic Center region and a number of sources fall into the field of view of the telescope. This might potentially affect the spectral analysis, particularly for non-imaging instruments. Even the LECS and MECS observations could be affected as the deep *Chandra* observation of the field reveals  $\sim 40$  sources within the standard region. However, GRO J1744–28 is the brightest of these sources, therefore source confusion is not an issue for the imaging instruments, MECS and LECS. We followed, therefore, the standard analysis procedure.

The situation for the non-imaging instruments is more complicated. The MECS image reveals at least two sources besides GRO J1744–28 within the field of view of collimating instruments. These are detected irrespective of the brightness of the pulsar (see Fig. 13.6) and are plausibly identified as 1E 1743.1-2843 and Sgr A\*. To account for the in-orbit instrumental background which is rapidly changing and for the contribution of the sources contaminating the PDS data, we extracted the background-subtracted spectra for all observations (including those in quiescence) using the standard pipeline. The standard pipeline allows to account for instrumental in-orbit background. Then we subtracted quiescent spectra (obtained during the 1998 observations) from the source spectra obtained for the first three obser-

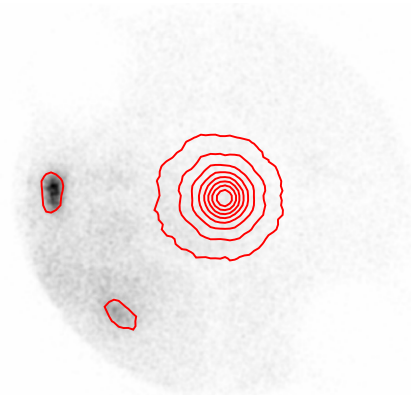


Figure 13.6: MECS image centered at GRO J1744–28 in quiescence on 1998-04-02 overlaid with contours from an observation in bright state (taken on 1997-03-21). Two additional sources detected in the MECS field of view contaminate also the PDS spectrum.

uations. Apparently, an important assumption here is that the flux of the contaminating sources remains constant. To verify that we compared the soft X-ray fluxes measured by the MECS which indeed remained constant. It is also important to note that given their short duration, the contribution of the bursts to the persistent spectrum is negligible.

We found that the observed broadband continuum spectrum can be described with *Highecut*, *Fdcut*, *NPEX* and *CompTT* continuum models. In all cases the inclusion of the fluorescent iron  $K_{\alpha}$  line at  $\sim 6.7$  keV, modeled with a simple Gaussian profile, was also required.

All continuum models, which also include interstellar absorption  $N_{\text{H}} \sim 5 \times 10^{22}$  atoms  $\text{cm}^{-2}$ , give a reasonably good  $\chi^2_{\text{red}}$  (from 0.94 for the *Highecut* model to 1.25 for *CompTT* model, see Tab. 13.2, Fig. 13.7). To demonstrate the evolution of the parameters with the luminosity we used *Highecut* based on the formal statistical quality and stability of the fit (Tab. 13.3). Regardless of the assumed continuum model, some residuals around 4 – 5 keV (Fig. 13.8) were clearly observed. The absorption-like feature at  $\sim 4$  keV was modeled with a multiplicative line with a gaussian profile. This significantly improved the fit (see residuals of Fig. 13.8). The parameters of the line are presented in Table 13.2. The chance probability for fit improvement based on the F-test is marginal  $\leq 10^{-20}$  for both observations where the line is required (see, however, Protassov et al. 2002). The feature also appeared in the phase resolved spectra (see Fig. 13.9, Tab. 13.4, 13.5). Our findings nicely agree with the absorption-like feature reported by D’Aì et al. (2015) based



Parameter	Highecut	Highecut no CRSF	Fdcut	NPEX	CompTT
$N_{\text{H}}^{(a)}$	5.7(2)	5.23(2)	5.55(8)	5.16(6)	5.84(3)
$\Gamma$	1.26(7)	1.147(3)	1.09(4)		
$E_{\text{cut}}$	18.4(1)	18.1(1)	15(1)		
$E_{\text{fold}}$	11.7(4)	11.76(7)	10.2(2)	6.1(1)	
$\alpha_1$				0.48(4)	
$\alpha_2$				-2.0	
$kT_{\text{s}}$					0.18(3)
$kT_{\text{e}}$					5.82(3)
$\tau_{\text{e}}$					13.1(1)
$E_{\text{Fe}}$	6.69(2)	6.71(2)	6.70(2)	6.68(2)	6.72(2)
$\sigma_{\text{Fe}}$	0.28(3)	0.38(2)	0.26(3)	0.23(3)	0.34(3)
$A_{\text{Fe}}^{(b)}$	7.2(6)	10.2(4)	5.8(5)	5.8(6)	8.8(5)
$E_{\text{cyc}}$	4.3(2)		4.47(9)	4.55(5)	4.2(3)
$\sigma_{\text{cyc}}$	1.2(3)		1.1(2)	1.2(1)	0.7(5)
$\delta_{\text{cyc}}$	0.12(4)		0.11(1)	0.15(1)	0.06(1)
$\chi^2_{\text{red}}/\text{dof}$	0.94 / 549	1.28 / 552	0.95 / 551	1.04 / 551	1.25 / 553

<sup>(a)</sup>in units  $10^{22}$  atoms  $\text{cm}^{-2}$

<sup>(b)</sup> $K_{\alpha}$  line normalisation in units  $10^{-3}$  ph  $\text{cm}^{-2}$   $\text{s}^{-1}$

Table 13.2: Spectral parameters of the persistent spectrum of GRO J1744–28 observed by *BeppoSAX* in 1997-03-21 for various spectral models. All energies and line widths are given in keV.

on *XMM-Newton* and *INTEGRAL* observations of the 2014 outburst. D’Aì et al. (2015) also found the two possible harmonics of the line at  $\sim 10$  keV and  $\sim 15$  keV. Unfortunately, we can not verify this result due to lack of the HPGSPS data in the 10 – 15 keV range.

By interpreting an absorption-like feature observed at  $E \sim 4.5$  keV in the spectrum of GRO J1744–28 as a CRSF, a magnetic field of  $B \sim 3.7 \times 10^{11} (1+z)$  G is obtained for the NS of the binary system. This is in strikingly good agreement with earlier estimates of the magnetic field of this pulsar, which fall in range  $(2-7) \times 10^{11}$  G (Finger et al. 1996; Rappaport & Joss 1997; Cui 1997; D’Aì et al. 2015)

We have also performed a pulse phase resolved spectral analysis to study the variation of spectral parameters with the angle of view to the NS. Only data from the observation on March 21, 1997 with highest luminosity and best counting statistics was considered. To describe the phase resolved spectra, we used the

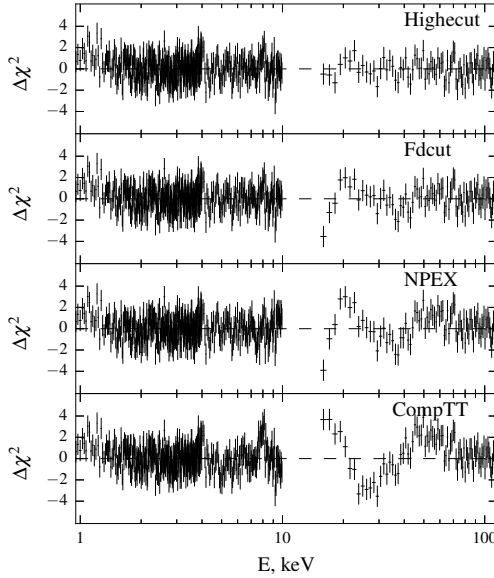


Figure 13.7: The best-fit residuals for spectra derived from the observation 1997-03-21 modeled as described in the main text. The best residuals obtained with the power law plus high-energy cutoff model, Highcut, at the top panel.

same model as for the phase averaged spectrum, i. e. a power law with high-energy cut-off (see Fig. 13.9, Tab. 13.4, 13.5). We divided the data in 10 equally spaced phase bins. We fixed the absorption component at the average value  $N_{\text{H}} = 5.7^{+0.2}_{-0.2} \times 10^{22}$  atoms  $\text{cm}^{-2}$ . The emission iron line at  $\sim 6.7$  keV and the absorption-like feature at  $\sim 4.5$  keV were also included in the phase resolved analysis. We can see the clear anti-correlation of the photon index with phase flux. The parameters of the absorption and iron lines (line centroid and width) did not exhibit any significant phase variation. The cut-off and folding energies appeared to be anti-correlated with each other.

### 13.2.2.1 Analysis of the Burst Spectra

To investigate the burst spectra with significant statistics we aligned and stacked all observed bursts using the burst start, defined as the flux increase above 150 cts/s, as a reference.

Parameter	1997-03-21	1997-03-27	1997-04-12
$N_{\text{H}}^{(a)}$	5.7(2)	5.7(2)	5.4(1)
$\Gamma$	1.26(7)	1.29(5)	1.24(3)
$E_{\text{cut}}$	18(1)	19.3(8)	24(4)
$E_{\text{fold}}$	11.7(4)	13.3(5)	12(3)
$E_{\text{Fe}}$	6.69(2)	6.70(3)	6.68(5)
$\sigma_{\text{Fe}}$	0.28(3)	0.27(4)	0.24(7)
$A_{\text{Fe}}^{(b)}$	7.2(7)	4.9(6)	1.2(2)
$E_{\text{cyc}}$	4.3(2)	4.3(1)	4.3
$\sigma_{\text{cyc}}$	1.2(3)	1.1(1)	1.1
$\delta_{\text{cyc}}$	0.12(4)	0.09(3)	0.00(1)
$F_{\text{ab}}^{(c)}$	10.1	6.5	1.2
$F_{\text{unab}}^{(c)}$	13.0	8.3	1.6
$\chi^2_{\text{red}}/\text{dof}$	0.94 / 549	1.04 / 531	1.06 / 487

<sup>(a)</sup>  $[10^{22} \text{ atoms cm}^{-2}]$

<sup>(b)</sup>  $K_{\alpha}$  line normalisation in units  $10^{-3} \text{ ph cm}^{-2} \text{ s}^{-1}$

<sup>(c)</sup> Absorbed and unabsorbed fluxes in units  $10^{-9} \text{ erg cm}^{-2} \text{ s}^{-1}$  and in 0.1 – 120 keV range.

Table 13.3: Spectral parameters of the persistent spectrum of the low mass X-ray pulsar GRO J1744–28 observed by *BeppoSAX* modelled by the *Highecut* continuum model. All energies and line widths are given in keV.

We also subtracted the contribution of the persistent emission. We found that the shape of the combined spectrum of the bursts departs significantly from that of the non-bursting spectrum (Fig. 13.8).

We first described the burst spectrum with the *Highecut* and *CompTT* models. Both models give formally acceptable results (see Tab. 13.6). The spectral parameters of the *Highecut* model are similar to the ones reported recently by Younes et al. (2015) for the burst spectra ( $\Gamma = 0.2 \pm 0.1$  and  $E_{\text{fold}} = 7.6 \pm 0.5 \text{ keV}$ ). Such a hard power law together with a soft cut-off are rather peculiar and not typical of X-ray pulsars. This might suggest that the model describes a bump-like feature at soft energies. In addition, the best-fit results for the bursts spectrum using the *CompTT* model reveals a significant change, with respect to the persistent spectrum, of both the seed photon temperature and the absorption column (see Tab. 13.6), which is difficult to understand. On the other hand, the apparent change of the seed photon temperature might suggest an additional soft component in the burst spectrum. Indeed, including a blackbody component in either model allows to achieve

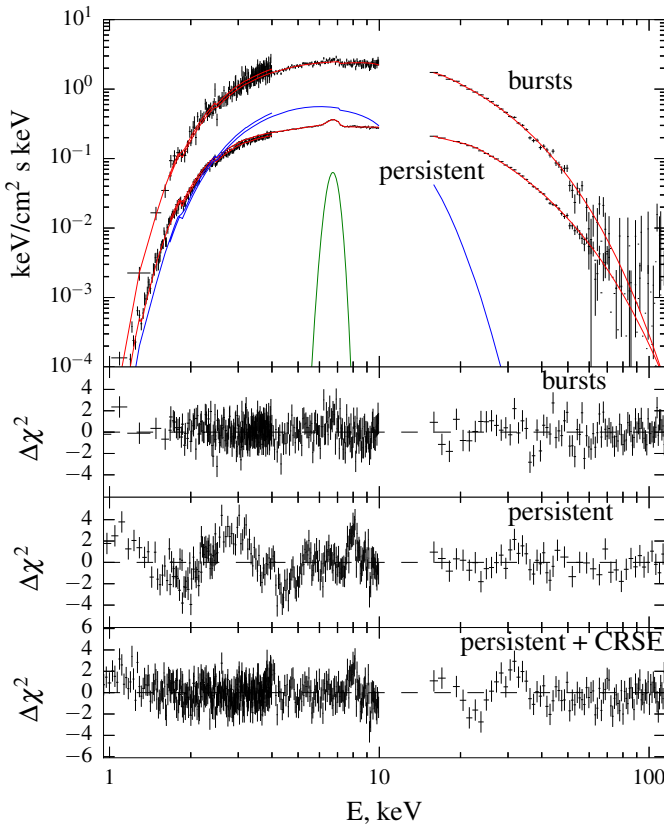


Figure 13.8: The best-fit unfolded average persistent spectrum, modelled with the Highcut continuum is shown in the top panel. We also present the best fit residuals without and with the inclusion of a cyclotron line at  $\sim 4.5$  keV. The best fit spectrum of the bursts modelled with Highcut and a black body continuum is also presented together with the residuals for the observation 1997-03-21.

comparable (or, in fact, slightly better) fit statistics while the other parameters of the continuum remain close to ones measured for the persistent spectrum. In other words, we find that the burst spectrum significantly differs from the persistent one at soft energies, and this change is well accounted for by adding a soft blackbody-like component to the unchanged continuum of the persistent spectrum. The blackbody

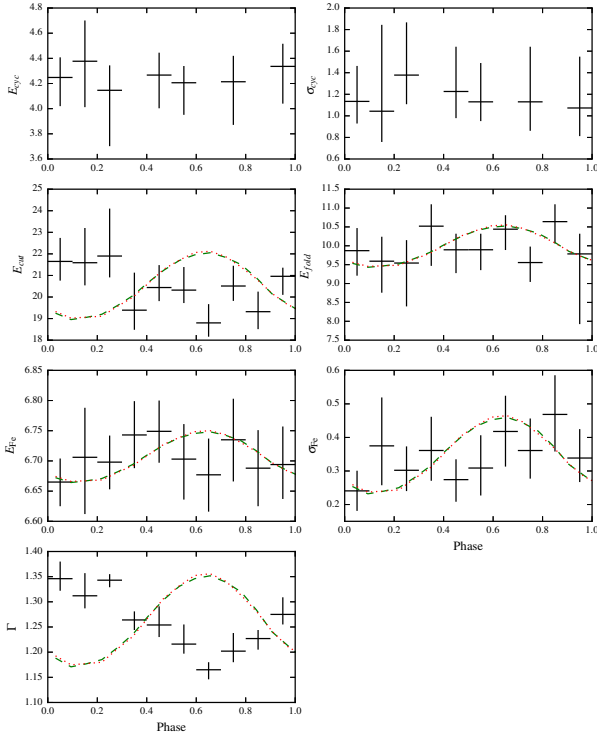


Figure 13.9: Spectral parameters of the pulsar GRO J1744–28 in 1997-03-21 with the Hightcut continuum model as function of pulse phase. Phase: 0 – 0.1, 0.1 – 0.2, 0.2 – 0.3, 0.3 – 0.4, 0.4 – 0.5, 0.5 – 0.6, 0.6 – 0.7, 0.7 – 0.8, 0.8 – 0.9, 0.9 – 1. Dashed lines are the MECS and PDS pulse profiles, they are the same.

component has a temperature about 2.1 – 2.2 keV and a size close to a NS radius (for an assumed distance of 8 kpc). The burst spectrum does not exhibit any residuals around the CRSF energy. The inclusion of a CRSF in the model, at the same energy and width as in the persistent spectrum, does not significantly improve the fit (F-test probability  $\sim 6 \times 10^{-2}$ ). We, therefore, consider the best-fit depth of 0.07(6) as an upper limit. A Fe-K line is also marginally significant in the burst spectra of the

Phase	0 - 0.1	0.1 - 0.2	0.2 - 0.3	0.3 - 0.4	0.4 - 0.5
$E_{\text{cyc}}^{(a)}$	4.25 <sup>+0.16</sup> <sub>-0.23</sub>	4.38 <sup>+0.32</sup> <sub>-0.36</sub>	4.15 <sup>+0.25</sup> <sub>-0.32</sub>	—	4.27 <sup>+0.18</sup> <sub>-0.26</sub>
$\sigma_{\text{cyc}}^{(a)}$	1.14 <sup>+0.33</sup> <sub>-0.21</sub>	1.04 <sup>+0.8</sup> <sub>-0.29</sub>	1.37 <sup>+0.27</sup> <sub>-0.22</sub>	—	1.22 <sup>+0.42</sup> <sub>-0.25</sub>
$\delta_{\text{cyc}}$	0.12 <sup>+0.02</sup> <sub>-0.02</sub>	0.09 <sup>+0.03</sup> <sub>-0.02</sub>	0.13 <sup>+0.02</sup> <sub>-0.02</sub>	—	0.11 <sup>+0.03</sup> <sub>-0.02</sub>
$\Gamma$	1.35 <sup>+0.03</sup> <sub>-0.02</sub>	1.31 <sup>+0.04</sup> <sub>-0.02</sub>	1.34 <sup>+0.02</sup> <sub>-0.02</sub>	1.26 <sup>+0.02</sup> <sub>-0.02</sub>	1.25 <sup>+0.04</sup> <sub>-0.02</sub>
$E_{\text{cut}}^{(a)}$	21.62 <sup>+1.12</sup> <sub>-0.86</sub>	21.57 <sup>+1.63</sup> <sub>-1.03</sub>	21.91 <sup>+2.24</sup> <sub>-1.01</sub>	19.39 <sup>+1.73</sup> <sub>-0.91</sub>	20.44 <sup>+1.04</sup> <sub>-0.63</sub>
$E_{\text{fold}}^{(a)}$	9.88 <sup>+0.58</sup> <sub>-0.68</sub>	9.6 <sup>+0.64</sup> <sub>-0.84</sub>	9.54 <sup>+0.62</sup> <sub>-1.18</sub>	10.51 <sup>+0.59</sup> <sub>-1.04</sub>	9.9 <sup>+0.42</sup> <sub>-0.62</sub>
$E_{\text{FeK}}^{(a)}$	6.66 <sup>+0.04</sup> <sub>-0.04</sub>	6.71 <sup>+0.08</sup> <sub>-0.09</sub>	6.7 <sup>+0.05</sup> <sub>-0.05</sub>	6.74 <sup>+0.06</sup> <sub>-0.05</sub>	6.75 <sup>+0.05</sup> <sub>-0.05</sub>
$\sigma_{\text{FeK}}^{(a)}$	0.24 <sup>+0.06</sup> <sub>-0.06</sub>	0.37 <sup>+0.14</sup> <sub>-0.12</sub>	0.3 <sup>+0.08</sup> <sub>-0.07</sub>	0.36 <sup>+0.1</sup> <sub>-0.09</sub>	0.27 <sup>+0.06</sup> <sub>-0.06</sub>
$A_{\text{FeK}}^{(b)}$	0.76 <sup>+0.12</sup> <sub>-0.1</sub>	0.8 <sup>+0.35</sup> <sub>-0.19</sub>	0.81 <sup>+0.17</sup> <sub>-0.12</sub>	1.09 <sup>+0.19</sup> <sub>-0.18</sub>	0.74 <sup>+0.14</sup> <sub>-0.11</sub>
$F_{\text{ab}}^{(c)}$	5.78	5.72	5.95	6.36	6.99
$F_{\text{unab}}^{(c)}$	8.05	7.95	8.36	8.55	9.34
$\chi_{\text{red}}^2 / \text{dof}$	1.109 / 478	1.191 / 415	1.193 / 476	1.191 / 423	1.1 / 476

<sup>(a)</sup>[keV]

<sup>(b)</sup>[ $10^{-2}$  ph cm $^{-2}$  s $^{-1}$ ]

<sup>(c)</sup>The values of absorbed and unabsorbed fluxes in 0.1 – 120 keV energy range in units  $10^{-9}$  erg/cm $^2$ /s.

Table 13.4: GRO J1744–28. Spectral parameters as function of pulse phase during the observation on 1997-03-21, Highcut continuum model. The interstellar absorption was fixed at the average value  $N_{\text{H}} = 5.7(2) \times 10^{22}$  atoms cm $^{-2}$ . Part 1.

observation on 1997-03-27. We have summarised the fit results for the 1997-03-21 data in Table 13.6.

The appearance of a prominent, blackbody-like, spectral component, typical of thermonuclear flashes in the combined burst spectra, might come from either all or just some bursts. To discriminate between the two possibilities we first checked the hardness ratio for individual bursts using the MECS/PDS light curves, but found no significant variation between the bursts. We also attempted to group bursts for spectral analysis, using different criteria (the bursts coming in a sequence of two, single bursts, bursts with the same classical I type shape - fast rise and slow decline). We found that for any grouping, the spectra had essentially the same shape with two prominent soft and hard components. We concluded that the soft component seen in the combined burst spectra is likely present in spectra of most, if not all, individual bursts.

To investigate the pulse phase dependence of the black body and power law components we carried out the phase resolved analysis of the burst spectrum. Unfortu-

Phase	0.5 - 0.6	0.6 - 0.7	0.7 - 0.8	0.8 - 0.9	0.9 - 1
$E_{\text{cyc}}^{(a)}$	$4.21^{+0.13}_{-0.26}$	—	$4.21^{+0.21}_{-0.34}$	—	$4.34^{+0.18}_{-0.3}$
$\sigma_{\text{cyc}}^{(a)}$	$1.13^{+0.36}_{-0.18}$	—	$1.13^{+0.51}_{-0.27}$	—	$1.07^{+0.48}_{-0.26}$
$\delta_{\text{cyc}}$	$0.11^{+0.03}_{-0.01}$	—	$0.08^{+0.03}_{-0.02}$	—	$0.09^{+0.02}_{-0.02}$
$\Gamma$	$1.22^{+0.04}_{-0.02}$	$1.16^{+0.02}_{-0.02}$	$1.2^{+0.04}_{-0.02}$	$1.23^{+0.02}_{-0.02}$	$1.28^{+0.04}_{-0.02}$
$E_{\text{cut}}^{(a)}$	$20.31^{+1.08}_{-0.59}$	$18.8^{+0.87}_{-0.64}$	$20.51^{+0.95}_{-0.69}$	$19.32^{+0.93}_{-0.81}$	$20.96^{+4.26}_{-0.86}$
$E_{\text{fold}}^{(a)}$	$9.89^{+0.42}_{-0.54}$	$10.44^{+0.37}_{-0.55}$	$9.55^{+0.42}_{-0.51}$	$10.64^{+0.46}_{-0.58}$	$9.78^{+0.54}_{-1.86}$
$E_{\text{FeK}}^{(a)}$	$6.7^{+0.06}_{-0.07}$	$6.68^{+0.06}_{-0.06}$	$6.73^{+0.07}_{-0.07}$	$6.69^{+0.06}_{-0.06}$	$6.69^{+0.06}_{-0.06}$
$\sigma_{\text{FeK}}^{(a)}$	$0.31^{+0.1}_{-0.08}$	$0.42^{+0.11}_{-0.1}$	$0.36^{+0.1}_{-0.08}$	$0.47^{+0.12}_{-0.11}$	$0.34^{+0.09}_{-0.07}$
$A_{\text{FeK}}^{(b)}$	$0.73^{+0.18}_{-0.12}$	$1.25^{+0.21}_{-0.23}$	$0.77^{+0.18}_{-0.14}$	$1.33^{+0.24}_{-0.24}$	$0.79^{+0.17}_{-0.12}$
$F_{\text{ab}}^{(c)}$	7.59	7.75	7.44	6.91	6.29
$F_{\text{unab}}^{(c)}$	9.93	10.17	10.08	9.28	8.63
$\chi^2_{\text{red}} / \text{dof}$	1.22 / 481	1.498 / 429	1.258 / 478	1.373 / 428	1.125 / 475

(a) [keV]

(b) [ $10^{-2}$  ph cm $^{-2}$  s $^{-1}$ ](c) The values of absorbed and unabsorbed fluxes in 0.1 – 120 keV energy range in units  $10^{-9}$  erg / cm $^2$  / s.

Table 13.5: GRO J1744–28. Spectral parameters as function of pulse phase during the observation on 1997-03-21, Highecut continuum model. The interstellar absorption was fixed at the average value  $N_{\text{H}} = 5.7(2) \times 10^{22}$  atoms cm $^{-2}$ . Part 2.

nately, the statistics was insufficient to constrain all model parameters, so we kept most of the parameters fixed to the best-fit phase averaged values, and only allowed the normalisation of the continuum components to vary. The results are shown in Figure 13.10. The pulse fraction for the soft and hard components are  $6.5\% \pm 3.4\%$  and  $13.8\% \pm 1.9\%$  respectively, i.e. the hard component varies with pulse-phase stronger than the soft one.

To explore the time evolution of both components along the burst, we performed also time-resolved spectral analysis using the stacked data of all bursts. Time intervals were selected so to have enough statistics to significantly constrain the fit parameters. It is interesting to note, that both the temperature and normalisation of the blackbody component (and thus the size of the emitting region) change along the burst as shown in Figure 13.11.

A possible nature of the thermal component could be caused by thermonuclear flashes which possibly trigger the accretion rate enhancement responsible for the bursts observed in the source. This hypothesis is based on several similarities be-

Parameter	Highecut	bb+Highecut	CompTT	bb+CompTT
$N_{\text{H}}^{(a)}$	5.0(3)	5.1(7)	3.4(2)	5.2
$kT_{\text{bb}}$		2.1(3)		2.2(1)
$R_{\text{bb}}^{(b)}$		8(5)		8(3)
$\Gamma$	0.26(8)	0.8(4)		
$E_{\text{cut}}$	4(1)	18(5)		
$E_{\text{fold}}$	7.6(2)	9(1)		
$kT_{\text{s}}$			1.51(8)	0.2
$kT_{\text{e}}$			5.4(2)	5.2(1)
$\tau_{\text{e}}$			4.6(5)	18(1)
$\chi_{\text{red}}^2/\text{dof}$	0.96 / 408	0.95 / 406	1.03 / 409	1.02 / 409

<sup>(a)</sup>in units  $10^{22}$  atoms  $\text{cm}^{-2}$

<sup>(b)</sup>in km

Table 13.6: The best-fit parameters of the bursts spectrum GRO J1744–28 in 1997-03-21. All the energies and the line widths are given in keV. The absorbed and unabsorbed fluxes in 0.1 – 120 keV energy range are  $F_{\text{ab}} = 6.09 \times 10^{-8}$  erg  $\text{cm}^{-2}$   $\text{s}^{-1}$ ,  $F_{\text{unab}} = 6.83 \times 10^{-8}$  erg  $\text{cm}^{-2}$   $\text{s}^{-1}$ .

tween typical Type I bursts and the thermal component, namely, the burst duration of 10 s, the inter-burst to burst fluence ratio and cooling as a burst progresses. There are some observational and theoretical arguments that disfavour this hypothesis. These cannot be verified with the existing data. The detailed discussion was published in our paper (Doroshenko et al. 2015).

### 13.3 Conclusion

We presented the results of the analysis of three *BeppoSAX* observations, with a total exposure time 270 ks, carried out in the declining phase of the 1997 outburst of the bursting pulsar GRO J1744–28.

Pulsations with a period of 0.4670 s with a stable pulse profile, that did not change with time and energy, were detected in all observations. The pulsed fraction was found to vary with energy, reaching a minimum of 10 – 20% in the energy range 5 – 40 keV and increasing for higher and lower energies, especially at lower luminosities. Several tens of bursts with typical durations of about 10 s were detected as well. Depletion in the light curve is observed after at least some of the bursts. The source luminosity typically increases by factor of ten during the bursts, although a number of dimmer bursts are also observed.



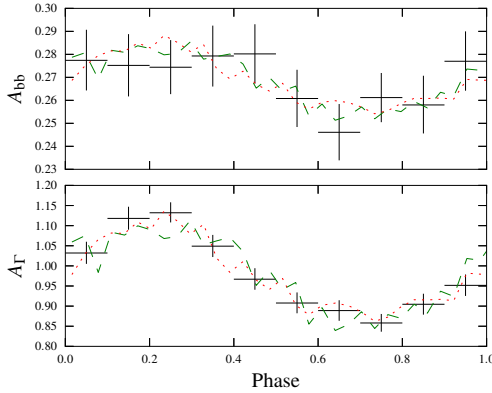


Figure 13.10: Changing normalisation of the soft (top) and hard (bottom) part of the bursts spectrum with phase for the GRO J1744–28 in 1997-09-21.  $\chi^2_{\text{red}}$  lies in region from 0.97 to 1.45.

The non-bursting broad band X-ray spectrum was found to be well described by several phenomenological models typically used for accreting pulsars. An iron line at  $\sim 6.7$  keV and an absorption feature at  $\sim 4.5$  keV were also required to fit the data. We interpret the absorption feature as a cyclotron line which implies a magnetic field of the NS of  $B \sim 3.7(1+z) \times 10^{11} \approx 5 \times 10^{11}$  G, considering the upper limit of the gravitational redshift  $z = 0.3$  for a canonical NS, if the line is produced

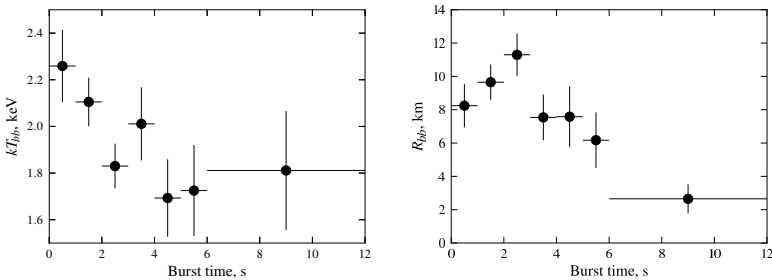


Figure 13.11: Cooling of the soft component, during the bursts. The probability that the observed temperatures are due to a statistical fluctuation is  $\leq 1.7 \times 10^{-8}$  (from Kolmogorov-Smirnov test), so the trend is significant.

at the NS surface. This value is in good agreement with earlier predictions and with the recent observations of the 2014 outburst with *XMM-Newton* and *INTEGRAL*. D’Aì et al. (2015) have detected the same feature at  $E \sim 4.7$  keV in agreement, within uncertainties, with our measurement.

The average burst spectrum could be represented as a combination of the harder non-bursting spectrum and an additional soft thermal component with temperature of about 2 keV. The burst spectrum requires neither the iron 6.7 keV line nor the absorption feature at 4.5 keV. Both components are pulsed although the amplitude is smaller for the soft component,  $\sim 6.5\%$  vs  $\sim 13.8\%$ .

## **Part III**

# **Discussion and Conclusions**



## CHAPTER 14

---

### Summary and Interpretation of Spectral Analysis Results

In the previous chapters, results of the broadband (0.1 – 120 keV) spectral analysis for the 9 accreting pulsars with cyclotron lines observed by the *BeppoSAX* satellite were presented. For the first time such an analysis was done on *BeppoSAX* data for a large sample of sources in a uniform and systematic way, so it is now interesting to compare the results and attempt to assess similarities and differences between the individual objects.

Tables 14.1, 14.2 summarise the basic parameters for the pulsars in the sample including the spin periods, the X-ray luminosities and the energies of the cyclotron lines determined in this work with representative observations. The best fit un-

	Type	$P_{\text{orb}}$ days	$P$ s	$L_X \times 10^{37}$ erg s <sup>-1</sup>	$D^{(*)}$ kpc
Her X-1 1996-07-24	LMXB	1.7	1.2377397(1)	3.6	6.6
4U 1626-67 1996-08-06	LMXB	0.02917	7.6679(1)	0.6	9
4U 1907+09 1997-09-27	HMXB	8.3753	440.99(1)	0.3	5
4U 1538-52 1998-07-29	HMXB	3.73	528.218(1)	0.3	5.5
Vela X-1 1996-12-24	HMXB	8.964	283.271(1)	0.3	2
Cen X-3 1997-02-27	HMXB	2.09	4.814(1)	21	8
4U 0115+63 1999-03-06	HMXB transient	24.3	3.6137(1)	8.7	7
XTE J1946+274 1998-10-09	HMXB transient	169.2	15.8262(1)	4.6	9.5
GRO J1744-28 1997-03-21	LMXB transient burster	11.8	0.467044(1)	10	8

(\*)Distance used to determine the luminosity of the source.

Table 14.1: Sample of the sources observed by *BeppoSAX*, their types, orbital and spin periods, X-ray luminosity (in the 0.1 – 120 keV energy band) and distance. Results are presented for one observation from each source.

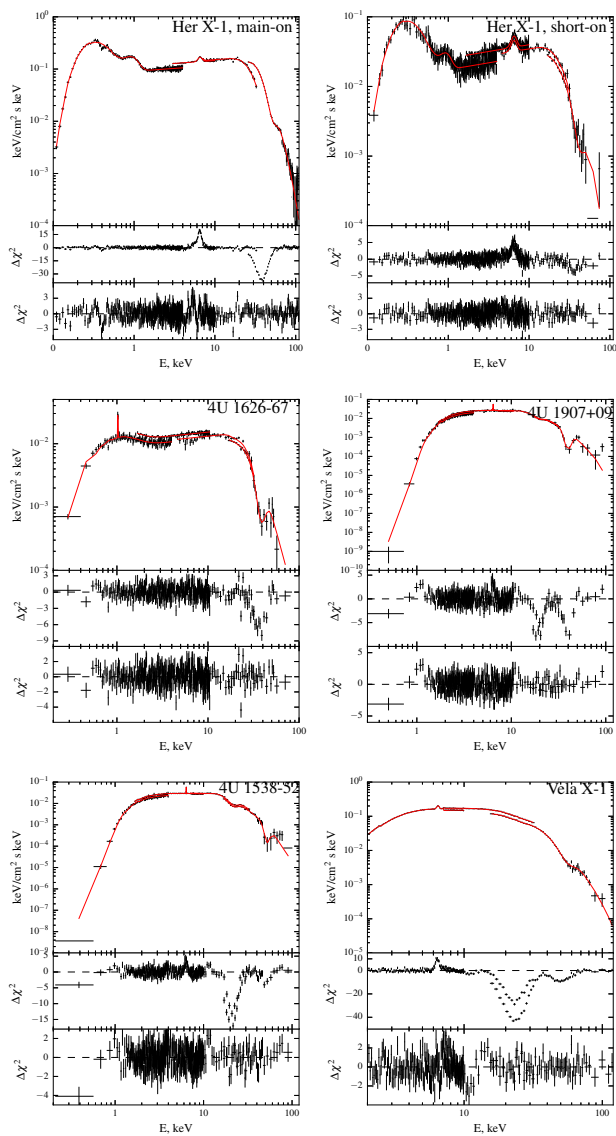


Figure 14.1: The best fits of the spectra for the sources observed by *BeppoSAX* and the residuals: Her X-1 (1996-07-24 - left, 1998-07-09 - right), 4U 1626-67 (1996-08-06), 4U 1907+09 (1997-09-27), 4U 1538-52 (1998-07-29), Vela X-1 (1996-12-24). Part 1.

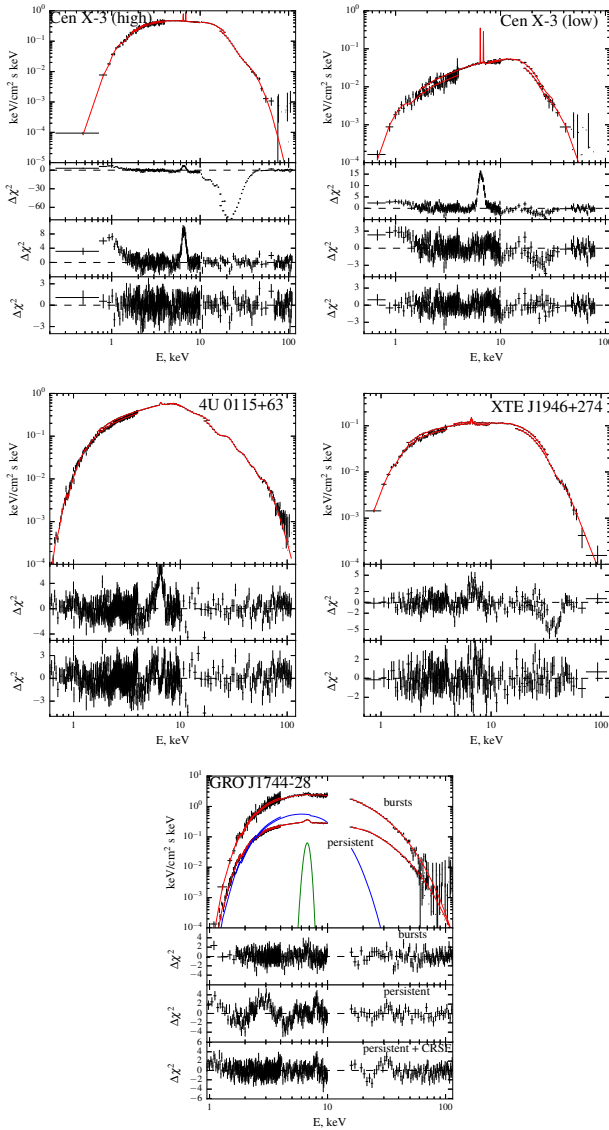


Figure 14.2: The best fits of the spectra for the sources observed by *BeppoSAX* and the respective residuals: Cen X-3 (1997-02-27 - left, 1996-08-12 - right), 4U 0115+63 (1999-03-06), XTE J1946+274 (1998-10-09), GRO J1744-28 (1997-03-21). Part 2.

	$E_{\text{cyc}}$ keV	$A_{\text{E}^*_{\text{cyc}}}$ %	$B(1+z)^{-1} \times 10^{12}$ G
Her X-1 1996-07-24	$42.18^{+0.15}_{-0.11}$	13(1)	3.6
4U 1626-67 1996-08-06	$38.38^{+1.28}_{-1.21}$	-	3.3
4U 1907+09 1997-09-27	$19.44^{+0.59}_{-0.61}$	8(3)	1.7
4U 1538-52 1998-07-29	$21.51^{+0.19}_{-0.19}$	6(2)	1.8
Vela X-1 1996-12-24	$25.03^{+0.18}_{-0.16}$	13(3)	2.2
Cen X-3 1997-02-27	$27.66^{+0.73}_{-0.65}$	8(3)	2.4
4U 0115+63 1999-03-06	$13.39^{+0.07}_{-0.04}$	10(3)	1.1
XTE J1946+274 1998-10-09	$38.34^{+1.45}_{-1.3}$	-	3.3
GRO J1744-28 1997-03-21	$4.3^{+0.2}_{-0.2}$	9(3)	0.4

\* $A_{\text{E}^*_{\text{cyc}}}$  is the amplitude of the change of the source cyclotron with pulse phase.

Table 14.2: Cyclotron lines energies and the values of the pulsars magnetic fields for the sources observed by *BeppoSAX*.

folded spectra for all sources obtained in previous chapters are presented in Figures 14.1, 14.2 for overview. The best fit residuals are also included (for Her X-1 and Cen X-3 separately for the two luminosity states).

Already visual inspection of the spectra reveals the peculiar continuum shape of the LMXB sources Her X-1 and 4U 1626-67, both of which exhibit a significant excess in the soft part of the spectrum. As discussed in Hickox et al. (2004), this excess is likely associated with reprocessing of X-rays in the inner regions of the accretion disc or atmosphere of the companion, which is consistent with the observed drop in the pulse fraction reported in Chapters 5, 6. The spectra of the other pulsars are qualitatively similar with each other, and are consistent with a comptonisation spectrum where differences can mainly be attributed to different optical depths, electron temperatures and cyclotron line parameters of individual objects.

Taking into account that there are likely significant variations of physical parameters across the emission region in X-ray pulsars, even the “physical” models used here are, in fact, just a rough approximation. Choice of the continuum model is thus somewhat arbitrary and may also affect the parameters of the cyclotron line. It is interesting, therefore, to investigate how the choice of the continuum model affects the deduced CRSF parameters from an observational point of view. This issue is often discussed in literature for individual sources. However, it was never addressed systematically using high quality data of a larger sample of pulsars.

In Figures 14.3, 14.4 the dependence of the line parameters for the six considered continuum models (Highecut, Fdcut, NPEX, Cutoffpl, CompTT, BW) is presented for all pulsars in the sample (including the best-fit  $\chi^2_{\text{red}}$  for reference).



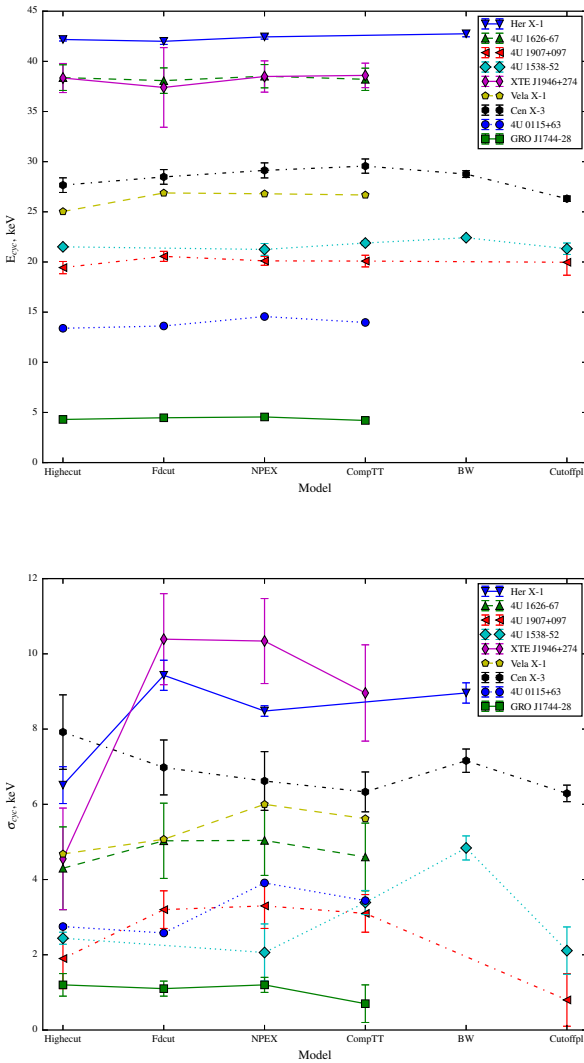


Figure 14.3: Changes of the cyclotron line energy and width with different continuum models of the *BeppoSAX* sources with the cyclotron line, which were analysed in this work.

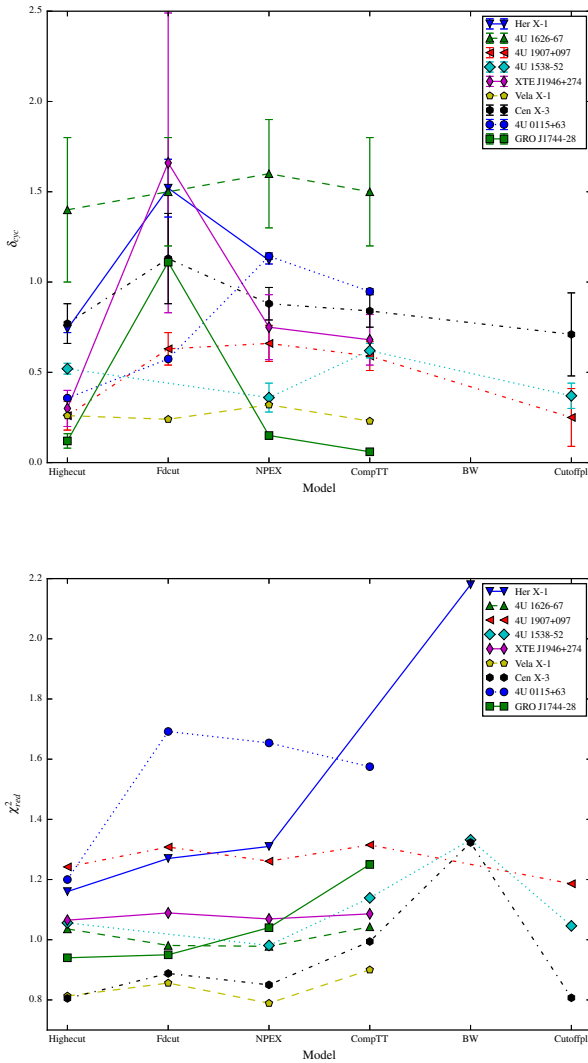


Figure 14.4: Changes of the cyclotron line depth and  $\chi^2_{red}$  with different continuum models of the *BeppoSAX* sources with the cyclotron line, which were analysed in this work.

Parameter	Her X-1 1996-07-24	4U 1626-67 1996-08-06	4U 1907+09 1997-09-27	4U 1538-52 1998-07-29	XTE J1946+274 1998-10-09
$N_{\text{H}}^{(a)}$	$0.0109^{+0.0003}_{-0.0002}$	$0.09^{+0.02}_{-0.02}$	$2.72^{+0.06}_{-0.09}$	$1.66^{+0.02}_{-0.02}$	$1.32^{+0.07}_{-0.06}$
$\Gamma$	$0.895^{+0.008}_{-0.002}$	$0.85^{+0.01}_{-0.01}$	$1.17^{+0.02}_{-0.02}$	$1.14^{+0.01}_{-0.01}$	$0.88^{+0.03}_{-0.03}$
$E_{\text{cut}}^{(b)}$	$20.94^{+0.44}_{-0.06}$	$19.19^{+1.19}_{-1.03}$	$12.64^{+0.77}_{-0.55}$	$13.96^{+0.18}_{-0.18}$	$18.04^{+0.53}_{-0.35}$
$E_{\text{fold}}^{(b)}$	$11.11^{+0.09}_{-0.13}$	$10.42^{+0.93}_{-1.0}$	$11.6^{+0.8}_{-0.77}$	$11.85^{+0.18}_{-0.19}$	$9.36^{+0.36}_{-0.54}$
$E_{\text{cyc}}^{(b)}$	$42.18^{+0.15}_{-0.11}$	$38.38^{+1.28}_{-1.21}$	$19.44^{+0.59}_{-0.61}$	$21.51^{+0.19}_{-0.19}$	$38.34^{+1.45}_{-1.3}$
$\sigma_{\text{cyc}}^{(b)}$	$6.51^{+0.49}_{-0.16}$	$4.3^{+1.1}_{-1.0}$	$1.9^{+0.8}_{-0.8}$	$2.44^{+0.16}_{-0.15}$	$4.55^{+1.35}_{-1.21}$
$\delta_{\text{cyc}}$	$0.74^{+0.01}_{-0.02}$	$1.4^{+0.4}_{-0.3}$	$3.06^{+1.62}_{-1.92}$	$3.64^{+1.04}_{-1.13}$	$0.3^{+0.1}_{-0.1}$
$\chi_{\text{red}}^2 / \text{dof}$	1.16 / 624	1.036 / 363	1.176 / 437	1.056 / 373	1.065 / 599
$^{(a)}[10^{22} \text{atoms cm}^{-2}]$					
$^{(b)}[\text{keV}]$					

Table 14.3: The best-fit parameters of the X-ray pulsars in the sample for the Highcut continuum with a smoothing Gaussian at the cutoff energy (one observation for each source). Part 1.

As can be seen in the figures, in most cases it is possible to achieve acceptable fits with all models and the line energy is not strongly affected by the model choice as long as it provides an adequate description for the broadband spectrum.

However, this is not always the case for the width and depth of the CRSF, which sometimes strongly depend on the choice of the continuum model. The greatest changes are visible for the Fdcut model, which results in wider and deeper lines compared to other models. This can be, for instance, due to the fact that this model is unable to fully describe the intrinsic cutoff of the spectrum and the remaining residuals are modelled as CRSF contribution. This shall be taken into consideration when comparing CRSF parameters published in literature assuming different continuum models, especially for data with low counting statistics. Indeed, in this case, an incorrect choice of the continuum model might still yield acceptable fit statistics, yet line parameters will be biased. It is important, therefore, to investigate several continuum models and verify that the results are consistent.

As we know from the previous chapters, the most “universal” continuum model out of all models considered is the Highcut with the smoothing Gaussian tied to the cutoff energy (Tab. 14.3, 14.4). This model also yields better statistical quality of the fit and stable fit in most cases. I conclude, therefore, that this model is the best choice for sample studies of multiple accreting pulsars. On the other hand, out of the two physical models considered, the ComTTT appears to be more flexible, although it still was not possible to achieve an acceptable fit for all sources

Parameter	Vela X-1 1996-12-24	Cen X-3 1997-02-27	4U 0115+63 1999-03-06	GRO J1744-28 1997-03-21
$N_{\text{H}}^{(a)}$	$3.15^{+0.03}_{-0.04}$	$1.88^{+0.04}_{-0.07}$	$1.13^{+0.01}_{-0.03}$	5.7(2)
$\Gamma$	$1.332^{+0.006}_{-0.003}$	$1.19^{+0.02}_{-0.04}$	$0.442^{+0.002}_{-0.003}$	1.26(7)
$E_{\text{cut}}^{(b)}$	$23.9^{+0.13}_{-0.13}$	$17.49^{+0.69}_{-1.09}$	$8.62^{+0.03}_{-0.06}$	18.4(1)
$E_{\text{fold}}^{(b)}$	$13.59^{+0.15}_{-0.14}$	$7.09^{+0.39}_{-0.30}$	$10.38^{+0.02}_{-0.03}$	11.7(4)
$E_{\text{cyc}}^{(b)}$	$25.03^{+0.18}_{-0.16}$ $55.27^{+0.6}_{-0.57}$	$27.66^{+0.73}_{-0.65}$	$13.39^{+0.07}_{-0.04}$ $22.55^{+0.05}_{-0.07}$ $33.94^{+0.46}_{-0.09}$ $44.08^{+0.96}_{-0.17}$ $54.32^{+0.44}_{-0.43}$	4.3(2)
$\sigma_{\text{cyc}}^{(b)}$	$4.68^{+0.21}_{-0.15}$ $6.9^{+0.43}_{-0.44}$	$7.92^{+0.99}_{-0.43}$	$2.75^{+0.04}_{-0.05}$ 4 4 4 4	1.2(3)
$\delta_{\text{cyc}}$	$0.26^{+0.01}_{-0.01}$ $0.62^{+0.05}_{-0.04}$	$0.77^{+0.11}_{-0.08}$	$0.357^{+0.007}_{-0.007}$ $0.78^{+0.01}_{-0.01}$ $0.71^{+0.01}_{-0.01}$ $0.62^{+0.02}_{-0.02}$ $0.52^{+0.03}_{-0.03}$	0.12(4)
$\chi_{\text{red}}^2 / \text{dof}$	0.813 / 283	0.805 / 383	1.2 / 581	0.94 / 549
$^{(a)}$ [ $10^{22}$ atoms $\text{cm}^{-2}$ ]				
$^{(b)}$ [keV]				

Table 14.4: The best-fit parameters of the X-ray pulsars in the sample for the `Highecut` continuum with a smoothing `Gaussian` at the cutoff energy (one observation for each source). Part 2.

(Tab. 14.5, 14.6). Taking into account that in some cases this model does provide very good description of the data, it is likely that in other cases additional components like reflection/partial covering absorption might contribute to the observed spectra, which results in more complex spectral shapes. Note that while it is easier to account for such components using the more flexible phenomenological models, interpretation of the results might actually become more complicated.

Nevertheless, the phenomenological `Highecut` model is the only model which does provide acceptable fits for all sources in our sample. The model was chosen for the quantitative comparison of the spectra. The respective best-fit parameters for all analysed pulsars are given in Tables 14.3, 14.4.

Parameter	4U 1626-67 1996-08-06	4U 1907+09 1997-09-27	4U 1538-52 1998-07-29	XTE J1946+274 1998-10-09
$N_H^{(a)}$	$0.04^{+0.01}_{-0.01}$	$3.00^{+0.03}_{-0.06}$	$0.88^{+0.07}_{-0.06}$	$1.37^{+0.06}_{-0.06}$
$kT^{(b)}$	$6.0^{+0.2}_{-0.2}$	$6.51^{+0.68}_{-0.54}$	$5.12^{+0.07}_{-0.07}$	$5.62^{+0.14}_{-0.16}$
$T_p^{(b)}$	$0.86^{+0.05}_{-0.05}$	$0.17^{+0.21}_{-0.16}$	$0.66^{+0.02}_{-0.02}$	$0.01^{+0.68}_{-0.01}$
$\tau$	$15.86^{+0.42}_{-0.48}$	$6.2^{+0.1}_{-0.2}$	$7.11^{+0.09}_{-0.09}$	$19.05^{+0.29}_{-0.57}$
$E_{cyc}^{(b)}$	$38.21^{+1.1}_{-0.95}$	$20.09^{+0.58}_{-0.44}$ $40.95^{+3.45}_{-2.1}$	$21.89^{+0.25}_{-0.24}$	$38.6^{+1.17}_{-1.22}$
$\sigma_{cyc}^{(b)}$	$4.6^{+0.9}_{-0.8}$	$3.1^{+0.5}_{-0.5}$ $9.65^{+2.81}_{-2.08}$	$3.39^{+0.32}_{-0.3}$	$8.96^{+0.99}_{-1.28}$
$\delta_{cyc}$	$1.5^{+0.3}_{-0.3}$	$0.59^{+0.08}_{-0.08}$ $2.0^{+0.5}_{-0.4}$	$0.62^{+0.04}_{-0.03}$	$0.68^{+0.11}_{-0.14}$
$\chi^2_{red} / dof$	1.043 / 365	1.315 / 437	1.139 / 376	1.086 / 600
$(a) [10^{22} \text{atoms cm}^{-2}]$				
$(b) [\text{keV}]$				

Table 14.5: The best-fit parameters of the X-ray pulsars in the sample for the CompTT continuum model (one observation for each source). Part 1.

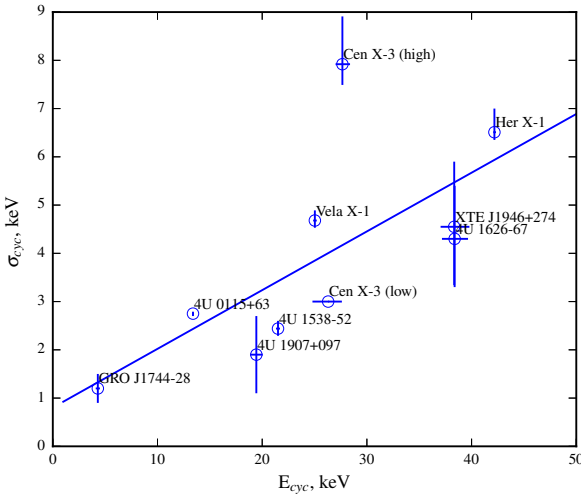


Figure 14.5: Correlation between the CRSF energy and width. The blue line shows the linear fit to the points with  $\sigma_{cyc} = 0.12E_{cyc} + 0.8$ .

Parameter	Vela X-1 1996-12-24	Cen X-3 1997-02-27	4U 0115+63 1999-03-06	GRO J1744-28 1997-03-21
$N_{\text{H}}^{(a)}$	$3.52^{+0.29}_{-0.46}$	$2.17^{+0.01}_{-0.06}$	$0.8^{+0.02}_{-0.01}$	5.84(3)
$kT^{(b)}$	$7.77^{+0.23}_{-0.11}$	$4.50^{+0.03}_{-0.09}$	$5.56^{+0.01}_{-0.01}$	5.82(3)
$T_{\text{p}}^{(b)}$	$0.001^{+6.016}_{0.0}$	$0.20^{+0.03}_{-0.08}$	$0.63^{+0.004}_{-0.003}$	0.18(3)
$\tau$	$10.6^{+0.2}_{-0.2}$	$14.69^{+0.18}_{-0.04}$	$27.07^{+0.05}_{-0.14}$	13.1(1)
$E_{\text{cyc}}^{(b)}$	$26.68^{+0.71}_{-0.45}$ $55.5^{+1.5}_{-1.14}$	$29.56^{+0.38}_{-0.71}$	$13.97^{+0.02}_{-0.02}$ $22.55^{+0.06}_{-0.03}$ $32.15^{+0.09}_{-0.03}$ $41.34^{+0.14}_{-0.05}$ $52.0^{+0.12}_{-0.11}$	4.2(3)
$\sigma_{\text{cyc}}^{(b)}$	$5.62^{+0.82}_{-0.49}$ $11.06^{+1.44}_{-1.32}$	$6.33^{+0.44}_{-0.53}$	$3.44^{+0.02}_{-0.02}$ 4 4 4 4	0.7(5)
$\delta_{\text{cyc}}$	$0.23^{+0.03}_{-0.02}$ $0.99^{+0.14}_{-0.14}$	$0.84^{+0.02}_{-0.09}$	$0.948^{+0.004}_{-0.015}$ $1.714^{+0.012}_{-0.005}$ $1.57^{+0.01}_{-0.01}$ $1.47^{+0.01}_{-0.02}$ $1.27^{+0.02}_{-0.03}$	0.06(1)
$\chi^2_{\text{red}} / \text{dof}$	0.900 / 284	0.944 / 384	1.575 / 582	1.25 / 553
$^{(a)}$ [ $10^{22}$ atoms $\text{cm}^{-2}$ ]				
$^{(b)}$ [keV]				

Table 14.6: The best-fit parameters of the X-ray pulsars in the sample for the CompTT continuum model (one observation for each source). Part 2.

Figures 14.5, 14.6 show the dependence between the cyclotron line energy and width, which appear to be correlated. A similar correlation was reported by Coburn et al. (2002) for the sample of pulsars observed with RXTE. The first figure shows only one measurement for each source (except for Cen X-3, which is presented in high and low states). As we can see, the Cen X-3 in high state seems to deviate from the general trend. However, as can also be seen from Table 14.1, Cen X-3 high state has the highest luminosity of all analysed sources. The low luminosity state for Cen X-3, exhibits a slightly different behaviour, more in line with the other sources. Figure 14.6 shows the same correlation for all *BeppoSAX* observations and all sources from the sample where the general trend appears clearer. While

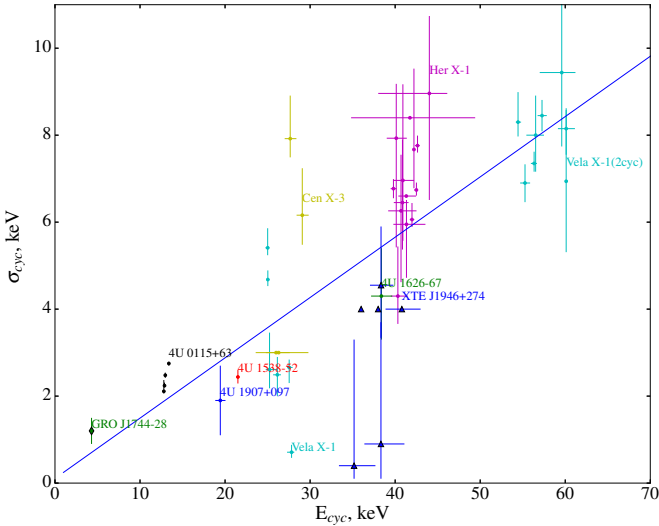


Figure 14.6: Correlation between CRSF energy and CRSF width for all *BeppoSAX* observations in the sample. The blue line shows the linear dependence  $\sigma_{\text{cyc}} = 0.14E_{\text{cyc}} + 0.1$ .

the correlation of line energy and width was reported previously, here I extend it to lower energies. Indeed, GRO J1744–28 with the lowest energy of the CRSF known so far seems to follow the same trend as other sources. Using the Monte Carlo sampling, Coburn et al. (2002) has demonstrated that this correlation is real and not due to the intrinsic correlation between the parameters in the spectral model, which is actually consistent with qualitative agreement with theoretical predictions for the Doppler line broadening.

Figures 14.7, 14.8 show the observed relation between the energy and depth and between the width and the depth of the cyclotron line. Both seem to be linearly correlated in most cases (except 4U 1626–67). The general trend is again consistent with findings by Coburn et al. (2002), i.e. the lines become deeper and broader with energy. This dependence is somewhat harder to interpret, as opposite behaviour could actually be expected based on the expected cyclotron scattering cross-sections alone. Photon spawning, non-isotropic angular re-distribution of photons and emission region geometry can be factors likely responsible for the observed correlation (Coburn et al. 2002). Note that the low mass pulsar 4U 1626–67 deviates from the general trend and exhibits a deeper line than typically observed.

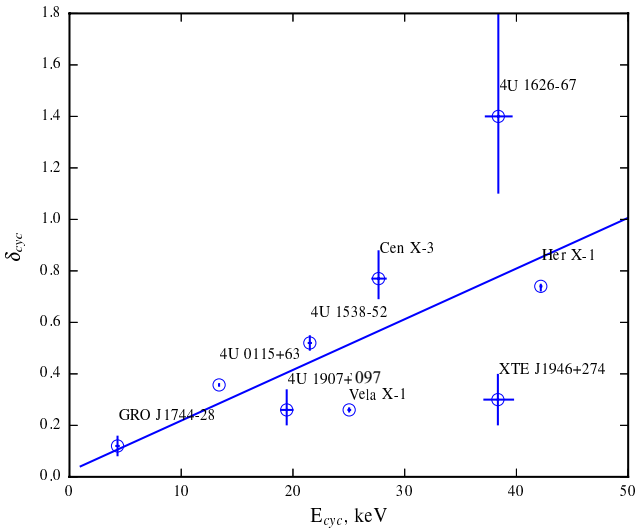


Figure 14.7: Correlation between CRSF energy and depth. The green line shows the linear dependence  $\delta_{\text{cyc}} = 0.02E_{\text{cyc}} + 0.02$ .

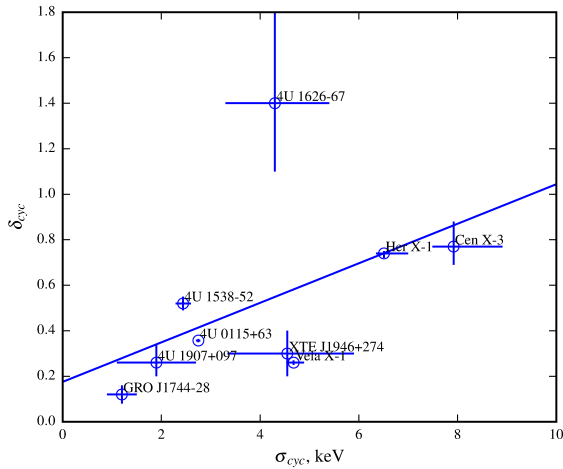


Figure 14.8: Correlation between CRSF width and CRSF depth. The green line shows the linear dependence  $\delta_{\text{cyc}} = 0.09\sigma_{\text{cyc}} + 0.175$ .



The line depth is not very well constrained, but if this deviation is real, it can be attributed to the fact that it has a low mass companion, which can imply a different accretion geometry and chemical composition of accreting plasma compared to other sources (see Chapter 6).

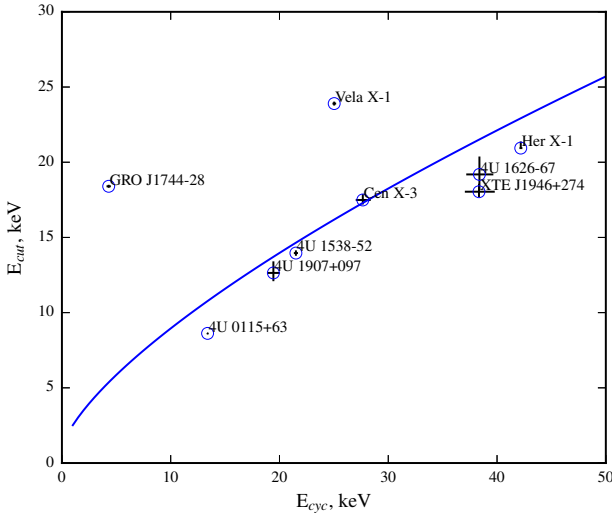


Figure 14.9: Correlation between CRSF energy and the Highest cutoff energy. The green line shows the approximation suggested by Makishima et al. (1999),  $E_{cut} \propto E_{cyc}^{0.7}$ .

Figures 14.9, 14.10 show the observed relation between the line centroid and the cutoff energies. This correlation was also reported previously by Makishima & Mihara (1992); Makishima et al. (1999); Coburn et al. (2002) who found  $E_{cut} \propto E_{cyc}^{0.7}$ , and associated cutoff with scattering around the cyclotron resonance energy. Coburn et al. (2002) confirmed this correlation based on a consistent analysis of a sample of pulsars observed by *RXTE* using the *Cutoffpl* model, and suggested a change of the correlation slope above  $\sim 35$  keV. *BeppoSAX* data is qualitatively consistent with this conclusion. Coburn et al. (2002) also discussed possible origins of this correlation. In particular, they argue that while the complex correlation between the CRSF and cutoff energies implies that the spectral break is related to the B-field, it is not necessarily a magnetic effect. For instance, the temperature in line forming region, which defines the cutoff, might depend on the magnetic field, thus resulting in a correlation of the CRSF and cutoff energies. Observations of a single

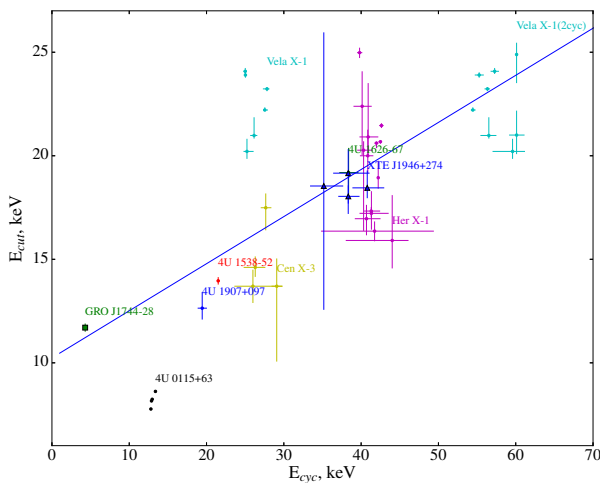


Figure 14.10: Correlation between CRSF energy and the Highcut cutoff energy for all *BeppoSAX* observations of all sources (with the first cyclotron line harmonic for Vela X–1). The blue line shows the linear dependence  $E_{\text{cut}} = 0.22E_{\text{cyc}} + 10.23$ .

source in a broad range of luminosities might be useful to clarify the situation. Unfortunately, none of the sources from our sample is suitable for such analysis due to the limited range of luminosities covered by *BeppoSAX* observations. Nevertheless, the observed phenomenological relation is definitively useful from an observational point of view, particularly if statistics are insufficient to really constrain the CRSF energy or even detect the line.

Besides the pulse-phase averaged spectroscopy, I have carried out also the pulse-phase resolved analysis. It is interesting, therefore, to investigate how variable the parameters of the cyclotron line are with respect to the pulse phase for the different sources. The width and depth of the line were not well constrained in most cases, so I focus here on the CRSF centroid behaviour. For each source and observation where pulse-phase resolved analysis was done, I calculated the relative amplitude of the CRSF centroid variability with pulse phase, defined in a same way as the pulsed fraction (i.e.  $A_{\text{E}_{\text{cyc}}} = (E_{\text{max}} - E_{\text{min}})/(E_{\text{max}} + E_{\text{min}})$ , Tab. 14.2). As illustrated in Figure 14.11, the amplitudes lie in the 5 – 10% range for all sources and do not strongly depend on line energy or luminosity.

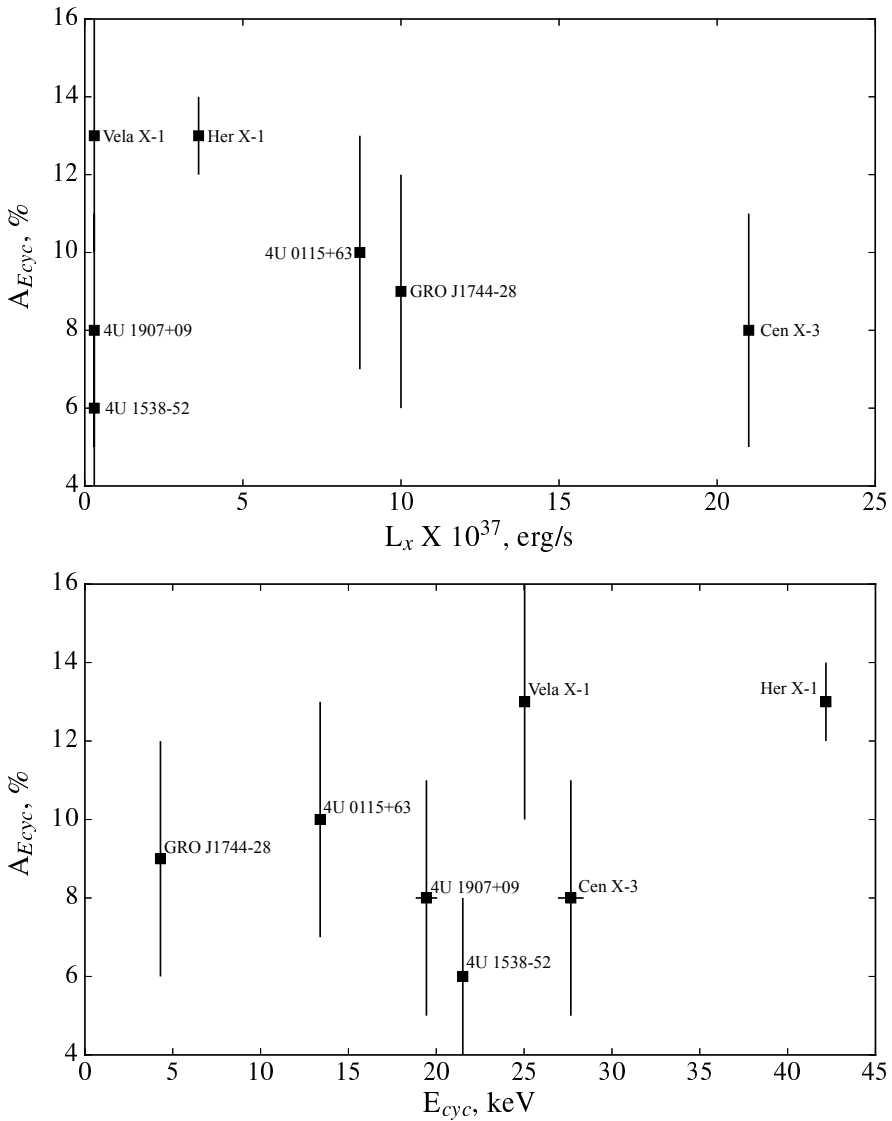


Figure 14.11: Dependence of the amplitude of the CRSF centroid variability with pulse phase (Tab. 14.2) on the X-ray luminosity (Tab. 14.1) and the average energy of the cyclotron line (Tab. 14.2).

### 14.1 The Accretion Regime and the Geometry of the Emission Region

In the X-ray pulsars with a strong magnetic field plasma is funnelled to the small regions on the NS surface close to the magnetic poles, the hotspots, at some distance from the NS where the magnetic pressure balances the ram pressure of the plasma (see Chapter 2). Above a certain luminosity, called *critical*, the strong radiation pressure force becomes dynamically significant and able to stop the infalling matter above the NS surface (Basko & Sunyaev 1976). The so-called accretion column starts to rise above the hotspot with the increase of the accretion rate. The two cases are usually referred to as sub- and super-critical accretion regimes. The column height depends on the luminosity and is believed to affect the observed CRSF energy, which is expected to be either correlated or anti-correlated with source flux (Tsygankov et al. 2006; Mushtukov et al. 2015).

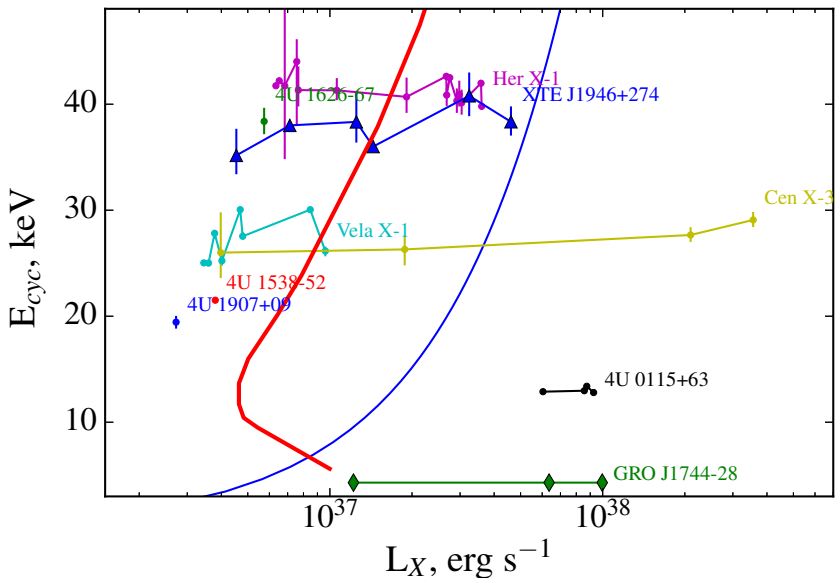


Figure 14.12: Dependence of the luminosity on the cyclotron line energy (the magnetic field strength). The red and blue curves corresponds to the critical luminosity calculated by Mushtukov et al. (2015) and Becker et al. (2012) respectively.

It is interesting, therefore, to compare the luminosities of the sources from our sample with their theoretically expected critical luminosities. Note that these are subject to large uncertainties both from a theoretical point of view and due to the uncertainty in the distances to individual sources. Nevertheless, Figure 14.12 shows the observed dependence of the CRSF energy on the estimated X-ray luminosity for sources observed by *BeppoSAX*. To reflect the uncertainty in the theoretical value of the critical luminosity, I also show two predictions: the red and blue lines correspond to the estimates by Mushtukov et al. (2015), and Becker et al. (2012) respectively. Table 14.1 lists the assumed distances which I used to determine the observed luminosities of the sources. Note, however, that in most cases these are based on photometry of the optical companion and as such subject to large uncertainties not reflected in Figure 14.12.

One could anticipate that the amplitude of the CRSF variability with pulse phase would be different for the two accretion regimes as the emission region geometries are different in two cases. This does not seem to be the case, however, as illustrated in Figure 14.11, which includes both sub- and super-critical observations. Note, however, that there are no theoretical predictions for the amplitude of the line variability, so it is not clear what to expect from a theoretical point of view.

Differences in the emission region geometry may also be expected to affect the observed width of the line. Since line width is correlated with line energy it is more appropriate, however, to look at the fractional width defined as  $\sigma_{\text{cyc}}/E_{\text{cyc}}$ . The line width is also expected to depend on temperature and, as discussed above, seems indeed to correlate with the cutoff energy, which traces the temperature. To investigate this in more detail, I calculated the fractional line width for each source and plotted it against the cutoff energy and temperature, as shown in Figure 14.13. It is interesting to note that the fractional line width appears to be higher for sources which are expected to be in super-critical accretion regime (i.e. Cen X-3, 4U 0115+63, GRO J1744-28). This could actually be anticipated as in this case the line forming region is expected to contain a range of field strengths which must broaden the line (Nishimura 2008).

As already mentioned, the observed widths of the line are most likely associated with Doppler broadening and the direction of photon propagation with respect to the magnetic field, i.e.  $\delta E_{\text{FWHM}}/E \sim \sqrt{kT} \langle \cos\theta \rangle$  with natural line widths of  $\sim 6$  keV at 40 keV (Meszaros 1992). The lines are thus expected to get broader with higher temperature and for photons propagating along the field lines. For super-critical accretion, the “fan” beam pattern is usually assumed, i.e. that the photons escape from side walls of the column and predominantly propagate perpendicularly to the field. Taking into account that the observed plasma temperatures are in fact comparable for all considered sources, one could expect that lines get narrower at high luminosities, i.e. in contrast to what is observed. This can be explained if

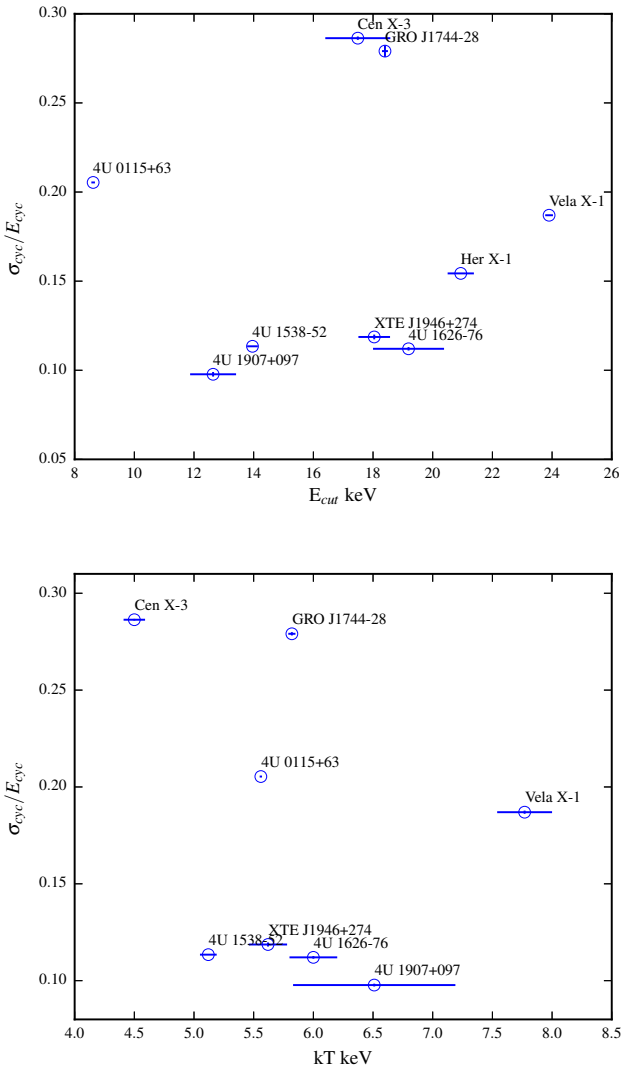


Figure 14.13: Dependences of the fractional line width ( $\sigma_{\text{cyc}}/E_{\text{cyc}}$ ) on the cutoff energy ( $E_{\text{cut}}$  in Highcut model, top figure) and plasma temperature ( $kT$  in CompTT model, bottom figure).

the field in the line forming region is not uniform, which is actually expected for an extended accretion column (Nishimura 2015). Alternatively, line broadening in the super-critical regime can be explained if the photons propagating along the field lines, rather than moving perpendicularly to them, are actually responsible for the observed CRSFs. This is realised in the “reflection” model of line formation recently proposed by Poutanen et al. (2013b).

The fractional line width is also correlated with the cutoff energy for both high- and low-luminosity sources. The correlation with temperature is, on the other hand, not so pronounced. The reason might be that, while the cutoff energy is generally expected to trace the temperature, the observed correlation between the two quantities is rather loose as illustrated in Figure 14.14. A possible explanation for that is related to the discussion of the correlation of the CRSF energy with the cutoff energy mentioned before. Makishima & Mihara (1992); Makishima et al. (1999) argued that the continuum cutoff is associated with scattering around the cyclotron resonance energy and, thus, is mostly a magnetic effect. On the contrary Coburn et al. (2002) suggested that the broadband continuum represents a comptonisation spectrum and, thus, the plasma temperature defines the cutoff energy. The latter interpretation seems to be more plausible, however, even in this case, the presence of the line may still affect the observed cutoff energy, which might explain its not so strong correlation with temperature and a tighter correlation of the cutoff energy with the CRSF parameters.

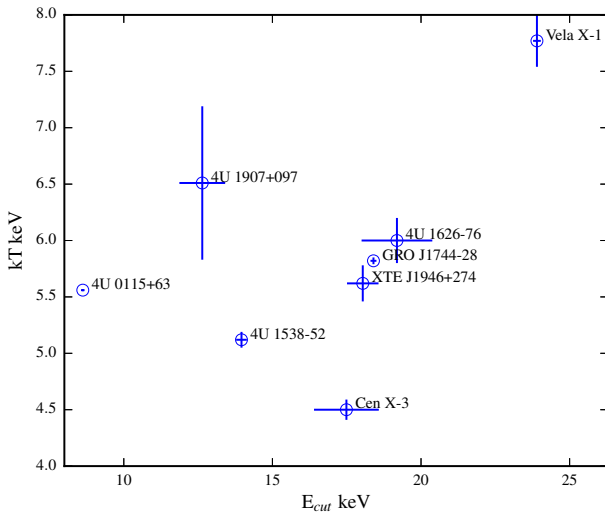


Figure 14.14: Dependence of the cutoff energy on the plasma temperature.



### Conclusion

The main goal of my work was to conduct a systematic and coherent investigation of the temporal and spectral properties of X-ray pulsars showing cyclotron lines. Therefore, I used as a homogeneous sample all bright accreting pulsars observed with instruments of the same satellite, the Italian-Dutch X-ray satellite *Bep-poSAX*, which provides high quality spectra in the broad energy range from 0.1 to 120 keV. Cyclotron lines in the spectra of X-ray pulsars are usually quite broad and shallow and, thus, the line parameters deduced from the spectral analysis can often be affected by the choice of the continuum model. I therefore systematically investigated, using different models, the influence of the spectral continuum on the determination of the CRSF parameters. In addition, for observations with high counting statistics, I performed pulse-phase resolved spectral analysis to investigate the phase dependence of the continuum and CRSF parameters for a variety of sources. Most of the data used in the project have not been analysed before and are presented in this thesis for the first time.

During the analysis, I have discovered a cyclotron line in the spectrum of the “bursting pulsar” GRO J1744–28, which was confirmed by D’Aì et al. (2015) using the observations of the source during its next major outburst in 2014. I have also identified a thermal component in the burst spectrum of the source, which appeared to be similar to that observed in classical bursters and which has been interpreted as evidence for thermonuclear burning episodes, likely triggered by rapid accretion rate fluctuations. These results were published in the Monthly Notices of the Royal Astronomical Society journal, MNRAS, (Doroshenko et al. 2015).

Analysis of observations of another poorly studied source, XTE J1946+274, also resulted in a publication (Doroshenko et al. 2017). Here we were able to clarify the long-standing debate regarding the energy of the CRSF observed in this source and we investigated in detail the phase dependence of the broadband spectrum.

A systematic analysis was performed for all sources in the sample, which lead to the results summarised in the thesis. In particular, for all sources and most observations I have

- carried out pulse-phase averaged spectral analysis using a set of six pre-defined continuum models,
- determined the spin periods of the neutron stars,
- obtained pulse profiles in several energy ranges and, if applicable, for several luminosities,
- investigated the dependence of the fraction of pulsed emission on energy and source flux,
- performed pulse-phase resolved spectral analysis for selected observations using models providing the best description of the spectrum for a given source.

The results were discussed in the context of finding already published literature, confirming in several cases results from other satellites. However, all commonly used continuum models were applied systematically to a large sample of sources for the first time. As a result, I have found that even the high quality *BeppoSAX* spectra can be approximated with all considered continuum models in most cases. Furthermore, I verified that the deduced cyclotron line energy does not strongly depend on the choice of the continuum model, if this properly describes the spectrum, as it is often claimed in the literature. On the other hand, it was not always possible to achieve a robust and well defined fit with all models and often the other line parameters, i.e. depth and width of the line, did depend on the choice of the continuum model.

I have found that in most cases the best and most robust description of the spectra is provided by a model consisting of a power law with an exponential cutoff at high energies (*Highecut* in *XSPEC*), complemented with a smoothing gaussian with energy tied to the cutoff energy.

In addition, I was able to empirically identify some features of the studied sample of pulsars, which are useful for future investigations of other sources and searches for new cyclotron lines:

- the cutoff and CRSF energies were found to be correlated in terms of  $E_{\text{cut}} \sim 0.2E_{\text{cyc}} + 10$ ,
- the width of the cyclotron line was found to be correlated with its energy in terms of  $\sigma_{\text{cyc}} \sim 0.14E_{\text{cyc}} + 0.1$ ,
- the depth of the cyclotron line was found to be correlated with its width as  $\delta_{\text{cyc}} \sim 0.1\sigma_{\text{cyc}} + 0.175$ ,
- the amplitude of variability of the observed line energy with pulse phase was  $\sim 10\%$  in all cases.

For some sources several observations at different luminosities were analysed, so I also investigated the luminosity dependence of the CRSF energy. No clear correlation or anti-correlation was found with only a hint for positive correlation of the line energy with flux observed for low luminosity sources like XTE J1946+274. I found, however, that the width of the CRSF seems to increase at high luminosities, likely due to the onset of an extended accretion column.

Finally, I also confirmed the presence of a soft excess below  $\sim 1$  keV for several objects, although it is hard to assess its origin based on *BeppoSAX* data alone.

# Bibliography

---

- Angelini, L., White, N. E., Nagase, F., et al. 1995, *ApJ*, 449, L41
- Arnaud, K. A. 1996, *Astronomical Data Analysis Software and Systems V*, 101, 17
- Ash, T. D. C., Reynolds, A. P., Roche, P., et al. 1999, *Monthly Notices of the Royal Astronomical Society*, 307, 357
- Baade, W. & Zwicky, F. 1934, *Proceedings of the National Academy of Sciences of the United States of America*, 20, 254
- Barbera, A. L., Burderi, L., Salvo, T. D., Iaria, R., & Robba, N. R. 2001, *The Astrophysical Journal*, 553, 375
- Barziv, O., Kaper, L., Van Kerkwijk, M. H., Telting, J. H., & Van Paradijs, J. 2001, *A&A*, 377, 925
- Basko, M. M. & Sunyaev, R. A. 1976, *Monthly Notices of the Royal Astronomical Society*, 175, 395, a&AA ID. AAA017.065.055
- Baykal, A., İnam, S. Ç., & Beklen, E. 2006, *Monthly Notices of the Royal Astronomical Society*, 369, 1760
- Becker, P. A., Klochkov, D., Schönherr, G., et al. 2012, *Astronomy & Astrophysics*, 544, 123
- Becker, P. A. & Wolff, M. T. 2007, *The Astrophysical Journal*, 654, 435
- Becker, R. H., Swank, J. H., Boldt, E. A., et al. 1977, *Astrophysical Journal*, 216, L11, a&AA ID. AAA020.142.013
- Bhalerao, V., Romano, P., Tomsick, J., et al. 2015, *Monthly Notices of the Royal Astronomical Society*, 447, 2274
- Bildsten, L. & Brown, E. F. 1997, *ApJ*, 477, 897
- Bildsten, L., Chakrabarty, D., Chiu, J., et al. 1994, *AIP Conf. Proc.*, 304, 294
- Bildsten, L., Chakrabarty, D., Chiu, J., et al. 1997, *Astrophysical Journal Supplement v.113*, 113, 367
- Bodaghee, A., Tomsick, J. A., Fornasini, F. M., et al. 2016, *ApJ*, 823, 146
- Boella, G., Butler, R. C., Perola, G. C., et al. 1997a, *A & A Supplement series*, 122, 299
- Boella, G., Chiappetti, L., Conti, G., et al. 1997b, *A & A Supplement series*, 122, 327
- Boldin, P. A., Tsygankov, S. S., & Lutovinov, A. A. 2013, *Astronomy Letters*, 39, 375
- Bondi, H. & Hoyle, F. 1944, *MNRAS*, 104, 273
- Bradt, H. V., Rothschild, R. E., & Swank, J. H. 1993, *A&AS*, 97, 355
- Brucato, R. J. & Kristian, J. 1972, *ApJ*, 173, L105
- Burderi, L., di Salvo, T., Robba, N. R., Barbera, A. L., & Guainazzi, M. 2000, *The Astrophysical Journal*, 530, 429

- Burderi, L., di Salvo, T., Robba, N. R., et al. 1998, *Astrophysical Journal* v.498, 498, 831
- Caballero, I., Pottschmidt, K., Bozzo, E., et al. 2010, *The Astronomer's Telegram*, 2692
- Caballero, I., Pottschmidt, K., Marcu, D. M., et al. 2013, *The Astrophysical Journal Letters*, 764, L23
- Camero-Arranz, A., Finger, M. H., Ikhsanov, N. R., Wilson-Hodge, C. A., & Beklen, E. 2010, *The Astrophysical Journal*, 708, 1500
- Camero-Arranz, A., Pottschmidt, K., Finger, M. H., et al. 2012, *Astronomy & Astrophysics*, 546, 40
- Campana, S., Gastaldello, F., Stella, L., et al. 2001, *ApJ*, 561, 924
- Campana, S., Israel, G., & Stella, L. 1999, *Astronomy and Astrophysics*, 352, L91
- Campana, S., Israel, G. L., Stella, L., & Santangelo, A. 1998, *IAU Circ.*, 7039, 2
- Campana, S., Stella, L., Israel, G. L., et al. 2002, *ApJ*, 580, 389
- Chakrabarty, D. 1998, *Astrophysical Journal* v.492, 492, 342
- Chakrabarty, D., Bildsten, L., Grunsfeld, J. M., et al. 1997, *Astrophysical Journal* v.474, 474, 414
- Chodil, G., Mark, H., Rodrigues, R., et al. 1967, *Physical Review Letters*, 19, 681
- Choi, C. S., Nagase, F., Makino, F., et al. 1994, *Astrophysical Journal*, 437, 449
- Citterio, O., Conti, G., Mattaini, E., Santambrogio, E., & Sacco, B. 1986, IN: *X-ray instrumentation in astronomy; Proceedings of the Meeting*, 597, 102
- Clark, G. W. 2000, *The Astrophysical Journal*, 542, L131
- Clark, G. W., Woo, J. W., Nagase, F., Makishima, K., & Sakao, T. 1990, *Astrophysical Journal*, 353, 274
- Coburn, W. 2001, PhD thesis, UNIVERSITY OF CALIFORNIA, SAN DIEGO
- Coburn, W., Heindl, W. A., Rothschild, R. E., et al. 2002, *ApJ*, 580, 394
- Cocchi, M., Bazzano, A., Natalucci, L., et al. 1999, *Astrophysical Letters and Communications*, 38, 133
- Cominsky, L., Clark, G. W., Li, F., Mayer, W., & Rappaport, S. 1978, *Nature*, 273, 367, a&AA ID. AAA021.142.143
- Conti, P. S. 1994, *Meeting: Evolution of massive stars*, 37
- Corbet, R. H. D., Woo, J. W., & Nagase, F. 1993, *Astronomy and Astrophysics*, 276, 52
- Cox, N. L. J., Kaper, L., Foing, B. H., & Ehrenfreund, P. 2005, *Astronomy and Astrophysics*, 438, 187
- Crampton, D. & Hutchings, J. B. 1974, *Astrophysical Journal*, 191, 483, a&AA ID. AAA012.121.005
- Crampton, D., Hutchings, J. B., & Cowley, A. P. 1978, *ApJ*, 225, L63
- Cui, W. 1997, *Astrophysical Journal Letters* v.482, 482, L163
- Cusumano, G., Salvo, T. D., Burderi, L., et al. 1998, *Astronomy and Astrophysics*, 338, L79
- D'Ai, A., Di Salvo, T., Iaria, R., et al. 2015, *ArXiv e-prints*
- Daigne, F., Goldoni, P., Ferrando, P., et al. 2002, *Astronomy and Astrophysics*, 386, 531
- dal Fiume, D., Orlandini, M., Cusumano, G., et al. 1998, *Astronomy and Astrophysics*, 329, L41
- Daumerie, P., Kalogera, V., Lamb, F. K., & Psaltis, D. 1996, *Nature*, 382, 141
- Davison, P. J. N., Watson, M. G., & Pye, J. P. 1977, *Monthly Notices of the Royal Astronom-*

- ical Society, 181, 73P, a&AA ID. AAA020.142.086
- Day, C. S. R. & Stevens, I. R. 1993, *Astrophysical Journal*, 403, 322
- Day, C. S. R. & Tennant, A. F. 1991, *Monthly Notices of the Royal Astronomical Society* (ISSN 0035-8711), 251, 76
- Decesar, M. E., Pottschmidt, K., & Wilms, J. 2009, *The Astronomer's Telegram*, 2036, 1
- Deeter, J. E., Boynton, P. E., & Pravdo, S. H. 1981, *Astrophysical Journal*, 247, 1003, a&AA ID. AAA030.142.009
- Degenaar, N., Miller, J. M., Harrison, F. A., et al. 2014, *ApJ*, 796, L9
- Degenaar, N., Wijnands, R., Cackett, E. M., et al. 2012, eprint arXiv, 1204, 6043, 25 pages, 13 figures, 4 tables, submitted to A&A
- del Sordo, S., dal Fiume, D., Oriandini, M., et al. 2000, *Advances in Space Research*, 25, 413
- Devasia, J., Paul, B., James, M., & Indulekha, K. 2010, *Research in Astronomy and Astrophysics*, 10, 1127
- di Salvo, T., Burderi, L., Robba, N. R., et al. 1999, *Astrophysical Letters and Communications*, 38, 117
- Doroshenko, R., Santangelo, A., Doroshenko, V., & Piraino, S. 2017, *A&A*, 600, A52
- Doroshenko, R., Santangelo, A., Doroshenko, V., Suleimanov, V., & Piraino, S. 2015, *MNRAS*, 452, 2490
- Doroshenko, V. 2011, PhD thesis, Universität Tübingen, Wilhelmstr. 32, 72074 Tübingen
- Doroshenko, V., Ducci, L., Santangelo, A., & Sasaki, M. 2014, *Astronomy & Astrophysics*, 567, A7
- Doroshenko, V., Santangelo, A., Ducci, L., & Klochkov, D. 2012, *A&A*, 548, A19
- Doroshenko, V., Santangelo, A., & Suleimanov, V. 2011, *A&A*, 529, A52
- Doroshenko, V., Santangelo, A., Suleimanov, V., et al. 2010a, *A&A*, 515, 10
- Doroshenko, V., Suchy, S., Santangelo, A., et al. 2010b, *Astronomy and Astrophysics*, 515, L1
- Dotani, T., Ueda, Y., Ishida, M., et al. 1996, *IAU Circ.*, 6337, 1
- Dupree, A. K., Gursky, H., Black, J. H., et al. 1980, *ApJ*, 238, 969
- Ebisawa, K., Ueda, Y., Inoue, H., Tanaka, Y., & White, N. E. 1996, *Astrophysical Journal* v.467, 467, 419
- Falanga, M., Bozzo, E., Lutovinov, A., et al. 2015, *A&A*, 577, A130
- Farinelli, R., Ferrigno, C., Bozzo, E., & Becker, P. A. 2016, *A&A*, 591, A29
- Ferrigno, C., Becker, P. A., Segreto, A., Mineo, T., & Santangelo, A. 2009, *Astronomy and Astrophysics*, 498, 825
- Ferrigno, C., Falanga, M., Bozzo, E., et al. 2011, *Astronomy & Astrophysics*, 532, 76
- Ferrigno, C., Segreto, A., Santangelo, A., et al. 2007, *A&A*, 462, 995
- Finger, M. H. 2010, *The Astronomer's Telegram*, 2847
- Finger, M. H., Beklen, E., Narayana Bhat, P., et al. 2009, *ArXiv e-prints*
- Finger, M. H., Koh, D. T., Nelson, R. W., et al. 1996, *Nature*, 381, 291
- Fishman, G. J., Kouveliotou, C., van Paradijs, J., et al. 1995, *IAU Circ.*, 6272, 1
- Forman, W., Jones, C., Cominsky, L., et al. 1978, *Astrophysical Journal*, 38, 357, a&AA ID. AAA022.002.059

- Forman, W., Jones, C., Tananbaum, H., et al. 1973, *ApJ*, 182, L103
- Fritz, S., Kreykenbohm, I., Wilms, J., et al. 2006, *Astronomy and Astrophysics*, 458, 885
- Frontera, F., Costa, E., dal Fiume, D., et al. 1997, *A & A Supplement series*, 122, 357
- Fürst, F., Kreykenbohm, I., Pottschmidt, K., et al. 2010, *A&A*, 519, A37
- Fürst, F., Pottschmidt, K., Wilms, J., et al. 2014, *The Astrophysical Journal Letters*, 784, L40
- Gerend, D. & Boynton, P. E. 1976, *Astrophysical Journal*, 209, 562, a&AA ID. AAA018.142.088
- Giacconi, R., Gursky, H., Kellogg, E., et al. 1973, *Astrophys. J.*, 184, 227, a&AA ID. AAA010.142.025
- Giacconi, R., Gursky, H., Kellogg, E., Schreier, E., & Tananbaum, H. 1971, *Astrophysical Journal*, 167, L67, a&AA ID. AAA006.142.005
- Giacconi, R., Murray, S., Gursky, H., et al. 1974, *ApJS*, 27, 37
- Giacconi, R., Murray, S., Gursky, H., et al. 1972, *Astrophysical Journal*, 178, 281, a&AA ID. AAA008.142.101
- Gnedin, I. N. & Sunyaev, R. A. 1974, *Astronomy and Astrophysics*, 36, 379, a&AA ID. AAA012.062.056
- Gruber, D. E., Heindl, W. A., Rothschild, R. E., et al. 2001, *ApJ*, 562, 499
- Haberl, F. & White, N. E. 1990, *ApJ*, 361, 225
- Heindl, W., Coburn, W., Kreykenbohm, I., & Wilms, J. 2003, *The Astronomer's Telegram*, 200, 1
- Heindl, W. A. & Chakrabarty, D. 1999, *Highlights in x-ray astronomy : international symposium in honour of Joachim Trümper's 65th birthday*, 25
- Heindl, W. A., Coburn, W., Gruber, D. E., et al. 1999, *The Astrophysical Journal*, 521, L49
- Heindl, W. A., Coburn, W., Gruber, D. E., et al. 2001a, *The Astrophysical Journal*, 563, L35
- Heindl, W. A., Coburn, W., Gruber, D. E., et al. 2001b, *The Astrophysical Journal*, 563, L35, (c) 2001: The American Astronomical Society
- Heinke, C. O., Ivanova, N., Engel, M. C., et al. 2013, *The Astrophysical Journal*, 768, 184
- Hemphill, P. B., Rothschild, R. E., Caballero, I., et al. 2013, *ApJ*, 777, 61
- Hewish, A., Bell, S. J., Pilkington, J. D. H., Scott, P. F., & Collins, R. A. 1968, *Nature*, 217, 709
- Hickox, R. C., Narayan, R., & Kallman, T. R. 2004, *The Astrophysical Journal*, 614, 881
- Hiltner, W. A., Werner, J., & Osmer, P. 1972, *ApJ*, 175, L19
- Howarth, I. D. & Wilson, B. 1983, *Monthly Notices of the Royal Astronomical Society*, 202, 347
- Hua, X.-M. & Titarchuk, L. 1995, *ApJ*, 449, 188
- Hutchings, J. B. 1976, *ApJ*, 203, 438
- Hutchings, J. B., Cowley, A. P., Crampton, D., van Paradijs, J., & White, N. E. 1979, *Astrophysical Journal*, 229, 1079, a&AA ID. AAA025.142.048
- Hutchings, J. B. & Crampton, D. 1981, *Astrophysical Journal*, 247, 222, a&AA ID. AAA029.114.166
- Illarionov, A. F. & Sunyaev, R. A. 1975, *A&A*, 39, 185
- in 't Zand, J. J. M., Baykal, A., & Strohmayer, T. E. 1998, *Astrophysical Journal* v.496, 496, 386

- Inam, S. Ç., Şahiner, Ş., & Baykal, A. 2009, *Monthly Notices of the Royal Astronomical Society*, 395, 1015
- in't Zand, J., Verbunt, F., Heise, J., et al. 2004, *Nuclear Physics B Proceedings Supplements*, 132, 486
- Iwakiri, W. B., Terada, Y., Mihara, T., et al. 2012, *The Astrophysical Journal*, 751, 35
- Iyer, N., Mukherjee, D., Dewangan, G. C., Bhattacharya, D., & Seetha, S. 2015, *MNRAS*, 454, 741
- Jager, R., Mels, W. A., Brinkman, A. C., et al. 1997, *A & A Supplement series*, 125, 557
- Jahoda, K., Stark, M. J., Strohmayer, T. E., et al. 1997, *ArXiv Astrophysics e-prints*
- Jaisawal, G. K. & Naik, S. 2015a, *MNRAS*, 453, L21
- Jaisawal, G. K. & Naik, S. 2015b, *eprint arXiv*, 1501, 1122
- Jaisawal, G. K. & Naik, S. 2016, *MNRAS*, 461, L97
- Jaisawal, G. K., Naik, S., & Paul, B. 2013, *The Astrophysical Journal*, 779, 54
- Kallman, T. R. & White, N. E. 1982, *ApJ*, 261, L35
- Kendziorra, E., Mony, B., Kretschmar, P., et al. 1992, In *NASA. Goddard Space Flight Center*, 3137, 217
- Kii, T., Hayakawa, S., Nagase, F., Ikegami, T., & Kawai, N. 1986, *Astronomical Society of Japan*, 38, 751
- Klochkov, D., Santangelo, A., Staubert, R., & Ferrigno, C. 2008, *Astronomy and Astrophysics*, 491, 833
- Klochkov, D., Staubert, R., Postnov, K., et al. 2015, *A&A*, 578, A88
- Kolliopoulos, F. & Gilfanov, M. 2016, *MNRAS*, 456, 3535
- Kommers, J. M., Chakrabarty, D., & Lewin, W. H. G. 1998, *Astrophysical Journal Letters* v.497, 497, L33
- Kouveliotou, C., van Paradijs, J., Fishman, G. J., et al. 1996, *Nature*, 379, 799
- Kraus, U. 2001, *ApJ*, 563, 289
- Kraus, U., Nollert, H.-P., Ruder, H., & Riffert, H. 1995, *Astrophysical Journal* v.450, 450, 763
- Kraus, U., Zahn, C., Weth, C., & Ruder, H. 2003, *ApJ*, 590, 424
- Kreykenbohm, I. 2004, PhD dissertation, Eberhard-Karls-Universität Tübingen
- Kreykenbohm, I., Coburn, W., Wilms, J., et al. 2002, *A&A*, 395, 129
- Kreykenbohm, I., Kretschmar, P., Wilms, J., et al. 1999, *A&A*, 341, 141
- Kreykenbohm, I., Wilms, J., Kretschmar, P., et al. 2008, *A&A*, 492, 511
- Krimm, H. A., Barthelmy, S. D., Baumgartner, W., et al. 2010, *The Astronomer's Telegram*, 2663, 1
- Krzeminski, W. 1974, *Astrophysical Journal*, 192, L135, a&AA ID. AAA012.142.073
- La Barbera, A., Santangelo, A., Orlandini, M., & Segreto, A. 2003, *A&A*, 400, 993
- Lai, D. 2001, *Reviews of Modern Physics*, 73, 629
- Landau, L. 1938, *Nature*, 141, 333
- Landau, L. D. 1932, *Phys. Zs. Sowjet.*, vol.1, p.285, 1932 (English and German), 1, 285
- Latal, H. G. 1986, *Astrophysical Journal*, 309, 372
- Lattimer, J. M. & Prakash, M. 2016, *Phys. Rep.*, 621, 127
- Levine, A., Ma, C. P., McClintock, J., et al. 1988, *Astrophysical Journal*, 327, 732



- Lewin, W. H. G., Doty, J., Clark, G. W., et al. 1976, *Astrophysical Journal*, 207, L95, a&AA ID. AAA018.142.026
- Lewin, W. H. G., Rutledge, R. E., Kommers, J. M., van Paradijs, J., & Kouveliotou, C. 1996, *ApJ*, 462, L39
- Lewin, W. H. G., van Paradijs, J., & Taam, R. E. 1993, *Space Science Reviews*, 62, 223
- Lewin, W. H. G., van Paradijs, J., & Taam, R. E. 1993, *Space Sci. Rev.*, 62, 223
- Li, J., Wang, W., & Zhao, Y. 2012, *MNRAS*, 423, 2854
- Li, J., Zhang, S., Torres, D. F., et al. 2012, eprint arXiv, 1207, 3989
- Liller, W. 1972, *IAU Circ.*, 2415, 1, a&AA ID. AAA007.142.129
- Lipunov, V. M., Börner, G., & Wadhwa, R. S. 1992, *Astrophysics of Neutron Stars*
- Liu, Q. Z., van Paradijs, J., & van den Heuvel, E. P. J. 2006, *Astronomy and Astrophysics*, 455, 1165
- Liu, Q. Z., van Paradijs, J., & van den Heuvel, E. P. J. 2007, *Astronomy and Astrophysics*, 469, 807
- Lutovinov, A., Tsygankov, S., Postnov, K., et al. 2016, ArXiv e-prints
- Lutovinov, A. A., Grebenev, S. A., & Sunyaev, R. A. 2000, *Astronomy Letters*, 26, 1
- Lutovinov, A. A., Grebenev, S. A., Syunyaev, R. A., & Pavlinskii, M. N. 1994, *Astronomy Letters*, 20, 538
- Lutovinov, A. A. & Tsygankov, S. S. 2009, *Astronomy Letters*, 35, 433
- Maitra, C. & Paul, B. 2013a, *ApJ*, 771, 96
- Maitra, C. & Paul, B. 2013b, *ApJ*, 763, 79
- Makishima, K. 1992, *Structure and Evolution of Neutron Stars*, 86
- Makishima, K., Kawai, N., Koyama, K., et al. 1984, *Astronomical Society of Japan*, 36, 679
- Makishima, K., Koyama, K., Hayakawa, S., & Nagase, F. 1987, *ApJ*, 314, 619
- Makishima, K. & Mihara, T. 1992, in *Frontiers Science Series*, ed. Y. Tanaka & K. Koyama, 23
- Makishima, K., Mihara, T., Ishida, M., et al. 1990, *Astrophysical Journal*, 365, L59
- Makishima, K., Mihara, T., Nagase, F., & Tanaka, Y. 1999, *The Astrophysical Journal*, 525, 978
- Malizia, A., Bassani, L., Stephen, J. B., et al. 2003, *The Astrophysical Journal*, 589, L17
- Manzo, G., Giarrusso, S., Santangelo, A., et al. 1997, *A & A Supplement series*, 122, 341
- Marcu-Cheatham, D. M., Pottschmidt, K., Kühnel, M., et al. 2015, *ApJ*, 815, 44
- Markwardt, C. B., Swank, J. H., & Corbet, R. 2007, *The Astronomer's Telegram*, 1176, 1
- McClintock, J. E., Bradt, H. V., Doxsey, R. E., et al. 1977, *Nature*, 270, 320, a&AA ID. AAA020.142.079
- McClintock, J. E., Li, F. K., Canizares, C. R., & Grindlay, J. E. 1980, *Astrophysical Journal*, 235, L81, a&AA ID. AAA027.142.007
- McClintock, J. E., Rappaport, S., Joss, P. C., et al. 1976, *ApJ*, 206, L99
- McCray, R. & Lamb, F. K. 1976, *Astrophysical Journal*, 204, L115, a&AA ID. AAA017.142.048
- McCray, R. A., Shull, J. M., Boynton, P. E., et al. 1982, *Astrophysical Journal*, 262, 301, a&AA ID. AAA032.142.106
- Meszáros, P. 1992, *Science*, 257, 1294

- Mihara, T. 1995, Ph.D. thesis, 215
- Mihara, T., Makishima, K., Kamijo, S., et al. 1991, *Astrophysical Journal*, 379, L61
- Mihara, T., Makishima, K., & Nagase, F. 1998, *Advances in Space Research*, 22, 987
- Mihara, T., Makishima, K., & Nagase, F. 2004, *The Astrophysical Journal*, 610, 390
- Mihara, T., Makishima, K., Ohashi, T., Sakao, T., & Tashiro, M. 1990, *Nature* (ISSN 0028-0836), 346, 250
- Mihara, T., Yamamoto, T., Sugizaki, M., & Yamaoka, K. 2010, *The Astronomer's Telegram*, 2796, 1
- Miller, G. S. 1996, *Astrophysical Journal Letters* v.468, 468, L29
- Müller, S., Ferrigno, C., Kühnel, M., et al. 2013, *Astronomy & Astrophysics*, 551, 6
- Müller, S., Kühnel, M., Caballero, I., et al. 2012, *Astronomy & Astrophysics*, 546, 125
- Mushtukov, A. A., Suleimanov, V. F., Tsygankov, S. S., & Poutanen, J. 2015, *MNRAS*, 447, 1847
- Nagase, F. 1989, in *ESA Special Publication, Vol. 296, Two Topics in X-Ray Astronomy, Volume 1: X Ray Binaries. Volume 2: AGN and the X Ray Background*, ed. J. Hunt & B. Batrick
- Nagase, F., Corbet, R. H. D., Day, C. S. R., et al. 1992, *Astrophysical Journal*, 396, 147
- Naik, S., Paul, B., & Ali, Z. 2011, *The Astrophysical Journal*, 737, 79
- Nakajima, M., Mihara, T., Makishima, K., & Niko, H. 2006, *The Astrophysical Journal*, 646, 1125
- Negueruela, I. & Okazaki, A. T. 2001, *Astronomy and Astrophysics*, 369, 108
- Nespoli, E., Fabregat, J., & Mennickent, R. E. 2008, *Astronomy and Astrophysics*, 486, 911
- Nishimura, O. 2008, *ApJ*, 672, 1127
- Nishimura, O. 2015, *ApJ*, 807, 164
- Nishiuchi, M., Koyama, K., Maeda, Y., et al. 1999, *The Astrophysical Journal*, 517, 436
- Okazaki, A. T. & Negueruela, I. 2001, *A&A*, 377, 161
- Oosterbroek, T., Parmar, A. N., Dal Fiume, D., et al. 2000, *A&A*, 353, 575
- Oosterbroek, T., Parmar, A. N., Martin, D. D. E., & Lammers, U. 1997, *Astronomy and Astrophysics*, 327, 215
- Oosterbroek, T., Parmar, A. N., Orlandini, M., et al. 2001, *A&A*, 375, 922
- Oppenheimer, J. R. & Volkoff, G. M. 1939, *Physical Review*, 55, 374
- Orlandini, M., dal Fiume, D., del Sordo, S., et al. 1999, *Astronomy and Astrophysics*, 349, L9
- Orlandini, M., dal Fiume, D., Frontera, F., et al. 1998, *A&A*, 332, 121
- Orlandini, M., dal Fiume, D., Frontera, F., et al. 1999, *Nuclear Physics B Proceedings Supplements*, 69, 158
- Orlandini, M., Fiume, D. D., Frontera, F., et al. 1998, *Astrophysical Journal Letters* v.500, 500, L163
- Orlandini, M., Frontera, F., Masetti, N., Sguera, V., & Sidoli, L. 2012, *ApJ*, 748, 86
- Özel, F. & Freire, P. 2016, *ARA&A*, 54, 401
- Pacini, F. 1968, *Nature*, 219, 145
- Parkes, G. E., Murdin, P. G., & Mason, K. O. 1978, *Monthly Notices of the Royal Astronomical Society*, 184, 73P, a&AA ID. AAA022.142.055

- Parmar, A. N., Martin, D. D. E., Bavdaz, M., et al. 1997, *A & A Supplement series*, 122, 309
- Parmar, A. N., Oosterbroek, T., dal Fiume, D., et al. 1999, *Astronomy and Astrophysics*, 350, L5
- Parmar, A. N., Pietsch, W., McKechnie, S., et al. 1985, *Nature* (ISSN 0028-0836), 313, 119
- Paul, B., Agrawal, P. C., Mukerjee, K., et al. 2001, *Astronomy and Astrophysics*, 370, 529
- Paul, B., Raichur, H., & Mukherjee, U. 2005, *Astronomy and Astrophysics*, 442, L15
- Perola, G. C., Matt, G., Cappi, M., et al. 2002, *Astronomy and Astrophysics*, 389, 802
- Piran, T. & Shaviv, N. J. 2004, eprint arXiv, 1553, 12 pages, 3 figure
- Poutanen, J., Mushtukov, A. A., Suleimanov, V. F., et al. 2013a, *ApJ*, 777, 115
- Poutanen, J., Mushtukov, A. A., Suleimanov, V. F., et al. 2013b, *ApJ*, 777, 115
- Pravdo, S. H., Becker, R. H., Boldt, E. A., et al. 1977, *Astrophysical Journal*, 215, L61, a&AA ID. AAA019.142.136
- Protassov, R., van Dyk, D. A., Connors, A., Kashyap, V. L., & Siemiginowska, A. 2002, *ApJ*, 571, 545
- Quaintrell, H., Norton, A. J., Ash, T. D. C., et al. 2003, *A&A*, 401, 313
- Raichur, H. & Paul, B. 2010, *Monthly Notices of the Royal Astronomical Society*, 401, 1532
- Ramsay, G., Zane, S., Jimenez-Garate, M. A., den Herder, J.-W., & Hailey, C. J. 2002, *Monthly Notice of the Royal Astronomical Society*, 337, 1185
- Rappaport, S., Clark, G. W., Cominsky, L., Li, F., & Joss, P. C. 1978, *Astrophysical Journal*, 224, L1, a&AA ID. AAA022.142.017
- Rappaport, S. & Joss, P. C. 1997, *Astrophysical Journal* v.486, 486, 435
- Rappaport, S., Joss, P. C., & Webbink, R. F. 1982, *Astrophysical Journal*, 254, 616, a&AA ID. AAA031.117.020
- Rawls, M. L., Orosz, J. A., McClintock, J. E., et al. 2011, *ApJ*, 730, 25
- Revnitsev, M. & Mereghetti, S. 2015, *Space Sci. Rev.*, 191, 293
- Reynolds, A. P., Bell, S. A., & Hilditch, R. W. 1992, *MNRAS*, 256, 631
- Reynolds, A. P., Quaintrell, H., Still, M. D., et al. 1997, *Monthly Notices of the Royal Astronomical Society*, 288, 43
- Robba, N. R., Burderi, L., Di Salvo, T., Iaria, R., & Cusumano, G. 2001, *ApJ*, 562, 950
- Rodes, J. J., Torrejón, J. M., & Bernabéu, J. G. 2008, "The X-ray Universe 2008" Symposium held in Granada, 56
- Rodes-Roca, J. J., Page, K. L., Torrejón, J. M., Osborne, J. P., & Bernabéu, G. 2011, *A&A*, 526, A64
- Rodes-Roca, J. J., Torrejón, J. M., Kreykenbohm, I., et al. 2009, *A&A*, 508, 395
- Rose, W. K. 1998, *Advanced Stellar Astrophysics*
- Roy, J., Tanti, K. K., Agrawal, P. C., & Duorah, K. 2011, *Proceedings of the 29th Meeting of the Astronomical Society of India*, 3, 139
- Rubin, B. C., Finger, M. H., Scott, D. M., & Wilson, R. B. 1997, *Astrophysical Journal* v.488, 488, 413
- Sadakane, K., Hirata, R., Jugaku, J., et al. 1985, *ApJ*, 288, 284
- Sako, M., Liedahl, D. A., Kahn, S. M., & Paerels, F. 1999, *ApJ*, 525, 921
- Santangelo, A., del Sordo, S., Segreto, A., et al. 1998, *Astronomy and Astrophysics*, 340, L55

- Santangelo, A., Segreto, A., Giarrusso, S., et al. 1999, *The Astrophysical Journal*, 523, L85
- Sasaki, M., Müller, D., Kraus, U., Ferrigno, C., & Santangelo, A. 2012, *A&A*, 540, A35
- Sasano, M., Makishima, K., Sakurai, S., Zhang, Z., & Enoto, T. 2014, *Publications of the Astronomical Society of Japan*, 66, 35
- Sato, N., Hayakawa, S., Nagase, F., et al. 1986, *PASJ*, 38, 731
- Schönherr, G., Schwarm, F.-W., Falkner, S., et al. 2014, *A&A*, 564, L8
- Schreier, E., Levinson, R., Gursky, H., et al. 1972, *Astrophysical Journal*, 172, L79, a&AA ID. AAA007.142.038
- Shakura, N. I., Prokhorov, M. E., Postnov, K. A., & Ketsaris, N. A. 1999, *Astronomy and Astrophysics*, 348, 917
- Shakura, N. I. & Sunyaev, R. A. 1973, *Astronomy and Astrophysics*, 24, 337, a&AA ID. AAA009.066.049
- Shinoda, K., Kii, T., Mitsuda, K., et al. 1990, *Astronomical Society of Japan*, 42, L27
- Smith, D. A. & Takeshima, T. 1998a, *IAU Circ.*, 7014, 1
- Smith, D. A. & Takeshima, T. 1998b, *The Astronomer's Telegram*, 36, 1
- Staubert, R., Bezler, M., & Kendziorra, E. 1983, *A&A*, 117, 215
- Staubert, R., Klochkov, D., Fürst, F., et al. 2017, *A&A*, 606, L13
- Staubert, R., Klochkov, D., Postnov, K., et al. 2009a, *Astronomy and Astrophysics*, 494, 1025
- Staubert, R., Klochkov, D., & Wilms, J. 2009b, *Astronomy and Astrophysics*, 500, 883
- Staubert, R., Klochkov, D., Wilms, J., et al. 2014, *A&A*, 572, A119
- Staubert, R., Kreykenbohm, I., Kretschmar, P., et al. 2004, in *ESA Special Publication*, Vol. 552, 5th INTEGRAL Workshop on the INTEGRAL Universe, ed. V. Schoenfelder, G. Lichti, & C. Winkler, 259
- Strickman, M. S., Dermer, C. D., Grove, J. E., et al. 1996, *Astrophysical Journal Letters* v.464, 464, L131
- Sturmer, S. J. & Dermer, C. D. 1996, *Astrophysical Journal Letters* v.465, 465, L31
- Suleimanov, V. F., Poutanen, J., Klochkov, D., & Werner, K. 2016, *European Physical Journal A*, 52, 20
- Sunyaev, R. A. & Titarchuk, L. G. 1985, *A&A*, 143, 374
- Takeshima, T., Dotani, T., Mitsuda, K., & Nagase, F. 1991, *Astronomical Society of Japan*, 43, L43
- Tamura, K., Tsunemi, H., Kitamoto, S., Hayashida, K., & Nagase, F. 1992, *Astrophysical Journal*, 389, 676
- Tananbaum, H., Gursky, H., Kellogg, E. M., et al. 1972, *Astrophysical Journal*, 174, L143, a&AA ID. AAA007.142.116
- Tauris, T. M. & van den Heuvel, E. P. J. 2006, *Formation and evolution of compact stellar X-ray sources*, 623–665
- Tendulkar, S. P., Fürst, F., Pottschmidt, K., et al. 2014, *The Astrophysical Journal*, 795, 154
- Titarchuk, L. 1994, *Astrophysical Journal*, 434, 570
- Titarchuk, L. & Lyubarskij, Y. 1995, *ApJ*, 450, 876
- Tolman, R. C. 1939, *Physical Review*, 55, 364
- Truemper, J., Pietsch, W., Reppin, C., et al. 1978, *Astrophysical Journal*, 219, L105, a&AA

- ID. AAA021.142.024
- Tsygankov, S. S., Krivonos, R. A., & Lutovinov, A. A. 2012, *Monthly Notices of the Royal Astronomical Society*, 421, 2407
- Tsygankov, S. S., Lutovinov, A. A., Churazov, E. M., & Sunyaev, R. A. 2006, *MNRAS*, 371, 19
- Tsygankov, S. S., Lutovinov, A. A., Churazov, E. M., & Sunyaev, R. A. 2007, *Astronomy Letters*, 33, 368
- Tsygankov, S. S., Lutovinov, A. A., Krivonos, R. A., et al. 2016, *MNRAS*, 457, 258
- Tutukov, A. & Yungelson, L. 1973, *Nauchnye Informatsii*, 27, 86, a&AA ID. AAA011.117.013
- van den Heuvel, E. P. J. 1983, *Accretion-Driven Stellar X-ray Sources*. Edited by Walter H.G. Lewin and Edward P.J. van den Heuvel. Cambridge: Cambridge University Press, 308
- van der Meer, A., Kaper, L., van Kerkwijk, M. H., Heemskerk, M. H. M., & van den Heuvel, E. P. J. 2007, *Astronomy and Astrophysics*, 473, 523
- van Kerkwijk, M. H., van Paradijs, J., Zuiderwijk, E. J., et al. 1995, *A&A*, 303, 483
- Vasco, D., Staubert, R., Klochkov, D., et al. 2013, *A&A*, 550, A111
- Verrecchia, F., Israel, G. L., Negueruela, I., et al. 2002, *Astronomy and Astrophysics*, 393, 983
- Voges, W., Pietsch, W., Reppin, C., et al. 1982, *ApJ*, 263, 803
- Vrtilek, S. D., Mihara, T., Primini, F. A., et al. 1994, *Astrophysical Journal*, 436, L9
- Watts, A. L., Andersson, N., Chakrabarty, D., et al. 2016, *Reviews of Modern Physics*, 88, 021001
- Wheaton, W. A., Doty, J. P., Primini, F. A., et al. 1979, *Nature*, 282, 240, a&AA ID. AAA026.142.064
- White, N. E., Swank, J. H., & Holt, S. S. 1983, *ApJ*, 270, 711
- Wijnands, R. & Wang, Q. D. 2002, *The Astrophysical Journal*, 568, L93
- Wilson, C. A., Finger, M. H., & Camero-Arranz, A. 2008, *The Astrophysical Journal*, 678, 1263
- Wilson, C. A., Finger, M. H., Coe, M. J., & Negueruela, I. 2003, *The Astrophysical Journal*, 584, 996
- Wilson, C. A., Finger, M. H., Wilson, R. B., & Scott, D. M. 1998, *IAU Circ.*, 7014, 2
- Wilson, R. B., Fishman, G. J., Finger, M. H., et al. 1993, *AIP Conf. Proc.*, 280, 291
- Woo, J. W., Clark, G. W., Levine, A. M., Corbet, R. H. D., & Nagase, F. 1996, *Astrophysical Journal* v.467, 467, 811
- Woods, P. M., Kouveliotou, C., van Paradijs, J., et al. 1999, *The Astrophysical Journal*, 517, 431
- Woods, P. M., Kouveliotou, C., van Paradijs, J., et al. 2000, *ApJ*, 540, 1062
- Yakovlev, D. G., Haensel, P., Baym, G., & Pethick, C. 2013, *Physics Uspekhi*, 56, 289
- Yamamoto, T., Mihara, T., Sugizaki, M., et al. 2014, *PASJ*, 66, 59
- Younes, G., Kouveliotou, C., Grefenstette, B. W., et al. 2015, *ApJ*
- Zane, S., Ramsay, G., Jimenez-Garate, M. A., den Herder, J. W., & Hailey, C. J. 2004, *Monthly Notices of the Royal Astronomical Society*, 350, 506
- Zasov, A. V. & Postnov, K. A. 2011, *General astrophysics* (978-5-85099-188-3)

Zhang, Z. & Li, X.-D. 2010, *Astronomy and Astrophysics*, 518, 19

## List of Figures

---

1.1	An up-to-date compilation of NS mass measurements in various source categories. From Özel & Freire (2016). . . . .	16
1.2	Artist’s representation of a binary system with a Roche lobe accretion. . . . .	17
1.3	A compact object in an eccentric orbit around <i>Be</i> star (i.e. accretion is coming directly from stellar wind, see Bondi & Hoyle 1944). When the compact object is in the periastron passage - the outbursts are observed. When it is outside the periastron, the <i>Be</i> XRB is in quiescence. Image from Kreykenbohm (2004) . .	20
1.4	Schematic view of the cross-section for equipotential surface in the Roche theory. Some equipotential lines and the Lagrange points are indicated. The star $M_2$ fills it’s Roche lobe. . . . .	21
1.5	Evolution of a massive close binary system with a NSs or a BHs formation (Tutukov & Yungelson 1973). T - is the characteristic duration of the stage, N - estimate of the number of binaries in the Galaxy, $\nu$ - frequency of events. Image from Zasov & Postnov (2011). . . . .	23
2.1	Summary of the various accretion regimes: from wind and from the accretion disk. Image from Doroshenko (2011). . . . .	27
2.2	Schematic representation of the two possible geometries of the accretion column: “hollow” and “solid”, as presented by Basko & Sunyaev (1976). . . . .	28
2.3	Theoretical model of the spectrum for Her X–1 by Becker & Wolff (2007). The plot shows the total spectrum as well as contributions from the comptonised thermal, bremsstrahlung and cyclotron emission. . . . .	30
2.4	Emission line at $\sim 58$ keV in spectrum of Her X–1 as reported by Truemper et al. (1978). Subsequent observations showed that it was in fact an absorption feature at $\sim 42$ keV. . . . .	33
3.1	<i>BeppoSAX</i> scientific payload accommodation (Boella et al. 1997a). . . . .	36

3.2	Effective area of BeppoSAX instruments as function of energy (Boella et al. 1997a). Picture courtesy of “Space Research Organisation”, Netherlands (SRON). . . . .	38
5.1	Her X–1 MECS light curves for observations summarised in Table 5.1. Top left picture is the main-on state on 24.07.1996 (257th 35 <sup>d</sup> cycle), at the top right is the end of main-on state on 27.06.1998 (277). Bottom left: the short-on state on 09.07.1998 (277). Bottom right: the short-on state on 12.07.1998 (277). . .	49
5.2	Her X–1 MECS light curve for observations summarised in Table 5.1. Top left: the short-on state (eclipse) on 14.07.1998 (277). Top right: the anomalous low state on 08.07.1999. Bottom left: the main-on state on 09.10.2000 (301). Bottom right: the short-on state on 08.02.2001 (304). . . . .	50
5.3	Her X–1, 24.07.1996. LECS (0.1–0.5, 0.5–1, 1–4 keV), MECS (4–10 keV), HP (10–15 keV) and PDS (15–20, 20–40, 40–60, 60–120 keV) pulse profiles. . . . .	51
5.4	Her X–1 pulse fraction in the main-on state, 24.07.1996, 257th 35-day cycle. . . . .	52
5.5	Her X–1 contours (1, 2 and 3 $\sigma$ ) for different continuum models in the main-on state, 24.07.1996, 257th 35-day cycle. . . . .	53
5.6	Her X–1 broadband spectrum. The top panel shows the 0.1–110 keV unfolded spectrum modeled using a cutoff power law and black body continuum model modified by Fe L and Fe K emission lines and an absorption gaussian line at $\sim 42$ keV to account for cyclotron line during the observation on 1996-07-24. The residuals are shown in the bottom panels (1. Cyclotron and Fe K lines residuals. 2. The best fit residuals, $\chi^2_{\text{red}} \approx 1.16$ .)	55
5.7	Her X–1. Photon Index as function of 35 <sup>d</sup> phase with (bottom panel) and without (top panel) inclusion of the partial covering absorber. . . . .	59
5.8	Her X–1. Variation of spectral parameters with pulse phase (dotted green line shows the MECS pulse profile for reference) during the observation on 1996-07-24 (main-on state, 257 cycle).	60
6.1	4U 1626–67 pulse profiles as a function of energy. LECS (0.1–2 keV), MECS (2–4, 4–6, 6–8, 8–10 keV), HP (10–15 keV) and PDS (15–30, 30–45, 45–60 keV). . . . .	66
6.2	4U 1626–67 pulse fraction computed from the pulse profiles. $P = 7.6679(1)$ s. . . . .	67



6.3	4U 1626–67 broadband 0.2 – 100 keV unfolded spectrum described with the best fit continuum model (cutoff power law with a soft black body component, a narrow emission line at $\sim 1$ keV and the absorption gaussian line at $\sim 38$ keV to account for the CRSF) as observed by <i>BeppoSAX</i> . The second panel shows residuals associated with the cyclotron line. The best fit residuals are also shown in the bottom panel. . . . .	69
6.4	4U 1626–67. Phase dependence of the parameters of the <i>Highcut</i> continuum models (blue dashed - MECS pulse profile in 2 – 10 keV, green dotted - PDS pulse profile in 15 – 60 keV energy range). . . . .	72
7.1	4U 1907+09, LECS, MECS, HPGSPC and PDS light curves during the <i>BeppoSAX</i> observation. . . . .	74
7.2	The pulse profiles of the X-ray pulsar 4U 1907+09 as a function of energy. LECS (0.1 – 4 keV), MECS (4 – 10 keV), HP (10 – 15 keV) and PDS (15 – 20, 20 – 30, 30 – 40, 40 – 50 keV). . . . .	75
7.3	4U 1907+09, pulse fraction. . . . .	76
7.4	4U 1907+09 contours (1, 2 and $3\sigma$ ) for different continuum models. . . . .	78
7.5	The top panel shows the 4U 1907+09 broadband 0.1 – 110 keV unfolded spectrum with high energy cutoff continuum model ( <i>Highcut</i> ) with Fe-emission line and two absorption gaussian lines at $\sim 19$ and $\sim 39$ keV as observed by <i>BeppoSAX</i> . The residuals are shown in the bottom panels (1. Two cyclotron and Fe-lines residuals. 2. The best fit residuals, $\chi^2_{\text{red}} \approx 1.24$ ). . . . .	79
7.6	4U 1907+09. Changing spectral parameters with phase with <i>Highcut</i> continuum model (dashed blue line is the MECS pulse profile in 2 – 10 keV, dotted green line - PDS pulse profile in 15 – 60 keV energy ranges). Absorption column $N_{\text{H}}$ and iron line parameters were fixed at the average values. . . . .	81
8.1	4U 1538–52, LECS, MECS, HPGSPC (with the 256 s bin time) and PDS (455 s bin time) light curves during the <i>BeppoSAX</i> observation. . . . .	83
8.2	The pulse profiles of the X-ray pulsar 4U 1538–52 as a function of energy. LECS (0.1 – 4 keV), MECS (4 – 10 keV), HP (10 – 20 keV) and PDS (20 – 25, 25 – 30, 30 – 50, 50 – 60 keV). . . . .	84
8.3	4U 1538–52, pulse fraction. . . . .	85

8.4	4U 1538–52. The best-fit residuals for the considered continuum models. Note that Fdcut does not provide an adequate description for the spectrum. The NPEX, Cutoffpl, CompTT models require additional emission line-like component, i.e. “bump” at $\sim 12$ keV which is not required for Highecut and BW models. Out of these two models the former provides a statistically better fit. . . . .	86
8.5	4U 1538–52 contours (1, 2 and $3\sigma$ ) for different continuum models. . . . .	87
8.6	4U 1538–52. Top panel shows the broadband 0.1 – 120 keV unfolded spectrum with the cut-off power law (Highecut) continuum model including the iron line line and two absorption features $\sim 21$ keV and $\sim 52$ keV as observed by <i>BeppoSAX</i> . Bottom panel shows residuals for (1.Cyclotron and Fe-lines residuals. 2. The best fit residuals with $\chi_{red}^2 \approx 1.06$ .) . . . . .	89
8.7	4U 1538–52. Changing spectral parameters with phase with the Highecut continuum model (the dashed blue line is the MECS pulse profile in the 2 – 10 keV energy range and the dotted green line is the PDS pulse profile in the 15 – 60 keV energy range). . . . .	90
9.1	The MECS light curves of Vela X–1 in 2 – 10 keV energy range. On the top panels are observations from 1996-07-14 (low and high states; left) and 1996-12-23/24 (right). Bottom: 1997-11-24 (the low state, the high state, contains several flares, and the eclipse; left) and 1997-12-24/25 (during this observation a few flares and the off-state were observed; right) dates of observations. . . . .	95
9.2	The pulse profiles of the X-ray pulsar Vela X–1, in 1996-12-24, as a function of energy. LECS (0.1 – 4 keV), MECS (4 – 7, 7 – 10 keV), HPGSPC (10 – 20 keV) and PDS (20 – 60, 60 – 120 keV). . . . .	96
9.3	Vela X–1, 1996-12-24, pulse fraction. . . . .	97
9.4	Vela X–1 spectral residuals for four different continuum models in 1996-12-24. . . . .	98
9.5	Top panel shows the broadband 2 – 120 keV unfolded spectrum of Vela X–1 observed on 1996-12-24 approximated with a cut-off power law continuum model (Highecut) modified by Fe-emission line and absorption Gaussian lines at $\sim 25$ keV and $\sim 55$ keV. Bottom panel shows residuals for: 1) Cyclotron and Fe-lines residuals; 2) The best fit residuals. $\chi_{red}^2 \approx 0.8$ .) . . . .	99

9.6	The best-fit residuals for Vela X-1 broadband spectrum for all <i>BeppoSAX</i> observations and <i>Highcut</i> continuum model. . . .	100
9.7	Vela X-1 spectral residuals after exclusion from the model of the emission iron and cyclotron lines for all <i>BeppoSAX</i> observations (again, for <i>Highcut</i> continuum model). . . . .	101
9.8	Vela X-1, 1996-12-24. Variation of the best-fit spectral parameters with pulse phase for <i>Highcut</i> continuum model. For reference the pulse profiles in the 2 – 10 keV (MECS data, dashed blue line), and 15 – 120 keV energy ranges (PDS data, dotted green line) are also shown. . . . .	102
10.1	On the top panels are the Cen X-3 light curves during the low states using the MECS data. The left panel shows the light curve on 1996-08-12, the right panel illustrates an X-ray eclipse during the low state on 2000-06-06. On the bottom panels are the Cen X-3 light curves during the high states using the MECS data. The two panels correspond to observations performed on 1997-02-27 (left) and 1999-06-24 (right). Both light curves also illustrate the X-ray eclipse. The time binning is 128 s in all cases.	110
10.2	The pulse profiles of the X-ray pulsar Cen X-3 from the 1997-02-27 observation as a function of energy using the LECS (0.1 – 2, 2 – 4 keV), MECS (4 – 7, 7 – 10 keV), HP (10 – 15 keV) and PDS (15 – 20, 20 – 40, 40 – 60 keV) data. . . . .	111
10.3	The pulse profiles of the X-ray pulsar Cen X-3 from the 1999-06-24 observations as a function of energy using the LECS (0.1 – 2, 2 – 4 keV), MECS (4 – 7, 7 – 10 keV) and PDS (15 – 20, 20 – 40, 40 – 60 keV) data. . . . .	112
10.4	Cen X-3 pulse fractions in high states: 1997-02-27 (top) and 1999-06-24 (bottom). . . . .	113
10.5	$E_{\text{cyc}} - \sigma_{\text{cyc}}$ contours for the different continuum models used for Cen X-3. High state, 1997-02-27. . . . .	114
10.6	The top panel shows the broadband 0.1 – 110 keV unfolded spectrum of Cen X-3 during the observation 1997-02-27 modeled with a power law, a high energy cutoff ( <i>Highcut</i> ), a black body soft excess, and two narrow iron emission lines. The absorption gaussian line at $\sim 28$ keV was also included to account for the CRSF. The other panels show the fit residuals for: 1) Cyclotron, Fe-lines and the black-body component residuals. 2) Fe-lines and black-body residuals. 3) The best fit residuals. . .	116

10.7	Cen X-3. Variation of spectral parameters with the pulse phase (dashed blue line shows the MECS pulse profile for reference, dotted green line shows the PDS) during the observation on 1997-02-27 (high state). . . . .	118
10.8	Cen X-3. MECS pulse profile in the low state in 1996-08-12 with the period of $P=4.823(1)$ s. . . . .	120
10.9	Cen X-3, observation 1996-08-12, low state. The top panel shows the broadband 0.5–100 keV unfolded spectrum modeled with partial covered absorbed cutoff power law (Highecut). The black-body excess, two iron lines and the absorption feature at $\sim 26$ keV are also included in the fit. The other panels shows residuals associated with 1) The cyclotron, the iron lines, and the soft-excess. 2) The cyclotron line and the soft excess. 3) The best-fit residuals. . . . .	121
11.1	4U 0115+63. ASM light curve. Dashed lines are the <i>BeppoSAX</i> observations: 1999-03-06, 1999-03-19, 1999-03-22, 1999-03-26, 1999-08-03, 2000-08-13. . . . .	126
11.2	The pulse profiles of 4U 0115+63 as observed on 1999-03-22 as a function of energy. LECS (0.1 – 2 keV), MECS (2 – 4, 4 – 6, 6 – 8, 8 – 10 keV), HPGSPC (10 – 15, 15 – 20 keV) and PDS (20 – 30, 30 – 60, 60 – 90, 90 – 120 keV). . . . .	127
11.3	4U 0115+63 pulse fraction in 1999-03-06. . . . .	128
11.4	4U 0115+63 spectral residuals for four different continuum models tested for the first <i>BeppoSAX</i> observation on 1999-03-06. . . . .	130
11.5	The top panel shows the broadband 0.6 – 120 keV unfolded spectrum of 4U 0115+63 modeled as a cutoff power law (Highecut) continuum modified by a Fe-emission line and a cyclotron line with its harmonics for the 1999-03-06 observation. The other panels show the residuals associated with: 1) the iron line, 2) the best-fit residuals ( $\chi^2_{\text{red}} \approx 1.2$ ). . . . .	131
11.6	4U 0115+63 residuals associated with the cyclotron line and its harmonics for the 1999-03-06 observation (Highecut continuum model) from top to bottom respectively: $E_{\text{cyc}1} = 13.39^{+0.07}_{-0.04}$ keV, $E_{\text{cyc}2} = 22.55^{+0.05}_{-0.07}$ keV, $E_{\text{cyc}3} = 33.94^{+0.46}_{-0.09}$ keV, $E_{\text{cyc}4} = 44.08^{+0.96}_{-0.17}$ keV, $E_{\text{cyc}5} = 54.32^{+0.44}_{-0.43}$ keV. . . . .	132
11.7	4U 0115+63 spectral residuals for four <i>BeppoSAX</i> observations during the 1999 outburst with the Highecut continuum model. . . . .	132

11.8	4U 0115+63. Variation of the spectral parameters with phase during the 1999-03-06 observation for the <i>Highecut</i> continuum model (dashed blue line is the MECS pulse profile in 2 – 10 keV, dotted green line is the PDS pulse profile in 15 – 120 keV energy ranges). . . . .	133
12.1	Light curves of XTE J1946+274 as observed by <i>RXTE/ASM</i> . Dashed lines are <i>BeppoSAX</i> observations. . . . .	139
12.2	XTE J1946+274 pulse period as observed by <i>BeppoSAX</i> . Uncertainties errors are given with $1\sigma$ confidence level (for the most points errors are inside the circles). . . . .	141
12.3	The pulse profiles of XTE J1946+274 in 11 energy bands observed with the <i>BeppoSAX</i> satellite by LECS, MECS, HPGSPC and PDS instruments in 9th of October, 1998. . . . .	142
12.4	The luminosity dependence of the soft (MECS data in 2 – 10 keV range, black points), and hard (PDS data in 20 – 40 keV, red crosses) normalised pulse profiles along the outburst. . . . .	143
12.5	XTE J1946+274 pulse fraction for the brightest <i>BeppoSAX</i> observation in 10-09-1998. The emission feature is around cyclotron line energy, $E_{\text{cyc}} \sim 38$ keV. . . . .	144
12.6	Unfolded spectrum of XTE J1946+274 on 1998-10-09 fitted with <i>Highecut</i> +bb continuum model (top panel). The middle and bottom panels show the best-fit residuals without and with inclusion of iron and cyclotron lines, respectively. . . . .	145
12.7	Phase dependence of the spectral parameters for the brightest observation with <i>Highecut</i> +bb model. Blue dashed and green dotted lines show for reference MECS (2 – 10 keV) and PDS (15 – 120 keV) pulse profiles, scaled to match the respective parameter range. The lower right panel shows the hardness ratio for the same energy bands. . . . .	149
13.1	The light curve of GRO J1744–28 observed by the ASM onboard <i>RXTE</i> . Dashed lines mark the <i>BeppoSAX</i> observations (Tab. 13.1). . . . .	155
13.2	MECS light curve with bursts of the pulsar GRO J1744–28 in 1997-03-21 with 2 s bin time in 2 – 10 keV energy range. On the zoom picture the flux drop after the burst is shown. . . . .	156
13.3	Light curves of all bursts of the pulsar GRO J1744–28 in 1997-03-21 (top) and 1997-03-27 (bottom), MECS. . . . .	157
13.4	Pulse profiles of the pulsar GRO J1744–28 in 1997-03-21 for LECS (0.1 – 4 keV), MECS (4 – 7, 7 – 11.5 keV) and PDS (12 – 45, 45 – 100 keV). The spin period is $P = 0.467044(1)$ s. . . . .	158

13.5	Pulse fraction of the pulsar GRO J1744–28 for 1997-03-21 - solid black line, 1997-03-27 - dashed red line, 1997-04-12 - dashed dotted blue line. . . . .	159
13.6	MECS image centered at GRO J1744–28 in quiescence on 1998-04-02 overlaid with contours from an observation in bright state (taken on 1997-03-21). Two additional sources detected in the MECS field of view contaminate also the PDS spectrum. . . . .	160
13.7	The best-fit residuals for spectra derived from the observation 1997-03-21 modeled as described in the main text. The best residuals obtained with the power law plus high-energy cutoff model, <i>Highecut</i> , at the top panel. . . . .	162
13.8	The best-fit unfolded average persistent spectrum, modelled with the <i>Highecut</i> continuum is shown in the top panel. We also present the best fit residuals without and with the inclusion of a cyclotron line at $\sim 4.5$ keV. The best fit spectrum of the bursts modelled with <i>Highecut</i> and a black body continuum is also presented together with the residuals for the observation 1997-03-21. . . . .	164
13.9	Spectral parameters of the pulsar GRO J1744–28 in 1997-03-21 with the <i>Highecut</i> continuum model as function of pulse phase. Phase: 0 – 0.1, 0.1 – 0.2, 0.2 – 0.3, 0.3 – 0.4, 0.4 – 0.5, 0.5 – 0.6, 0.6 – 0.7, 0.7 – 0.8, 0.8 – 0.9, 0.9 – 1. Dashed lines are the MECS and PDS pulse profiles, they are the same. . . . .	165
13.10	Changing normalisation of the soft (top) and hard (bottom) part of the bursts spectrum with phase for the GRO J1744–28 in 1997-09-21. $\chi^2_{\text{red}}$ lies in region from 0.97 to 1.45. . . . .	169
13.11	Cooling of the soft component, during the bursts. The probability that the observed temperatures are due to a statistical fluctuation is $\leq 1.7 \times 10^{-8}$ (from Kolmogorov-Smirnov test), so the trend is significant. . . . .	169
14.1	The best fits of the spectra for the sources observed by <i>Bep-poSAX</i> and the residuals: Her X–1 (1996-07-24 - left, 1998-07-09 - right), 4U 1626–67 (1996-08-06), 4U 1907+09 (1997-09-27), 4U 1538–52 (1998-07-29), Vela X–1 (1996-12-24). Part 1. . . . .	174
14.2	The best fits of the spectra for the sources observed by <i>Bep-poSAX</i> and the respective residuals: Cen X–3 (1997-02-27 - left, 1996-08-12 - right), 4U 0115+63 (1999-03-06), XTE J1946+274 (1998-10-09), GRO J1744–28 (1997-03-21). Part 2. . . . .	175

14.3	Changes of the cyclotron line energy and width with different continuum models of the <i>BeppoSAX</i> sources with the cyclotron line, which were analysed in this work. . . . .	177
14.4	Changes of the cyclotron line depth and $\chi_{\text{red}}^2$ with different continuum models of the <i>BeppoSAX</i> sources with the cyclotron line, which were analysed in this work. . . . .	178
14.5	Correlation between the CRSF energy and width. The blue line shows the linear fit to the points with $\sigma_{\text{cyc}} = 0.12E_{\text{cyc}} + 0.8$ . . . . .	181
14.6	Correlation between CRSF energy and CRSF width for all <i>BeppoSAX</i> observations in the sample. The blue line shows the linear dependance $\sigma_{\text{cyc}} = 0.14E_{\text{cyc}} + 0.1$ . . . . .	183
14.7	Correlation between CRSF energy and depth. The green line shows the linear dependance $\delta_{\text{cyc}} = 0.02E_{\text{cyc}} + 0.02$ . . . . .	184
14.8	Correlation between CRSF width and CRSF depth. The green line shows the linear dependance $\delta_{\text{cyc}} = 0.09\sigma_{\text{cyc}} + 0.175$ . . . . .	184
14.9	Correlation between CRSF energy and the <i>Highecut</i> cutoff energy. The green line shows the approximation suggested by Makishima et al. (1999), $E_{\text{cut}} \propto E_{\text{cyc}}^{0.7}$ . . . . .	185
14.10	Correlation between CRSF energy and the <i>Highecut</i> cutoff energy for all <i>BeppoSAX</i> observations of all sources (with the first cyclotron line harmonic for Vela X-1). The blue line shows the linear dependance $E_{\text{cut}} = 0.22E_{\text{cyc}} + 10.23$ . . . . .	186
14.11	Dependence of the amplitude of the CRSF centroid variability with pulse phase (Tab. 14.2) on the X-ray luminosity (Tab. 14.1) and the average energy of the cyclotron line (Tab. 14.2). . . . .	187
14.12	Dependence of the luminosity on the cyclotron line energy (the magnetic field strength). The red and blue curves corresponds to the critical luminosity calculated by Mushtukov et al. (2015) and Becker et al. (2012) respectively. . . . .	188
14.13	Dependences of the fractional line width ( $\sigma_{\text{cyc}}/E_{\text{cyc}}$ ) on the cut-off energy ( $E_{\text{cut}}$ in <i>Highecut</i> model, top figure) and plasma temperature (kT in <i>CompTT</i> model, bottom figure). . . . .	190
14.14	Dependence of the cutoff energy on the plasma temperature. . . . .	192

## List of Tables

---

2.1	List of cyclotron sources . . . . .	34
4.1	List of sources with cyclotron line observed by <i>BeppoSAX</i> . . .	40
5.1	<i>BeppoSAX</i> observations of Her X-1. . . . .	48
5.2	Her X-1. Main-on state on 1996-07-24, 257 35-day cycle. Parameters of the 4 different continuum models of the phase averaged Her X-1 spectrum. The values of an absorbed and unabsorbed fluxes are $F_{\text{ab}} = 6.68 \times 10^{-9} \text{erg / cm}^2/\text{s}$ , $F_{\text{unab}} = 6.97 \times 10^{-9} \text{erg / cm}^2/\text{s}$ respectively. . . . .	54
5.3	Her X-1. Changing parameters with orbital cycles of the Her X-1 in power law with high energy cut off continuum model ( <i>Highecut</i> ). Part 1, main-on states. . . . .	58
5.4	Her X-1. Variation of the parameters with orbital cycles of the Her X-1 in power law with high energy cut off continuum model ( <i>Highecut</i> ). There are no low energy data (LECS) in some observations to determine values of $N_{\text{H}}$ and $kT_{\text{bb}}$ .Part 2, main-on states. . . . .	61
5.5	Her X-1. Changing parameters with orbital cycles of the Her X-1 in power law with high energy cut off ( <i>Highecut</i> ) and power law, high energy cut off with partial covering continuum model. Part 3, short-on states. . . . .	62
5.6	Her X-1. Spectral parameters as a function of pulse phase during the observation on 1996-07-27 (main-on state, 257 cycle). The interstellar absorption was fixed to the average value of $N_{\text{H}} = 1.09 \times 10^{20} \text{atoms cm}^{-2}$ . Part 1. . . . .	63
5.7	Her X-1. Spectral parameters as a function of pulse phase during the observation on 1996-07-27 (main-on state of 257 cycle). The interstellar absorption was fixed to the average value of $N_{\text{H}} = 1.09 \times 10^{20} \text{atoms cm}^{-2}$ . Part 2. . . . .	64



6.1	4U 1626–67 parameters of the 4 different continuum models of the phase averaged spectrum. The absorbed and unabsorbed fluxes in the range 0.1 – 120 keV are $F_{\text{ab}} = 5.78 \cdot 10^{-10}$ ergs $\text{cm}^{-2}\text{s}^{-1}$ , $F_{\text{unab}} = 5.92 \cdot 10^{-10}$ ergs $\text{cm}^{-2}\text{s}^{-1}$ respectively. . . . .	70
6.2	4U 1626–67. Best-fit parameters for the pulse phase resolved spectrum for <b>Highecut</b> continuum model. The interstellar absorption was fixed at the average value $N_{\text{H}} = 9.3 \times 10^{20}$ atoms $\text{cm}^{-2}$ for all phase bins. . . . .	71
7.1	4U 1907+09 parameters of the 5 different continuum models of the phase averaged spectrum. The absorbed and unabsorbed fluxes in the range 0.1 – 120 keV are $F_{\text{ab}} = 7.72 \cdot 10^{-10}$ ergs $\text{cm}^{-2}\text{s}^{-1}$ , $F_{\text{unab}} = 9.14 \cdot 10^{-10}$ ergs $\text{cm}^{-2}\text{s}^{-1}$ respectively. . . . .	77
7.2	Phase resolved spectral parameters of 4U 1907+09 for the <b>Highecut</b> continuum model. The interstellar absorption and Fe-line parameters were fixed at the average values: $N_{\text{H}} = 2.72^{+0.06}_{-0.09}$ atoms $\text{cm}^{-2}$ ; $E_{\text{Fe}} = 6.44^{+0.07}_{-0.03}$ keV, $\sigma_{\text{Fe}} = 0.005$ keV, $A_{\text{Fe}} = 2.2^{+0.5}_{-0.4} \times 10^{-4}$ ph $\text{cm}^{-2}\text{s}^{-1}$ . . . . .	80
8.1	The best-fit parameters of the 5 different continuum models of the phase averaged spectrum of 4U 1538–52. The absorbed and unabsorbed fluxes are $F_{\text{ab}} = 9.24 \times 10^{-10}$ erg / $\text{cm}^2/\text{s}$ , $F_{\text{unab}} = 1.05 \times 10^{-9}$ erg / $\text{cm}^2/\text{s}$ respectively. . . . .	88
8.2	4U 1538–52. Phase resolved spectral parameters for the <b>Highecut</b> continuum model. The interstellar absorption and parameters of the first cyclotron line harmonic were fixed at the average values: $N_{\text{H}} = 2.72^{+0.06}_{-0.09}$ atoms $\text{cm}^{-2}$ ; $E_{2\text{cyc}} = 52.09^{+2.0}_{-1.71}$ keV, $\sigma_{2\text{cyc}} = 3.64^{+1.04}_{-1.13}$ keV. Part 1. . . . .	92
8.3	4U 1538–52. Dependence of spectral parameters of 4U 1538–52 on pulse phase for the <b>Highecut</b> continuum model. The interstellar absorption and parameters of the first cyclotron line harmonic were fixed at the average values: $N_{\text{H}} = 2.72^{+0.06}_{-0.09}$ atoms $\text{cm}^{-2}$ ; $E_{2\text{cyc}} = 52.09^{+2.0}_{-1.71}$ keV, $\sigma_{2\text{cyc}} = 3.64^{+1.04}_{-1.13}$ keV. Part 2. . . . .	92
9.1	<i>BeppoSAX</i> observations of Vela X–1 analysed in our work. . .	94
9.2	The best-fit parameters of the broadband phase averaged spectrum of Vela X–1 for four different continuum models (for the representative observation performed on 1996-12-24). The absorbed and unabsorbed fluxes in 2 – 120 keV energy range are $F_{\text{ab}} = 6.2 \times 10^{-9}$ erg / $\text{cm}^2/\text{s}$ , $F_{\text{unab}} = 7.2 \times 10^{-9}$ erg / $\text{cm}^2/\text{s}$ respectively. . . . .	103

9.3	Variation of the spectral parameters of Vela X-1 with time/orbital phase for the cutoff power law continuum model ( <i>Highcut</i> ). Part 1. . . . .	104
9.4	Variation of the spectral parameters of Vela X-1 with time/orbital phase for the cutoff power law continuum model ( <i>Highcut</i> ). Part 2. . . . .	105
9.5	Part 1. The best-fit parameters for pulse phase resolved spectral analysis of Vela X-1 using the <i>Highcut</i> continuum model (observation 1996-12-24). The absorption column has been fixed to the average value $N_{\text{H}} = 3.15^{+0.03}_{-0.04}$ atoms $\text{cm}^{-2}$ . . . . .	106
9.6	Part 2. The best-fit parameters for pulse phase resolved spectral analysis of Vela X-1 using the <i>Highcut</i> continuum model (observation 1996-12-24). The absorption column has been fixed to the average value $N_{\text{H}} = 3.15^{+0.03}_{-0.04}$ atoms $\text{cm}^{-2}$ . . . . .	107
10.1	<i>BeppoSAX</i> observations of Cen X-3. . . . .	109
10.2	Cen X-3. The best-fit parameters for different continuum models for the high state observations 1997-02-27 and 1999-06-24. The absorbed and unabsorbed fluxes in the range of 0.1 – 120 keV for the first observation are $F_{\text{ab}} = 9.55 \cdot 10^{-9}$ erg $\text{cm}^{-2}\text{s}^{-1}$ , $F_{\text{unab}} = 2.74 \cdot 10^{-8}$ erg $\text{cm}^{-2}\text{s}^{-1}$ respectively. For the second observation: $F_{\text{ab}} = 1.03 \cdot 10^{-8}$ erg $\text{cm}^{-2}\text{s}^{-1}$ , $F_{\text{unab}} = 4.65 \cdot 10^{-8}$ erg $\text{cm}^{-2}\text{s}^{-1}$ . . . . .	117
10.3	Phase resolved spectral parameters of Cen X-3 during the high state observation in 1997-02-27 with the <i>Highcut</i> continuum model. The interstellar absorption and black body parameters have been fixed at the average values. . . . .	119
10.4	Parameters of the phase averaged spectrum of Cen X-3 in low states with <i>Highcut</i> +PC continuum model. . . . .	122
11.1	<i>BeppoSAX</i> observations of 4U 0115+63. . . . .	126
11.2	4U 0115+63. Continuum models for the observation in the 1999-03-06. The absorbed and unabsorbed fluxes in the range 0.1 – 120 keV are $F_{\text{ab}} = 1.42 \cdot 10^{-8}$ erg $\text{cm}^{-2}\text{s}^{-1}$ , $F_{\text{unab}} = 1.49 \cdot 10^{-8}$ erg $\text{cm}^{-2}\text{s}^{-1}$ respectively. . . . .	129
11.3	Variation of the spectral parameters of 4U 0115+63 with luminosity during the outburst from <i>BeppoSAX</i> observations and the <i>Highcut</i> continuum model. . . . .	134
11.4	Part 1. Variation of the spectral parameters of 4U 0115+63 with pulse phase during the observation 1999-03-06 for <i>Highcut</i> continuum model. The absorption column, the iron line energy and the width, and all cyclotron lines widths have been fixed to the phase-average values. . . . .	135

11.5	Part 2. Variation of the spectral parameters of 4U 0115+63 with pulse phase during the observation 1999-03-06 for <i>Highecut</i> continuum model. The absorption column, the iron line energy and the width, all cyclotron lines widths and the cyclotron line harmonic energy $E_{cyc5}$ have been fixed to the phase-average values. . . . .	136
12.1	Observations of the X-ray pulsar XTE J1946+274 by <i>BeppoSAX</i> . 140	
12.2	Pulse-period history of XTE J1946+274. For the <i>BeppoSAX</i> data, pulsations have been obtained using the phase connection method. Values for <i>RXTE</i> , <i>IXAE</i> and <i>Suzaku</i> are known from Smith & Takeshima (1998b); Paul et al. (2001); Müller et al. (2012); Maitra & Paul (2013a). . . . .	140
12.3	XTE J1946+274 parameters of the four continuum models applied to the phase averaged spectrum during the brightest observation. The absorbed and unabsorbed fluxes reported in the range 0.1 – 120 keV are $F_{ab} = 4.03 \cdot 10^{-9}$ ergs $\text{cm}^{-2}\text{s}^{-1}$ , $F_{unab} = 4.27 \cdot 10^{-9}$ ergs $\text{cm}^{-2}\text{s}^{-1}$ respectively. . . . .	146
12.4	Variation parameters of XTE J1946+274 with flux, during decay of the 1998 yr outburst observed by <i>BeppoSAX</i> with <i>Highecut</i> continuum model. . . . .	147
12.5	Parameters of the spectrum of XTE J1946+274 in 1998-10-09 with different description of the continuum: <i>Highecut</i> + <i>bb</i> , <i>Highecut</i> + <i>PC</i> and <i>Fdcut</i> + <i>Gauss</i> . The values of absorbed and unabsorbed fluxes in 0.1 – 120 keV energy range are $F_{ab} = 4.04 \times 10^{-9}$ erg/cm <sup>2</sup> /s, $F_{unab} = 4.27 \times 10^{-9}$ erg/cm <sup>2</sup> /s. . . .	148
12.6	XTE J1946+274, 1998-10-09. Variation of the spectral parameters with pulse phase assuming <i>Highecut</i> continuum model. The absorption, the energy and width of the emission iron and cyclotron lines and the temperature of the black body component were fixed at the average values. . . . .	150
13.1	Observations of the X-ray source GRO J1744–28 by <i>BeppoSAX</i> . Luminosity is estimated using unabsorbed flux in the energy range 2 – 10 keV (MECS) for the distance $D = 8$ kpc. . . . .	154
13.2	Spectral parameters of the persistent spectrum of GRO J1744–28 observed by <i>BeppoSAX</i> in 1997-03-21 for various spectral models. All energies and line widths are given in keV. . . . .	161
13.3	Spectral parameters of the persistent spectrum of the low mass X-ray pulsar GRO J1744–28 observed by <i>BeppoSAX</i> modelled by the <i>Highecut</i> continuum model. All energies and line widths are given in keV. . . . .	163

13.4	GRO J1744–28. Spectral parameters as function of pulse phase during the observation on 1997-03-21, <i>Highecut</i> continuum model. The interstellar absorption was fixed at the average value $N_{\text{H}} = 5.7(2) \times 10^{22}$ atoms $\text{cm}^{-2}$ . Part 1. . . . .	166
13.5	GRO J1744–28. Spectral parameters as function of pulse phase during the observation on 1997-03-21, <i>Highecut</i> continuum model. The interstellar absorption was fixed at the average value $N_{\text{H}} = 5.7(2) \times 10^{22}$ atoms $\text{cm}^{-2}$ . Part 2. . . . .	167
13.6	The best-fit parameters of the bursts spectrum GRO J1744–28 in 1997-03-21. All the energies and the line widths are given in keV. The absorbed and unabsorbed fluxes in 0.1 – 120 keV energy range are $F_{\text{ab}} = 6.09 \times 10^{-8}$ erg $\text{cm}^{-2}$ $\text{s}^{-1}$ , $F_{\text{unab}} = 6.83 \times 10^{-8}$ erg $\text{cm}^{-2}$ $\text{s}^{-1}$ . . . . .	168
14.1	Sample of the sources observed by <i>BeppoSAX</i> , their types, orbital and spin periods, X-ray luminosity (in the 0.1 – 120 keV energy band) and distance. Results are presented for one observation from each source. . . . .	173
14.2	Cyclotron lines energies and the values of the pulsars magnetic fields for the sources observed by <i>BeppoSAX</i> . . . . .	176
14.3	The best-fit parameters of the X-ray pulsars in the sample for the <i>Highecut</i> continuum with a smoothing Gaussian at the cutoff energy (one observation for each source). Part 1. . . . .	179
14.4	The best-fit parameters of the X-ray pulsars in the sample for the <i>Highecut</i> continuum with a smoothing Gaussian at the cutoff energy (one observation for each source). Part 2. . . . .	180
14.5	The best-fit parameters of the X-ray pulsars in the sample for the <i>CompTT</i> continuum model (one observation for each source). Part 1. . . . .	181
14.6	The best-fit parameters of the X-ray pulsars in the sample for the <i>CompTT</i> continuum model (one observation for each source). Part 2. . . . .	182

# Acronyms

---

**BH** Black Hole

**CRSF** Cyclotron Resonance Scattering Feature

**FWHM** Full Width at Half Maximum

**GRB** Gamma Ray Burst

**HMXB** High Mass X-ray Binary

**HPGSPC** High Pressure Gas Scintillation Proportional Counter

**LECS** Low Energy Concentrator Spectrometer

**LMXB** Low Mass X-ray Binary

**MECS** Medium Energy Concentrator Spectrometers

**NFI** Narrow Field Instruments

**NS** Neutron Star

**PDS** Phoswich Detector System

**QPO** Quasi-Periodic Oscillation

**UCXB** Ultra Compact X-ray Binary

**WD** White Dwarf

**WFC** Wide Field Cameras

**WR-star** Wolf-Rayet star

**XRB** X-ray Binary System

## Curriculum Vitae

---

- 18.01.1983 Born in Kazan, Russia
- 1990 – 1998 School N39, Kazan, Russia
- 1998 – 2000 Physics and Mathematics Lyceum N1 at Kazan State University, Kazan, Russia
- 2000 – 2002 Kazan State University, Faculty of Physics, Kazan, Russia
- 2002 – 2007 M.S. equivalent, faculty of Physics at Moscow State University, Russia.  
Specialisation: Astrophysics  
Degree Thesis: *Study of X-Ray Pulsars Using INTEGRAL Data*;  
Supervisor: Prof. Dr. K. Postnov
- Since 08/2007 Ph.D. student at the University of Tübingen, Germany.  
Project title: *A systematic study of the X-ray cyclotron-line sources observed by BeppoSAX*;  
Supervisor: Prof. Dr. A. Santangelo

## List of Publications:

---

Doroshenko, R. F.; Doroshenko, V. A.; Postnov, K. A.; Cherepashchuk, A. M.; Tsygankov, S. S.: “*INTEGRAL Observations of X-Ray Pulsars X 1845-024 and XTE J1858+034*” 2007, Proc. of the 6th INTEGRAL workshop.

Doroshenko, V. A.; Doroshenko, R. F.; Postnov, K. A.; Cherepashchuk, A. M.; Tsygankov, S.: “*A study of the X-ray pulsars X1845-024 and XTE J1858+034 based on INTEGRAL observations.*” 2008, Astronomy Reports, 52, 138-151

Doroshenko, V.; Santangelo, A.; Kreykenbohm, I.; Doroshenko, R.: “*The hard X-ray emission of X Persei*” 2012, Astronomy and Astrophysics, 540, L1

Doroshenko, V.; Santangelo, A.; Doroshenko, R; Caballero, I.; Tsygankov, S.; Rothschild, R.: “*XMM-Newton observations of 1A 0535+262 in quiescence*” 2014, Astronomy and Astrophysics, 561, A96

Doroshenko, R.; Santangelo, A.; Doroshenko, V.; Suleimanov, V.; Piraino, S.: “*BeppoSAX observations of GRO J1744-28: cyclotron line detection and the softening of the burst spectra*” 2015, MNRAS, 452, 2490

Doroshenko, R.; Santangelo, A.; Doroshenko, V.; Piraino, S.: “*BeppoSAX observations of XTE J1946+274*” 2017, Astronomy and Astrophysics, 600, A52

## Acknowledgements

---

This thesis would not have been possible without the support of many people, and I would like to express my deep gratitude to all those who have helped me over the years. I would like to thank my colleagues for the warm and friendly atmosphere I found myself surrounded when joining you, and working with you over these years.

First of all, I would like to express my sincere gratitude to my supervisor, Prof. Dr. Andrea Santangelo, for having invited me to Tübingen ten years before, putting up with me, supporting and encouraging me, and believing in me. Thank you.

I would also like to thank Dr. Santina Piraino for teaching how to work with the BeppoSAX, and always being ready to help, explain, and show how to make the right decision.

My words of gratitude are also sent to Dr. Eckhard Kendziorra for everything he had done for us. We remember.

I would also like to thank Dr. Chris Tenzer for his work and responsiveness, and Angela Heynen for her willingness to help with the documents, and her warmth.

Thank you, Cornelia Heinitz, for being a good office mate, greening our office, and for the ventilator that saved us on those hot days. And, of course, for help with the manuscript, and translating the abstract into German.

My special thanks and appreciation also go to my cousin Dr. Bulat Khalitov, Dr. Alejandro Guzman, Dr. Sara Saeedi, and Daniel Gottschall for their willingness to help and proofread the manuscript.

I would like to express my gratitude to Dr. Valery Suleimanov, my teacher, colleague and a very good friend, for his help, encouragement, and support, his care, and all the knowledge he gave me.

I would like to thank Prof. Dr. Konstantin Aleksandrovich Postnov, who supervised my diploma thesis in Moscow, and taught me to study.

I am also deeply grateful to Dr. Georgy Viktorovich Zhukov, my first teacher of astronomy at school, who showed me the way to the world of stars.

I would like to thank my friends, Dr. Elena Salakhyan and Eduard Vlad, who have been patient with me, encouraged me, and shared the joy with me.

My deepest gratitude and a low bow go to my grandparents, Ludmila Andreevna Tajsina and Anvar Safovich Tajsin, who are no longer with us. They have made a



huge and invaluable contribution to my education, and instilled a love for science in me.

I would also like to deeply thank my parents, Aleksander Vladimirovich Kokorin and Lilia Anvarovna Kokorina. Mama, you are the very best and loving mother in the world, who always believe in me, is proud of me, and support me in everything. You had the courage to let me first go to another city, and then to another country. My mum, so far away from me, and always next to me, I always feel your presence and support.

I would also like to thank my sister, Dr. Sofia Batrshina, for being here for me, and finding the right words in every situation.

Finally, I thank you, my beloved husband Victor for your continuous support and encouragement, care and understanding, your faith, patience, and love. For 15 years now, almost half of my life, we have been together in sorrow and joy. There would have been nothing without you. Thank you. And I thank you, my wonderful and beloved children, Olesya and Maxim. You are my life; you are my everything, and you are part of this thesis.

I appreciate each of you. Thank you.